Geology and stable isotope geochemistry of Paleoarchean sulfur

Formation, preservation and geobiology of ancient pyrite and barite

Desiree Roerdink

UTRECHT STUDIES IN EARTH SCIENCE

No. 031

Members of the dissertation committee:

Prof. Dr. James Farquhar
Department of Geology, University of Maryland
College Park, United States

Prof. Dr. Gary Stevens
Department of Geology, Stellenbosch University
Stellenbosch, South Africa

Prof. Dr. Jan Wijbrans
Faculty of Science, University of Leiden
Leiden, The Netherlands

Prof. Dr. Harald Strauss
Institut für Geologie und Paläontologie, Westfälische Wilhelms-Universität
Münster, Germany

Dr. Martin J. Whitehouse
Swedish Museum of Natural History
Stockholm, Sweden

ISBN 978-90-6266-324-8
Printed by Wöhrmann Print Service, Zutphen

All photos in this thesis were made by Desiree Roerdink.
Photo on cover: the Barberton Greenstone Belt from Malolotja Nature Reserve, Swaziland.

The work described in this thesis was financially supported by the User Support Programme Space Research and The Netherlands Organization for Scientific Research, and was carried out at the Faculty of Geosciences, Utrecht University, The Netherlands.

Geology and stable isotope geochemistry of Paleoarchean sulfur

Formation, preservation and geobiology of ancient pyrite and barite

Geologie en stabiele isotope geochemie van Paleoarchaeische zwavel

Oorsprong, behoud en geobiologie van miljarden jaren oude pyriet en bariet

(met een samenvatting in het Nederlands)

PROEFSCHRIFT

ter verkrijging van de graad van doctor aan de Universiteit Utrecht
op gezag van de rector magnificus, prof. dr. G.J. van der Zwaan, ingevolge het
besluit van het college voor promoties in het openbaar te verdedigen
op vrijdag 17 mei 2013 des middags te 4.15 uur.

door

Desirée Lisette Roerdink

geboren op 26 februari 1985
te Apeldoorn

Promotor:

Prof. dr. M.R. Drury

Co-promotors:

Dr. P.R.D. Mason

Dr. C.J. Peach

TABLE OF CONTENTS

Sibebe Rock, Hhohho, Swaziland

Chapter 1

Introduction

1.1 INTRODUCTION

Less than one billion years after its formation, the Earth changed from a lifeless planet into a habitable world (Fig. 1.1). The oldest putative evidence for microbial activity comes from reduced carbon in 3.8 Ga* rocks from West Greenland (Rosing, 1999), although most claims for early life from this region (e.g. Schidlowski et al., 1979; Schidlowski, 1988; Mojzsis et al., 1996) are controversial because of intense metamorphism that complicates geological interpretations and disputes the biogenicity of the samples (Rose et al., 1996; Rosing et al., 1996; Fedo and Whitehouse, 2002; Van Zuilen et al., 2002). More convincing evidence comes from microfossils, stromatolites and geochemical signatures in low metamorphic grade sedimentary rocks from South Africa and Australia that suggest flourishing of microbial life by the Paleoarchean, the period from 3.6 Ga to 3.2 Ga covered in this thesis (e.g. Walsh, 1992; Ohmoto et al., 1993; Shen et al., 2001; Westall et al., 2001; Banerjee et al., 2006; Allwood et al., 2007; Ueno et al., 2008; Allwood et al., 2009; Shen et al., 2009; Javaux et al., 2010; Wacey et al., 2010; Wacey et al., 2011a; Wacey et al., 2011b).

Many studies have shown that the element sulfur played an important role in the emergence and evolution of early microbial life (reviewed by Shen and Buick, 2004), which is supported by the presence of micro-organisms at the base of the phylogenetic tree that metabolize sulfur compounds to obtain energy for growth (Canfield and Raiswell, 1999). Evidence for the ancient origin of such microbial activity can be also found in the rock record from the stable isotopic compositions of well-preserved oxidized and reduced sulfur minerals in sedimentary rocks (Ohmoto et al., 1993; Shen et al., 2001; Ueno et al., 2008; Shen et al., 2009; Wacey et al., 2010). Sulfur is an element especially suited for this study, because biological redox reactions generate characteristic isotope ratios in their reactants and products (reviewed by Johnston, 2011). As such, this principle provides us with an important tool for the reconstruction of the early sulfur cycle on Earth and possibly other planetary bodies, such as Mars where sulfate deposits are present (Squyres et al., 2004).

* *Giga annum*, or billion years ago.

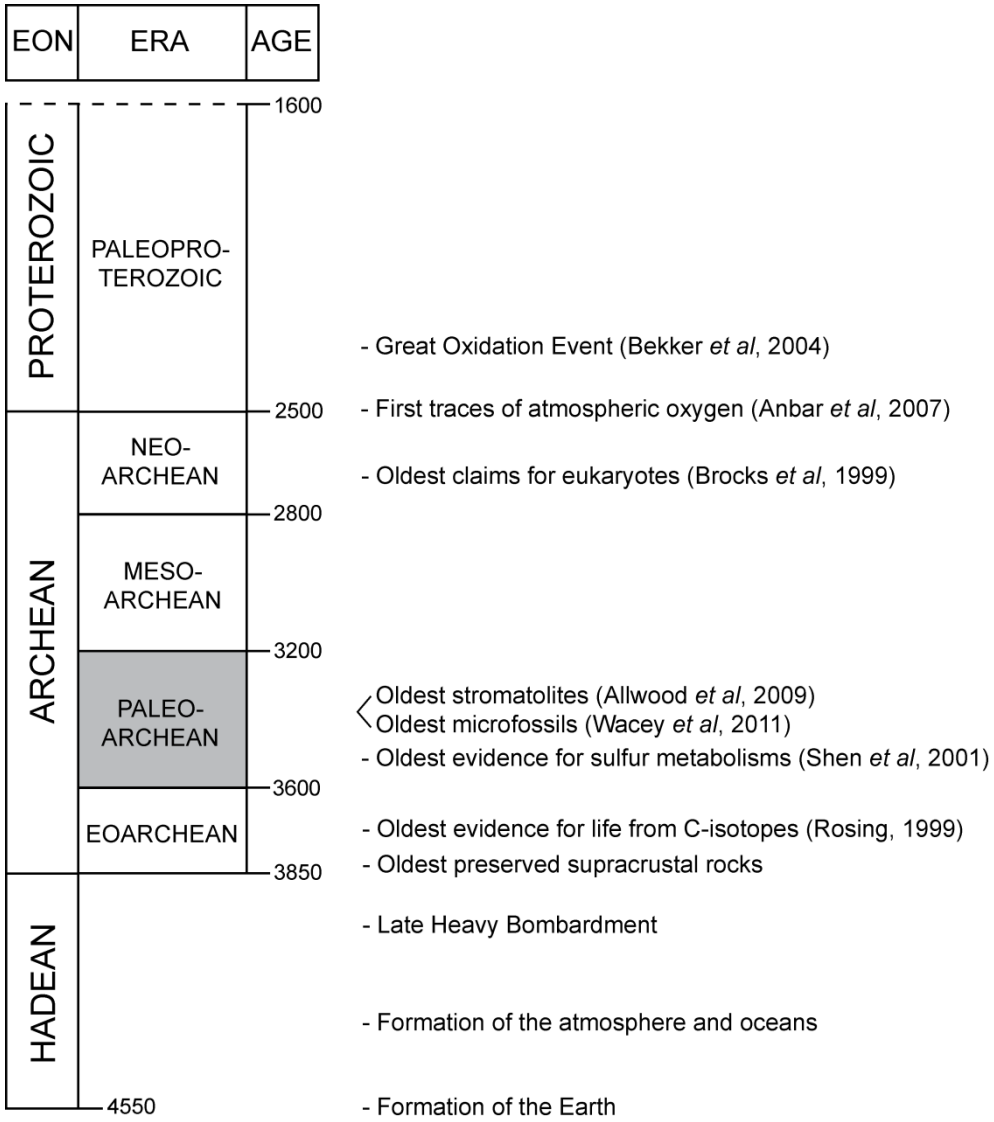

Figure 1.1 *Geological timeline of the Precambrian, consisting of the Hadean (4.55-3.85 Ga), the Archean (3.85-2.50 Ga) and the Proterozoic (2.50-0.54 Ga), of which only the Paleoproterozoic is shown here. Important geological and biological events are shown at the right side of the diagram, and the Paleoarchean era that is covered by this thesis is indicated with the shaded area. Although the oldest evidence for biological activity on Earth comes from reduced carbon in Eoarchean sediments from the Isua Supracrustal Belt in West Greenland (Rosing, 1999), the oldest evidence for sulfur metabolisms was derived from Paleoarchean sediments of Western Australia (Shen et al., 2001).*

A major limitation to this approach is that abiotic chemical reactions can produce similar degrees of isotope fractionation to biological pathways (Ohmoto and Goldhaber, 1997), preventing the direct identification of ancient biological processes without additional supporting evidence. This is also likely to hamper the calibration of Martian sulfur isotope data against the terrestrial record in future studies.

This thesis thus explores to what extent sulfur isotope ratios in Paleoarchean rocks can record microbial reaction pathways and how they are affected or overprinted by abiotic processes. It investigates for the first time in detail the complete succession of sulfate and sulfide-bearing rocks that occur throughout the stratigraphy of the Barberton Greenstone Belt in South Africa and Swaziland. An overview is given below of the principles of stable sulfur isotope geochemistry and the Paleoarchean sulfur cycle to provide a background for the new results presented here.

1.2 SULFUR ISOTOPE GEOCHEMISTRY

Stable isotopes are non-radioactive varieties of a chemical element with the same number of protons, but different numbers of neutrons in their nuclei (as indicated by the superscript before the element symbol). Sulfur has four naturally occurring stable isotopes, including major isotopes ^{32}S and ^{34}S with natural abundances of 95.02% and 4.21%, respectively, and minor isotopes ^{33}S (0.76%) and ^{36}S (0.02%) (Thode et al., 1949; MacNamara and Thode, 1950; Szabo et al., 1950). Abundance ratios of these isotopes (e.g. $^{34}S/^{32}S$) change as a result of biological and chemical reactions, a process called fractionation. The magnitude of isotope fractionation is expressed relative to a standard in per mil (‰) in the delta notation, defined for ^{34}S by:

$$\delta^{34}S = [((^{34}S/^{32}S)_{sample} / (^{34}S/^{32}S)_{V\text{-}CDT}) - 1] \times 1000 \qquad [1.1]$$

Similarly, $\delta^{33}S$ and $\delta^{36}S$ can be calculated by replacing the abundance ratios with $^{33}S/^{32}S$ and $^{36}S/^{32}S$, respectively. Delta-values are calculated relative to the Vienna Canyon Diablo Troilite (V-CDT) with $\delta^{34}S = 0.0‰$, representing the composition of the bulk Earth.

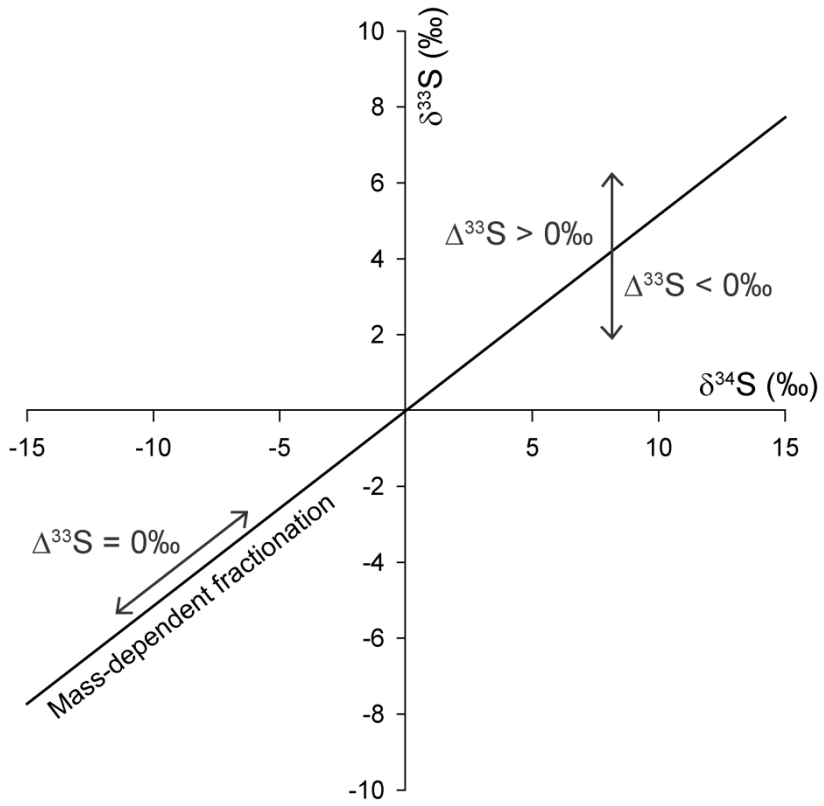

Figure 1.2 *Mass-dependent and mass-independent isotope effects in a diagram of $\delta^{33}S$ versus $\delta^{34}S$. Mass-dependent fractionation produces data points that plot onto the line defined by $\delta^{33}S \approx 0.515\ \delta^{34}S$ (straight line) and $\Delta^{33}S = 0‰$. In contrast, mass-independent fractionation results in anomalous isotope effects with data points plotting above ($\Delta^{33}S > 0‰$) or below ($\Delta^{33}S < 0‰$) this line.*

The magnitude of isotopic fractionation is controlled by the masses of the isotopes, so that the change in $^{33}S/^{32}S$ is approximately half of the change in $^{34}S/^{32}S$ during normal mass-dependent fractionation, represented by the line shown in Fig. 1.2 (Hulston and Thode, 1965). Likewise, the variation in $^{36}S/^{32}S$ is close to twice the variation in $^{34}S/^{32}S$ for ordinary equilibrium and kinetic processes. Deviations from the standard mass-dependent relationship were found in natural samples and experimental studies and have been linked to photochemical reactions in the atmosphere (Farquhar et al., 2000; Farquhar et al., 2001), which result in isotopic compositions plotting above or below the mass-

dependent fractionation line (Fig. 1.2). This type of sulfur isotope effect is referred to as mass-independent fractionation (MIF)†, and is defined as the difference from the mass-dependent relationship in equations 1.2 and 1.3:

$$\Delta^{33}S = \delta^{33}S - 1000 \times [(1-\delta^{34}S/1000)^{0.515} - 1] \quad [1.2]$$

$$\Delta^{36}S = \delta^{36}S - 1000 \times [(1-\delta^{34}S/1000)^{1.91} - 1] \quad [1.3]$$

Processes leading to mass-independent and mass-dependent fractionation of sulfur isotopes are discussed in the following sections.

1.2.1 Mass-independent fractionation

Mass-independent isotope fractionation was first discovered for oxygen isotopes in carbonaceous meteorites (Clayton et al., 1973; Clayton, 1979) and was suggested by Thiemens and Heidenreich (1983) to be related to photochemical reactions in the atmosphere. Comparable anomalous isotope effects were reported by Farquhar et al. (2000) for sulfur isotopes in early Proterozoic and Archean sedimentary rocks, and subsequent experimental and theoretical work demonstrated a similar atmospheric origin for these signatures related to the photolysis of sulfur dioxide in the absence of oxygen (Farquhar et al., 2001; Pavlov and Kasting, 2002). The underlying fractionation mechanism remains unknown, but it has been suggested that self-shielding, photoabsorption effects and primary photochemical processes may be responsible for the mass-independent isotope signatures (Farquhar et al., 2001; Lyons, 2007; Danielache et al., 2008; Lyons, 2009; Masterson et al., 2011). Nevertheless, experimental work and sulfur isotope data from the rock record prior to the Great Oxidation Event (see Fig. 1.1) suggest that atmospheric photolysis in the Archean atmosphere produced zero-valent elemental sulfur with positive $\Delta^{33}S$, and oxidized sulfate with negative $\Delta^{33}S$ (Fig. 1.3) (Farquhar et al., 2000; Farquhar et al., 2001; Farquhar and Wing, 2003). Isotopic analysis of Paleoarchean and Neoarchean sulfides suggests that the photochemical sulfate was characterized by negative $\delta^{34}S$-values (Ono et al., 2003;

† The term *mass-independent* is somewhat misleading because fractionation still depends on the mass of the isotopes, but the mass dependency is different from the standard relationship.

Kamber and Whitehouse, 2007; Kaufman et al., 2007; Ueno et al., 2008; Ono et al., 2009), consistent with broadband UV radiation photolysis models and experiments predicting a positive array in $\Delta^{33}S/\delta^{34}S$, shown in Fig. 1.3 (Lyons, 2009; Masterson et al., 2011; Whitehill and Ono, 2012).

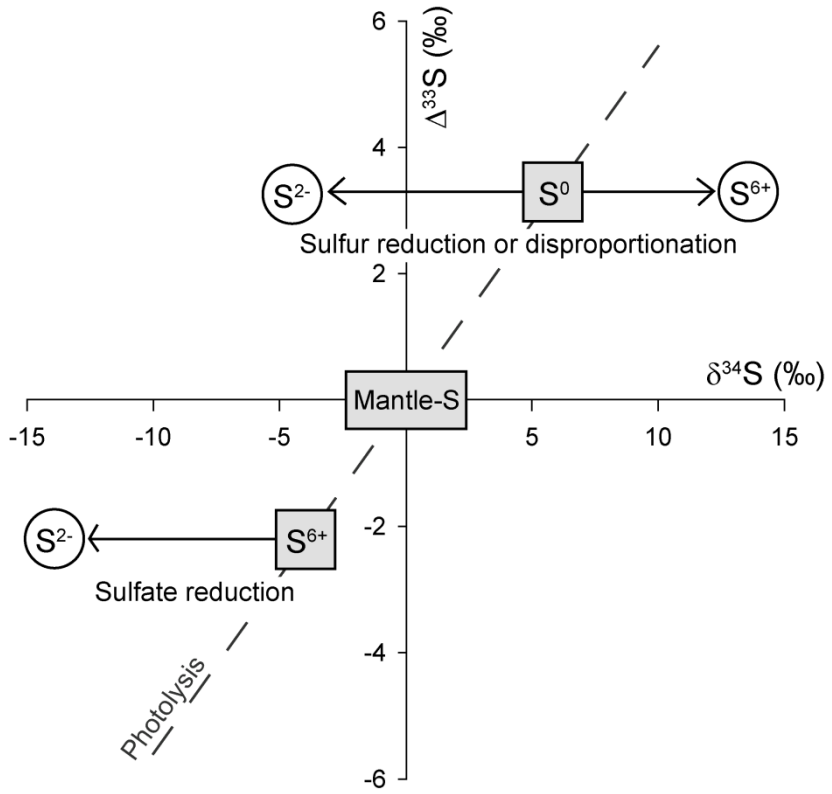

Figure 1.3 *Plot of $\Delta^{33}S$ versus $\delta^{34}S$ illustrating the preservation of mass-independent isotope signatures during biological redox transformations. Photochemical reactions in the Archean atmosphere produced sulfate and elemental sulfur with distinct $\Delta^{33}S$-values, here approximated by the photolysis array (dashed line) defined by Neoarchean and Paleoarchean sulfide isotope data (Ono et al., 2003; Kamber and Whitehouse, 2007; Kaufman et al., 2007; Ueno et al., 2008; Ono et al., 2009). Subsequent processing of this sulfur, e.g. during microbial or abiotic sulfate reduction or elemental sulfur disproportionation, produces sulfur compounds that still carry this distinct sulfur-MIF signature.*

Alternatively, Philippot et al. (2007; 2012) suggested from pyrite sulfur isotope data that photochemical sulfate was characterized by positive $\delta^{34}S$, similar to results from single-wavelength photochemistry experiments using a 193 nm ArF excimer laser (Farquhar et al., 2001). However, the relevance of such narrow-band radiation spectra for the Archean atmosphere has been questioned (Danielache et al., 2008; Lyons, 2009). Finally, ratios of mass-independent isotope signatures ($\Delta^{36}S/\Delta^{33}S$) were consistently found to be between -0.9 and -1.0 for Paleoarchean and Neoarchean sediments (Farquhar et al., 2000; Kaufman et al., 2007; Ueno et al., 2008), and similar values were reported from experimental work (Farquhar et al., 2001; Masterson et al., 2011; Whitehill and Ono, 2012), suggesting that SO_2 photolysis produced a general Archean reference array with $\Delta^{36}S/\Delta^{33}S \approx -1$.

1.2.2 Mass-dependent fractionation

Mass-dependent fractionation results from isotopic exchange between two compounds in equilibrium or kinetic processes. In general, heavier isotopes form more stable chemical bonds, so that lighter isotopes react faster and are preferentially enriched in the products of unidirectional reactions (O'Neil, 1986). Mass-independent isotope signatures are preserved during subsequent mass-dependent reactions or may be diluted during addition of juvenile sulfur, so that the sign of $\Delta^{33}S$ and $\Delta^{36}S$-values of Archean pyrite can be used to determine whether sulfide was derived from elemental sulfur ($\Delta^{33}S > 0‰$) or sulfate ($\Delta^{33}S < 0‰$) (Fig. 1.3). In addition, small but diagnostic shifts in the minor isotopic compositions associated with microbial activity enables discrimination between low-temperature biological and high-temperature abiotic fractionations with similar ^{34}S-depletions (Farquhar et al., 2003; Johnston et al., 2005; Johnston et al., 2007). An overview is given below of the isotope effects associated with these biological and abiotic redox reactions.

1.2.2.1 Biological isotope fractionation

Biological reactions are the dominant pathways for sulfur isotope fractionation at temperatures below 100°C and result from preferential processing of the light isotopes by micro-organisms (Ohmoto and Goldhaber, 1997). The largest shifts in $\delta^{34}S$ occur during microbial sulfate reduction (i.e. the reduction of sulfate to

sulfide) and elemental sulfur disproportionation (i.e. the generation of sulfide and sulfate from elemental sulfur), whereas smaller isotope effects have been reported for the biological reduction of elemental sulfur and microbial sulfide oxidation (see overview by Johnston, 2011). The variation in isotope fractionation, defined as the difference in isotopic composition between reactants and metabolic products (i.e. $\Delta^{34}S_{sulfate\text{-}sulfide} = \delta^{34}S_{sulfate} - \delta^{34}S_{sulfide} \approx {}^{34}\varepsilon$, has been measured extensively for microbial sulfate reduction in sediments and laboratory culture studies and ranges from -3 to +70‰ (Harrison and Thode, 1958; Kaplan and Rittenberg, 1964; Kemp and Thode, 1968; Habicht and Canfield, 1997; Bruchert et al., 2001; Canfield, 2001; Detmers et al., 2001; Canfield et al., 2006; Hoek et al., 2006; Farquhar et al., 2008; Canfield et al., 2010; Stam et al., 2010; Sim et al., 2011; Stam et al., 2011), which is consistent with the theoretical fractionation model of Brunner and Bernasconi (2005). Strongly suppressed isotope fractionation was observed at sulfate concentrations below 200 µM, decreasing to less than 6‰ at levels below 50 µM (Habicht et al., 2002). In addition, experimental and modeling work demonstrated that small but significant changes in minor isotope ratios $\Delta^{33}S$ and $\Delta^{36}S$ accompany microbial sulfate reduction when the degree of mass-dependent fractionation is relatively large (${}^{34}\varepsilon$ > 30‰) (Farquhar et al., 2003; Johnston et al., 2005; Johnston et al., 2007). Compared to the isotopic composition of the reactant sulfate, $\Delta^{33}S$-values of the biogenic sulfide increase slightly (up to 0.2‰ difference) whereas $\Delta^{36}S$-values decrease (up to 2‰).

Microbial disproportionation of elemental sulfur and other intermediate sulfur species results in the formation of sulfide and sulfate, with an associated ^{34}S-depletion in the sulfide of 4-7‰ versus ^{34}S-enrichment in sulfate of 7-20‰ (Thamdrup et al., 1993; Canfield and Thamdrup, 1994; Canfield et al., 1998; Habicht et al., 1998; Böttcher et al., 2001; Böttcher et al., 2005; Johnston et al., 2005). Shifts in minor isotope signatures associated with this metabolic pathways are opposite to effects observed during sulfate reduction, with small increases in $\Delta^{36}S$ and decreases in $\Delta^{33}S$ relative to reactant sulfur (Johnston et al., 2005; Johnston et al., 2007). Finally, limited isotope effects were observed for the biological reduction and oxidation of elemental sulfur and sulfide. Microbial reduction of elemental sulfur in laboratory culture studies produced only small isotope fractionations in $\delta^{34}S$ of 1-5‰ between sulfur and sulfide (Surkov et al., 2012), and similar small isotope effects were observed during phototrophic oxidation of sulfide and elemental sulfur (Zerkle et al., 2009).

1.2.2.2 Abiotic isotope fractionation

Fractionation of sulfur isotopes is not exclusively limited to microbial processes, but can also result from abiotic redox reactions at elevated temperatures. In high-temperature diagenetic environments (80-200°C), pore-water sulfate can be reduced by organic compounds during thermochemical sulfate reduction that produces similar magnitudes of ^{34}S-depletion as observed for biological pathways, ranging from 20‰ at 100°C to 10‰ at 200°C (Machel et al., 1995; Ohmoto and Goldhaber, 1997). In addition to mass-dependent fractionation, significant mass-independent fractionation was reported for ^{33}S during thermochemical sulfate reduction with amino acids (Watanabe et al., 2009; Oduro et al., 2011) and Watanabe et al. (2009) also observed anomalous fractionation of ^{36}S, although these minor isotope effects have not (yet) been identified in modern geochemical systems. At slightly higher temperatures (200-350°C), dissolved sulfate can be reduced via inorganic pathways with ferrous iron-bearing minerals in hydrothermal systems, resulting in equilibrium isotope effects of 20‰ at 350°C and 30‰ at 200°C (Mottl et al., 1979; Shanks et al., 1981; Shanks and Seyfried, 1987; Ohmoto and Goldhaber, 1997). Finally, in magmatic systems at temperatures above 400°C, sulfur is present in fluids as SO_2 and becomes hydrolyzed to H_2S and H_2SO_4 upon cooling (Ellis and Giggenbach, 1971; Ohmoto and Goldhaber, 1997), which results isotope fractionation between sulfide and sulfate of 15‰ at 400°C to 30‰ 200°C (Robinson, 1973; Ohmoto and Goldhaber, 1997).

1.3 THE PALEOARCHEAN SULFUR CYCLE

Fractionation of stable sulfur isotopes recorded in well-preserved rocks from ancient greenstone belts have provided valuable insights into the earliest sulfur cycle, and demonstrate that it was considerably different from the one operating today. The observation and preservation of mass-independent isotope effects in Paleoarchean rocks is one of the strongest pieces of evidence for an early anoxic atmosphere, indicating oxygen concentrations of less than 10^{-5} times present day levels (Farquhar et al., 2000; Pavlov and Kasting, 2002). Deep ocean waters were also anoxic (Canfield, 2004), so that sulfide minerals such as detrital pyrite and uraninite were stable during seafloor and continental weathering (Holland, 1994;

Rasmussen and Buick, 1999). Consequently, the input of sulfate to the oceans from oxidative sulfide weathering was negligible, in contrast to the modern sulfur cycle where riverine fluxes supply more than 90% of all sulfur to the oceans (Walker and Brimblecombe, 1985; Ono et al., 2003). The only significant source of sulfur was the direct outgassing of volcanic sulfur dioxide (SO_2) and hydrogen sulfide (H_2S) to the atmosphere (Fig. 1.4), and the lack of a stratospheric ozone layer allowed ultraviolet radiation to reach the troposphere and interact with these volcanic gasses (Farquhar et al., 2000).

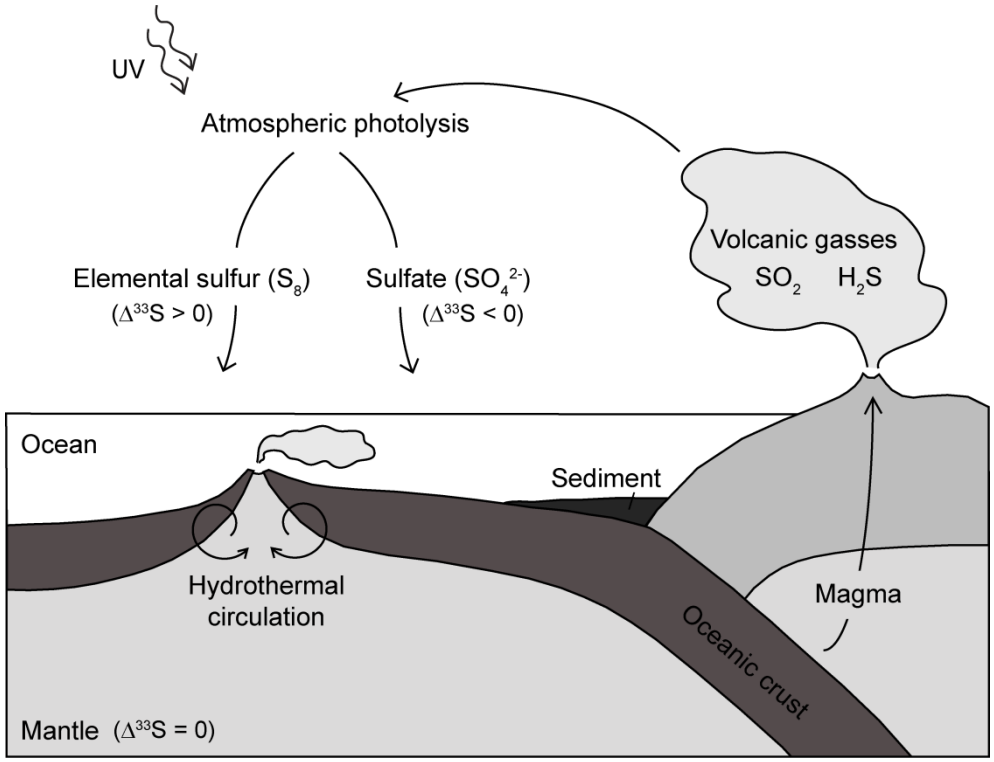

Figure 1.4 *Cartoon illustrating the main reservoirs and redox pathways in the Paleoarchean sulfur cycle, modified after Farquhar et al. (2002). Volcanic gasses provided the most important source of sulfur to the Earth's surface, whereas hydrothermal circulation supplied minor amounts of sulfide to the deep ocean. See text for more details.*

Photolysis of SO_2 resulted in atmospheric production of zero-valent elemental sulfur particles (S^0) with positive $\Delta^{33}S$ and oxidized sulfur in sulfate (SO_4^{2-}) with negative $\Delta^{33}S$ (Farquhar et al., 2001), which were eventually deposited into the oceans via insoluble aerosol particles or acid rain leading to the formation of barite deposits (barium sulfate, $BaSO_4$) and sedimentary pyrite (iron sulfide, FeS_2) in local marine basins (Farquhar et al., 2000; Jewell, 2000; Huston and Logan, 2004). In addition, the oxidized and reduced sulfur compounds provided energy sources for microbial respiration in the anoxic oceans. Although marine sulfate concentrations were on average less than one-hundredth of present levels (Habicht et al., 2002), the conversion of sulfate into sulfide by dissimilatory sulfate reducing micro-organisms was probably an important redox pathway in the early sulfur cycle, as suggested from the sulfur isotopic compositions of Paleoarchean sedimentary rocks (Shen et al., 2001; Ueno et al., 2008; Shen et al., 2009; Wacey et al., 2010; Wacey et al., 2011a). In addition, the presence of sulfide with positive $\Delta^{33}S$ signatures suggests that elemental sulfur disproportionating or sulfur reducing microbes co-existed with these sulfate reducers as early as 3.4 Ga (Philippot et al., 2007; Wacey et al., 2010).

1.4 OBJECTIVES OF THIS STUDY

As outlined above, the preservation of mass-dependent and mass-independent sulfur isotope signatures in ancient volcano-sedimentary rocks on Earth provides unique insights into the earliest sulfur cycle. However, similar magnitudes of ^{34}S-depletion associated with abiotic and biological redox reactions, as discussed in Section 1.3, can complicate the interpretation of sulfur isotope data. Although complementary measurement of minor isotopes ^{33}S and ^{36}S can provide better constraints on the biogenicity of ^{34}S-depleted sulfide (e.g. Ono et al., 2006; Ueno et al., 2008; Shen et al., 2009), additional evaluation of the geological and metamorphic history of Paleoarchean sulfur deposits is required to determine whether sulfur isotope fractionation could have resulted from high-temperature abiotic processes or low-temperature microbial pathways.

This thesis presents a combined study of the geology and multiple sulfur isotope geochemistry (^{32}S, ^{33}S, ^{34}S, ^{36}S) of Paleoarchean pyrite and barite from the Barberton Greenstone Belt in South Africa and Swaziland, in order to evaluate the geobiology of these 3.5-3.2 Ga minerals. In particular, this work aimed to

determine from sulfur isotope signatures whether micro-organisms were involved in the formation of barite and pyrite deposits at this time, and investigate to what extent abiotic factors such as the environment of formation and especially metamorphism may have affected or blurred these isotopic compositions. It represents the first study to assess the preservation of biogenic isotope signatures in a high-metamorphic grade barite deposit from the Paleoarchean, using novel analytical techniques to measure all four stable sulfur isotopes in pyrite *in situ* by secondary ion mass spectrometry. This work contributes significantly to our understanding of sulfur isotopic variations preserved in ancient rocks on Earth, and thereby provides an important background for the interpretation and calibration of sulfur isotope data from potential future Mars missions.

1.5 THESIS OUTLINE

This thesis consists of three main parts, covering (1) the sulfur isotopic compositions of four Paleoarchean barite deposits from the Barberton Greenstone Belt (Chapter 2), (2) sulfur isotopic compositions of pyrite from a low-metamorphic grade barite deposit at Barite Valley, South Africa (Chapter 3), and (3) the geological history and sulfur isotopic compositions of pyrite from a high-metamorphic grade barite deposit at Londozi, Swaziland (Chapters 4-6).

Chapter 2 reports on the bulk measurement of all four stable sulfur isotopes in barite deposits from the Barberton Greenstone Belt at Londozi (ca. 3.5 Ga), Vergelegen (ca. 3.4 Ga), Stentor (3.26 Ga) and Barite Valley (3.26-3.23 Ga), and reveals the presence of distinct isotopic trends preserved in barite of all metamorphic grades. Modeling of the isotopic co-variation provides an alternative method to pyrite sulfur isotope analyses to determine the role of sulfur metabolisms in the earliest marine environments. In Chapter 3, data is presented from in situ quadruple sulfur isotope analyses by secondary ion mass spectrometry of pyrite from a drill core through the 3.26-3.23 Ga Barite Valley barite deposit, South Africa. The low metamorphic grade of this deposit and the presence of pyrite in different types of sedimentary rocks allows for evaluation of the role of the depositional environment on the preservation of primary atmospheric arrays and biological isotope signatures. In addition, this chapter demonstrates that high-resolution stable isotope analyses are critical to identify the sulfur reservoirs that were present in the Paleoarchean.

Chapter 4 provides a comprehensive study on the geological and metamorphic history of the Londozi barite deposit in Swaziland, which is identified for the first time in this chapter as the oldest-known sulfate deposit on Earth by laser ablation ICP-MS zircon U-Pb dating. Geochemical analyses of the volcanic host rocks are used to constrain the geodynamic setting in which the barite formed, and mineral compositions analyzed by electron microprobe are used to calculate the conditions of high-grade metamorphism using conventional thermobarometers. In Chapter 5, the geochemistry and mineralogy of alteration zones associated with the Londozi barite are investigated to determine the conditions of synvolcanic hydrothermal alteration, and assess the possibility of sulfur remobilization during late-stage metasomatism. Both Chapter 4 and Chapter 5 provide the geological background for the interpretation of pyrite sulfur isotope data from the Londozi deposit in Chapter 6, which expand the current sulfide isotope record back in time by 30 Myr. In addition, Chapter 6 demonstrates that analysis of all four sulfur isotopes is important to distinguish between biological and abiotic fractionation. General conclusions and implications of this study are finally discussed in Chapter 7, with an additional outlook on how the stable sulfur isotope biomarker could be applied in the planetary exploration of Mars.

References

Allwood, A.C., Grotzinger, J.P., Knoll, A.H., Burch, I.W., Anderson, M.S., Coleman, M.L., Kanik, I., 2009. Controls on development and diversity of Early Archean stromatolites. Proceedings of the National Academy of Sciences 106, 9548-9555.

Allwood, A.C., Walter, M.R., Burch, I.W., Kamber, B.S., 2007. 3.43 billion-year-old stromatolite reef from the Pilbara Craton of Western Australia: Ecosystem-scale insights to early life on Earth. Precambrian Res. 158, 198-227.

Banerjee, N.R., Furnes, H., Muehlenbachs, K., Staudigel, H., de Wit, M., 2006. Preservation of ~3.4-3.5 Ga microbial biomarkers in pillow lavas and hyaloclastites from the Barberton Greenstone Belt, South Africa. Earth Planet. Sci. Lett. 241, 707-722.

Böttcher, M.E., Thamdrup, B., Gehre, M., Theune, A., 2005. 34S/34S and 18O/16O fractionation during sulfur disproportionation by Desulfobulbus propionicus. Geomicrobiol. J. 22, 219-226.

Böttcher, M.E., Thamdrup, B., Vennemann, T.W., 2001. Oxygen and sulfur isotope fractionation during anaerobic bacterial disproportionation of elemental sulfur. Geochim. Cosmochim. Acta 65, 1601-1609.

Bruchert, V., Knoblauch, C., Jørgensen, B.B., 2001. Controls on stable sulfur isotope fractionation during bacterial sulfate reduction in arctic sediments. Geochim. Cosmochim. Acta 65, 763-776.

Brunner, B., Bernasconi, S.M., 2005. A revised isotope fractionation model for dissimilatory sulfate reduction in sulfate reducing bacteria. Geochim. Cosmochim. Acta 69, 4759-4771.

Canfield, D.E., 2001. Isotope fractionation by natural populations of sulfate-reducing bacteria. Geochim. Cosmochim. Acta 65, 1117-1124.

Canfield, D.E., 2004. The evolution of the Earth surface sulfur reservoir. Am. J. Sci. 304, 839-861.

Canfield, D.E., Farquhar, J., Zerkle, A.L., 2010. High isotope fractionations during sulfate reduction in a low-sulfate euxinic ocean analog. Geology 38, 415-418.

Canfield, D.E., Olesen, C.A., Cox, R.P., 2006. Temperature and its control of isotope fractionation by a sulfate-reducing bacterium. Geochim. Cosmochim. Acta 70, 548-561.

Canfield, D.E., Raiswell, R., 1999. The evolution of the sulfur cycle. Am. J. Sci. 299, 697-723.

Canfield, D.E., Thamdrup, B., 1994. The production of 34S-depleted sulfide during bacterial disproportionation of elemental sulfur. Science 266, 1973-1975.

Canfield, D.E., Thamdrup, B., Fleischer, S., 1998. Isotope Fractionation and Sulfur Metabolism by Pure and Enrichment Cultures of Elemental Sulfur-Disproportionating Bacteria. Limnol. Oceanogr. 43, 253-264.

Clayton, R.N., 1979. Isotopic anomalies in the early solar system. Phys. Chem. Earth. 11, 121-125.

Clayton, R.N., Grossman, L., Mayeda, T.K., 1973. A component of primitive nuclear composition in carbonaceous meteorites. Science 182, 485-488.

Danielache, S.O., Eskebjerg, C., Johnson, M.S., Ueno, Y., Yoshida, N., 2008. High-precision spectroscopy of ^{32}S, ^{33}S and ^{34}S sulfur dioxide: Ultraviolet absorption cross sections and isotope effects. J. Geophys. Res. 113, D17414.

Detmers, J., Bruchert, V., Habicht, K.S., Kuever, J., 2001. Diversity of sulfur

isotope fractionations by sulfate-reducing prokaryotes. Appl. Environ. Microbiol. 67, 888-894.

Ellis, A.J., Giggenbach, W., 1971. Hydrogen sulphide ionization and sulphur hydrolysis in high temperature solution. Geochim. Cosmochim. Acta 35, 247-260.

Farquhar, J., Bao, H., Thiemens, M., 2000. Atmospheric Influence of Earth's Earliest Sulfur Cycle. Science 289, 756-758.

Farquhar, J., Canfield, D.E., Masterson, A., Bao, H., Johnston, D.T., 2008. Sulfur and oxygen isotope study of sulfate reduction in experiments with natural populations from Faellestrand, Denmark. Geochim. Cosmochim. Acta 72, 2805-2821.

Farquhar, J., Johnston, D.T., Wing, B.A., Habicht, K.S., Canfield, D.E., Airieau, S., Thiemens, M.H., 2003. Multiple sulphur isotopic interpretations of biosynthetic pathways: implications for biological signatures in the sulphur isotope record. Geobiology 1, 27-36.

Farquhar, J., Savarino, J., Airieau, S., Thiemens, M.H., 2001. Observation of wavelength-sensitive mass-independent sulfur isotope effects during SO_2 photolysis: Implications for the early atmosphere. J. Geophys. Res. 106, 32829-32839.

Farquhar, J., Wing, B.A., 2003. Multiple sulfur isotopes and the evolution of the atmosphere. Earth Planet. Sci. Lett. 213, 1-13.

Farquhar, J., Wing, B.A., McKeegan, K.D., Harris, J.W., Cartigny, P., Thiemens, M.H., 2002. Mass-independent sulfur of inclusions in diamond and sulfur recycling on early Earth. Science 298, 2369-2372.

Fedo, C.M., Whitehouse, M.J., 2002. Metasomatic Origin of Quartz-Pyroxene Rock, Akilia, Greenland, and Implications for Earth's Earliest Life. Science 296, 1448-1452.

Habicht, K.S., Canfield, D.E., 1997. Sulfur isotope fractionation during bacterial sulfate reduction in organic-rich sediments. Geochim. Cosmochim. Acta 61, 5351-5361.

Habicht, K.S., Canfield, D.E., Rethmeier, J., 1998. Sulfur isotope fractionation during bacterial reduction and disproportionation of thiosulfate and sulfite. Geochim. Cosmochim. Acta 62, 2585-2595.

Habicht, K.S., Gade, M., Thamdrup, B., Berg, P., Canfield, D.E., 2002. Calibration of sulfate levels in the Archean ocean. Science 298, 2372-2374.

Harrison, A.G., Thode, H.G., 1958. Mechanism of the bacterial reduction of sulphate from isotope fractionation studies. Transactions of the Faraday Society 53, 84-92.

Hoek, J., Reysenbach, A.L., Habicht, K.S., Canfield, D.E., 2006. Effect of hydrogen limitation and temperature on the fractionation of sulfur isotopes by a deep-sea hydrothermal vent sulfate-reducing bacterium. Geochim. Cosmochim. Acta 70, 5831-5841.

Holland, H.D., 1994. Early Proterozoic atmospheric change, in: Bengtson, S. (Ed.), Early life on Earth. Columbia University Press, New York.

Hulston, J.R., Thode, H.G., 1965. Variations in the S33, S34, and S36 Contents of Meteorites and Their Relation to Chemical and Nuclear Effects. J. Geophys. Res. 70, 3475-3484.

Huston, D.L., Logan, G.A., 2004. Barite, BIFs and bugs: evidence for the evolution of the Earth's early hydrosphere. Earth Planet. Sci. Lett. 220, 41-55.

Javaux, E.J., Marshall, C.P., Bekker, A., 2010. Organic-walled microfossils in 3.2-billion-year-old shallow-marine

siliciclastic deposits. Nature 463, 934-938.
Jewell, P.W., 2000. Bedded barite in the geologic record, Marine Authigenesis: From Global to Microbial. SEPM (Society for Sedimentary Geology), pp. 147-161.
Johnston, D.T., 2011. Multiple sulfur isotopes and the evolution of Earth's surface sulfur cycle. Earth-Science Reviews 106, 161-183.
Johnston, D.T., Farquhar, J., Canfield, D.E., 2007. Sulfur isotope insights into microbial sulfate reduction: When microbes meet models. Geochim. Cosmochim. Acta 71, 3929-3947.
Johnston, D.T., Farquhar, J., Wing, B.A., Kaufman, A.J., Canfield, D.E., Habicht, K.S., 2005. Multiple sulfur isotope fractionations in biological systems: A case study with sulfate reducers and sulfur disproportionators. Am. J. Sci. 305, 645-660.
Kamber, B.S., Whitehouse, M.J., 2007. Micro-scale sulphur isotope evidence for sulphur cycling in the late Archean shallow ocean. Geobiology 5, 5-17.
Kaplan, I.R., Rittenberg, S.C., 1964. Microbiological fractionation of sulfur isotopes. J. Gen. Microbiol. 34, 195-212.
Kaufman, A.J., Johnston, D.T., Farquhar, J., Masterson, A.L., Lyons, T.W., Bates, S., Anbar, A.D., Arnold, G.L., Garvin, J., Buick, R., 2007. Late Archean Biospheric Oxygenation and Atmospheric Evolution. Science 317, 1900-1903.
Kemp, A.L.W., Thode, H.G., 1968. The mechanism of the bacterial reduction of sulphate and sulphite from isotope fractionation studies. Geochim. Cosmochim. Acta 32, 71-91.
Lyons, J.R., 2007. Mass-independent fractionation of sulfur isotopes by isotope-selective photodissociation of SO2. Geophys. Res. Lett. 34.
Lyons, J.R., 2009. Atmospherically-derived mass-independent sulfur isotope signatures, and incorporation into sediments. Chem. Geol. 267, 164-174.
Machel, H.G., Krouse, H.R., Sassen, R., 1995. Products and distinguishing criteria of bacterial and thermochemical sulfate reduction. Appl. Geochem. 10, 373-389.
MacNamara, J., Thode, H.G., 1950. Comparison of the isotopic constitution of terrestrial and meteoritic sulfur. Physical Review 78, 307-308.
Masterson, A.L., Farquhar, J., Wing, B.A., 2011. Sulfur mass-independent fractionation patterns in the broadband UV photolysis of sulfur dioxide: Pressure and third body effects. Earth Planet. Sci. Lett. 306, 253-260.
Mojzsis, S.J., Arrhenius, G., McKeegan, K.D., Harrison, T.M., Nutman, A.P., Friend, C.R.L., 1996. Evidence for life on Earth before 3,800 million years ago. Nature 384, 55-59.
Mottl, M.J., Holland, H.D., Corr, R.F., 1979. Chemical exchange during hydrothermal alteration of basalt by seawater--II. Experimental results for Fe, Mn, and sulfur species. Geochim. Cosmochim. Acta 43, 869-884.
O'Neil, J.R., 1986. Theoretical and experimental aspects of isotopic fractionation. Stable Isotopes in High Temperature Geological Processes, 1-40.
Oduro, H., Harms, B., Sintim, H.O., Kaufman, A.J., Cody, G., Farquhar, J., 2011. Evidence of magnetic isotope effects during thermochemical sulfate reduction. Proceedings of the National Academy of Sciences 108, 17635-17638.
Ohmoto, H., Goldhaber, M.B., 1997. Sulfur and carbon isotopes, in: Barnes, H.L. (Ed.), Geochemistry of hydrothermal

ore deposits. John Wiley & Sons, New York.

Ohmoto, H., Kakegawa, T., Lowe, D.R., 1993. 3.4-Billion-Year-Old Biogenic Pyrites from Barberton, South Africa: Sulfur Isotope Evidence. Science 262, 555-557.

Ono, S., Eigenbrode, J.L., Pavlov, A.A., Kharecha, P., Rumble Iii, D., Kasting, J.F., Freeman, K.H., 2003. New insights into Archean sulfur cycle from mass-independent sulfur isotope records from the Hamersley Basin, Australia. Earth Planet. Sci. Lett. 213, 15-30.

Ono, S., Kaufman, A.J., Farquhar, J., Sumner, D.Y., Beukes, N.J., 2009. Lithofacies control on multiple-sulfur isotope records and Neoarchean sulfur cycles. Precambrian Res. 169, 58-67.

Ono, S., Wing, B., Johnston, D., Farquhar, J., Rumble, D., 2006. Mass-dependent fractionation of quadruple stable sulfur isotope system as a new tracer of sulfur biogeochemical cycles. Geochim. Cosmochim. Acta 70, 2238-2252.

Pavlov, A.A., Kasting, J.F., 2002. Mass-independent fractionation of sulfur isotopes in Archean sediments: strong evidence for an anoxic Archean atmosphere. Astrobiology 2, 27-41.

Philippot, P., Van Zuilen, M., Lepot, K., Thomazo, C., Farquhar, J., Van Kranendonk, M.J., 2007. Early Archaean Microorganisms Preferred Elemental Sulfur, Not Sulfate. Science 317, 1534-1537.

Philippot, P., van Zuilen, M., Rollion-Bard, C., 2012. Variations in atmospheric sulphur chemistry on early Earth linked to volcanic activity. Nat. Geosci. 5, 668-674.

Rasmussen, B., Buick, R., 1999. Redox state of the Archean atmosphere: Evidence from detrital heavy minerals in ca. 3250-2750 Ma sandstones from the Pilbara Craton, Australia. Geology 27, 115-118.

Robinson, B.W., 1973. Sulphur isotope equilibrium during sulphur hydrolysis at high temperatures. Earth Planet. Sci. Lett. 18, 443-450.

Rose, N.M., Rosing, M.T., Bridgwater, D., 1996. The origin of metacarbonate rocks in the archaean Isua supracrustal belt, west Greenland. Am. J. Sci. 296, 1004-1044.

Rosing, M.T., 1999. ^{13}C-Depleted Carbon Microparticles in >3700-Ma Sea-Floor Sedimentary Rocks from West Greenland. Science 283, 674-676.

Rosing, M.T., Rose, N.M., Bridgwater, D., Thomsen, H.S., 1996. Earliest part of Earth's stratigraphic record: A reappraisal of the >3.7 Ga Isua (Greenland) supracrustal sequence. Geology 24, 43-46.

Schidlowski, M., 1988. A 3,800-million-year isotopic record of life from carbon in sedimentary rocks. Nature 333, 313-318.

Schidlowski, M., Appel, P.W.U., Eichmann, R., Junge, C.E., 1979. Carbon isotope geochemistry of the 3.7 x 10^9-yr-old Isua sediments, West Greenland: implications for the Archaean carbon and oxygen cycles. Geochim. Cosmochim. Acta 43, 189-199.

Shanks, W.C., Bischoff, J.L., Rosenbauer, R.J., 1981. Seawater sulfate reduction and sulfur isotope fractionation in basaltic systems: Interaction of seawater with fayalite and magnetite at 200-350°C. Geochim. Cosmochim. Acta 45, 1977-1995.

Shanks, W.C., Seyfried, W.E., 1987. Stable isotope studies of vent fluids and chimney minerals, Southern Juan de Fuca Ridge: Sodium metasomatism and seawater sulfate reduction. J. Geophys. Res. 92, 11387-11399.

Shen, Y., Buick, R., 2004. The antiquity of microbial sulfate reduction. Earth-Science Reviews 64, 243-272.

Shen, Y., Buick, R., Canfield, D.E., 2001. Isotopic evidence for microbial sulphate reduction in the early Archaean era. Nature 410, 77-81.

Shen, Y., Farquhar, J., Masterson, A., Kaufman, A.J., Buick, R., 2009. Evaluating the role of microbial sulfate reduction in the early Archean using quadruple isotope systematics. Earth Planet. Sci. Lett. 279, 383-391.

Sim, M.S., Bosak, T., Ono, S., 2011. Large sulfur isotope fractionation does not require disproportionation. Science 333, 74-77.

Squyres, S.W., Grotzinger, J.P., Arvidson, R.E., Bell, J.F., Calvin, W., Christensen, P.R., Clark, B.C., Crisp, J.A., Farrand, W.H., Herkenhoff, K.E., Johnson, J.R., Klingelhöfer, G., Knoll, A.H., McLennan, S.M., McSween, H.Y., Morris, R.V., Rice, J.W., Rieder, R., Soderblom, L.A., 2004. In Situ Evidence for an Ancient Aqueous Environment at Meridiani Planum, Mars. Science 306, 1709-1714.

Stam, M.C., Mason, P.R.D., Laverman, A.M., Pallud, C.l., Cappellen, P.V., 2011. 34S/32S fractionation by sulfate-reducing microbial communities in estuarine sediments. Geochim. Cosmochim. Acta 75, 3903-3914.

Stam, M.C., Mason, P.R.D., Pallud, C., Van Cappellen, P., 2010. Sulfate reducing activity and sulfur isotope fractionation by natural microbial communities in sediments of a hypersaline soda lake (Mono Lake, California). Chem. Geol. 278, 23-30.

Surkov, A.V., Böttcher, M.E., Kuever, J., 2012. Sulphur isotope fractionation during the reduction of elemental sulphur and thiosulphate by Dethiosulfovibrio spp. Isot. Environ. Health Stud. 48, 65-75.

Szabo, A., Tudge, A., Macnamara, J., Thode, H.G., 1950. The Distribution of S34 in Nature and the Sulfur Cycle. Science 111, 464-465.

Thamdrup, B., Finster, K., Hansen, J.W., Bak, F., 1993. Bacterial Disproportionation of Elemental Sulfur Coupled to Chemical Reduction of Iron or Manganese. Appl. Environ. Microbiol. 59, 101-108.

Thiemens, M.H., Heidenreich Iii, J.E., 1983. The mass-independent fractionation of oxygen: A novel isotope effect and its possible cosmochemical implications. Science 219, 1073-1075.

Thode, H.G., Macnamara, J., Collins, C.B., 1949. Natural variations in the isotopic content of sulphur and their significance. Can. J. Res. 27b, 361-373.

Ueno, Y., Ono, S., Rumble, D., Maruyama, S., 2008. Quadruple sulfur isotope analysis of ca. 3.5 Ga Dresser Formation: New evidence for microbial sulfate reduction in the early Archean. Geochim. Cosmochim. Acta 72, 5675-5691.

Van Zuilen, M.A., Lepland, A., Arrhenius, G., 2002. Reassessing the evidence for the earliest traces of life. Nature 418, 627-630.

Wacey, D., Kilburn, M.R., Saunders, M., Cliff, J., Brasier, M.D., 2011a. Microfossils of sulphur-metabolizing cells in 3.4-billion-year-old rocks of Western Australia. Nat. Geosci. 4, 698-702.

Wacey, D., McLoughlin, N., Whitehouse, M.J., Kilburn, M.R., 2010. Two coexisting sulfur metabolisms in a ca. 3400 Ma sandstone. Geology 38, 1115-1118.

Wacey, D., Saunders, M., Brasier, M.D., Kilburn, M.R., 2011b. Earliest microbially mediated pyrite oxidation in ~3.4 billion-year-old sediments. Earth Planet. Sci. Lett. 301, 393-402.

Walker, J.C.G., Brimblecombe, P., 1985. Iron and sulfur in the pre-biologic ocean. Precambrian Res. 28, 205-222.
Walsh, M.W., 1992. Microfossils and possible microfossils from the early archean onverwacht group, Barberton mountain land, South Africa. Precambrian Res. 54, 271-293.
Watanabe, Y., Farquhar, J., Ohmoto, H., 2009. Anomalous Fractionations of Sulfur Isotopes During Thermochemical Sulfate Reduction. Science 324, 370-373.
Westall, F., de Wit, M.J., Dann, J., van der Gaast, S., de Ronde, C.E.J., Gerneke, D., 2001. Early Archean fossil bacteria and biofilms in hydrothermally-influenced sediments from the Barberton greenstone belt, South Africa. Precambrian Res. 106, 93-116.
Whitehill, A.R., Ono, S., 2012. Excitation band dependence of sulfur isotope mass-independent fractionation during photochemistry of sulfur dioxide using broadband light sources. Geochim. Cosmochim. Acta 94, 238-253.
Zerkle, A.L., Farquhar, J., Johnston, D.T., Cox, R.P., Canfield, D.E., 2009. Fractionation of multiple sulfur isotopes during phototrophic oxidation of sulfide and elemental sulfur by a green sulfur bacterium. Geochim. Cosmochim. Acta 73, 291-306

Execution Rock from Mantenga Reserve, Hhohho, Swaziland

Chapter 2

Multiple sulfur isotopes in Paleoarchean barites identify an important role for microbial sulfate reduction in the early marine environment

This chapter was previously published as: Desiree L. Roerdink, Paul R.D. Mason, James Farquhar and Thomas Reimer, 2012, Earth and Planetary Science Letters, v. 331-332, p. 177-186.

ABSTRACT

Bedded barites from the Barberton greenstone belt (South Africa and Swaziland) preserve a comprehensive record of atmospheric, oceanic and microbial processes involved in the formation and evolution of the Paleoarchean (3.6-3.2 Ga) oceanic sulfate reservoir. Here, we report multiple sulfur isotopic compositions from four of these barite occurrences. Relatively constant mass-independent signatures ($\Delta^{36}S/\Delta^{33}S$ = -1.0 ± 0.2) within deposits support an important role for atmospheric photolysis in the production of oxidized sulfur, whereas ^{34}S enrichments relative to the inferred composition of photolytic sulfate suggest drawdown of ^{32}S by microbial sulfate reduction. Strong compositional overlap with barites from India and Western Australia indicates the presence of a large-scale and well-mixed marine sulfate pool. Covariation between $\delta^{34}S$ and $\Delta^{33}S$ within individual deposits also suggests a role for processes occurring in semi-closed basins fed by this global reservoir. Based on modeling results, we interpret variations in $\delta^{34}S$ by local microbial sulfate reduction and correlations with $\Delta^{33}S$ by weak inputs of sulfur from magmatic sources, microbial sulfide oxidation or sulfur disproportionation. This agrees with the early occurrence of sulfate reducers in the geological record as inferred from published microscopic pyrite data, and identifies their role as important in both global oceans and local basins in the Paleoarchean.

2.1 INTRODUCTION

Multiple sulfur isotopes in sulfide-sulfate mineral pairs from Paleoarchean (3.6-3.2 Ga) greenstone belts preserve evidence for an early sulfur cycle with important roles for atmospheric and microbial processes. Mass-independent isotopic signatures (MIF) found in sedimentary pyrite and barite have been interpreted to reflect photolysis of volcanic SO_2 in a low-oxygen atmosphere (Farquhar et al., 2000; Pavlov and Kasting, 2002), suggesting atmospheric deposition of photochemical reaction products sulfate and elemental sulfur. Alternative origins of anomalous isotope fractionation include chemisorption reactions (Lasaga et al., 2008) or thermochemical sulfate reduction with amino acids (Watanabe et al., 2009), but it remains controversial whether these processes were relevant for sulfur-MIF in the Archean rock record (Farquhar et al., 2010; Golding et al., 2011). Moreover, isotopic and textural evidence from sulfides in the Dresser Formation (Western Australia) suggests that different microbial communities existed by 3.5 Ga. At least three types of sulfur metabolic pathways were probably present in the Paleoarchean: dissimilatory sulfate reduction (Shen et al., 2001; Ueno et al., 2008; Shen et al., 2009; Wacey et al., 2010; Wacey et al., 2011a), elemental sulfur disproportionation (Philippot et al., 2007; Wacey et al., 2010; Wacey et al., 2011a) and chemotrophic and/or phototrophic sulfide oxidation (Wacey et al., 2011b), but preservation of mass-independent signatures suggests limited biological sulfur cycling as this would homogenize and remove MIF-signals.

It remains unclear how these microbial processes were linked to sulfur cycling in the atmosphere and oceans. Disentangling the importance of biological and abiotic aspects of the early sulfur cycle requires information about the compositions of dominant sulfur sources, including multiple sulfur isotopic compositions of photolytic sulfate and elemental sulfur, which are currently poorly constrained because results from atmospheric models (Lyons, 2007, 2009) and experiments (Farquhar et al., 2001; Danielache et al., 2008; Masterson et al., 2011) do not match values found in the rock record. Information is also required about microbial and chemical pathways by which sulfur was transformed, and about the amount of material transferred between different pools in the Paleoarchean sulfur cycle.

Here, we describe the sulfur isotopic record of atmospheric, oceanic and biological processes involved in the formation and evolution of the Paleoarchean marine

sulfate reservoir preserved by 3.55 – 3.23 Ga sedimentary barites from the Barberton greenstone belt in South Africa and Swaziland. Barite occurrences in this area cover the entire time span from which sulfate deposits are known in the Paleoarchean (Huston and Logan, 2004) and provide a comprehensive record of the earliest sulfate pools. Data presented in this paper allow us to compare and contrast basin-scale patterns observed within individual deposits, with those observed between units from southern Africa and previously analyzed barites in Western Australia (Farquhar et al., 2000; Ueno et al., 2008; Shen et al., 2009) and India (Hoering, 1989), which might reflect larger-scale or global processes. We explore local sources and sinks of sulfate and their relative importance using a semi-closed reservoir model, and propose that microbial sulfate reduction was important on both a global and basin scale.

2.2 BARITE SAMPLES

Samples were collected from four barite deposits in the Barberton greenstone belt of South Africa and Swaziland (Fig. 2.1), as described below.

2.2.1 Londozi

The Londozi deposit is located in the southeastern part of the Barberton greenstone belt close to the South African-Swaziland border (26°11'20"S, 31°0'28"E). It occurs just east of the 3.51-3.50 Ga Steynsdorp pluton, a TTG gneiss dome which has intruded into the strongly deformed and metamorphosed supracrustal rocks of the Theespruit Formation in the lower Onverwacht Group (Kröner et al., 1996). Characteristic lithologies at the base of the succession include variably silicified, finely laminated volcanics and pillow lavas of (ultra)mafic composition, metamorphosed to actinolite-epidote-chlorite schists during amphibolite facies metamorphism (Barton, 1982; Kröner et al., 1996). Above the barite horizon, more felsic volcaniclastics are present together with quartz-muscovite gneisses. Barite occurs in lenses of variable thickness (0.5-10 m) in a zone that can be traced continuously for at least 1.25 km along strike. Its presence is associated with strongly silicified host rocks, and finely crystalline barite is often interbedded with thin layers of brown and green chert (1-5 cm) with some slivers of mafic host rock. Sulfides associated with the deposit include

disseminated and layered pyrite, sphalerite and to a lesser extent chalcopyrite and galena (Reimer, 1980). Samples were collected from barite outcrops (08-LON-01) and old quarry waste dumps (08-LON-02).

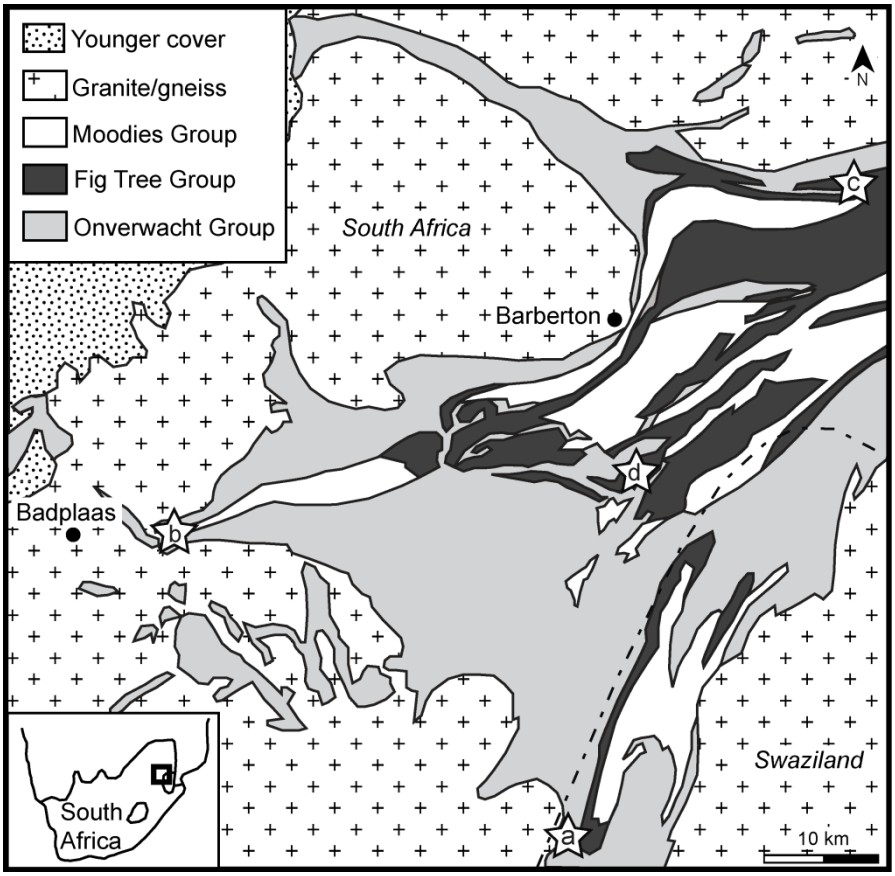

Figure 2.1 *Locations of barite deposits in the Barberton greenstone belt shown on a simplified geological map of the Barberton greenstone belt modified from Hofmann (2005). Barite deposits indicated: (a) Londozi barite, 3.55 Ga Theespruit Formation, lower Onverwacht Group; (b) Vergelegen barite, ca. 3.41 Ga Kromberg Formation, upper Onverwacht Group; (c) Stentor barite, 3.26 Ga Bien Venue Formation, Fig Tree Group; (d) Barite Valley, 3.26-3.23 Ga Mapepe Formation, Fig Tree Group.*

The abundance of (ultra)mafic and finely laminated volcanics, pillow lavas as well as the absence of andesitic rocks (Kröner et al., 1996) indicates barite deposition in a relatively low-energy marine setting, similar to a modern oceanic plateau or plume-related oceanic island (Kröner et al., 1996), or a back-arc basin in an active convergent margin (Armstrong et al., 1990; De Ronde and De Wit, 1994; Dziggel et al., 2006). Intense silicification of host rocks suggests strong hydrothermal activity and a sedimentary-exhalative origin of the barite (Reimer, 1980; Barton, 1982; Reimer, 1990). Intense deformation produced strong foliation and lineation in the surrounding amphibolites, but lithologies can be traced linearly for at least 10 km along the N-S strike (Barton, 1982). Therefore, an age for the barite can be derived from felsic volcanics 3 km north of the deposit, dated at 3547 ± 2 Ma by Kröner et al. (1996). Although it is unclear whether these rocks are syn-volcanic and part of the Theespruit Formation (Kröner et al., 1996), or older and representing a section of tectonically emplaced crust (Armstrong et al., 1990; De Ronde and De Wit, 1994; Dziggel et al., 2006), this does not affect our age estimate because the felsic volcanics occur in the same tectonic unit as the barite horizon. An age of 3.55 Ga for the Londozi barite implies that this is the oldest sulfate deposit currently identified in the geological record.

2.2.2 Vergelegen

A small barite deposit occurs in the westernmost part of the Barberton greenstone belt on Farm Vergelegen (25°58'31"S, 30°39'39"E), 4 km south of the Stolzburg asbestos mine. Barite occurs in a narrow chert band that likely represents the westward extension of the Buck Reef chert (Reimer, 1980) in the lower part of the Kromberg Formation (Byerly et al., 1996) or upper part of the Hooggenoeg Formation (Viljoen and Viljoen, 1969). Sheared mafic to intermediate lavas occur below the chert-barite zone in the south, while it is overlain by talc-carbonate schists and sheared serpentinites in the north (Reimer, 1980). The deposit occurs as two thinly-bedded and intensely folded chert-barite bands in a 13.5 m thick zone of chlorite schists (Reimer, 1980; Reimer, 1990). Barite is up to 30 cm thick in the main outcrop and is white to light grey and coarse crystalline. In contrast to the other barite occurrences, sulfides are absent in the Vergelegen deposit. The deposit becomes strongly deformed towards the western part of the outcrop and has been affected by lower-middle greenschist facies metamorphism

(Tice et al., 2004). Samples were collected from the eastern (08-VER-01) and western part (08-VER-02) of the outcrop.

Age constraints are relatively poor due to compressed and complex stratigraphy, but the spatial association with the Buck Reef chert suggests that the age of the Vergelegen deposit is similar to this chert unit, and not of Theespruit Formation age as suggested by Reimer et al. (1990). Dacitic sandstones at the base of the Buck Reef chert were dated at 3416 ± 5 Ma (Kröner et al., 1991), whereas an age of 3334 ± 3 Ma was obtained from tuffaceous cherts at the top of the Kromberg Formation (Byerly et al., 1996). Although this strictly represents a minimum age for Vergelegen, an age of circa 3.41 Ga (cf. de Vries et al., 2010) is more consistent with the large (1200 m) difference in stratigraphic level between the Buck Reef chert and the top of the Kromberg Formation.

The formation of the Buck Reef chert and associated volcano-sedimentary complex was shown to be related to normal growth faulting that produced small-scale extensional half-grabens, in which mainly felsic volcaniclastics were deposited (Lowe et al., 1999; de Vries et al., 2006). Detailed sedimentological work by De Vries et al. (2010) showed that the chert unit reflects a regressive-transgressive succession after deposition of pillow basalts in the underlying Hooggenoeg Formation. Associated environments include a high-energy shallow-marine environment with occasional subaerial conditions during regression, changing towards lagoonal/lacustrine and coastal environments during transgression (de Vries et al., 2010). Interpretations by Tice and Lowe (2006) differ slightly in that these authors suggest deposition below storm wave-base during transgression, but nevertheless imply a shallow marine environment. Strong hydrothermal activity during sediment deposition was inferred from silicified structures (de Vries et al., 2010), consistent with a sedimentary-exhalative origin of the Vergelegen barite (Reimer, 1980). Silicified evaporites were reported by Lowe and Worrell (1999) of which some resemble gypsum, but the close association with volcanic rocks argues against an evaporitic gypsum precursor for the barite (Reimer, 1980).

2.2.3 Stentor

Two closely related seams of barite occur near the Stentor pluton in the northeast of the greenstone belt on farms Stentor and Amo (25º35’37”S 31º24’25”E), here referred to as the Stentor deposit. Samples were collected from two barite seams

at the farms Amo (TR-03) and Stentor (TR-04). The deposit belongs to the Bien Venue Formation of the Fig Tree Group (Kohler and Anhaeusser, 2002). Fine-grained, grayish barite occurs within steeply dipping cherts hosted by quartz-muscovite schists that represent sheared mafic lavas and felsic tuffs, and forms thin (1-15 cm) lenses and layers with finely disseminated pyrite sometimes concentrated along bedding planes (Reimer, 1980; Reimer, 1990; Kohler and Anhaeusser, 2002). The total thickness of the barite-chert unit is approximately 70 m and can be traced for 700 m along strike (Reimer, 1980). Rocks in this region have been affected by contact metamorphism and alteration linked to the intrusion of the Nelspruit batholith and the Stentor pluton, resulting in middle greenschist facies metamorphism (Kohler and Anhaeusser, 2002). Zircons from a quartz-muscovite schist close to the Bien Venue VHMS deposit, circa 3.5 km west of the Stentor deposit (Reimer, 1990), were dated at 3259 ± 5 Ma (Kröner et al., 1991), whereas the age of similar schists at the stratigraphic top of the formation was found to be 3256 ± 1 Ma (Kohler, 2003). The latter is considered by Kohler and Anhaeusser (2002) as best age estimate for the Bien Venue Formation, and an age of 3.26 Ga is therefore used for the Stentor barite.

Trace element analyses indicate that quartz-muscovite schists hosting the barite deposit represent transitional to calc-alkaline assemblages, similar to rock compositions found in modern continental arc settings (Kohler and Anhaeusser, 2002). In addition to subduction-related volcanism, schistose conglomerates hint at post-eruptive reworking with strong fluvial or wave-related abrasion, whereas laminated phyllites and slates indicate sedimentation under quiet-water conditions. All lithologies of the Bien Venue Formation were deposited in subaqueous environments with considerable volcanic relief, resulting in water depths varying from shallow marine to more than 1200 m for the VHMS deposit (Kohler and Anhaeusser, 2002). Barite was deposited under relatively low-energy conditions from submarine hydrothermal exhalations (Reimer, 1980; Kohler and Anhaeusser, 2002), and faint cross-laminations in the Stentor deposit suggest that some of the barite may have been of clastic origin and deposited in relatively shallow waters (Reimer, 1980; Reimer, 1990).

2.2.4 Barite Valley

The youngest barite occurrence is located in the area of Barite Valley (25°53’38”S, 31°4’8 ”E) in the central part of the greenstone belt (Heinrichs and Reimer, 1977;

Reimer, 1980; Bao et al., 2007). In contrast to metavolcanic host rocks elsewhere in the Barberton region, this large deposit is hosted by terrigeneous clastic sediments belonging to the 3.26-3.23 Ga Lower and Middle Mapepe Formation of the Fig Tree Group (Heinrichs and Reimer, 1977). Stratigraphically, the barite horizon occurs unconformably above a chert-rich zone containing the basal chert of the Fig Tree Group, jaspilitic silicified sediments and chert conglomerates with an originally dolomitic matrix, and is overlain by sandy tuffaceous sediments, coarser greywackes and shales (Heinrichs and Reimer, 1977). Deformation and metamorphism in this region were relatively low, i.e. lower greenschist facies (Condie et al., 1970; Hofmann, 2005), so that original sedimentary and diagenetic structures have been preserved. Barite is frequently found as green-colored accumulations of sand-sized grains in a chert matrix, with 2-5% pyrite and heavy mineral phases including chromite and zircon (Heinrichs and Reimer, 1977; Ward, 1999). Bladed barite is common, either as upwards diverging bundles formed during syn-sedimentary growth or as 2-10 cm long blades at high angles to the bedding, possibly formed during early diagenesis (Heinrichs and Reimer, 1977). Samples were collected from a core drilled below quarry workings in Barite Valley (FT-155.5 to FT-188.2) and from surface outcrops (08-BV), and contain both bladed and detrital barite.

Lithologies of the Mapepe Formation indicate sedimentation in a foreland basin, with deposition of fine tuffs, mud and locally ferruginous chert in a shallow subaqueous basin, and sandstones and conglomerates in a fan-delta adjacent to uplifted land areas (Lowe and Nocita, 1999). Away from the fan-dominated areas, bedded barite formed in shallow water on local structural highs, together with chert, jasper and fine-grained terrigeneous or volcaniclastic units. Heinrichs and Reimer (1977) suggested that the deposition of these shallow-water sequences was controlled by the emergence and erosion of tectonically unstable highs leading to the rapid changes in lithology, and postulated that this structural high was closely related to the Inyoka fault. Hydrothermal fluids seeping through faults associated with the tectonically active Proto-Inyoka zone provided a source of barium, leading to barite precipitation on the uplifted region.

2.3 ANALYTICAL METHODS

2.3.1 Sample preparation

Barite powders were obtained by microdrilling using a 2.4 mm diamond drill bit that was thoroughly pre-cleaned. Powders drilled from the surface layer were discarded in order to avoid contamination from weathered surfaces, and no sulfides were observed in the barite powders. Approximately 10 mg of pure barite was reduced to hydrogen sulfide by boiling with a Thode reduction solution (a pre-boiled mixture of concentrated HCl, HI and H_3PO_2) for 3 hours, following methods described by Forrest and Newman (1977). Hydrogen sulfide produced during the conversion was transported in argon gas, washed in a 30 ml water trap with ultrapure water and collected in an acidified silver nitrate solution (15 ml ultrapure water, 1 ml 0.3 M $AgNO_3$ and 2 ml 1.5 M HNO_3) to precipitate silver sulfide. Precipitated Ag_2S was subsequently washed with diluted ammonia and ultra-pure water, filtered with 0.2 µm cellulose-acetate filters and dried for 1-2 days. The dry Ag_2S was scraped from the filter and stored in glass bottles.

2.3.2 Isotope analysis

Multiple sulfur isotope analyses were performed at the University of Maryland stable isotope laboratory. Circa 2-3 mg of Ag_2S powder was wrapped in cleaned aluminum foil and placed into a Ni-reaction vessel to react with approximately 10 times excess F_2 at 250°C for 8 hours. The product SF_6 was purified by cryogenic and gas chromatographic methods, as described by Farquhar et al (2007a). The multiple sulfur isotope composition of the purified sulfur hexafluoride was measured on a dual-inlet ThermoFinnigan MAT 253, with an average external precision (2σ) of 0.1‰ on $\delta^{34}S$, 0.02‰ on $\Delta^{33}S$ and 0.2‰ on $\Delta^{36}S$ based on repeated measurements of IAEA-S2 and IAEA-S3 reference materials. Sulfur isotope data is reported relative to the V-CDT standard.

2.4 RESULTS

Measured barite $\delta^{34}S$-values (Table 2.1) were positive and ranged within individual deposits from 2.9‰ to 6.8‰, with an average $\delta^{34}S$ of 4.9 ± 1.2‰ (1σ).

Sample	Deposit	Age (Ga)	$\delta^{34}S$	2σ	$\Delta^{33}S$	2σ	$\Delta^{36}S$	2σ
LON-02-A1 1	Londozi	3.55	6.37	0.02	-1.01	0.02	1.2	0.3
LON-02-A1 2	Londozi	3.55	4.78	0.01	-1.06	0.03	0.97	0.04
LON-02-A1 4	Londozi	3.55	6.42	0.02	-1.02	0.02	1.0	0.2
LON-02-A1 5	Londozi	3.55	4.25	0.01	-1.07	0.02	1.0	0.3
LON-02-B1 1	Londozi	3.55	5.81	0.01	-1.01	0.03	0.9	0.1
LON-02-B1 2	Londozi	3.55	9.40	0.01	-0.80	0.03	0.9	0.4
LON-02-B1 3	Londozi	3.55	6.42	0.01	-0.92	0.03	0.88	0.07
LON-02-D2 1	Londozi	3.55	6.83	0.01	-0.94	0.01	0.90	0.06
LON-02-E1 1	Londozi	3.55	5.25	0.01	-1.06	0.01	1.2	0.3
LON-02-E1 2	Londozi	3.55	5.14	0.01	-1.04	0.02	1.1	0.2
LON-02-F1 1	Londozi	3.55	6.77	0.03	-1.04	0.03	1.1	0.6
LON-02-F1 2	Londozi	3.55	5.96	0.01	-1.05	0.01	1.0	0.2
LON-02-G1 1	Londozi	3.55	5.80	0.01	-1.05	0.02	1.1	0.1
LON-02-G1 2	Londozi	3.55	4.91	0.01	-1.07	0.01	1.0	0.2
LON-02-I1 2	Londozi	3.55	4.94	0.02	-1.04	0.03	1.03	0.09
LON-02-I1 3	Londozi	3.55	6.02	0.01	-1.01	0.03	1.0	0.1
LON-01-A1	Londozi	3.55	4.92	0.01	-1.15	0.01	1.2	0.2
LON-01-A2	Londozi	3.55	5.55	0.01	-1.12	0.01	1.16	0.09
LON-01-A3	Londozi	3.55	3.59	0.01	-1.03	0.01	0.9	0.2
LON-01-A4	Londozi	3.55	3.77	0.01	-1.00	0.03	0.98	0.02
LON-01-B1	Londozi	3.55	4.78	0.01	-1.05	0.03	1.1	0.2
LON-01-D1	Londozi	3.55	5.85	0.01	-1.05	0.02	1.0	0.2
LON-01-E1	Londozi	3.55	5.04	0.02	-1.04	0.05	1.0	0.2

Table 2.1 *Multiple sulfur isotope data with 2σ errors for barite deposits from the Barberton greenstone belt. Footnotes: (a) approximate age, (b) average age (between 3.26 and 3.23 Ga), (c) drilled from bladed barite, (d) drilled from barite sand matrix.*

Sample	Deposit	Age (Ga)	$\delta^{34}S$	2σ	$\Delta^{33}S$	2σ	$\Delta^{36}S$	2σ
VER-01 A	Vergelegen	3.41[a]	4.51	0.01	-0.88	0.04	0.9	0.2
VER-01 B	Vergelegen	3.41	4.94	0.01	-0.88	0.03	0.8	0.2
VER-01 C	Vergelegen	3.41	3.99	0.01	-0.87	0.01	0.88	0.06
VER-01 D	Vergelegen	3.41	2.91	0.01	-1.00	0.01	0.98	0.02
VER-01 E	Vergelegen	3.41	4.59	0.02	-0.87	0.03	0.7	0.1
VER-01 F	Vergelegen	3.41	3.44	0.01	-0.86	0.01	0.6	0.1
VER-02 1	Vergelegen	3.41	4.49	0.01	-0.40	0.02	0.5	0.3
VER-02 2	Vergelegen	3.41	4.43	0.01	-0.43	0.02	0.6	0.1
TR-03-1	Stentor	3.26	4.15	0.02	-0.58	0.03	0.5	0.1
TR-03-2	Stentor	3.26	2.90	0.02	-0.55	0.01	0.5	0.2
TR-04-1	Stentor	3.26	4.60	0.01	-0.54	0.03	0.6	0.1
TR-04-2 1	Stentor	3.26	4.67	0.02	-0.43	0.01	0.2	0.3
TR-04-2 2	Stentor	3.26	5.66	0.02	-0.47	0.04	0.3	0.2
FT-155.5 1	Barite Valley	3.25[b]	3.46	0.01	-0.40	0.03	0.3	0.4
FT-155.5 2	Barite Valley	3.25	3.99	0.01	-0.48	0.02	0.6	0.2
FT-173	Barite Valley	3.25	4.57	0.02	-0.58	0.03	0.76	0.06
FT-179	Barite Valley	3.25	4.10	0.01	-0.47	0.04	0.5	0.4
FT-188.2 1	Barite Valley	3.25	6.25	0.02	-0.41	0.03	0.0	0.2
BV-07-1	Barite Valley	3.25	4.30	0.01	-0.34	0.03	0.52	0.09
BV-07-2	Barite Valley	3.25	6.40	0.01	-0.44	0.07	0.2	0.3
BV-01-2[c]	Barite Valley	3.25	3.23	0.01	-0.75	0.02	0.6	0.2
BV-01-3[c]	Barite Valley	3.25	3.98	0.02	-0.70	0.01	0.7	0.1
BV-01-4[d]	Barite Valley	3.25	3.90	0.02	-0.64	0.02	0.7	0.3
BV-01-5[d]	Barite Valley	3.25	3.66	0.01	-0.70	0.01	0.6	0.1

Table 2.1 (continued)

One sample from Londozi (LON-02-B1 2) showed an exceptionally high $\delta^{34}S$-value of 9.4‰. Minor isotopes showed mass-independent fractionation, with negative $\Delta^{33}S$ between -1.15‰ and -0.34‰ and positive $\Delta^{36}S$ between 0.0‰ and 1.2‰ (Fig. 2.2 and 2.3). Magnitudes of $\Delta^{33}S$ and $\Delta^{36}S$ were found to decrease with decreasing age, from average values of $\Delta^{33}S$ = -1.03 ± 0.07‰ and $\Delta^{36}S$ = 1.0 ± 0.1‰ for Londozi (3.55 Ga) to $\Delta^{33}S$ = -0.54 ± 0.14‰ and $\Delta^{36}S$ = 0.5 ± 0.2‰ for Barite Valley (3.26-3.23 Ga). In contrast, average $\delta^{34}S$-values were similar for all deposits (5.6 ± 1.2‰ for Londozi, 4.2 ± 0.7‰ for Vergelegen and 4.4 ± 1.0‰ for Barite Valley).

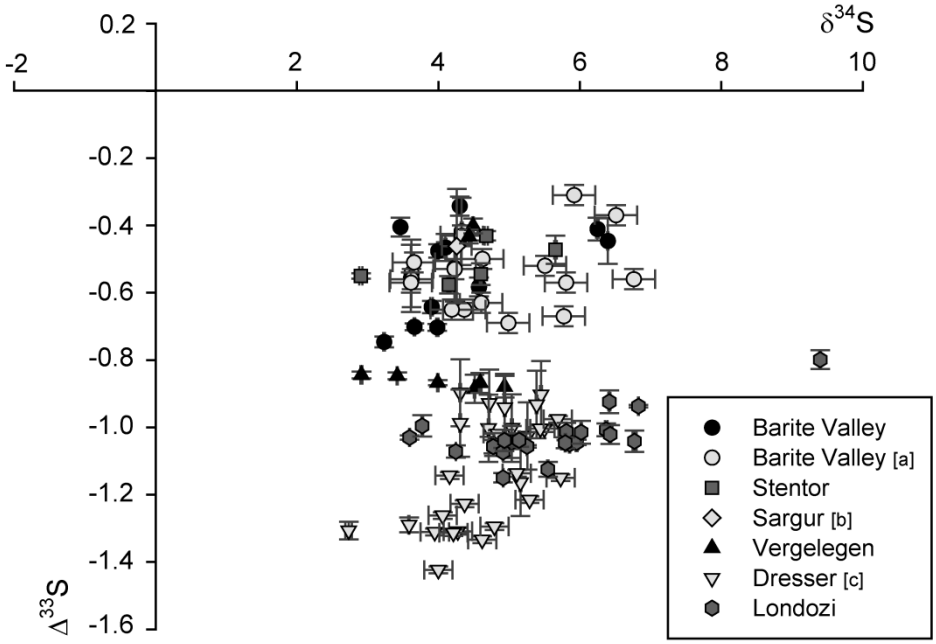

Figure 2.2 *Plot of $\Delta^{33}S$ versus $\delta^{34}S$ for all Paleoarchean barite deposits. Closed symbols represent barites analyzed in this study, open symbols indicate previously published data from the Barite Valley deposit ([a] Bao et al., 2007), Sargur barite ([b] Hoering, 1989) and Dresser barite ([c] Farquhar et al., 2000; Ueno et al., 2008; Shen et al., 2009). Error bars represent 2σ errors. The plot demonstrates isotopic homogeneity of the sulfate reservoir, with slightly more negative $\Delta^{33}S$-values for barites older than 3.4 Ga. Isotopic compositions of the Indian Sargur (ca. 3.29 Ga) and Australian Dresser barite (3.49 Ga) agree well with deposits of similar age from Southern Africa.*

Weak trends in $\Delta^{33}S/\delta^{34}S$ were observed in individual deposits (Table 2.2). We calculated regression lines for the Londozi, Vergelegen and Fig Tree barites, the latter representing combined data from the Stentor and Barite Valley deposits because of their similar ages. Trends were calculated using linear regression at the 95% confidence level, taking analytical errors into account. Significantly different $\Delta^{33}S$ values for VER-01 and VER-02 resulted in large errors on calculated slopes and intercepts for Vergelegen (R^2 = 0.05), whereas the trend line for sample VER-01 is more similar to those found for Londozi and Fig Tree, except for a slightly negative slope. The intercept is larger for the Londozi (-1.4 ± 0.2) than for the Fig Tree barites (-0.9 ± 0.4), consistent with the observation that the magnitude of $\Delta^{33}S$ decreases with decreasing age of the deposit.

For the same datasets, we calculated regression lines in $\delta^{33}S/\delta^{34}S$ that showed stronger correlations with $R^2 > 0.97$ (Table 2.2), except for Vergelegen. Slopes for the Londozi and Fig Tree barites are larger than the theoretical slopes expected for either microbial sulfate reduction (0.509-0.512) or sulfur disproportionation (0.515-0.517) (Johnston et al., 2007), but smaller than slopes of 0.63-0.649 found in UV photolysis experiments (Farquhar et al., 2001). Large errors on $\delta^{33}S/\delta^{34}S$ for Vergelegen hamper comparison with published values.

Using data from all four barite deposits we determined a value of -1.0 ± 0.2 for the ratio $\Delta^{36}S/\Delta^{33}S$ (Table 2.3). Despite lower correlation coefficients, $\Delta^{36}S/\Delta^{33}S$-values for the individual Londozi, Vergelegen and Fig Tree barites are statistically equal to the slope defined by all deposits.

Dataset	$\delta^{33}S/\delta^{34}S$	$\delta^{33}S/\delta^{34}S_i$	R^2	$\Delta^{33}S/\delta^{34}S$	$\Delta^{33}S/\delta^{34}S_i$	R^2
Londozi	0.55 ± 0.02	-1.3 ± 0.1	0.99	0.068 ± 0.03	-1.4 ± 0.2	0.47
VER-01[a]	0.49 ± 0.01	-0.78 ± 0.04	0.99	-0.021 ± 0.001	-0.78 ± 0.03	0.83
Vergelegen	0.65 ± 0.32	-1.3± 1.3	0.79	0.7 ± 1.5	-3.5 ± 6.2	0.05
Fig Tree[b]	0.58 ± 0.06	-0.8 ± 0.3	0.97	0.074 ± 0.06	-0.9 ± 0.4	0.22

Table 2.2 *Results from linear regression on $\delta^{33}S/\delta^{34}S$ and $\Delta^{33}S/\delta^{34}S$, with errors indicating 95% confidence interval. $\delta^{33}S/\delta^{34}S_i$ and $\Delta^{33}S/\delta^{34}S_i$ denote value of intercept. Footnotes: (a) sample VER-01 only, (b) Stentor and Barite Valley deposits with a similar age of barite deposition.*

Dataset	$\Delta^{36}S/\Delta^{33}S$	$\Delta^{36}S/\Delta^{33}S_i$	R^2
Londozi	-0.8 ± 0.5	0.1 ± 0.6	0.43
Vergelegen[a]	-0.9 ± 1.6	0.1 ± 1.5	0.88
Fig Tree[b]	-1.0 ± 0.7	0.0 ± 0.4	0.40
All data[c]	-1.0 ± 0.2	-0.1 ± 0.2	0.88

Table 2.3 *Results from linear regression on $\Delta^{36}S/\Delta^{33}S$ with errors indicating 95% confidence level. $\Delta^{36}S/\Delta^{33}S_i$ denotes the value of the intercept. Footnote: (a) large error due to choice of outliers in dataset (b) Stentor and Barite Valley deposits, (c) all data from this study.*

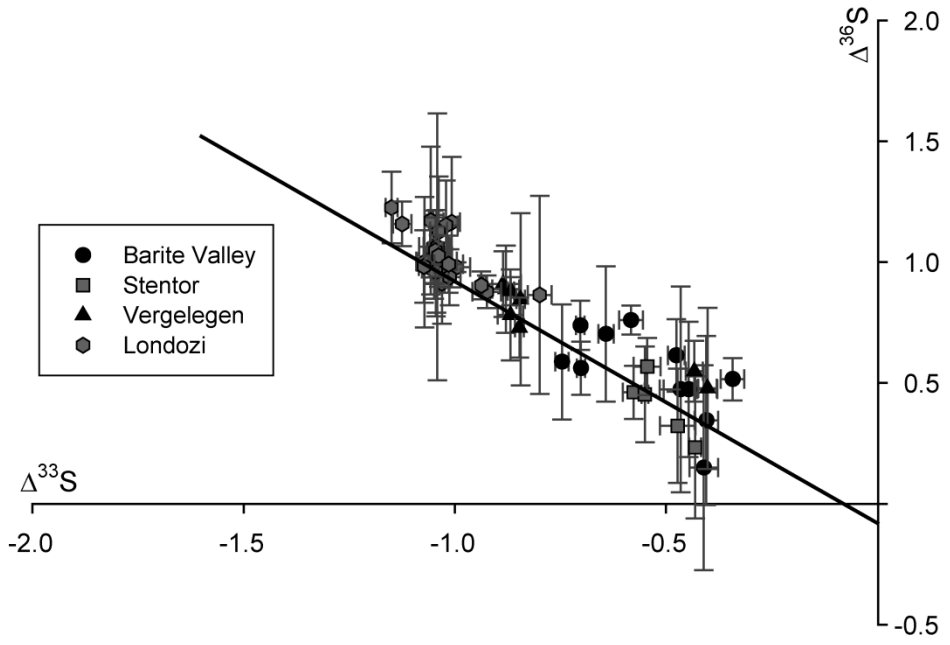

Figure 2.3 *Plot of $\Delta^{36}S$ versus $\Delta^{33}S$ for Paleoarchean barites in the Barberton greenstone belt. Error bars represent 2σ errors. The equation $\Delta^{36}S = (-1.0 \pm 0.2)\Delta^{33}S - 0.08 \pm 0.2$ defines the average regression line and is consistent with an important role for atmosphere photolysis in the production of sulfate. Slopes of trend lines for individual barite deposits are statistically equal. Previously published data from the Dresser barite and Sargur barite were omitted from this plot due to lower analytical precision on $\Delta^{36}S$.*

2.5 MODEL

2.5.1 Model outline

To test possible origins of isotopic variations in the barite deposits, we present a model that describes the multiple sulfur isotopic evolution of a basin-scale sulfate reservoir with extraction of ^{34}S-depleted sulfate during microbial sulfate reduction, and addition of ^{33}S-enriched ($\Delta^{33}S \geq 0‰$) sulfur from magmatic sources, microbial sulfide oxidation and/or disproportionation of reduced sulfur (Fig. 2.4). For fractionation occurring during microbial sulfate reduction we assumed a Rayleigh distillation model, consistent with barite precipitating from a batch of seawater sulfate delivered to semi-closed basins.

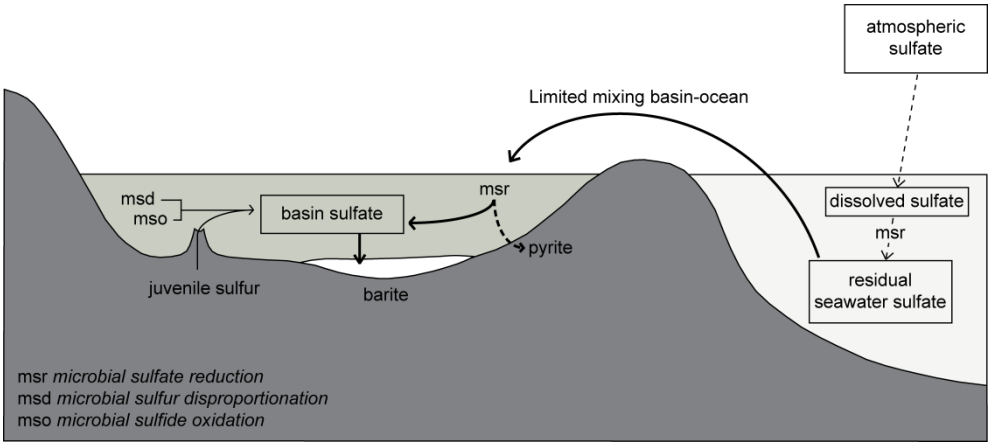

Figure 2.4 *Graphical representation of the basin-scale sulfate reservoir model described in this chapter, showing relevant sources and sinks of sulfate. Atmospheric (photolytic) sulfate with $\delta^{34}S \approx -2‰$ dissolved into the ocean, where global-scale microbial sulfate reduction produced a residual seawater sulfate reservoir with $\delta^{34}S \approx +2‰$. Semi-closed basins were fed by this oceanic pool, and the isotopic composition of basin sulfate was subsequently affected by local microbial sulfate reduction and inputs from juvenile sulfur, microbial sulfide oxidation or sulfur disproportionation. Barite precipitated in these basins. Sources and sinks of other sulfur species were omitted from the figure for clarity, and deposition of atmospheric sulfate into the basin was assumed to be negligible due to the significantly larger surface area of the ocean relative to local basins.*

Isotopic compositions were calculated in the model as isotope ratios, where ^{34}R indicates $^{34}S/^{32}S$. The composition of the sulfide produced during microbial sulfate reduction was calculated following equation 2.1 for $^{34}S/^{32}S$:

$$^{34}R_{sulfide} = \alpha^{34}R_{sulfate} \quad [2.1]$$

The fractionation factor α defined for $^{34}S/^{32}S$ was recalculated for $^{33}S/^{32}S$ and $^{36}S/^{32}S$ after Johnston et al. (2007), and applied in equations 2.2 and 2.3:

$$^{33}R_{sulfide} = (\alpha^{0.511})^{33}R_{sulfate} \quad [2.2]$$

$$^{36}R_{sulfide} = (\alpha^{1.915})^{36}R_{sulfate} \quad [2.3]$$

Isotope ratios for the product sulfide were used in equation 2.4 to calculate the isotopic composition of the residual sulfate through mass balance (only shown for $^{34}S/^{32}S$):

$$^{34}R_{initial} = (1\text{-}f)^{34}R_{residual} + f\,^{34}R_{sulfide} \quad [2.4]$$

Here, f denotes the fraction of sulfate reduced during each step and $^{34}R_{initial}$ is the initial isotopic composition of the sulfate in the basin. After each incremental step of sulfate reduction, residual sulfate was mixed with sulfate derived from either juvenile sulfur, microbial sulfide oxidation or sulfur disproportionation, indicated by $^{34}R_{added}$. Isotopic mass balance was used to calculate the composition of the total sulfate reservoir after mixing, following equation 2.5:

$$^{34}R_{total} = (1\text{-}y)^{34}R_{residual} + y^{34}R_{added} \quad [2.5]$$

Variable y indicates the fraction of sulfate added, equal to f (fraction of sulfate reduced) times ratio r (sulfate added/sulfate reduced). The calculated $^{34}R_{total}$ was subsequently used as source for the next sulfate reduction step.

Three different scenarios were modeled: (1) addition of juvenile sulfur with $\delta^{34}S = \Delta^{33}S = \Delta^{36}S = 0‰$; (2) addition of microbially oxidized magmatic sulfide with $\delta^{34}S = -2‰$ (Zerkle et al., 2009) and $\Delta^{33}S = \Delta^{36}S = 0‰$; and (3) addition of sulfate derived from microbial disproportionation of photolytic elemental sulfur with $\delta^{34}S = 13‰$, $\Delta^{33}S = 3‰$ and $\Delta^{36}S = -3‰$, based on the ^{34}S-enrichments observed in experiments with sulfur disproportionating micro-organisms (Canfield and Thamdrup, 1994; Böttcher et al., 2001). For scenario (2), we assumed that oxidation of magmatic sulfide was more important in hydrothermally-influenced basins than oxidation of biogenic sulfide. For scenario (3), we used an isotopic composition of photochemical elemental sulfur with $\delta^{34}S \approx +2‰$ based on the array proposed by Ueno et al. (2008), and estimated $\Delta^{33}S$ and $\Delta^{36}S$ from maximum values reported by Philippot et al. (2007) and $\Delta^{36}S/\Delta^{33}S$ observed in Fig. 2.3. A fractionation factor $^{32/34}\alpha$ of 0.99 was used for the isotope effect during microbial sulfate reduction, reflecting initially intermediate sulfate concentrations of around 200-500 µm in the basin (Habicht et al., 2002). Seawater sulfate representing the initial sulfate in the basin was assumed to have $\delta^{34}S = 2‰$ based on the minimum value observed in our dataset ($\delta^{34}S = 2.9‰$) and an ~1‰ isotope effect between dissolved sulfate and barite (Ohmoto et al., 1990), with $\Delta^{33}S = -1.25‰$ for Londozi

and $\Delta^{33}S$ = -0.80‰ for deposits from the Fig Tree Group (Stentor and Barite Valley deposits). Data from Vergelegen was not used in the model, because of the small dataset and large statistical uncertainties on trends. For each scenario, the ratio r of added sulfate divided by the amount of sulfate removed through microbial sulfate reduction was varied to obtain best approximations of measured isotopic compositions and co-variations. Note that the model only explores end members of added sulfate compositions, whereas the actual added pool may represent a mixture of juvenile and biogenic sulfur.

2.5.2 Model results

Modeling results are shown in Fig. 2.5 and Table 2.4. Addition of juvenile sulfur to residual sulfate from microbial sulfate reduction was found to produce trends and isotopic compositions similar to those observed at Londozi when r = 0.4, indicating that more than twice as much sulfate is reduced than added. Sulfate with $\delta^{34}S \approx 7.5$‰ is produced when 50% of the initial sulfate has been metabolized. Fig Tree barites require a ratio r = 0.75 in this scenario, and 60% of the sulfate must be reduced to produce sulfate with the heaviest $\delta^{34}S$ measured in these deposits. Mixing of biogenic sulfate derived from microbial sulfide oxidation with residual basin sulfate produced isotopic compositions in agreement with measured values, using r = 0.4 for Londozi and r = 0.65 for the Fig Tree barites with 53% and 63% of the sulfate reduced to explain the most ^{34}S-enriched barites, respectively. In the final scenario, mixing with sulfate derived from microbially-disproportionated photolytic elemental sulfur required a ratio r = 0.13 for Londozi and r = 0.22 for the Fig Tree barites, suggesting that microbial sulfate reduction was more important than sulfur disproportionation in the basins where barites formed. Approximately 40% of the sulfate must be reduced to produce the most ^{34}S-enriched barites.

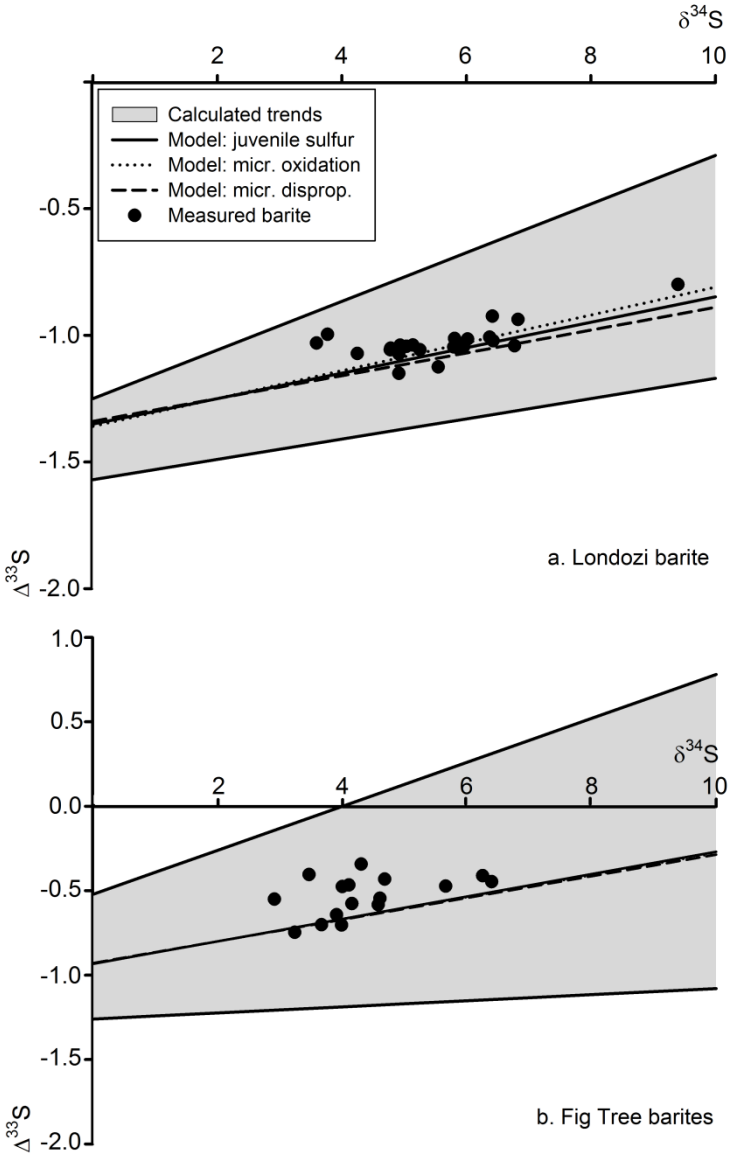

Figure 2.5 *Model results for the Londozi barite (a) and Stentor and Barite Valley deposits grouped here as Fig Tree barites (b). Grey areas indicate ranges of calculated trendlines, taking errors on slopes and intercepts into account (95% confidence level). Solid, dotted and dashed lines indicate model results for addition of juvenile sulfur, sulfate from microbial oxidation or disproportionation, respectively. The ratio of added sulfate over reduced sulfate varies from 0.13-0.22 for the disproportionation scenario, to 0.4-0.75 for addition of juvenile sulfur and 0.4-0.65 for sulfide oxidation at Londozi and Stentor/Barite Valley, respectively. Reduction of 40-65% of sulfate is required to explain the most* ^{34}*S-enriched barites.*

Model, dataset	$\delta^{33}S/\delta^{34}S$	$\delta^{33}S/\delta^{34}S_i$	$\Delta^{33}S/\delta^{34}S$	$\Delta^{33}S/\delta^{34}S_i$	$\Delta^{36}S/\Delta^{33}S$	$\Delta^{36}S/\Delta^{33}S_i$
JUV, Londozi	0.56	-1.35	0.050	-1.35	-0.88	0.15
JUV, Fig Tree	0.58	-0.93	0.066	-0.93	-0.91	0.07
OX, Londozi	0.57	-1.36	0.055	-1.36	-0.87	0.16
OX, Fig Tree	0.58	-0.93	0.060	-0.93	-0.88	0.10
DIS, Londozi	0.56	-1.34	0.045	-1.34	-0.89	0.13
DIS, Fig Tree	0.58	-0.93	0.064	-0.93	-0.94	0.05

Table 2.4 *Model results for the Londozi barite and Fig Tree barites (Stentor and Barite Valley) for three different scenarios. $\delta^{33}S/\delta^{34}S$, $\Delta^{33}S/\delta^{34}S_i$ and $\Delta^{36}S/\Delta^{33}S_i$ denote modeled intercept values. JUV: addition of juvenile sulfur, OX: addition of sulfate from microbial sulfide oxidation, DIS: addition of sulfate from microbial disproportionation of elemental sulfur.*

2.6 DISCUSSION

2.6.1 Atmospheric source of sulfate

Data presented in this paper expand the isotopic record of sulfate back to 3.55 Ga and confirm that Paleoarchean barites from southern Africa contain mass-independently fractionated sulfur (cf. Farquhar et al., 2000; Bao et al., 2007; Ueno et al., 2008; Shen et al., 2009). Observation of these isotope signatures has been interpreted to reflect photochemical reactions in an anoxic atmosphere (Farquhar et al., 2000; Pavlov and Kasting, 2002), suggesting that the barites provide evidence for a dominant atmospheric source of sulfate to the oceans. Strong correlation between $\Delta^{36}S$ and $\Delta^{33}S$ is consistent with a photolytic origin of the barite-sulfur (Farquhar et al., 2001), and the magnitude of $\Delta^{36}S/\Delta^{33}S$ of -1.0 ± 0.2 found in this study is similar to trends observed in Paleoarchean and Neoarchean sulfides (Farquhar et al., 2000; Kaufman et al., 2007; Ueno et al., 2008). This agreement between oxidized and reduced sulfur MIF-compositions leads us to conclude that in the Paleoarchean, atmospheric photolysis of sulfur dioxide produced sulfur species with a $\Delta^{36}S/\Delta^{33}S$ ratio of -1. The correlation between mass-independent signatures is statistically the same for the individual barite deposits compared to the overall ratio, suggesting that $\Delta^{36}S/\Delta^{33}S$ in sulfate did not change between 3.55-3.23 Ga. This contrasts strongly with the Mesoarchean rock record that displays changes in $\Delta^{36}S/\Delta^{33}S$ and $\Delta^{33}S/\delta^{34}S$, which were interpreted to reflect differences in atmospheric chemical reaction pathways (Farquhar et al., 2007b; Domagal-Goldman et al., 2008; Ueno et al., 2009), biological and abiotic redox cycling (Kaufman et al., 2007), or a combination of processes operating in the atmosphere, at the Earth's surface and in the oceans (Halevy et al., 2010).

Although $\Delta^{36}S/\Delta^{33}S$ was found to be constant, our data indicate that the magnitude of both mass-independent signatures decreased from 3.55 to 3.23 Ga in the Barberton region, with an average $\Delta^{33}S$ of -0.99‰ for the Onverwacht Group deposits older than 3.4 Ga, and -0.53‰ for younger barites from the Fig Tree Group. This confirms previous observations by Bao et al. (2007) and is consistent with the more negative average $\Delta^{33}S$ (-1.13‰) in the 3.49 Ga Dresser barite (Farquhar et al., 2000; Ueno et al., 2008; Shen et al., 2009) compared to the ca. 3.29 Ga Indian Sargur barite with $\Delta^{33}S$ = -0.46‰ (Hoering, 1989; Peucat et al., 1995). The difference is unlikely to reflect changing photochemical source reactions because a shift in $\Delta^{36}S/\Delta^{33}S$ was not observed at 3.4 Ga, but may be related to changes in the composition of the atmosphere that cause attenuation of

certain wavelengths. A decline in atmospheric carbonyl sulfide (OCS) due to diminished volcanic emissions could produce positive sulfate $\Delta^{33}S$ (Ueno et al., 2009), but evidence for decreasing volcanic activity during the Paleoarchean is lacking from the rock record and seems inconsistent with the suggested onset of subduction at 3.22 Ga in the Barberton region (De Ronde and De Wit, 1994).

We hypothesize that suppressed MIF-signatures were related to a smaller proportion of photolytic sulfur relative to non-photolytic sulfur that entered the seawater directly from volcanic degassing of SO_2. Observed timescales of variation in $\Delta^{33}S$ ($\sim 10^7$-10^8 yr) appear to correspond to significant changes in the tectonic regime of the Barberton greenstone belt, from plume-related processes at 3.55 Ga to convergent arc-like and accretionary tectonics at 3.22 Ga (De Ronde and De Wit, 1994). This shift in tectonic style possibly led to an increased input of juvenile sulfur to the marine sulfate pool due to elevated volcanic SO_2/H_2S, caused by a decreased H_2O-content of the mantle related to volcanic degassing (Keppler, 2011), the onset of subduction of sulfur-rich minerals (Holland, 2009), or a change from submarine venting of reduced gasses to subaerial eruptions of more oxidized gasses (Gaillard et al., 2011). Nevertheless, clear mixing trends towards juvenile sulfur were not observed in our dataset, suggesting that inputs of juvenile sulfate remained relatively weak in comparison to the dominant atmospheric source.

2.6.2 Large-scale microbial reduction of seawater sulfate

Multiple sulfur isotopic compositions of microscopic pyrite have been interpreted as evidence for the presence of sulfate reducing micro-organisms in the Paleoarchean (Shen et al., 2001; Ueno et al., 2008; Shen et al., 2009; Wacey et al., 2010; Wacey et al., 2011a), suggesting that atmospheric sulfate deposited into the oceans was subsequently processed via microbial pathways. Inferring the extent of biological sulfate reduction in the global oceans strongly depends on the assumed isotopic composition of photolytic sulfate aerosols. Two suggestions have been made about the composition of this atmospheric sulfate (Fig. 2.6), both of which are based on the principle that it should isotopically balance ^{33}S-enriched sulfur removed from the same juvenile sulfur pool. Ueno et al. (2008) proposed a composition with $\delta^{34}S$ = -5 ± 2‰ and $\Delta^{33}S$ = -3 ± 1‰ that was derived by extrapolating a positive $\Delta^{33}S/\delta^{34}S$ array found in vein-hosted pyrites from the Dresser Formation and similar arrays found in Neoarchean sulfides (Ono et al.,

2003). Alternatively, Philippot et al. (2007) suggested that atmospheric sulfate is better represented by the composition of the barites themselves ($\delta^{34}S \approx +5‰$, $\Delta^{33}S \approx -1‰$), based on the fractionation effect seen in SO_2 photolysis experiments at 193 nm (Farquhar et al., 2001) and a different array in microscopic sulfides from the Dresser barite that extends to negative $\delta^{34}S$ and positive $\Delta^{33}S$. Both proposed photolysis arrays do not match predictions from models (Lyons, 2009) and magnitudes of $\delta^{34}S$ and $\Delta^{33}S$ are significantly smaller than seen for oxidized sulfur produced in photolysis experiments (Farquhar et al., 2001; Masterson et al., 2011), but it has also been demonstrated that these suggestions are sensitive to a variety of other factors including atmospheric composition and transparency (Farquhar et al., 2001; Pavlov and Kasting, 2002; Lyons, 2009).

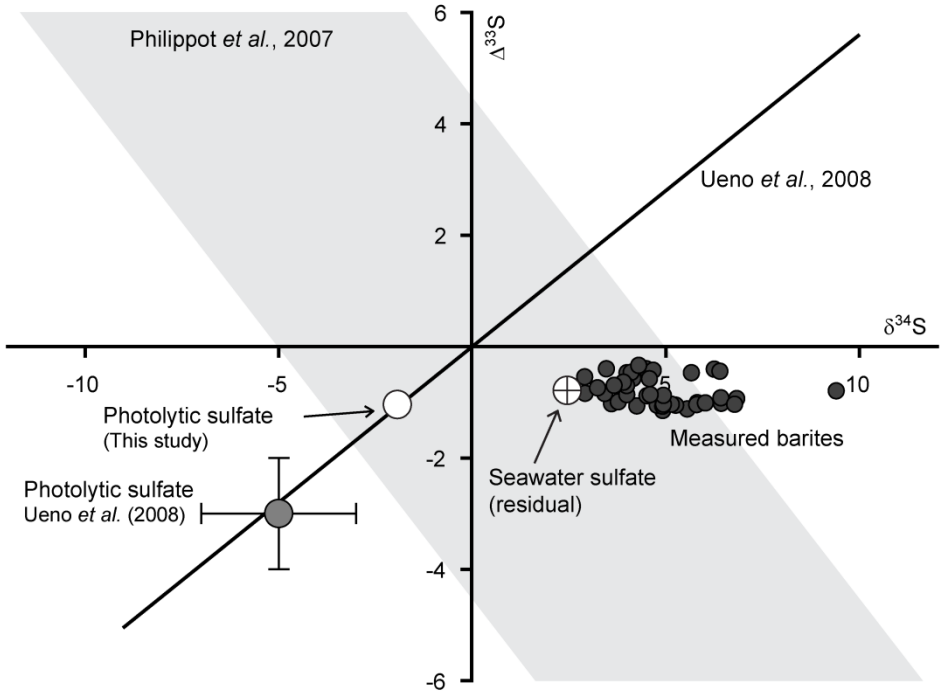

Figure 2.6 *Plot showing SO_2 photolysis arrays between elemental sulfur ($\Delta^{33}S > 0‰$) and sulfate ($\Delta^{33}S < 0‰$) as suggested by Philippot et al. (2007) and Ueno et al. (2008), the isotopic composition of photolytic sulfate from Ueno et al. (2008) and this study, and the inferred composition of residual seawater sulfate. The isotope effect between photolytic and seawater sulfate is thought to reflect global-scale microbial sulfate reduction, while the variation in $\delta^{34}S$ in the barites represents basin-scale biological reduction of sulfate.*

The implications of the two inferred compositions for sulfate deposited from the Paleoarchean atmosphere are very different. The estimate of Philippot et al. (2007) implies no isotope fractionation during sulfate cycling in the oceans, so that the composition of the barite represents the oxidized photolysis products. However, this appears to contradict evidence from pyrite for the presence of microbial sulfate reduction. Biological isotope fractionation is suppressed at sulfate concentrations below 200 μM (Habicht et al., 2002), but significantly ^{34}S-depleted pyrites (10-20‰) are suggestive of local sulfate levels above this threshold for sulfate-limited isotope fractionation (Shen et al., 2001; Ueno et al., 2008; Shen et al., 2009; Wacey et al., 2010). In contrast, the estimate of Ueno et al. (2008) calls for a high proportion of pyrite burial associated with microbial sulfate reduction. Assuming $\delta^{34}S$ = -5‰ for photolytic sulfate and a sizeable fractionation of 10-15‰ associated with the biological sink, isotopic mass-balance for an open system predicts that 70-99% of all sulfate must be reduced to obtain a residual with $\delta^{34}S \approx 5‰$ and product sulfide with $\delta^{34}S \approx -5‰$.

The photolytic sulfate composition of Ueno et al. (2008) was determined from the intersection of an inferred photolysis array with weak trends observed in $\Delta^{33}S/\delta^{34}S$, interpreted by Bao et al. (2007) to reflect mixing between volcanic non-MIF and photochemically-derived MIF end members. We observed similar trends in $\Delta^{33}S/\delta^{34}S$ (Table 2.2), but argue that these are unlikely to represent mixing between two reservoirs, because variable slopes were observed for different deposits and trends did not converge to a single non-MIF end member, but varied from $\delta^{34}S \approx 19‰$ for Barite Valley to very high values of $\delta^{34}S \approx 32‰$ for Londozi.

We used an alternative approach to calculate the isotopic composition of photolytic sulfate, assuming that atmospheric photolysis is the only pathway in the sulfur cycle to produce significant mass-independent fractionation. The most negative $\Delta^{33}S$-values measured in the barites were therefore assumed to be indicative of atmospherically produced $\Delta^{33}S$-signatures, although magnitudes of $\Delta^{33}S$ are smaller than in experimentally produced oxidized sulfur and weak inputs of juvenile volcanic SO_2 might have shifted the barite-sulfate $\Delta^{33}S$ slightly towards zero. Using minimum $\Delta^{33}S$-values of -1.15‰ for Londozi and -0.75‰ for Barite Valley, we calculated $\delta^{34}S$-values of -2.7‰ and -2.0‰ respectively, following the trend reported by Ueno et al. (2008). These compositions are slightly less ^{34}S-depleted than those proposed by Ueno et al., but imply an average isotope effect between photolytic and residual seawater sulfate ($\delta^{34}S \approx 2.0‰$) of approximately 5‰. Based on the widespread occurrence of barite before 3.2 Ga (Huston and

Logan, 2004) and the considerable overlap between isotopic compositions of these deposits from southern Africa, India and Western Australia ($\delta^{34}S$ = 2-7‰), we argue that this isotope effect represents a large-scale or global role for microbial sulfate reduction, with small magnitude biological fractionations producing residual seawater sulfate with $\delta^{34}S \approx 2‰$ (cf. Ohmoto et al., 1993). Preservation of mass-independent signatures indicates that the amount of cycling between reduced, zero-valent and oxidized forms of sulfur was limited (Farquhar et al., 2000) and that global recycling of the microbially produced sulfide was minimal.

2.6.3 Oceanic mixing and sulfate residence time

Data obtained in this study and by Bao et al. (2007) demonstrate that multiple sulfur isotopic compositions of southern African barites are consistent with the narrow range observed in barites from India and Western Australia, showing less than 5‰ variation in $\delta^{34}S$ and 1-2‰ in $\Delta^{33}S$ and $\Delta^{36}S$ per deposit (Hoering, 1989; Farquhar et al., 2000; Ueno et al., 2008; Shen et al., 2009). The $\Delta^{33}S$ and $\Delta^{36}S$ in individual deposits, and even deposits of similar age, are remarkably uniform when compared to reduced forms of Paleoarchean sedimentary sulfur (Philippot et al., 2007; Ueno et al., 2008; Shen et al., 2009; Wacey et al., 2010; Golding et al., 2011), suggesting that barite-sulfate was derived from a comparatively well-mixed pool, or at least one supplied by sources with stable compositions and fluxes. Homogenization of the marine sulfate pool requires the residence time to exceed the whole ocean mixing time, estimated at $\sim 10^3$ years for the modern ocean. However, the preservation of a temporal trend in $\Delta^{33}S$ defined by barite deposits that differ 30-140 million years in age indicates that residence times were shorter than $\sim 10^7$-10^8 years, because oceanic mixing on these timescales would have erased isotopic trends. Based on the relatively narrow range in $\Delta^{33}S$ seen in individual deposits versus the decreasing $\Delta^{33}S$ observed on longer timescales, we argue that the residence time of Paleoarchean marine sulfate was comparable to, but not significantly longer than the $\sim 10^4$ years required for barite formation (Reimer, 1980). This calculated residence time is considerably shorter than the estimate of 1.3 Myr for sulfate in the Neoarchean (Ono et al., 2009), and supports the presence of an important microbial sink as early as the Paleoarchean.

Exceptions to the relative homogeneity in $\Delta^{33}S$ are seen in samples from Vergelegen and Barite Valley. The latter deposit consists of detrital barite and recrystallized blades, indicating different events of barite reworking and chemical recycling. In contrast to Reimer (1980), we did not observe isotopic differences between blades ($\delta^{34}S$ = 3.6‰) and detrital matrix ($\delta^{34}S$ = 3.8‰) at Barite Valley, but variable sources for the detrital phase are consistent with a higher variability in $\Delta^{33}S$ than in non-detrital deposits. The origin of the significant difference in $\Delta^{33}S$ between samples VER-01 (-0.89‰) and VER-02 (-0.42‰) from the Vergelegen deposit remains unknown, but the overlap in isotopic composition between VER-02 and younger Fig Tree barites tentatively suggests a different origin for the two Vergelegen samples. Further field constraints on the complex stratigraphic relations at this location may help to elucidate whether the samples represent different barite horizons.

Finally, to argue for homogenization by oceanic mixing processes requires proof that metamorphism did not cause isotopic resetting. Although all deposits experienced some degree of metamorphism, metamorphic homogenization of sulfur isotopes in barite by dissolution is severely hampered by its low solubility product at high pressures and temperatures, i.e. ~2 µM SO_4^{2-} at 400ºC and 2 kbar (Hanor, 2000). Theoretical work suggests that barite may become solubilized through reactions with reducing gasses above 200ºC and low pH (Kritsotakis and Von Platen, 1980), but the extent of these reactions is probably limited as field evidence indicates remarkable stability of barite during metamorphism in the presence of reducing agents (Hanor, 2000). Furthermore, temporal trends in $\Delta^{33}S$ and $\Delta^{36}S$ are preserved by all deposits despite considerably different metamorphic conditions, e.g. isotopic compositions of the Londozi (3.55 Ga, amphibolite facies) and Dresser barite (3.49 Ga, prehnite-pumpellyite facies (Buick and Dunlop, 1990)) show considerable overlap. The absence of diluted $\Delta^{33}S$-signatures in more metamorphosed deposits and the lack of obvious mixing trends with juvenile-S from metamorphic fluids suggests that that isotopic homogenization of the sulfate resulted from oceanic processes and not metamorphic resetting.

2.6.4 Local microbial sulfate reduction and mixing

Geological evidence suggests that Paleoarchean barites were deposited in semi-closed marine environments (Sections 2.2.1-2.2.4). Therefore, we argue that the weak trends in $\Delta^{33}S/\delta^{34}S$ observed per individual deposit reflect redox processes and mixing in these basins, instead of global hydrothermal mixing suggested by Bao et al. (2007) and Ueno et al. (2008) and discussed in 2.6.2. Our alternative model attributes changes in $\delta^{34}S$ to reservoir affects associated with a ^{34}S-depleted sink, and co-variation with $\Delta^{33}S$ to a weak supply of juvenile sulfur from magmatic sources or biogenic sulfate from microbial sulfide oxidation or elemental sulfur disproportionation. Possible basin-scale sinks include abiotic and microbial sulfate reduction, of which we consider the latter most important. Abiotic sulfate reduction is known to occur at intermediate temperatures (100-200ºC) when organic material is available, or at high temperatures (250-350ºC) in hydrothermal systems with ferrous iron (Ohmoto and Goldhaber, 1997), with associated isotope effects between 10‰ and 20‰ (Shanks III et al., 1981; Machel et al., 1995). However, in the modern sulfate-rich (28 mM SO_4^{2-}) oceans, the amount of inorganically reduced sulfur is only 1-2% of the microbial reduction flux (Jørgensen and Kasten, 2006). Since the amount of sulfur initially present in the system represents an important kinetic control on reaction rates (Machel, 2001), it seems unlikely that in Paleoarchean marine environments with significantly lower sulfate concentrations (~200 μM SO_4^{2-}) relative abiotic sulfate reduction fluxes exceeded those of the modern oceans. Furthermore, whereas pyrite is present at Londozi, Stentor and Barite Valley, sulfides are absent from the Vergelegen deposit. This suggests that sulfide-generating sinks responsible for the $\delta^{34}S$-variability were not associated with barite formation near hydrothermal vents releasing Ba-rich fluids, but reflected processes occurring elsewhere in the basin, consistent with microbial sulfate reduction.

Fig. 2.5 shows that our model with a dominant biological sink produced arrays that match observations in isotopic co-variation in the Londozi and Fig Tree Group deposits. Inputs of sulfur with zero or positive $\Delta^{33}S$ were modeled to be 13-40% of the amount of sulfate reduced for Londozi and 22-75% for Fig Tree, suggesting that microbial sulfate reduction was more important in local basins than sulfide oxidation or sulfur disproportionation. Results were calculated for three distinct sources of sulfate, although combined biological and magmatic inputs may be more representative for Paleoarchean basins. This would suggest an even lower importance of microbial oxidation and disproportionation

pathways relative to sulfate reduction, considerably different from roles inferred for these metabolisms from Neoarchean successions (Kaufman et al., 2007).

2.7 CONCLUSIONS

We describe atmospheric, oceanic and biological processes involved in the formation and evolution of the Paleoarchean marine sulfate reservoir, based on multiple sulfur isotopic compositions of 3.55-3.23 Ga sedimentary barites from the Barberton greenstone belt in South Africa and Swaziland. Our results indicate an oceanic sulfate pool with stable $\delta^{34}S$ and conserved $\Delta^{33}S$ and $\Delta^{36}S$ that evolved on relatively long timescales ($\sim 10^6$-10^7 years). Levels of sulfate were maintained in the Paleoarchean oceans by a balance of sources related to atmospheric deposition of photolytic sulfate ($\Delta^{36}S/\Delta^{33}S = -1.0 \pm 0.2$) and sinks related to global-scale microbial sulfate reduction, with an average isotope effect in $\delta^{34}S$ between atmospheric and residual seawater sulfate of $\sim 5‰$. Observation of co-evolving $\delta^{34}S$ and $\Delta^{33}S$ within individual deposits suggests a role for processes occurring in semi-closed basins fed by this large-scale or global oceanic sulfate pool. We propose a model that associates basin-scale isotopic evolution with local microbial sulfate reduction removing ^{34}S-enriched sulfur from a small pool, and limited contributions of sulfate from magmatic inputs, microbial sulfide oxidation and/or sulfur disproportionation. Processes are shared by different basins, but the balance between supplies and sinks varies slightly from deposit to deposit. Our data suggest that microbial sulfate reduction was important on both a global and local scale in the marine environments of the Paleoarchean, consistent with the inferred importance of this metabolism on the early Earth from microscopic pyrite data (Shen et al., 2001; Ueno et al., 2008; Shen et al., 2009; Wacey et al., 2010).

Acknowledgements

The Mpumalanga parks authority provided field support and access to the Somingvelo Game reserve in the Barberton Mountain Land. We thank Aubrey Zerkle for analytical support. This research was funded by a grant from the User Support Programme Space Research and the Netherlands Organization for Scientific Research. Fieldwork in South Africa was financially supported by the dr. Schürmannfonds.

References

Armstrong, R.A., Compston, W., de Wit, M.J., Williams, I.S., 1990. The stratigraphy of the 3.5-3.2 Ga Barberton Greenstone Belt revisited: A single zircon ion microprobe study. Earth Planet. Sci. Lett. 101, 90-106.

Bao, H., Rumble Iii, D., Lowe, D.R., 2007. The five stable isotope compositions of Fig Tree barites: Implications on sulfur cycle in ca. 3.2 Ga oceans. Geochim. Cosmochim. Acta 71, 4868-4879.

Barton, C.M., 1982. Geology and mineral resources of Northwest Swaziland (Barberton Greenstone Belt). Bulletin of the Swaziland Geological Survey and Mines Department 10.

Böttcher, M.E., Thamdrup, B., Vennemann, T.W., 2001. Oxygen and sulfur isotope fractionation during anaerobic bacterial disproportionation of elemental sulfur. Geochim. Cosmochim. Acta 65, 1601-1609.

Buick, R., Dunlop, J.S.R., 1990. Evaporitic sediments of Early Archaean age from the Warrawoona Group, North Pole, Western Australia. Sedimentology 37, 247-277.

Byerly, G.R., Kröner, A., Lowe, D.R., Todt, W., Walsh, M.M., 1996. Prolonged magmatism and time constraints for sediment deposition in the early Archean Barberton greenstone belt: evidence from the Upper Onverwacht and Fig Tree groups. Precambrian Res. 78, 125-138.

Canfield, D.E., Thamdrup, B., 1994. The production of 34S-depleted sulfide during bacterial disproportionation of elemental sulfur. Science 266, 1973-1975.

Condie, K.C., Macke, J.E., Reimer, T.O., 1970. Petrology and Geochemistry of Early Precambrian Graywackes from the Fig Tree Group, South Africa Geol. Soc. Am. Bull. 81, 2759-2776.

Danielache, S.O., Eskebjerg, C., Johnson, M.S., Ueno, Y., Yoshida, N., 2008. High-precision spectroscopy of ^{32}S, ^{33}S and ^{34}S sulfur dioxide: Ultraviolet absorption cross sections and isotope effects. J. Geophys. Res. 113, D17414.

De Ronde, C.E.J., De Wit, M.J., 1994. Tectonic history of the Barberton greenstone belt, South Africa: 490 million years of Archean crustal evolution. Tectonics 13, 983-1005.

de Vries, S.T., Nijman, W., Armstrong, R.A., 2006. Growth-fault structure and stratigraphic architecture of the Buck Ridge volcano-sedimentary complex, upper Hooggenoeg Formation, Barberton Greenstone Belt, South Africa. Precambrian Res. 149, 77-98.

de Vries, S.T., Nijman, W., de Boer, P.L., 2010. Sedimentary geology of the

Palaeoarchaean Buck Ridge (South Africa) and Kittys Gap (Western Australia) volcano-sedimentary complexes. Precambrian Res. 183, 749-769.

Domagal-Goldman, S.D., Kasting, J.F., Johnston, D.T., Farquhar, J., 2008. Organic haze, glaciations and multiple sulfur isotopes in the Mid-Archean Era. Earth Planet. Sci. Lett. 269, 29-40.

Dziggel, A., Stevens, G., Poujol, M., Armstrong, R.A., 2006. Contrasting source components of clastic metasedimentary rocks in the lowermost formations of the Barberton greenstone belt. Geol. Soc. Am. Spec. Pap. 405, 157-172.

Farquhar, J., Bao, H., Thiemens, M., 2000. Atmospheric Influence of Earth's Earliest Sulfur Cycle. Science 289, 756-758.

Farquhar, J., Kim, S.-T., Masterson, A., 2007a. Implications from sulfur isotopes of the Nakhla meteorite for the origin of sulfate on Mars. Earth Planet. Sci. Lett. 264, 1-8.

Farquhar, J., Peters, M., Johnston, D.T., Strauss, H., Masterson, A., Wiechert, U., Kaufman, A.J., 2007b. Isotopic evidence for Mesoarchaean anoxia and changing atmospheric sulphur chemistry. Nature 449, 706-709.

Farquhar, J., Savarino, J., Airieau, S., Thiemens, M.H., 2001. Observation of wavelength-sensitive mass-independent sulfur isotope effects during SO_2 photolysis: Implications for the early atmosphere. J. Geophys. Res. 106, 32829-32839.

Farquhar, J., Wu, N., Canfield, D.E., Oduro, H., 2010. Connections between Sulfur Cycle Evolution, Sulfur Isotopes, Sediments, and Base Metal Sulfide Deposits. Econ. Geol. 105, 509-533.

Forrest, J., Newman, L., 1977. Silver-110 microgram sulfate analysis for the short time resolution of ambient levels of sulfur aerosol. Anal. Chem. 49, 1579-1584.

Gaillard, F., Scaillet, B., Arndt, N.T., 2011. Atmospheric oxygenation caused by a change in volcanic degassing pressure. Nature 478, 229-232.

Golding, S.D., Duck, L.J., Young, E., Baublys, K.A., Glikson, M., Kamber, B.S., 2011. Earliest seafloor hydrothermal systems on Earth: Comparison with modern analogues, in: Golding, S.D., Glikson, M. (Eds.), Earliest life on Earth: Habitats, environments and methods of detection. Springer, pp. 15-49.

Habicht, K.S., Gade, M., Thamdrup, B., Berg, P., Canfield, D.E., 2002. Calibration of sulfate levels in the Archean ocean. Science 298, 2372-2374.

Halevy, I., Johnston, D.T., Schrag, D.P., 2010. Explaining the Structure of the Archean Mass-Independent Sulfur Isotope Record. Science 329, 204-207.

Hanor, J.S., 2000. Barite-Celestine Geochemistry and Environments of Formation, in: Alpers, C.N., Jambor, J.L., Nordstrom, D.K. (Eds.), Reviews in Mineralogy and Geochemistry: Sulfate minerals. Crystallography, Geochemistry and Environmental Significance. . Mineralogical Society of America, Washington, D.C.

Heinrichs, T.K., Reimer, T., 1977. A sedimentary barite deposit from the Archean Fig Tree Group of the Barberton Mountain Land (South Africa). Econ. Geol. 72, 1426-1441.

Hoering, T.C., 1989. The isotopic composition of bedded barites from the Archean of Southern India. J. Geol. Soc. India 34, 461-466.

Hofmann, A., 2005. The geochemistry of sedimentary rocks from the Fig Tree Group, Barberton greenstone belt: Implications for tectonic, hydrothermal and surface processes

during mid-Archaean times. Precambrian Res. 143, 23-49.
Holland, H.D., 2009. Why the atmosphere became oxygenated: A proposal. Geochim. Cosmochim. Acta 73, 5241-5255.
Huston, D.L., Logan, G.A., 2004. Barite, BIFs and bugs: evidence for the evolution of the Earth's early hydrosphere. Earth Planet. Sci. Lett. 220, 41-55.
Johnston, D.T., Farquhar, J., Canfield, D.E., 2007. Sulfur isotope insights into microbial sulfate reduction: When microbes meet models. Geochim. Cosmochim. Acta 71, 3929-3947.
Jørgensen, B.B., Kasten, S., 2006. Sulfur cycling and methane oxidation, in: Schulz, H.D., Zabel, M. (Eds.), Marine geochemistry. Springer, Berlin, pp. 271-309.
Kaufman, A.J., Johnston, D.T., Farquhar, J., Masterson, A.L., Lyons, T.W., Bates, S., Anbar, A.D., Arnold, G.L., Garvin, J., Buick, R., 2007. Late Archean Biospheric Oxygenation and Atmospheric Evolution. Science 317, 1900-1903.
Keppler, H., 2011. Water in the mantle, melting, and the evolution of Earth's atmosphere. Mineral. Mag. 75, 1172.
Kohler, E.A., 2003. The geology of the Archean granitoid-greenstone terrane in the vicinity of three sisters, Barberton greenstone belt. . Bulletin of the Council for Geoscience, Geological Survey of South Africa 133.
Kohler, E.A., Anhaeusser, C.R., 2002. Geology and geodynamic setting of Archaean silicic metavolcaniclastic rocks of the Bien Venue Formation, Fig Tree Group, northeast Barberton greenstone belt, South Africa. Precambrian Res. 116, 199-235.
Kritsotakis, K., Von Platen, H., 1980. Reduktive Barytmobilisation. Neues Jahrb. Mineral. Abh. 137, 282-306.
Kröner, A., Byerly, G.R., Lowe, D.R., 1991. Chronology of early Archaean granite-greenstone evolution in the Barberton Mountain Land, South Africa, based on precise dating by single zircon evaporation. Earth Planet. Sci. Lett. 103, 41-54.
Kröner, A., Hegner, E., Wendt, J.I., Byerly, G.R., 1996. The oldest part of the Barberton granitoid-greenstone terrain, South Africa: evidence for crust formation between 3.5 and 3.7 Ga. Precambrian Res. 78, 105-124.
Lasaga, A.C., Otake, T., Watanabe, Y., Ohmoto, H., 2008. Anomalous fractionation of sulfur isotopes during heterogeneous reactions. Earth Planet. Sci. Lett. 268, 225-238.
Lowe, D.R., Byerly, G.R., Heubeck, C., 1999. Structural divisions and development of the west-central part of the Barberton Greenstone Belt. Geological Society of America Special Papers 329, 37-82.
Lowe, D.R., Nocita, B.W., 1999. Foreland basin sedimentation in the Mapepe Formation, southern-facies Fig Tree Group, in: Lowe, D.R., Byerly, G.R. (Eds.), Geologic evolution of the Barberton greenstone belt, South Africa. Geological Society of America Special Paper, pp. 233-258.
Lowe, D.R., Worrell, G.F., 1999. Sedimentology, mineralogy and implications of silicified evaporites in the Kromberg Formation, Barberton Greenstone Belt, South Africa. Geol. Soc. Am. Spec. Pap. 329, 167-188.
Lyons, J.R., 2007. Mass-independent fractionation of sulfur isotopes by isotope-selective photodissociation of SO2. Geophys. Res. Lett. 34.
Lyons, J.R., 2009. Atmospherically-derived mass-independent sulfur isotope signatures, and incorporation into sediments. Chem. Geol. 267, 164-174.

Machel, H.G., 2001. Bacterial and thermochemical sulfate reduction in diagenetic settings -- old and new insights. Sediment. Geol. 140, 143-175.

Machel, H.G., Krouse, H.R., Sassen, R., 1995. Products and distinguishing criteria of bacterial and thermochemical sulfate reduction. Appl. Geochem. 10, 373-389.

Masterson, A.L., Farquhar, J., Wing, B.A., 2011. Sulfur mass-independent fractionation patterns in the broadband UV photolysis of sulfur dioxide: Pressure and third body effects. Earth Planet. Sci. Lett. 306, 253-260.

Ohmoto, H., Goldhaber, M.B., 1997. Sulfur and carbon isotopes, in: Barnes, H.L. (Ed.), Geochemistry of hydrothermal ore deposits. John Wiley & Sons, New York.

Ohmoto, H., Kaiser, C.J., Geer, K.A., 1990. Systematics of sulphur isotopes in recent marine sediments and ancient sediment-hosted basemetal deposits, in: Herbert, H.K., Ho, S.E. (Eds.), Stable Isotopes and Fluid Processes in Mineralization. University of Western Australia, Perth.

Ohmoto, H., Kakegawa, T., Lowe, D.R., 1993. 3.4-Billion-Year-Old Biogenic Pyrites from Barberton, South Africa: Sulfur Isotope Evidence. Science 262, 555-557.

Ono, S., Beukes, N.J., Rumble, D., 2009. Origin of two distinct multiple-sulfur isotope compositions of pyrite in the 2.5 Ga Klein Naute Formation, Griqualand West Basin, South Africa. Precambrian Res. 169, 48-57.

Ono, S., Eigenbrode, J.L., Pavlov, A.A., Kharecha, P., Rumble Iii, D., Kasting, J.F., Freeman, K.H., 2003. New insights into Archean sulfur cycle from mass-independent sulfur isotope records from the Hamersley Basin, Australia. Earth Planet. Sci. Lett. 213, 15-30.

Pavlov, A.A., Kasting, J.F., 2002. Mass-independent fractionation of sulfur isotopes in Archean sediments: strong evidence for an anoxic Archean atmosphere. Astrobiology 2, 27-41.

Peucat, J.J., Bouhallier, H., Fanning, C.M., Jayananda, M., 1995. Age of the Holenarsipur Greenstone Belt, relationships with the surrounding gneisses (Karnataka, South India). J. Geol. 103, 701-710.

Philippot, P., Van Zuilen, M., Lepot, K., Thomazo, C., Farquhar, J., Van Kranendonk, M.J., 2007. Early Archaean Microorganisms Preferred Elemental Sulfur, Not Sulfate. Science 317, 1534-1537.

Reimer, T.O., 1980. Archean sedimentary baryte deposits of the Swaziland Supergroup (Barberton Mountain Land, South Africa). Precambrian Res. 12, 393-410.

Reimer, T.O., 1990. Archaean baryte deposits of Southern Africa. J. Geol. Soc. India 35, 131-150.

Shanks III, W.C., Bischoff, J.L., Rosenbauer, R.J., 1981. Seawater sulfate reduction and sulfur isotope fractionation in basaltic systems: Interaction of seawater with fayalite and magnetite at 200-350°C. Geochim. Cosmochim. Acta 45, 1977-1995.

Shen, Y., Buick, R., Canfield, D.E., 2001. Isotopic evidence for microbial sulphate reduction in the early Archaean era. Nature 410, 77-81.

Shen, Y., Farquhar, J., Masterson, A., Kaufman, A.J., Buick, R., 2009. Evaluating the role of microbial sulfate reduction in the early Archean using quadruple isotope systematics. Earth Planet. Sci. Lett. 279, 383-391.

Tice, M.M., Bostick, B.C., Lowe, D.R., 2004. Thermal history of the 3.5-3.2 Ga

Onverwacht and Fig Tree Groups, Barberton greenstone belt, South Africa, inferred by Raman microspectroscopy of carbonaceous material. Geology 32, 37-40.

Tice, M.M., Lowe, D.R., 2006. The origin of carbonaceous matter in pre-3.0 Ga greenstone terrains: A review and new evidence from the 3.42 Ga Buck Reef Chert. Earth-Science Reviews 76, 259-300.

Ueno, Y., Johnson, M.S., Danielache, S.O., Eskebjerg, C., Pandey, A., Yoshida, N., 2009. Geological sulfur isotopes indicate elevated OCS in the Archean atmosphere, solving faint young sun paradox. Proc. Nat. Acad. Sci. U.S.A. 106, 14784-14789.

Ueno, Y., Ono, S., Rumble, D., Maruyama, S., 2008. Quadruple sulfur isotope analysis of ca. 3.5 Ga Dresser Formation: New evidence for microbial sulfate reduction in the early Archean. Geochim. Cosmochim. Acta 72, 5675-5691.

Viljoen, M.J., Viljoen, R.P., 1969. The geological and geochemical significance of the upper formations of the Onverwacht Group. Spec. Publ. Geol. Soc. S. Afr. 2, 113-151.

Wacey, D., Kilburn, M.R., Saunders, M., Cliff, J., Brasier, M.D., 2011a. Microfossils of sulphur-metabolizing cells in 3.4-billion-year-old rocks of Western Australia. Nat. Geosci. 4, 698-702.

Wacey, D., McLoughlin, N., Whitehouse, M.J., Kilburn, M.R., 2010. Two coexisting sulfur metabolisms in a ca. 3400 Ma sandstone. Geology 38, 1115-1118.

Wacey, D., Saunders, M., Brasier, M.D., Kilburn, M.R., 2011b. Earliest microbially mediated pyrite oxidation in ~3.4 billion-year-old sediments. Earth Planet. Sci. Lett. 301, 393-402.

Ward, J.H.W., 1999. Barytes, in: Ward, J.H.W. (Ed.), The metallogeny of the Barberton Greenstone Belt, South-Africa and Swaziland. Geological Survey of South-Africa Memoirs, pp. 32-34.

Watanabe, Y., Farquhar, J., Ohmoto, H., 2009. Anomalous Fractionations of Sulfur Isotopes During Thermochemical Sulfate Reduction. Science 324, 370-373.

Zerkle, A.L., Farquhar, J., Johnston, D.T., Cox, R.P., Canfield, D.E., 2009. Fractionation of multiple sulfur isotopes during phototrophic oxidation of sulfide and elemental sulfur by a green sulfur bacterium. Geochim. Cosmochim. Acta 73, 291-306

Male lion in Hlane Royal National Park, Lumbobo, Swaziland

Chapter 3

High-resolution quadruple sulfur isotope analyses of 3.2 Ga pyrite from the Barberton Greenstone Belt in South Africa reveal distinct environmental controls on sulfide isotopic arrays

This chapter was submitted to Geochimica et Cosmochimica Acta with co-authors Paul R.D. Mason, Martin J. Whitehouse, Thomas Reimer and is under review.

ABSTRACT

Multiple sulfur isotopes in Paleoarchean pyrite record valuable information on atmospheric processes and emerging microbial activity in the early sulfur cycle. Here, we report the first quadruple sulfur isotope data (^{32}S, ^{33}S, ^{34}S, ^{36}S) analyzed by secondary ion mass spectrometry from pyrite in a 3.26 to 3.23 Ga barite deposit in the Barberton Greenstone Belt, South Africa. Our results demonstrate the presence of distinct pyrite populations and isotopic arrays in barite-free and barite-rich lithologies. The most ^{34}S-depleted signatures with weakly positive $\Delta^{33}S/\delta^{34}S$ were found in disseminated pyrite in barite, whereas positive $\Delta^{33}S$-values with negative $\Delta^{33}S/\delta^{34}S$ and $\Delta^{36}S/\Delta^{33}S$ = -0.9 ± 0.2 were exclusively observed in pyrite hosted by chert, dolomite, conglomerate and breccia. We interpret these variations to be related to local redox reactions and mixing in the sulfide phase, rather than representing primary atmospheric variability. The strong correlation between lithology and isotopic compositions indicates distinct environments of sulfide formation linked to local sulfate concentrations and fluctuating inputs from different sulfur metabolisms. Strongly ^{34}S-depleted sulfide was formed by microbial sulfate reduction at $[SO_4^{2-}]$ > 200 µM during deposition of barite-rich sediments, whereas isotope effects were suppressed when sulfate levels decreased during deposition of terrigeneous clastic rocks. Positive $\Delta^{33}S$-values indicate an increased input of sulfide derived from elemental sulfur metabolisms when sulfate concentrations fell below 200 µM. Our results support an important role for the environment on the expression of isotopic arrays in the rock record preserved in one of the oldest rocks on Earth.

3.1 INTRODUCTION

Sulfur isotopes in sedimentary pyrite from Paleoarchean (3.6-3.2 Ga) greenstone belts provide a comprehensive record of biological and atmospheric controls on the early sulfur cycle. Mass-dependent fractionations in $\delta^{34}S$ up to 22‰ between microscopic pyrite and co-existing barite in the 3.49 Ga Dresser Formation of Western Australia were interpreted to reflect early microbial sulfate reduction (2001), providing the first evidence for microbiological sulfur cycling in the rock record. An important role for atmospheric deposition of sulfur species was revealed with the discovery of mass-independent fractionation (MIF) of minor isotopes ($\Delta^{33}S$, $\Delta^{36}S$) in sulfide and sulfate deposits older than 2.45 Ga (Farquhar et al., 2000), which was linked to UV-photolysis of volcanic SO_2 in a low-oxygen atmosphere (Pavlov and Kasting, 2002; Farquhar and Wing, 2003). Additional mass-independent fractionation was observed during thermochemical sulfate reduction (Watanabe et al., 2009; Oduro et al., 2011) and suggested for chemisorption reactions (Lasaga et al., 2008), but the relevance of these processes for the Archean rock record remains disputed (Farquhar et al., 2010; Oduro et al., 2011). Because mass-independent signatures of photochemical sulfate and elemental sulfur are preserved during subsequent mass-dependent fractionation, except for small shifts observed during microbial sulfate reduction and elemental sulfur disproportionation (Johnston et al., 2005; Ono et al., 2006; Johnston et al., 2007), atmospheric inputs of reduced and oxidized sulfur into the early environment as well as different sulfur metabolisms can be distinguished from the rock record based on triple or quadruple sulfur isotope analyses (Philippot et al., 2007; Ueno et al., 2008; Shen et al., 2009; Wacey et al., 2010).

However, the interpretation of these data requires information on the isotopic composition of the primary photolytic products and photochemical arrays, but it remains unclear how results from atmospheric chemistry modeling and experiments can be linked with isotope signatures observed in rocks. Early experimental work by Farquhar et al. (2001) showed that SO_2 photolysis at 193 nm produced $\Delta^{36}S/\Delta^{33}S$ correlations similar to those observed in Paleoarchean and Neoarchean sulfide (Farquhar et al., 2000), and a corresponding negative array in $\Delta^{33}S/\delta^{34}S$ was observed in Paleoarchean pyrite from the Dresser Formation (Philippot et al., 2007) and more recently, in sulfides from volcanic ash layers in the South African Mapepe Formation (Philippot et al., 2012). Alternatively, Ueno et al. (2008) reported a positive correlation between $\Delta^{33}S$ and $\delta^{34}S$ from the Dresser Formation, which is in good agreement with results from

Neoarchean shales, carbonates and iron formations of Hamersley basin in Western Australia and Transvaal Supergroup in South Africa (Ono et al., 2003; Kamber and Whitehouse, 2007; Kaufman et al., 2007; Ono et al., 2009b). However, the empirical value of ~0.56 for $\Delta^{33}S/\delta^{34}S$ differs significantly from the shallow slope of ~0.05 proposed from broadband solar radiation photolysis models and experiments (Lyons, 2007, 2009; Masterson et al., 2011; Whitehill and Ono, 2012), which were considered to be more realistic for the Archean atmosphere than the narrow band experiments by Farquhar et al. (2001) (Lyons, 2009). A possible explanation for these discrepancies between theoretical and natural data is that local redox processes shifted $\delta^{34}S$ values of photolytic end members, thereby hampering the interpretation of Paleoarchean photochemical arrays from the rock record.

Here, we evaluate the preservation of primary photochemical signatures in the quadruple sulfur isotope record of pyrite from the 3.26 to 3.23 Ga Barite Valley barite deposit in the Barberton Greenstone Belt of South Africa, similar to the study area of Philippot et al. (2012). Our high-resolution isotope analyses by secondary ion mass spectrometry (SIMS) enable us to distinguish large isotopic variability in macro- and microscopic pyrite preserved in barite-rich and barite-free sediments from a single drill core. We compare isotopic arrays preserved in different sedimentary environments represented by these distinct lithological units, and explore the roles of local redox processes and mixing on the expression of isotopic arrays in the rock record. We show that distinct pyrite isotopic compositions in barite-rich and barite-free sediments can be explained by environmental controls, instead of representing primary atmospheric processes.

3.2 GEOLOGICAL BACKGROUND

The Barite Valley barite deposit represents one the largest sulfate occurrences from the Paleoarchean and is located in the central part of the Barberton Greenstone Belt of South Africa (25°53'38"S, 31°4'8"E), as shown in Fig. 3.1. Here, barite occurs within terrigeneous clastic sediments that belong to the 3.26-3.23 Ga (Lowe, 1999) Lower and Middle Mapepe Formation of the Fig Tree Group (Heinrichs and Reimer, 1977; Reimer, 1980), which consists of cherts, jaspilitic

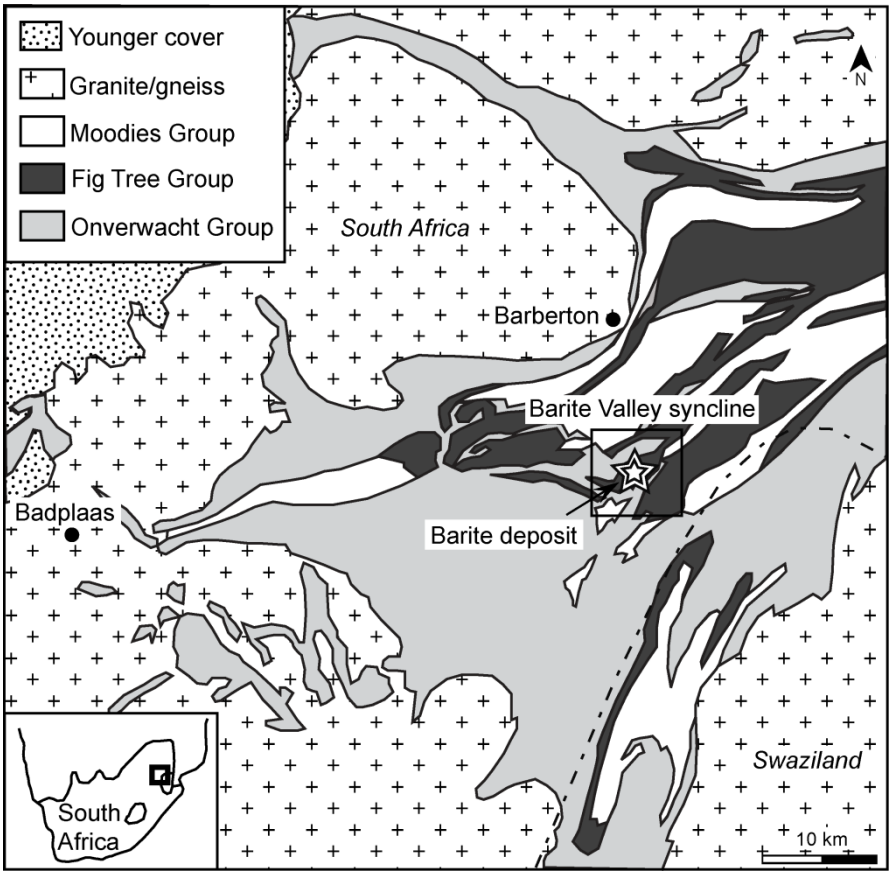

Figure 3.1 *Geological map of the Barberton Greenstone Belt showing the location of the drilled barite deposit in Barite Valley, South Africa. Modified after Hofmann et al (2005).*

silicified sediments and cherty or dolomitic conglomerates below and sandy tuffaceous sediments, greywackes and shales above the deposit (Heinrichs and Reimer, 1977). Horizons of green-colored barite sands with accessory pyrite, zircon and chromite as well as bladed crystals occur within a chert-rich zone that can be traced laterally for approximately 10 km. Original sedimentary and crystallographic textures were preserved due to relatively low degrees of metamorphism (lower greenschist facies) and minor deformation (Condie et al., 1970; Tice et al., 2004; Hofmann, 2005), showing faint traces of cross-lamination in silicified barite sands and large bundles of euhedral bladed barite crystals at high angles to the bedding (Heinrichs and Reimer, 1977). These features,

supported by lithological associations of the Mapepe Formation, suggest that the deposit formed from locally reworked barite in a foreland basin setting (Lowe and Nocita, 1999), with syn-sedimentary or diagenetic crystal growth of barite blades at the water-sediment interface (Reimer, 1980). Subduction-related fault zones such as the Inyoka thrust provided pathways for transport of barium-rich hydrothermal fluids and created a shallow submarine ridge where barite precipitation and syn-sedimentary reworking occurred. Fine tuffs, greywackes and ferruginous cherts were deposited in shallow subaqueous foreland basins, whereas coarser-grained sandstone and conglomerate formed in the fan-delta environment adjacent to the uplifted land areas (Lowe and Nocita, 1999).

3.3 MATERIAL AND METHODS

3.3.1 Samples

Pyrite samples for sulfur isotope analysis were derived from drill core ETC 1975 Heemsteede No. 5 (Fig. 3.2), which provides a section below the main barite quarry workings at Farm Heemsteede 378 JU in Barite Valley, in the central part of Barberton Greenstone Belt. The core intersects 45 m of barite-chert rich units with an overlying 45 m of well-preserved shale, greywacke, chert, dolomite and conglomerate (Fig. 3.2), which correlates well with the stratigraphy reported by Heinrichs and Reimer (1977) based on surface outcrops. All material was sampled from a depth of more than 150 m beneath the surface.

Studied pyrite-bearing barite-free lithologies include cherty conglomerate from a core depth of 166.8 m, massive chert at 173 m and 216.3 m, dolomite at 225.5 m, and brecciated chert at the base of the drill core or top of the stratigraphy at 254.8 m (see Fig. 3.2). Silicified barite sands were observed at 155.2 m, 155.5 m and 180.5, whereas (silicified) bladed barite was found at core depths of 173 m, 179 m and 188.2 m.

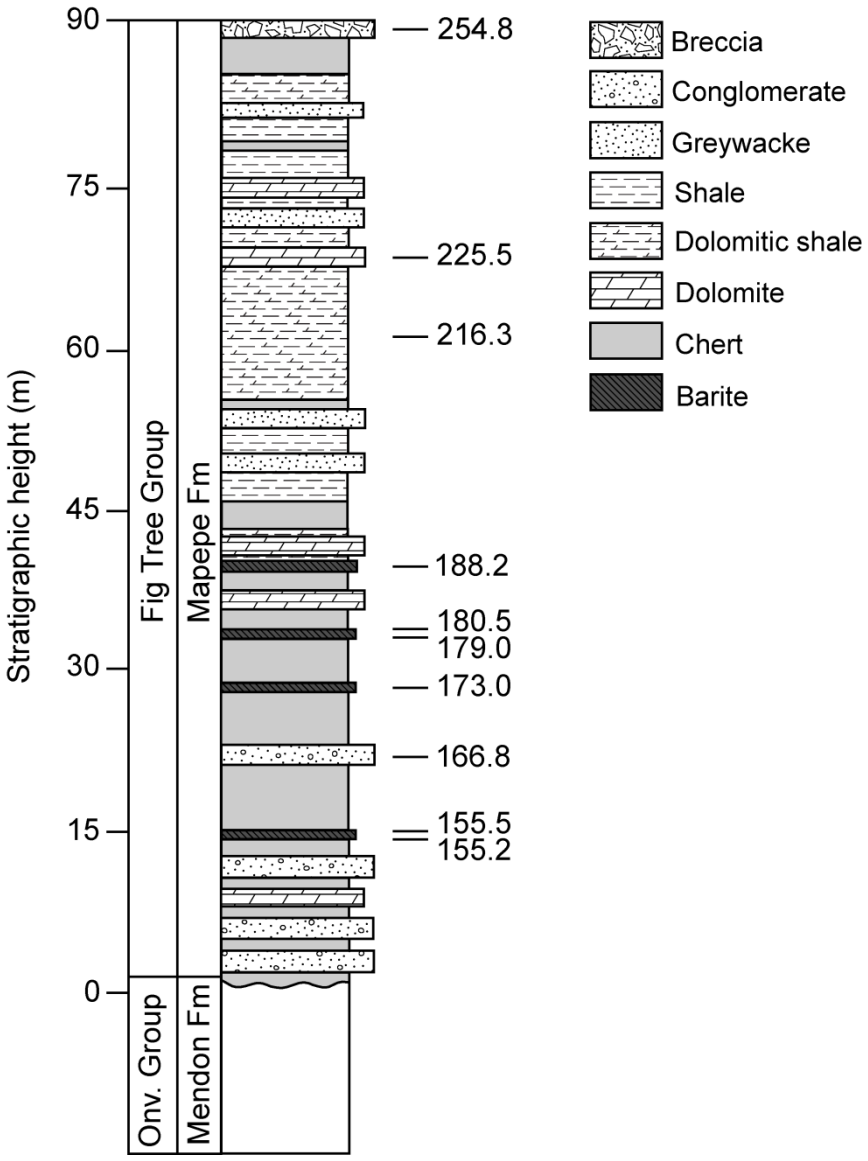

Figure 3.2 *Stratigraphy of drill core ETC 1975 Heemsteede No. 5 drilled through the Lower Mapepe Formation of the Fig Tree Group (well head coordinates 25°53'37.87"S, 31°04'08.46"E, bearing 322°, inclination -50° NW and recovery 97.8%). The section unconformably overlies the Mendon Formation of the Onverwacht Group. The core was drilled to a final depth of 254.9 m, which corresponds to a stratigraphic height of 90 m (indicated on left of the stratigraphic column). Sample names, defined in m of core depth, are shown to the right of the drill core to show the horizons from which they were taken.*

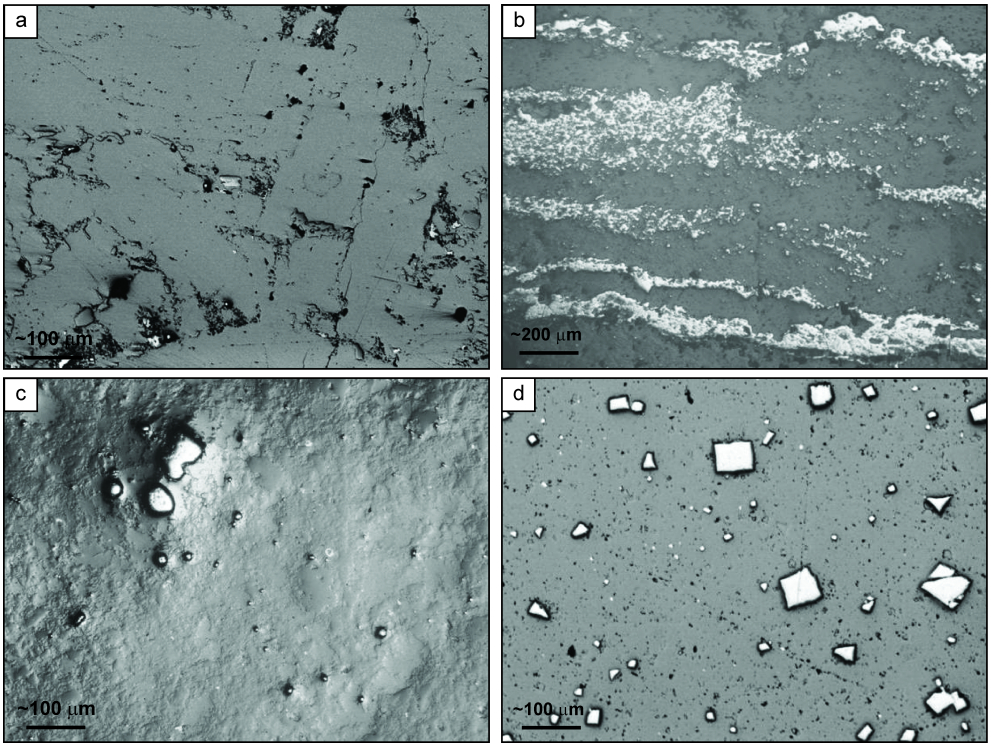

Figure 3.3 *Pyrite textures observed in drill core ETC 1975 Heemsteede No.5, showing (a) disseminated pyrite in between bladed barite, (b) layered pyrite in barite sands, (c) disseminated pyrite in chert and (d) euhedral pyrite from cherty conglomerate.*

The selected fragments of drill core contain four distinct pyrite populations based on texture and host lithology. Disseminated 20-50 µm pyrite occurs in (silicified) bladed barite in between crystal faces (Fig. 3.3a), with some grains up to 100 µm. A similar spatial association between barite crystals and microscopic pyrite was observed in the Dresser barite, which was interpreted to reflect a syngenetic origin of the two sulfur species (Shen et al., 2001). Silicified barite sands display distinct textures with macroscopic massive subhedral pyrite of at least 1000 µm at 155.5 m, as well as pyrite layers of at least several hundreds of micrometer thickness at 155.2 m and 180.5 m (Fig. 3.3b). In hand specimen, these layers extend on a centimeter-scale with relatively intact pyrite horizons at contacts between thin chert horizons and within barite sands, possibly hinting at late introduction of the sulfide into the reworked barite, but prior to a late stage of silicification. Finely disseminated pyrite grains of 10-50 µm size were also

observed in massive chert horizons in between barite at 173 m and dolomitic shales at 216.3 m (Fig. 3.3c), and occur in hand specimens in localized areas intersected by small, texturally late chert veins. Other sulfate-free lithologies (cherty conglomerate at 166.8 m, dolomite at 225.5 m, brecciated chert at 254.8 m) contained larger sub- to euhedral pyrite of ca. 100-200 μm. In particular, a limited number of cherty clasts in the conglomerate at 166.8 m contain very euhedral pyrite grains (Fig. 3.3d) with no pyrite in the host matrix, suggesting that the pyrite is of the same age as the clasts that predate formation of the conglomerate.

3.3.2 Quadruple sulfur isotope analyses

All four sulfur isotopes (^{32}S, ^{33}S, ^{34}S, ^{36}S) were analyzed in situ in selected pyrite using a CAMECA IMS-1280 instrument at the Swedish Museum of Natural History (Nordsim facility) during two sessions in 2009 and 2012. Analyses were conducted on polished rock chips mounted in 25 mm diameter epoxy blocks with 30 nm gold coating. A sector was cut from the sample blocks to allow co-mounting with three epoxy-embedded sulfide standards, the Ruttan pyrite with $\delta^{34}S = 1.2‰$ and Balmat pyrite with $\delta^{34}S = 15.1‰$ (Crowe and Vaughan, 1996), as well as anomalously fractionated pyrite from the Isua greenstone belt with $\delta^{34}S = 1.99 \pm 0.36‰$ and $\Delta^{33}S = +3.31 \pm 0.19‰$ based on conventional sulfur isotope analysis (Baublys et al., 2004), or $\Delta^{33}S = +3.15 \pm 0.36‰$ by SIMS (Whitehouse, 2012). The latter was also used as a monitor during ^{36}S measurements, for which replicate analyses during several analytical runs yielded $\Delta^{36}S = -2.20 \pm 0.21‰$ (2σ) (Whitehouse, 2012).

Instrument parameters and methods were broadly similar to those described by Whitehouse et al. (2005), Kamber and Whitehouse (2007) and Ulrich et al. (2011) for the collection of triple isotope data (^{32}S, ^{33}S, ^{34}S), and by Whitehouse (2012) for quadruple isotope data. Measurement of ^{36}S required the additional operation of an Hamamatsu 416 pulse-counting electron multiplier, because the low natural abundance of this isotope generates count rates which are inadequate for precise data from ordinary Faraday detectors (Whitehouse, 2012). Simultaneous analyses of all four isotopes in this configuration required measurement of ^{34}S on the axis, and an additional drift correction routine was required for $^{36}S/^{32}S$ to correct for linear gain drift on the electron multiplier during the course of an analytical session (Whitehouse, 2012). Analyses were

performed with a 10 kV and 2.5 nA Cs^+ focused primary beam with an average spot size of 10 μm, with operation of the low-energy electron flooding gun to compensate for charge build-up on the sample. Gold coating was removed during a 90 seconds pre-sputter over a 20 x 20 μm rastered area, during which detector backgrounds were measured for 30 seconds. Magnetic field stability was maintained using NMR regulation. Measurement of the -10 kV secondary ion beam was done at an effective mass resolution of approximately 4500 on ^{33}S, which was sufficient to resolve ^{33}S from $^{32}S^1H$. The Ruttan pyrite was used as the primary reference to correct raw sulfur isotope ratios for instrumental mass bias while both Ruttan and Balmat reference pyrites were used to constrain the mass dependent fractionation line (see Supplementary Tables S3-1 and S3-2)*.

The external precision on $\delta^{34}S$, $\Delta^{33}S$ and $\Delta^{36}S$ was propagated together with internal errors to yield typical overall 1σ uncertainties of 0.2‰ on $\delta^{34}S$ and $\Delta^{33}S$, and 0.5‰ on $\Delta^{36}S$ for analyses where the secondary ion signal on ^{32}S was $\sim 10^9$ cps. During the triple sulfur isotope runs in 2009, 47 analyses of the Isua monitor (Supplementary Table S3-3) yielded weighted averages with 2σ errors of $\delta^{34}S$ = 2.44 ± 0.1‰ (MSWD = 7.1, four outliers) and $\Delta^{33}S$ = 3.24 ± 0.04‰ (MSWD = 0.89, one outlier). For the 2012 quadruple isotope runs, 27 measurements yielded weighted averages of $\delta^{34}S$ = 2.33 ± 0.04‰ (MSWD = 0.84), $\Delta^{33}S$ = 3.16 ± 0.04‰ (MSWD = 0.69) and $\Delta^{36}S$ = -2.28 ± 0.2‰ (MSWD = 0.71, n = 21). These data agree well with previously published values from conventional (Baublys et al., 2004) and SIMS (Whitehouse, 2012) sulfur isotope analyses. In addition, excellent agreement between $\Delta^{36}S/\Delta^{33}S$ values measured in a 2.5 Ga concretionary pyrite from the Campbellrand Group in this study and during previous analytical runs (both reported by Whitehouse, 2012), which were consistent with reported MIF-ratios for Neoarchean sulfide (Kaufman et al., 2007), demonstrate the accurate determination of $\Delta^{33}S$ and $\Delta^{36}S$ as well as good reproducibility between different analytical sessions.

3.4 RESULTS

Measured pyrite $\delta^{34}S$ values (n = 386) varied from -12.24‰ to 6.96‰ with significant mass-independent signatures for $\Delta^{33}S$ between -0.70‰ to +3.09‰

* Supplementary tables for this chapter are available at http://hdl.handle.net/10411/10143.

and $\Delta^{36}S$ between -2.96‰ and +1.49‰ (n = 123), as shown in Supplementary Table S3-4. This wide range in isotopic composition is consistent with published data for sulfides from the Paleoarchean Dresser Formation in the Pilbara Block, Australia (Shen et al., 2001; Philippot et al., 2007; Ueno et al., 2008; Shen et al., 2009), although magnitudes of $\Delta^{36}S$ in our results are larger than those previously reported by Ueno et al. (2008) and Shen et al. (2009). The Barite Valley pyrites were found to be up to 18‰ lighter in $\delta^{34}S$ than barite from the same locality, whereas $\Delta^{36}S$ was generally more negative and $\Delta^{33}S$ similar to or more positive than the range reported for the barite (Chapter 2 and Bao et al., 2007).

Distinct differences were observed between the isotopic compositions of pyrite from barite-free and barite-rich lithologies in the drill core. The most ^{34}S and ^{33}S-depleted signatures were found in barite-hosted disseminated pyrite (n = 110) with an average $\delta^{34}S$ of -4.05‰ and $\Delta^{33}S$ = -0.21‰ (Fig. 3.4a), whereas disseminated pyrite from chert horizons (n = 44) gave an average $\delta^{34}S$ of 1.80‰ with $\Delta^{33}S$ = 0.45‰ (Fig. 3.4c). Layered and massive pyrite from barite-rich sections (n = 134) was found to be slightly more ^{34}S-enriched compared to their disseminated equivalents, with an average $\delta^{34}S$ = 0.61‰ and $\Delta^{33}S$ = 0.13‰ (Fig. 3.4b). In contrast, pyrite hosted by non-sulfur bearing lithologies including dolomite, cherty conglomerate and chert breccia (n = 98) gave an average composition of $\delta^{34}S$ = 2.26‰ with $\Delta^{33}S$ = 0.40‰ (Fig. 3.4d). Sulfur isotope data from these individual pyrite populations define different trends in $\Delta^{33}S$ versus $\delta^{34}S$ (Fig. 3.4a-d, trendlines not shown). A shallow positive slope of 0.03 ± 0.01 (2σ) was observed for both the pyrite layers and disseminated grains in barite-rich lithologies, with intercept values of $\Delta^{33}S$ = 0.1 ± 0.03 and -0.1 ± 0.03, respectively. On the other hand, isotopic compositions of pyrite from barite-free lithologies at 216.3, 225.5 and 254.8 m core depth define a distinct negative trend with $\Delta^{33}S/\delta^{34}S$ = -0.5 ± 0.2 and non-zero intercept of 2.4 ± 0.5, with the exception

Figure 3.4 (next pages) *Plots of $\Delta^{33}S$ versus $\delta^{34}S$ for (a) disseminated pyrite in barite, (b) layered and massive pyrite in barite, (c) disseminated pyrite in chert and (d) pyrite in conglomerate, dolomite and breccia, showing distinct isotopic trends in barite-rich and barite-free sediments. Error bars indicate 2σ internal precision. Barite isotope data is taken from Bao et al. (2007) and Chapter 2.*

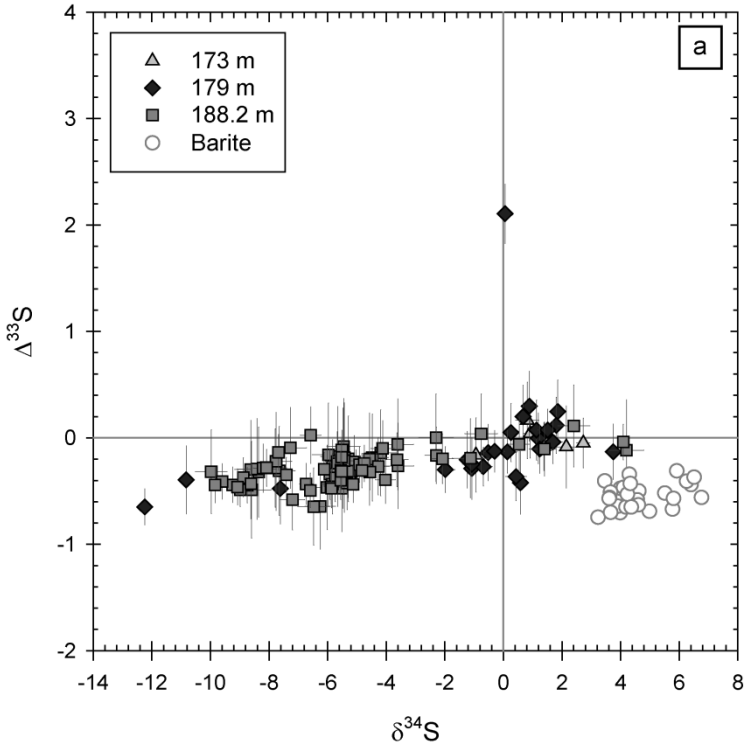
a
173 m
179 m
188.2 m
Barite
$\Delta^{33}S$
$\delta^{34}S$

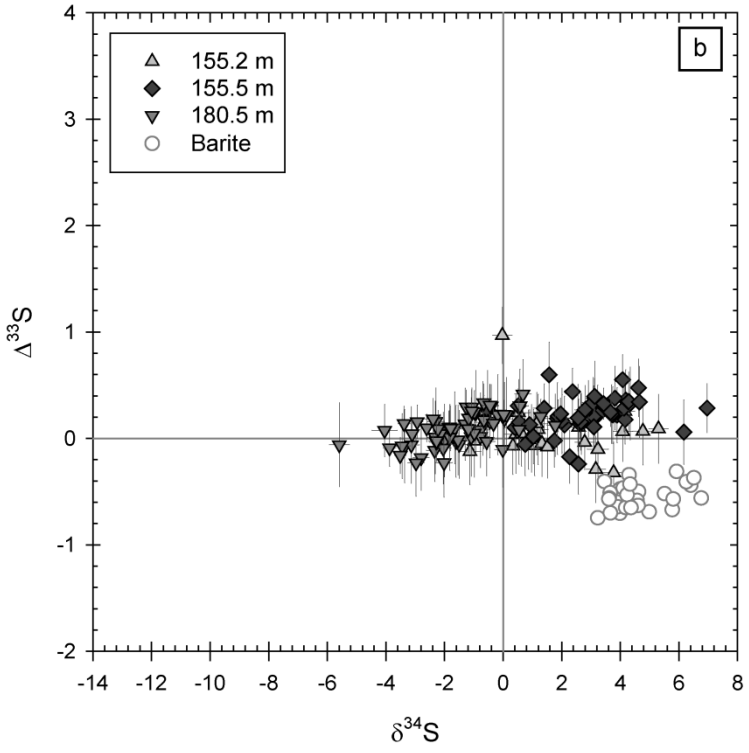
b
155.2 m
155.5 m
180.5 m
Barite
$\Delta^{33}S$
$\delta^{34}S$

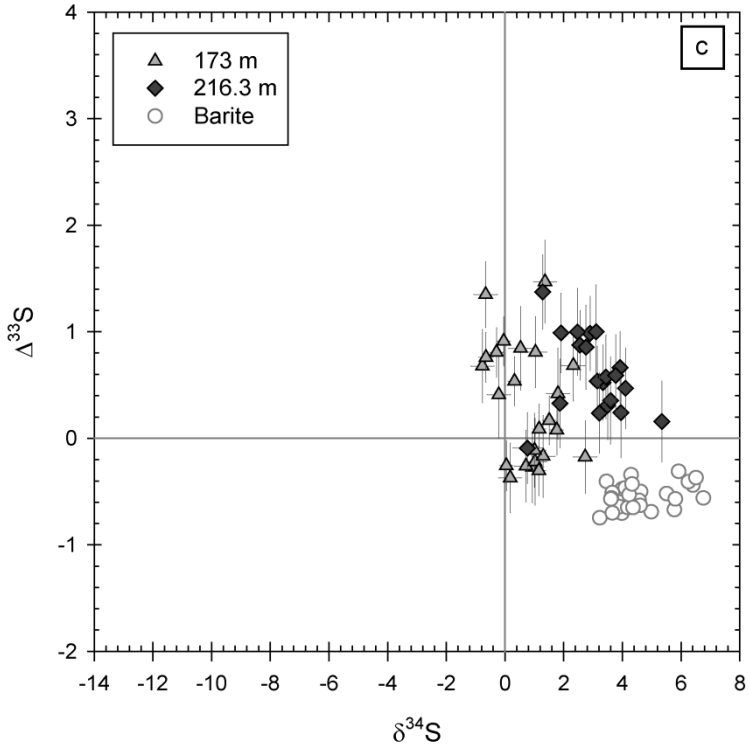
c
173 m
216.3 m
Barite
$\Delta^{33}S$
$\delta^{34}S$

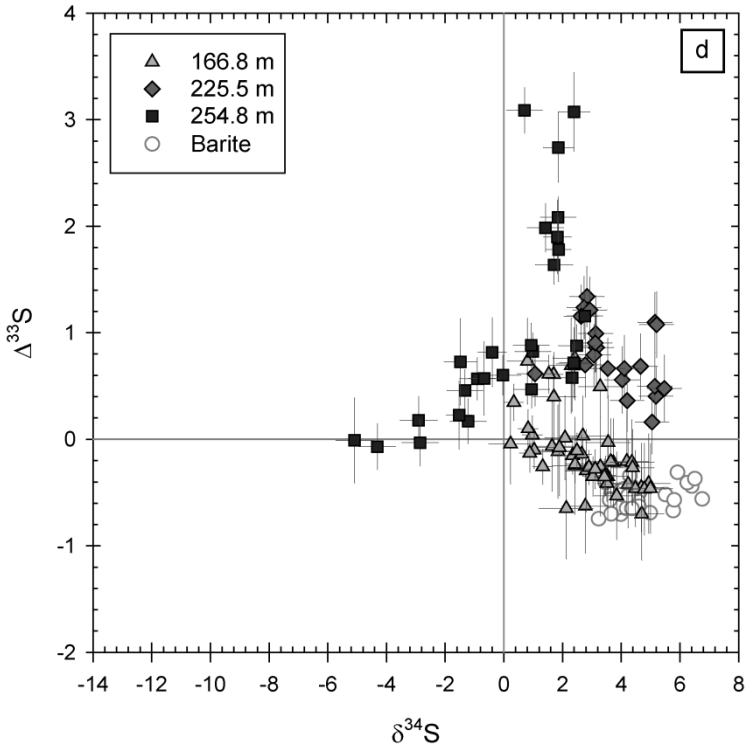
d
166.8 m
225.5 m
254.8 m
Barite
$\Delta^{33}S$
$\delta^{34}S$

of data from 254.8 m that define a positive trend with $\Delta^{33}S/\delta^{34}S = 0.2 \pm 0.1$ and intercept 0.6 ± 0.1. Finally, pyrite in cherty conglomerate (166.8 m) and chert (173 m) show a similar negative correlation as the samples from the upper part of the stratigraphy, with a slope of -0.4 ± 0.1 and smaller intercept value for $\Delta^{33}S$ of 0.8 ± 0.2. The trends calculated from our sulfur isotope data are notably different from those previously observed in Paleoarchean pyrite from the Dresser Formation (Philippot et al., 2007; Ueno et al., 2008), or sedimentary Neoarchean sulfide (Ono et al., 2003; Kamber and Whitehouse, 2007; Kaufman et al., 2007; Ono et al., 2009b).

Despite a lower precision on $\Delta^{36}S$, similar compositional differences between the distinct pyrite populations were observed in $\Delta^{36}S/\Delta^{33}S$. Pyrite in barite-free lithologies defines a trend in $\Delta^{36}S$ vs. $\Delta^{33}S$ space with a slope of -0.9 ± 0.2 (2σ, MSWD = 1.4) and intercept of 0.1 ± 0.2 (Fig. 3.5c-d trendlines not shown), which plots onto the same trend as defined by the barite (Chapter 2) and the Archean reference slope (Farquhar et al., 2000; Kaufman et al., 2007; Ueno et al., 2008). Compared to the barite $\Delta^{33}S$ (-0.7 to -0.3‰) and $\Delta^{36}S$ (0.0 to 0.8‰), isotopic compositions of this pyrite population are shifted towards higher $\Delta^{33}S$ (-0.4 to 3.1‰) and generally lower $\Delta^{36}S$ (-3.0 to 1.5‰). Conversely, data from layered pyrite in barite plots onto a significantly steeper trend with $\Delta^{36}S/\Delta^{33}S = -5.9 \pm 2.0$ (MSWD = 0.75, Fig. 3.5b) and shows much more negative $\Delta^{36}S$-values (-2.7 to 0.1‰) compared to the barite, with slightly more positive $\Delta^{33}S$ (-0.3 to 1.0‰). Mass-independent isotope signatures of barite-hosted disseminated pyrite also appear to define a steeper trend ($\Delta^{36}S/\Delta^{33}S \approx -3$) than the Archean reference array and overlap partially with the minor sulfur isotopic composition of the barite (Fig. 3.5a). However, the accuracy of this slope is limited by the small range in $\Delta^{33}S$ in these sulfides combined with the relatively large error on $\Delta^{36}S$ measurements.

Figure 3.5 (next pages) *Plots of $\Delta^{36}S$ versus $\Delta^{33}S$ for (a) disseminated pyrite in barite, (b) layered and massive pyrite in barite, (c) disseminated pyrite in chert and (d) pyrite in conglomerate and breccia. Dashed lines indicates the Archean reference line (medium dash) with $\Delta^{36}S/\Delta^{33}S = -1$ (Chapter 2 and Farquhar et al., 2000; Kaufman et al., 2007; Ueno et al., 2008; Ono et al., 2009a), and mass-dependent fractionation line (long dash) with $\Delta^{36}S/\Delta^{33}S = -6.85$ (Ono et al., 2006), as indicated in panel a. Error bars show 2σ precision. Barite data is from Chapter 2 only, due to the lower precision in $\Delta^{36}S$ data reported by Bao et al. (2007).*

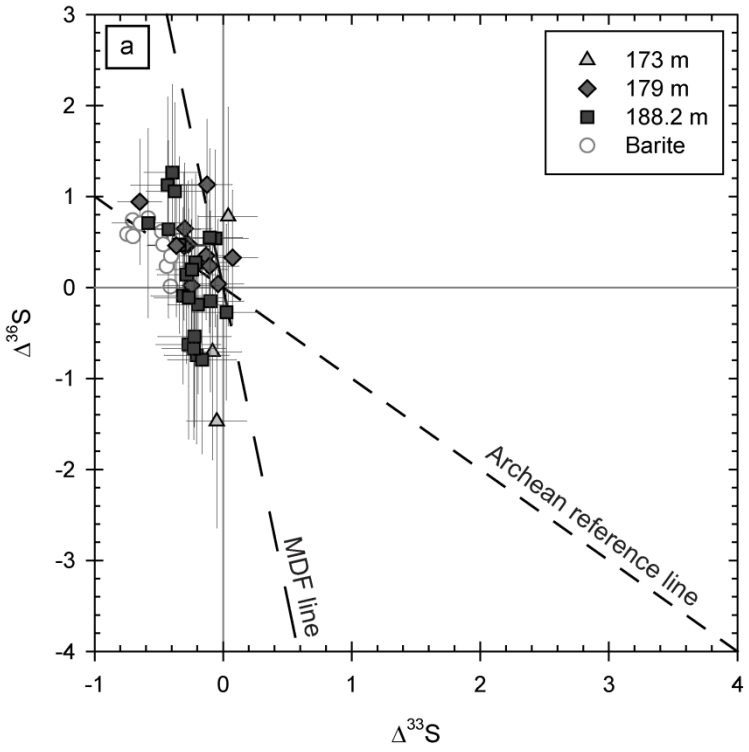
a
173 m
179 m
188.2 m
Barite
MDF line
Archean reference line
$\Delta^{36}S$
$\Delta^{33}S$

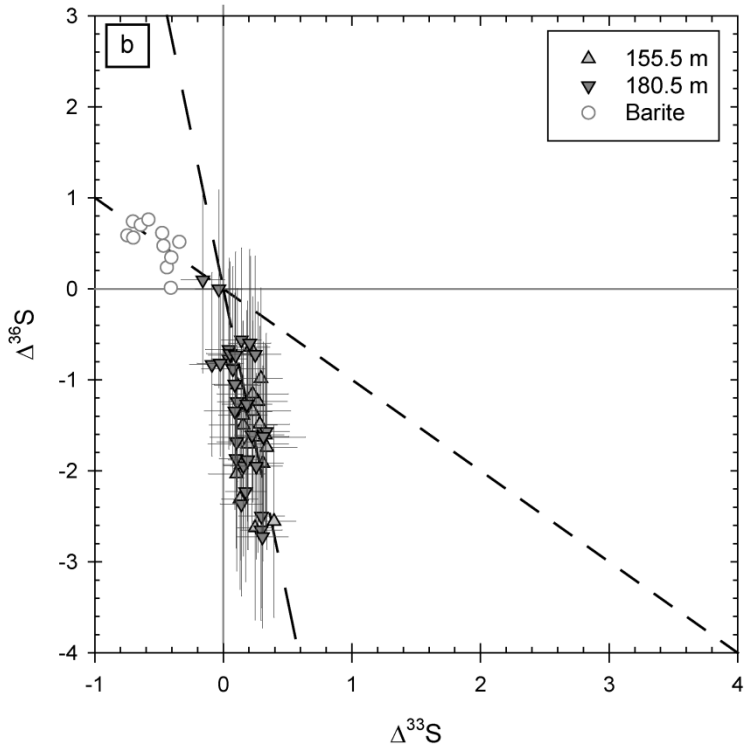
b
155.5 m
180.5 m
Barite
$\Delta^{36}S$
$\Delta^{33}S$

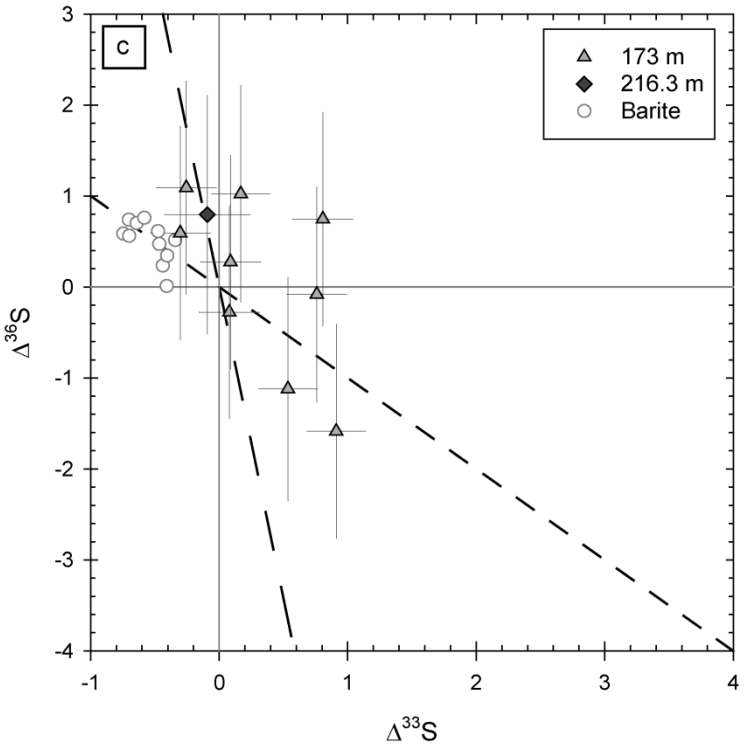
c
173 m
216.3 m
Barite
$\Delta^{36}S$
$\Delta^{33}S$

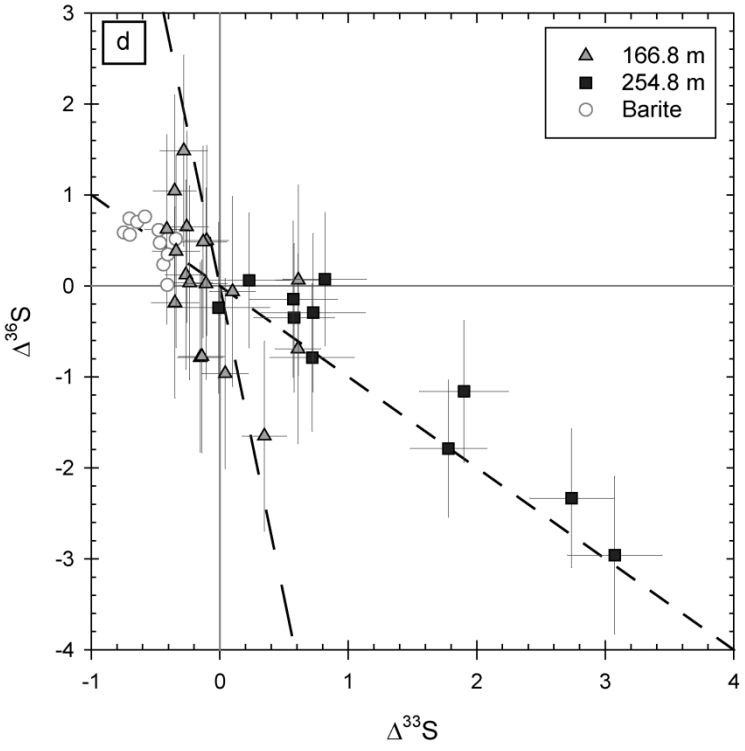
d
166.8 m
254.8 m
Barite
$\Delta^{36}S$
$\Delta^{33}S$

3.5 DISCUSSION

Our in situ quadruple sulfur isotope data enable us to distinguish distinct isotopic arrays in sedimentary sulfide formed in the Barberton region between 3.26 and 3.23 Ga, and possibly the Mesoarchean. A strong link exists between sulfur isotope signatures and lithology, with highly positive $\Delta^{33}S$ values and correlations of $\Delta^{36}S/\Delta^{33}S \approx -0.9$ and $\Delta^{33}S/\delta^{34}S \approx -0.5$ only observed in pyrite from sulfate-free rocks such as chert, cherty conglomerate, breccia and dolomite. In contrast, strongly ^{34}S-depleted pyrite with more negative $\Delta^{36}S/\Delta^{33}S$ but weakly positive $\Delta^{33}S/\delta^{34}S$ was limited to bedded barite and barite-rich sediments. Layered pyrite in barite sands displays the most negative slope in $\Delta^{36}S/\Delta^{33}S$ close to the mass-dependent fractionation line (Ono et al., 2006). In the following discussion, we focus on the processes that produced these positive and negative $\Delta^{33}S/\delta^{34}S$ trends in close stratigraphic proximity to one another. We argue that these isotopic arrays are best explained by mixing processes in the sulfide phase during diagenetic pyrite formation, rather than representing primary atmospheric variability (cf. Philippot et al., 2012).

3.5.1 Origin of distinct sulfur isotopic arrays

3.5.1.1 Positive $\Delta^{33}S/\delta^{34}S$ in disseminated pyrite from barite-rich lithologies

Pyrite occurs in association with bedded barite and silicified reworked barite sands as microscopic disseminated grains (Fig. 3.3a) and as macroscopic layers (Fig. 3.3b). Isotope data from both sulfide populations define a similar weakly positive trend in $\Delta^{33}S$ versus $\delta^{34}S$ with a slope of 0.03 ± 0.01 and near-zero intercept values (Fig. 3.4a-b). However, mass-independent signatures show much stronger anomalous fractionation of ^{36}S for the macroscopic pyrite (Fig. 3.5b) than for the microscopic pyrite (Fig. 3.5a). We thus treat these groups independently and will first discuss the origin of isotopic arrays defined by the disseminated grains (173 m, 179 m, 188.2 m). Disseminated pyrite shows a range in compositions from juvenile sulfur ($\delta^{34}S = \Delta^{33}S = \Delta^{36}S = 0‰$) towards strongly ^{34}S-depleted sulfide with $\delta^{34}S = -12.2‰$ and negative $\Delta^{33}S$. The slope of this trend in $\Delta^{33}S/\delta^{34}S$ is very similar to the array calculated by Lyons (2009) for atmospheric photolysis by broadband UV radiation and intersects the composition of volcanic SO_2, which is required for the isotopic mass balance of photolysis products.

However, several lines of evidence argue against the interpretation of this trend as a primary photochemical array. First, the shallow slope of this array would imply that photolytic oxidized sulfur had strongly negative $\delta^{34}S$, which is inconsistent with positive $\delta^{34}S$-values in barite that were interpreted to reflect a residual sulfate pool after pyrite extraction (Chapter 2). Such strongly ^{34}S-depleted atmospheric sulfate would require very large isotope effects related to pyrite burial to explain the positive shift in $\delta^{34}S$ in barite, but none of the Paleoarchean pyrite measured so far has sufficiently negative $\delta^{34}S$-signatures to support this hypothesis. The composition of photochemical sulfate is more likely to lie off the array observed in Fig. 3.4a and closer to the values suggested by Ueno et al. (2008).

Second, textural and isotopic evidence suggests that isotopic compositions of the disseminated pyrite were primarily controlled by reduction of a local sulfate pool, and not by atmospheric processes. A syngenetic relationship between the sulfide and the sulfate is likely since disseminated pyrite grains commonly occur on grain boundaries in bladed barite, and have a similar sign and magnitude of $\Delta^{33}S$ to that measured in barite from the Mapepe Formation (Chapter 2 and Bao et al., 2007). Elsewhere microscopic pyrite occurs in detrital barite, but sedimentological evidence suggests that barite and pyrite were transported over very limited distances (Heinrichs and Reimer, 1977) and that the sulfide and sulfate were derived from the same basin. A negative shift in $\delta^{34}S$ from barite to pyrite supports reduction of the local sulfate reservoir to form sulfide. Evaluation of $\Delta^{36}S/\Delta^{33}S$ data from the disseminated pyrite (Fig. 3.5a) appears to confirm the operation of mass-dependent processes, as in addition to partial overlap with the barite, scatter above but mostly below the Archean reference line with $\Delta^{36}S/\Delta^{33}S = -1$ was observed. This reference line is assumed to reflect early photochemical pathways, because it is consistent with MIF-ratios reported from experiments (Farquhar et al., 2001; Masterson et al., 2011; Whitehill and Ono, 2012), Archean sulfide from various locations (Farquhar et al., 2000; Kaufman et al., 2007; Ueno et al., 2008; Ono et al., 2009a) as well as the barite deposits from the Barberton region, including Barite Valley (Chapter 2). The small deviations that we observe from this general correlation suggest that isotopic signatures were affected by post-photolysis fractionation pathways (Johnston et al., 2005; Johnston et al., 2007; Lasaga et al., 2008; Watanabe et al., 2009), and that the co-variation in $\Delta^{33}S$ versus $\delta^{34}S$ is more likely explained by local redox reactions and mixing processes.

3.5.1.2 Positive $\Delta^{33}S/\delta^{34}S$ in macroscopic pyrite from barite-rich lithologies

Similar correlations between $\Delta^{33}S$ and $\delta^{34}S$ were observed in the pyrite clump at 155.5 m and layers at 155.2 and180.5 m, possibly indicating analogous fractionation pathways as inferred for the microscopic grains. However, the macroscopic pyrite is significantly less ^{34}S-depleted and shows dissimilar $\Delta^{33}S$-values from the barite (Fig. 3.4b), arguing against local redox transformations of sulfate to sulfide. Overlap of measured $\delta^{34}S$ signatures with those reported for mantle-derived sulfide (Marini et al., 2011) suggests that the population might contain sulfide derived from magmatic or volcanic sources, but the strong shifts away from the composition of juvenile sulfur on the $\Delta^{36}S$ versus $\Delta^{33}S$ plot (Fig. 3.5b) precludes this origin. The slope of the correlation in $\Delta^{36}S/\Delta^{33}S$ (-5.9 ± 2.0) is very similar to values demonstrated for mass-dependent fractionation processes (Ono et al., 2006), but unlike the variability in the disseminated pyrite the range in $\delta^{34}S$ observed here is too restricted to explain the large $\Delta^{33}S$ and $\Delta^{36}S$ variations by a single mass-dependent fractionation process. Although the slope deviates from the reference line for SO_2 photolysis derived from Paleoarchean and Neoarchean rocks (Chapter 2 and Farquhar et al., 2000; Kaufman et al., 2007; Ueno et al., 2008; Ono et al., 2009a), similar $\Delta^{36}S/\Delta^{33}S$ arrays have been observed in Mesoarchean sulfide from the 3.2 Ga Moodies Group in the Barberton Greenstone Belt and the 3.0 Ga Nsuzi Group in the Pongola Supergroup, South Africa (Farquhar et al., 2007). This distinctive $\Delta^{36}S/\Delta^{33}S$ was linked to photolysis reactions in a Mesoarchean atmosphere that was chemically different from the Paleoarchean, suggesting that the microscopic pyrite was produced during a later stage of sulfide precipitation. The $\Delta^{33}S/\delta^{34}S$ array recorded by the sulfur isotope data could be related to mixing between sulfide reservoirs during pyrite formation, with compositions reflecting a distinctive Mesoarchean photolytic component and possibly mantle-sulfide. Textural observations support the late precipitation of these centimeter-scale pyrite layers, as the layers occur in between barite sands and chert layers and is sometimes infiltrated with silica, suggesting that formation or modification from late-stage silica- and sulfide-rich fluids was possible. However, in situ dating of these layers would be necessary to confirm this hypothesis.

3.5.1.3 Negative $\Delta^{33}S/\delta^{34}S$ in pyrite from barite-free lithologies

The majority of pyrite in cherts, conglomerate, breccia and dolomite shows a negative correlation between $\Delta^{33}S$ and $\delta^{34}S$ (Fig. 3.4c-d) that is distinctively

different from trends observed in barite-rich lithologies. The array points towards the isotopic composition of the barite from the same Mapepe Formation rocks (Fig. 3.4c-d) (Chapter 2 and Bao et al., 2007) and is similar to the trend observed in microscopic sulfides from the Dresser Formation (Philippot et al., 2007). It appears to mimic the co-variation between $\Delta^{33}S$ and $\delta^{34}S$ observed in 193 nm photolysis experiments (Farquhar et al., 2001), which was used as evidence by Philippot et al. (2007) to argue that this negative array reflects photochemical reactions in the Paleoarchean atmosphere. However, the highly non-zero intercept ($\Delta^{33}S$ = 2.4 ± 0.5‰) observed in our data is inconsistent with this interpretation, because any atmospheric photolysis array should cross the origin in a plot of $\Delta^{33}S$ versus $\delta^{34}S$ in order to mass balance photochemical elemental sulfur (positive $\Delta^{33}S$) with sulfate (negative $\Delta^{33}S$) through the composition of the reactant juvenile volcanic SO_2. A further problem with an atmospheric origin for the negative trend is that it would require the barite to represent primary photolytic sulfate, because equivalent $\Delta^{36}S/\Delta^{33}S$ values in barite-free (Fig. 3.5d) and barite-rich lithologies (Chapter 2) support a similar photochemical source reaction for the upper and lower part of the stratigraphy. Therefore, if barite was formed from this array generating oxidized sulfur with positive $\delta^{34}S$, it would imply that the isotopic composition of the marine sulfate reservoir was unaffected by biological processes and pyrite removal in the Paleoarchean oceans. We consider this unlikely, because it strongly conflicts with both textural (Wacey et al., 2011) and sulfur isotopic evidence from pyrite and barite supporting the activity of sulfate-reducing micro-organisms at this time (Chapter 2 and Shen et al., 2001; Ueno et al., 2008; Shen et al., 2009; Wacey et al., 2010). Moreover, the consistency between $\Delta^{36}S/\Delta^{33}S$ defined by the pyrite in barite-free sediments (-0.9 ± 0.2) and the Archean reference line does not provide unambiguous evidence for a photolytic origin of the negative array in $\Delta^{33}S/\delta^{34}S$, because not every mass-dependent process that fractionates $^{34}S/^{32}S$ produces shifts in $\Delta^{33}S$ or $\Delta^{36}S$ (cf. 'equilibrium effects' in Shen et al., 2009). This is also demonstrated by the presence of two trends with opposite slopes in $\Delta^{33}S$ versus $\delta^{34}S$ at 254.8 m (Fig. 3.4d) of which at least one is likely to result from secondary redox transformations and mixing, but mass-independent signatures from both arrays plot within error onto the Archean reference line with $\Delta^{36}S/\Delta^{33}S$ = -1 (Fig. 3.5d). Thus, although the negative correlation between $\Delta^{33}S$ and $\delta^{34}S$ in our barite-free lithologies has a similar slope to the atmospheric array suggested by Philippot et al. (2012) from sulfides in felsic ashes from the Mapepe Formation, our sulfur

isotope data could not confirm the existence of this photochemical pathway during barite formation and sediment deposition and in the Barite Valley area.

We conclude that local mixing and mass-dependent fractionation processes provide a better explanation for the observation of the dominant negative $\Delta^{33}S/\delta^{34}S$ array in pyrite from barite-free sediments, and that the small variations observed in trends between different samples reflect a fluctuating balance between these processes. Observation of a slope in $\Delta^{36}S$ versus $\Delta^{33}S$ that is similar to the Archean reference array and $\Delta^{36}S/\Delta^{33}S$ in local barite (Chapter 2) supports a photochemical origin of mass-independent isotope signatures, but the original atmospheric compositions were blurred by local sulfur cycling. Below, we discuss the different redox and mixing processes that produced the distinct isotopic variations in barite-rich and barite-free sediments, and continue in Section 3.5.4 to discuss how the expression of these arrays was controlled by the local environment.

3.5.2 Redox processes and mixing in barite-rich environments

Isotopic arrays in the microscopic pyrite from barite-rich sediments can be explained by a combination of mass-dependent fractionation, shifting $\delta^{34}S$ values along a horizontal line in $\Delta^{33}S$ versus $\delta^{34}S$ space, and mixing processes that produce variation in both $\Delta^{33}S$ and $\delta^{34}S$ along diagonal lines (Fig. 3.6a). The difference in $\delta^{34}S$ between barite and the most isotopically depleted pyrite is 19‰ (Fig. 3.4a), which would be consistent with microbial sulfate reduction at sulfate levels above 200 µM (Canfield, 2001; Habicht et al., 2002) or thermochemical sulfate reduction at temperatures above 250°C in hydrothermal systems (Ohmoto and Goldhaber, 1997). Evaluating the possibility of abiotic reduction during barite precipitation is complicated as part of the barite has been reworked and transported from its original depositional environment. However, primary barite is found in a shallow-water sedimentary setting in between finely laminated cherts and channels filled with conglomerate, with an absence of hydrothermal veining (Heinrichs and Reimer, 1977). In addition, Heinrichs and Reimer (1977) suggested that the barium-rich fluids necessary for barite precipitation from seawater were transported through fissures and faults associated with the submarine tectonic high of the Proto-Inyoka zone, eliminating the requirement of high-temperature systems within the basin where barite was

formed. Furthermore, thermochemical sulfate reduction is limited in the modern sulfate-rich oceans (28 mM SO_4^{2-}) compared to microbial pathways (Jørgensen and Kasten, 2006), so that relatively high abiotic reduction fluxes are unlikely in Paleoarchean basins with significantly lower sulfate levels (~200 μM) (Chapter 2). An alternative abiotic reduction mechanism is reductive dissolution of barite (as suggested for the high-metamorphic grade Londozi deposit in Chapter 5 and Chapter 6), but the low-metamorphic grade of the Barite Valley deposit suggests that these processes were insignificant. Therefore, we argue that the redox transformation of sulfate to sulfide in the barite-rich sediments was related to microbial sulfate reduction at ambient temperatures. Sulfur diffusion through pyrite was found to be sufficiently slow to preserve isotopic signatures in 50 μm grains at temperatures below 400°C (Watson et al., 2009), supporting the preservation of biogenic isotope signatures at lower greenschist facies conditions. A microbial origin for the ^{34}S-depleted disseminated pyrite appears to be consistent with our $\Delta^{36}S/\Delta^{33}S$ data as well (Fig. 3.5a), as a small number of data points are significantly shifted from the barite towards more negative $\Delta^{36}S$ with small shifts in $\Delta^{33}S$. Despite the relatively large errors in SIMS $\Delta^{36}S$ measurements, microbial fractionation seems to be most likely explanation for these shifts because results are similar to the effects on $\Delta^{33}S$ and $\Delta^{36}S$ reported by Shen et al. (2009) for microbial sulfate reduction, and differ from the shifts inferred for high-temperature equilibrium fractionation. Co-variation of $\Delta^{33}S$ and $\delta^{34}S$ in the disseminated pyrite (Fig. 3.4a) suggests that the biogenic sulfide mixed with a pool of unfractionated sulfide (Fig. 3.6a).

Figure 3.6 (next page) *Sulfide reservoirs present between 3.26 and 3.23 Ga at Barite Valley, inferred from pyrite isotopic compositions. Results from this study are shown in light grey. During deposition of barite-rich lithologies (a) microbial sulfate reduction at $[SO_4^{2-}] > 200$ μM produced strongly ^{34}S-depleted sulfide, which mixed with hydrothermally-derived juvenile sulfur to produce shallow positive mixing trends in $\Delta^{33}S/\delta^{34}S$. During deposition of barite-free lithologies (b), pyrite formed from combination of sulfide derived from photochemical elemental sulfur through microbial reduction or disproportionation, and unfractionated sulfide from microbial sulfate reduction at $[SO_4^{2-}] < 200$ μM, generating steep negative mixing trends. Published barite data is from Chapter 2 and Bao et al. (2007).*

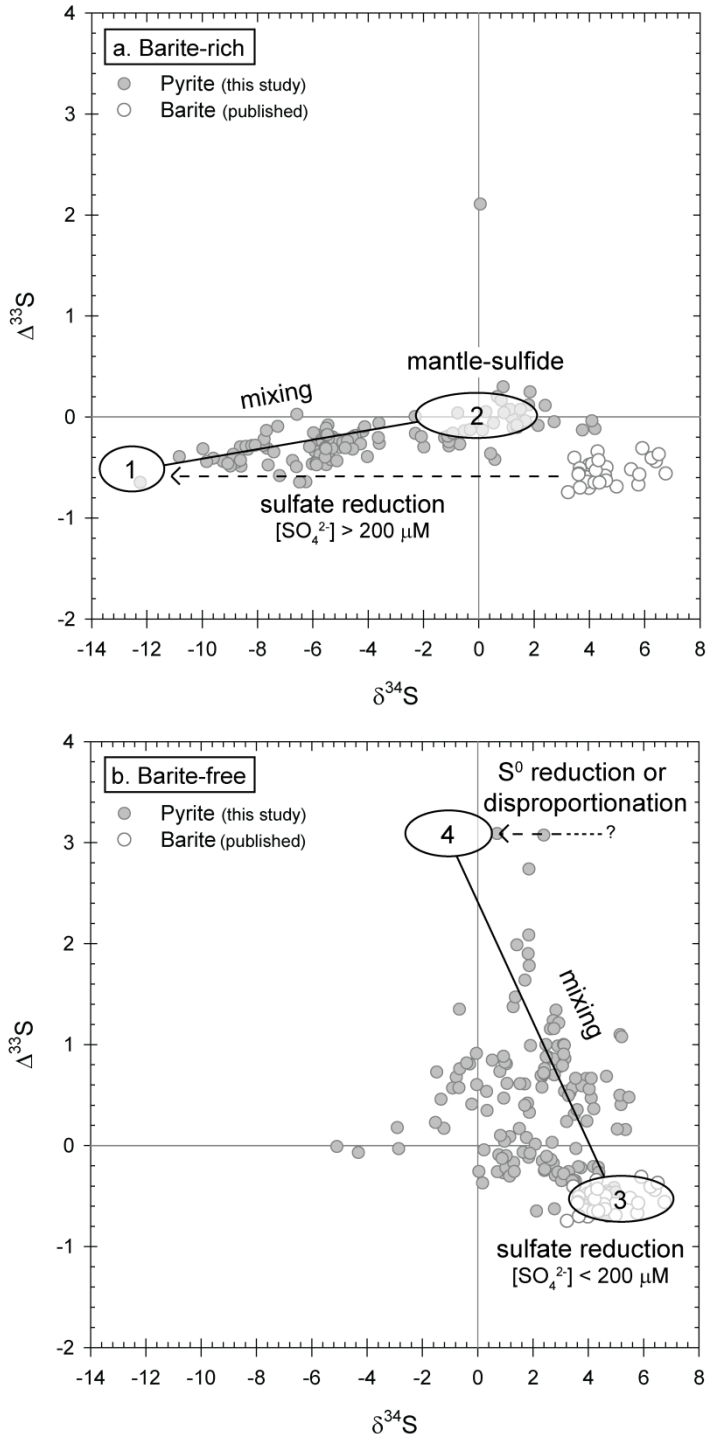
a. Barite-rich
Pyrite (this study)
Barite (published)
mantle-sulfide
mixing
2
1
sulfate reduction
[SO4 2-] > 200 μM
Δ33S
δ34S
b. Barite-free
Pyrite (this study)
Barite (published)
S0 reduction or
disproportionation
4
?
mixing
3
sulfate reduction
[SO4 2-] < 200 μM
Δ33S
δ34S

The near-zero $\delta^{34}S$ values of this end member are very similar to compositions reported for sulfur in mantle xenoliths with $\delta^{34}S$ between -3 and 5‰, mid ocean ridge basalts with $\delta^{34}S$ between -2 and 4‰ and oceanic island basalts with $\delta^{34}S$ between -2 and 6‰ (Marini et al., 2011), and similar negligible mass-independent signatures were observed in diamond inclusions (Farquhar et al., 2002) and igneous rocks from the Bushveld Complex (Penniston-Dorland et al., 2008). Therefore, our isotope data support the presence of a mantle-derived sulfide pool during deposition of barite-rich sediments, which could have been derived from the magmatic-hydrothermal fluids delivering barium to the basin. Sulfide mixing during diagenetic pyrite formation is consistent with the intermediate isotopic compositions in $\Delta^{33}S$ versus $\delta^{34}S$ (Fig. 3.4a), as well as the relatively large shifts in $\Delta^{33}S$ associated with changes in $\Delta^{36}S$ (Fig. 3.5a), which are larger than expected from microbial sulfate reduction alone (Johnston et al., 2005; Johnston et al., 2007; Shen et al., 2009).

3.5.3 Redox processes and mixing in barite-free environments

Local sulfur cycling during deposition of siliciclastics, dolomites and chert produced arrays in $\Delta^{33}S/\delta^{34}S$ which are considerably different from those observed in barite-rich sediments (compare Fig. 3.6a and 3.6b). Unlike the microbially-derived sulfide described in Section 5.2, the sulfide pool with negative $\Delta^{33}S$ in barite-free sediments is unfractionated in $\delta^{34}S$ relative to the isotopic composition of the Mapepe Formation barite (Chapter 2 and Bao et al., 2007), which we assume to reflect the residual sulfate present after deposition of the barite-rich sediments. Nonetheless, the conversion of oxidized to reduced sulfur is required to explain mixing in the sulfide phase, and the lack of isotope fractionation associated with this processes either suggests microbial sulfate reduction under sulfate-limiting conditions (Habicht et al., 2002), or complete biological or abiotic reduction of a batch of sulfate. However, such closed system reduction should be accompanied by a progressive ^{34}S-enrichment in the produced sulfide following Rayleigh distillation, but we did not observe such a horizontal array from strongly ^{34}S-depleted sulfide towards the composition of barite in our individual pyrite grains (Fig. 3.4c-d). Moreover, complete abiotic reduction in magmatic-hydrothermal systems is inconsistent with the lack of mixing trends towards juvenile sulfur, which would be expected from the

significant contribution of mantle-derived sulfide (73-89%) observed in modern hydrothermal systems (Ono et al., 2007).

We suggest that microbial sulfate reduction at very low levels of sulfate provides a more probable explanation for the lack of isotope effect between barite and pyrite. Habicht et al. (2002) demonstrated that isotope fractionation in $\delta^{34}S$ by freshwater and marine sulfate reducers becomes strongly suppressed at sulfate levels below 200 μM, decreasing to less than 6‰ at 50 μM. The absence of barite in this part of the stratigraphy might reflect these low levels of ambient sulfate. In addition, fractionation of minor isotopes and resulting shifts in $\Delta^{33}S$ and $\Delta^{36}S$ (Johnston et al., 2005; Johnston et al., 2007) will be equally restricted at low levels of sulfate so that original photochemical trends with $\Delta^{36}S/\Delta^{33}S = -1$ are preserved in the pyrite, consistent with the observed lack of deviation from the Archean reference line (Fig. 3.5c-d). Other environmental variables, such as temperature, electron donor type and concentration might have provided additional limitations to the expression of biological isotope effects, but it is difficult to constrain this from the rock record.

The presence of pyrite with positive $\Delta^{33}S$ in the barite-free sediments (Fig. 3.4c-d) is distinct from the exclusively negative $\Delta^{33}S$-values found for pyrite associated with barite, and suggests that the sulfide was derived from photochemical elemental sulfur. Because the direct reaction of zero-valent sulfur particles with iron monosulfide to form pyrite is mechanistically unlikely (Rickard and Luther, 2007), transformation of elemental sulfur into reduced sulfur species is required to explain the observed mixing arrays in $\Delta^{33}S$ versus $\delta^{34}S$. High-temperature sulfur reduction through magmatic hydrolysis reactions (Ellis and Giggenbach, 1971) is inconsistent with the absence of mantle-derived sulfide as well as the dominant siliciclastic lithologies in this part of the stratigraphy, suggesting a low-temperature depositional environment. Microbial disproportionation or reduction of elemental sulfur (Thamdrup et al., 1993; Canfield and Raiswell, 1999) provides more plausible conversion pathways in this geological setting, but the unknown isotopic composition of photochemical elemental sulfur complicates determination whether observed pyrite $\delta^{34}S$-values are related to small isotope effects during elemental sulfur reduction (Tada et al., 2008; Surkov et al., 2012), or larger fractionations associated with disproportionation (Canfield et al., 1998; Böttcher et al., 2001; Johnston et al., 2005). Mass-dependent fractionation associated with both metabolisms does not produce significant shifts in $\Delta^{33}S$ and $\Delta^{36}S$-values (Johnston et al., 2005; Johnston

et al., 2007; Tada et al., 2008; Shen et al., 2009), concurring with the preservation of photolytic $\Delta^{36}S/\Delta^{33}S$ in our data (Fig. 3.5c-d).

We conclude that the negative array in $\Delta^{33}S/\delta^{34}S$ observed in barite-free sediments of the Mapepe Formation represents variable degrees of mixing between two biogenic sulfide pools during pyrite formation. Small variations in apparent end members observed in different samples (e.g. pyrite at 173 m versus 216.3 m; Fig. 3.4c) may be explained by mass-dependent fractionation prior to mixing. The additional positive $\Delta^{33}S/\delta^{34}S$ array in brecciated chert at 254.8 m (Fig. 3.4d) possibly reflects mixing between temporary or localized sulfide pools different from those observed elsewhere in the stratigraphy, but the exact origin of these pools remains unknown.

3.5.4 Environmental controls on the expression of sulfide isotopic arrays

Our sulfur isotope data suggest that different redox reactions and mixing processes operated during deposition of barite-rich and barite-free sediments between 3.26 and 3.23 Ga in the Barberton Greenstone Belt, resulting in distinct non-photochemical isotopic arrays. We propose that local sulfur cycling and isotope fractionation was predominantly controlled by the concentration of sulfate and variable roles of different microbial metabolisms generating sulfide in the basin. Although the presence of barite in the lower part of the stratigraphy does not provide unambiguous evidence for elevated sulfate levels because the solubility product of barium sulfate is very low (Hanor, 2000) and some of the barite is of detrital origin (Heinrichs and Reimer, 1977), relatively large magnitudes of isotope fractionation in associated pyrite (Fig. 3.4a) are consistent with concentrations above the threshold of sulfate-limited microbial reduction at 200 μM SO_4^{2-} (Habicht et al., 2002). The loss of this strongly ^{34}S-depleted pyrite coincides with the disappearance of bedded barite in the studied drill core. In addition, reworking was probably of minor significance as detrital material was only transported over limited distances, and barite sands were found together with primary barite (Heinrichs and Reimer, 1977). We thus interpret the barite-rich sediments to reflect the delivery of a batch of seawater sulfate to the sedimentary basin with progressive reduction by sulfate reducing micro-organisms, producing ^{34}S-enriched residual sulfate that precipitated as barite upon reaction with hydrothermal barium (Chapter 2). Microbial consumption of a

limited amount of sulfate in a semi-closed basin is supported by the increase in barite-$\delta^{34}S$ from 3.7‰ at 155.5 m to 6.3‰ at 188.2 m (Chapter 2) shown in Fig. 3.7, which suggests progressive depletion of isotopically light sulfur through time. In addition to barium, hydrothermal fluids supplied mantle-derived sulfide to the basin, which mixed with the microbially-produced sulfide to produce pyrite with intermediate isotopic compositions. The observed decrease in pyrite-$\delta^{34}S$ from 173 m to 188.2 m (Fig. 3.7) might be related to suppressed hydrothermal inputs towards the end of the barite-rich interval, resulting in diminished dilution of biogenic sulfide with juvenile sulfur. Furthermore, the absence of pyrite with positive $\Delta^{33}S$ in the barite-rich sediments indicates that the amount of sulfide derived from microbial sulfur reduction and disproportionation was strongly limited under these conditions. Perhaps this was related to the lack of abundant ferrous iron as sulfide-scavenging agent, which is required to support growth of sulfur disproportionating communities (Thamdrup et al., 1993; Canfield et al., 1998), or to an energetic preference for sulfate reduction over elemental sulfur reduction in the presence of oxidized sulfur (Amend et al., 2004).

Removal of sulfate by barite formation and microbial reduction eventually led to decreasing levels of sulfate in the basin (schematically shown in Fig. 3.7), which is reflected by the change from barite-rich to barite-free lithologies in the upper part of the stratigraphy (Fig. 3.2). Suppressed sulfate concentrations in the uppermost sediments are consistent with the absence of significant mass-dependent isotope effects between barite (assumed to reflect residual sulfate in the basin) and pyrite in this section of the drill core (Fig. 3.4c-d, Fig. 3.7). Furthermore, the appearance of shale, greywacke and conglomerate as well as the lack of mantle-derived sulfide indicates a changing environment with increased input of continental material and weakened hydrothermal influences. Positive $\Delta^{33}S$-signatures identify a more important role for elemental sulfur reducing or disproportionating micro-organisms in this setting, which might be related to the exhaustion of oxidized sulfur in the basin or an increased availability of photochemical S_8 particles due to higher SO_2 outgassing rates (Ono et al., 2003). Enhanced input of iron from continental weathering also might have increased the preservation potential of elemental sulfur isotopic signatures as suggested by Ono et al. (2009b). Finally, observation of a similar negative $\Delta^{33}S/\delta^{34}S$ array in cherty conglomerate at the base of the stratigraphy (166.8 m; Fig. 3.4d) suggests that comparable low-sulfate conditions were prevalent during deposition of the lower Fig Tree or upper Onverwacht source rocks, consistent with the absence of barite from these

formations. However, analogous co-variation between $\Delta^{33}S$ and $\delta^{34}S$ in chert at 173 m (Fig. 3.4c) might be linked to temporal and local exhaustion of sulfate in the sediment pore waters, as the association with barite and ^{34}S-depleted pyrite at the same stratigraphic level supports generally elevated sulfate levels in the basin.

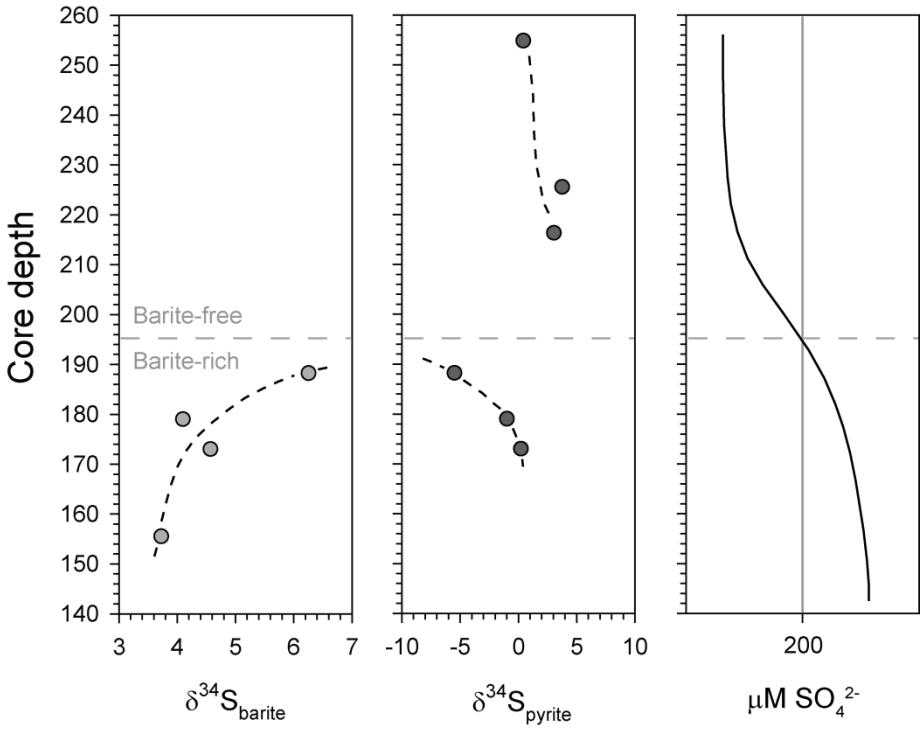

Figure 3.7 *Basin-scale evolution of sulfate levels inferred from sulfur isotope data. Average pyrite $\delta^{34}S$ becomes more negative with increasing core depth in the barite-rich section of the stratigraphy whereas barite shows ^{34}S-enrichment, consistent with progressive microbial reduction of a batch of sulfate at sulfate concentrations above the 200 μM threshold for suppressed isotope fractionation. Less ^{34}S-depleted pyrite in the overlying barite-free sediments supports decreasing sulfate levels to values below this threshold. Barite $\delta^{34}S$-data from Chapter 2.*

3.6 CONCLUSIONS

This study describes the quadruple sulfur isotope record of processes involved in the formation of pyrite between 3.26 and 3.23 Ga at Barite Valley in the Barberton Greenstone Belt, South Africa. High spatial-resolution isotope analyses by SIMS demonstrated the presence of distinct pyrite populations and isotopic arrays in barite-rich and barite-free lithologies, which we interpret to be related to local redox reactions and mixing in the sulfide phase, instead of primary photochemical variability. The most ^{34}S-depleted sulfide was found in barite-hosted disseminated pyrite, with negative $\Delta^{33}S$-values suggesting a syngenetic relationship with sulfate. Isotope signatures show small shifts in $\Delta^{36}S$ consistent with microbial sulfate reduction, and a weakly positive co-variation between $\Delta^{33}S$ and $\delta^{34}S$ supports mixing of biogenic and mantle-derived sulfide. In contrast, the occurrence of pyrite with positive $\Delta^{33}S$ and $\Delta^{36}S/\Delta^{33}S = -0.9 \pm 0.2$ was limited to chert, dolomite and terrigeneous siliciclastics, suggesting incorporation of photochemical elemental sulfur with preservation of the primary photolysis MIF-ratio. The negative trend in $\Delta^{33}S/\delta^{34}S$ that extends towards the isotopic composition of barite was interpreted to reflect mixing between sulfide derived from both sulfate and elemental sulfur metabolisms. We propose that the expression of these distinct isotopic arrays in the rock record was predominantly controlled by local fluctuations in sulfate concentration coupled with variable roles of different microbial metabolisms. Elevated sulfate concentrations (>200 μM) during deposition of barite-rich lithologies resulted in dominance of sulfate reducers producing strongly ^{34}S-depleted sulfide, while isotope effects were suppressed at the diminished levels of sulfate (<200 μM) prevalent during deposition of terrigeneous clastic and precipitative sediments. Positive $\Delta^{33}S$-signatures indicate a more important role for microbial reduction or disproportionation of elemental sulfur in this sulfate-depleted environment, whereas mantle-derived sulfide was only supplied to the basin in significant quantities by hydrothermal fluids during barite precipitation. Late formation of pyrite layers with sulfide of possible Mesoarchean photochemical origin was identified from a steep $\Delta^{36}S/\Delta^{33}S$ array that differed significantly from the Paleoarchean reference line. Our data support an important role for environmental controls on the expression of sulfide isotopic arrays in the rock record, and demonstrates that local redox processes and mixing may hamper interpretation of pyrite sulfur isotope data in terms of primary atmospheric variations.

Acknowledgements

We thank Wout Nijman for assistance during fieldwork. The Mpumalanga parks authority provided field support and access to the Somingvelo Game reserve in South Africa. We thank the Technical University of Darmstadt for the curation of the drill core samples, and Otto Stiekema and Kerstin Lindén are greatly acknowledged for their help with sample preparation. Tessa van der Voort is thanked for performing electron microprobe analyses on barium-feldspars and Tilly Bouten is thanked for technical EMP support. This project (SE-TAF-3362) received support from SYNTHESYS (http://www.synthesys.info) which is financed by the European Community – Research Infrastructure Action under the FP6 "Structuring the European Research Area" Program, the dr Schürmannfonds for fieldwork in South Africa and a grant from the User Support Programme Space Research and the Netherlands Organization for Scientific Research (NWO). The Nordsim facility is operated under a contract between the research funding agencies of Denmark, Iceland, Norway and Sweden, the Geological Survey of Finland and the Swedish Museum of Natural History.

References

Amend, J.P., Rogers, K.L., Meyer-Dombard, D.A.R., 2004. Microbially mediated sulfur-redox: Energetics in marine hydrothermal vent systems. Geological Society of America Special Papers 379, 17-34.

Bao, H., Rumble Iii, D., Lowe, D.R., 2007. The five stable isotope compositions of Fig Tree barites: Implications on sulfur cycle in ca. 3.2 Ga oceans. Geochim. Cosmochim. Acta 71, 4868-4879.

Baublys, K.A., Golding, S.D., Young, E., Kamber, B.S., 2004. Simultaneous determination of 33S V-CDT and 34S V-CDT using masses 48, 49 and 50 on a continuous flow isotope ratio mass spectrometer. Rapid Commun. Mass Spectrom. 18, 2765-2769.

Böttcher, M.E., Thamdrup, B., Vennemann, T.W., 2001. Oxygen and sulfur isotope fractionation during anaerobic bacterial disproportionation of elemental sulfur. Geochim. Cosmochim. Acta 65, 1601-1609.

Canfield, D.E., 2001. Isotope fractionation by natural populations of sulfate-reducing bacteria. Geochim. Cosmochim. Acta 65, 1117-1124.

Canfield, D.E., Raiswell, R., 1999. The evolution of the sulfur cycle. Am. J. Sci. 299, 697-723.

Canfield, D.E., Thamdrup, B., Fleischer, S., 1998. Isotope Fractionation and Sulfur Metabolism by Pure and Enrichment Cultures of Elemental Sulfur-Disproportionating Bacteria. Limnol. Oceanogr. 43, 253-264.

Condie, K.C., Macke, J.E., Reimer, T.O., 1970. Petrology and Geochemistry of Early Precambrian Graywackes from the Fig Tree Group, South Africa Geol. Soc. Am. Bull. 81, 2759-2776.

Crowe, D.E., Vaughan, R.G., 1996. Characterization and use of isotopically homogeneous standards for in situ laser microprobe analysis of 34S/32S ratios. Am. Mineral. 81, 187-193.

Ellis, A.J., Giggenbach, W., 1971. Hydrogen sulphide ionization and sulphur hydrolysis in high temperature solution. Geochim. Cosmochim. Acta 35, 247-260.

Farquhar, J., Bao, H., Thiemens, M., 2000. Atmospheric Influence of Earth's Earliest Sulfur Cycle. Science 289, 756-758.

Farquhar, J., Peters, M., Johnston, D.T., Strauss, H., Masterson, A., Wiechert, U., Kaufman, A.J., 2007. Isotopic evidence for Mesoarchaean anoxia and changing atmospheric sulphur chemistry. Nature 449, 706-709.

Farquhar, J., Savarino, J., Airieau, S., Thiemens, M.H., 2001. Observation of wavelength-sensitive mass-independent sulfur isotope effects during SO_2 photolysis: Implications for the early atmosphere. J. Geophys. Res. 106, 32829-32839.

Farquhar, J., Wing, B.A., 2003. Multiple sulfur isotopes and the evolution of the atmosphere. Earth Planet. Sci. Lett. 213, 1-13.

Farquhar, J., Wing, B.A., McKeegan, K.D., Harris, J.W., Cartigny, P., Thiemens, M.H., 2002. Mass-independent sulfur of inclusions in diamond and sulfur recycling on early Earth. Science 298, 2369-2372.

Farquhar, J., Wu, N., Canfield, D.E., Oduro, H., 2010. Connections between Sulfur Cycle Evolution, Sulfur Isotopes, Sediments, and Base Metal Sulfide Deposits. Econ. Geol. 105, 509-533.

Habicht, K.S., Gade, M., Thamdrup, B., Berg, P., Canfield, D.E., 2002. Calibration of sulfate levels in the Archean ocean. Science 298, 2372-2374.

Hanor, J.S., 2000. Barite-Celestine Geochemistry and Environments of Formation, in: Alpers, C.N., Jambor, J.L., Nordstrom, D.K. (Eds.), Reviews in Mineralogy and Geochemistry: Sulfate minerals. Crystallography, Geochemistry and Environmental Significance. . Mineralogical Society of America, Washington, D.C.

Heinrichs, T.K., Reimer, T., 1977. A sedimentary barite deposit from the Archean Fig Tree Group of the Barberton Mountain Land (South Africa). Econ. Geol. 72, 1426-1441.

Hofmann, A., 2005. The geochemistry of sedimentary rocks from the Fig Tree Group, Barberton greenstone belt: Implications for tectonic, hydrothermal and surface processes during mid-Archaean times. Precambrian Res. 143, 23-49.

Johnston, D.T., Farquhar, J., Canfield, D.E., 2007. Sulfur isotope insights into microbial sulfate reduction: When microbes meet models. Geochim. Cosmochim. Acta 71, 3929-3947.

Johnston, D.T., Farquhar, J., Wing, B.A., Kaufman, A.J., Canfield, D.E., Habicht, K.S., 2005. Multiple sulfur isotope fractionations in biological systems: A case study with sulfate reducers and sulfur disproportionators. Am. J. Sci. 305, 645-660.

Jørgensen, B.B., Kasten, S., 2006. Sulfur cycling and methane oxidation, in: Schulz, H.D., Zabel, M. (Eds.), Marine geochemistry. Springer, Berlin, pp. 271-309.

Kamber, B.S., Whitehouse, M.J., 2007. Micro-scale sulphur isotope evidence for sulphur cycling in the late Archean shallow ocean. Geobiology 5, 5-17.

Kaufman, A.J., Johnston, D.T., Farquhar, J., Masterson, A.L., Lyons, T.W., Bates, S., Anbar, A.D., Arnold, G.L., Garvin, J., Buick, R., 2007. Late Archean Biospheric Oxygenation and

Atmospheric Evolution. Science 317, 1900-1903.
Lasaga, A.C., Otake, T., Watanabe, Y., Ohmoto, H., 2008. Anomalous fractionation of sulfur isotopes during heterogeneous reactions. Earth Planet. Sci. Lett. 268, 225-238.
Lowe, D.R., 1999. Geologic evolution of the Barberton Greenstone Belt and vicinity. Geol. Soc. Am. Spec. Pap. 329, 287-312.
Lowe, D.R., Nocita, B.W., 1999. Foreland basin sedimentation in the Mapepe Formation, southern-facies Fig Tree Group, in: Lowe, D.R., Byerly, G.R. (Eds.), Geologic evolution of the Barberton greenstone belt, South Africa. Geological Society of America Special Paper, pp. 233-258.
Lyons, J.R., 2007. Mass-independent fractionation of sulfur isotopes by isotope-selective photodissociation of SO2. Geophys. Res. Lett. 34.
Lyons, J.R., 2009. Atmospherically-derived mass-independent sulfur isotope signatures, and incorporation into sediments. Chem. Geol. 267, 164-174.
Marini, L., Moretti, R., Accornero, M., 2011. Sulfur Isotopes in Magmatic-Hydrothermal Systems, Melts, and Magmas. Rev. Mineral. Geochem. 73, 423-492.
Masterson, A.L., Farquhar, J., Wing, B.A., 2011. Sulfur mass-independent fractionation patterns in the broadband UV photolysis of sulfur dioxide: Pressure and third body effects. Earth Planet. Sci. Lett. 306, 253-260.
Oduro, H., Harms, B., Sintim, H.O., Kaufman, A.J., Cody, G., Farquhar, J., 2011. Evidence of magnetic isotope effects during thermochemical sulfate reduction. Proceedings of the National Academy of Sciences 108, 17635-17638.
Ohmoto, H., Goldhaber, M.B., 1997. Sulfur and carbon isotopes, in: Barnes, H.L. (Ed.), Geochemistry of hydrothermal ore deposits. John Wiley & Sons, New York.
Ono, S., Beukes, N.J., Rumble, D., 2009a. Origin of two distinct multiple-sulfur isotope compositions of pyrite in the 2.5 Ga Klein Naute Formation, Griqualand West Basin, South Africa. Precambrian Res. 169, 48-57.
Ono, S., Eigenbrode, J.L., Pavlov, A.A., Kharecha, P., Rumble Iii, D., Kasting, J.F., Freeman, K.H., 2003. New insights into Archean sulfur cycle from mass-independent sulfur isotope records from the Hamersley Basin, Australia. Earth Planet. Sci. Lett. 213, 15-30.
Ono, S., Kaufman, A.J., Farquhar, J., Sumner, D.Y., Beukes, N.J., 2009b. Lithofacies control on multiple-sulfur isotope records and Neoarchean sulfur cycles. Precambrian Res. 169, 58-67.
Ono, S., Shanks Iii, W.C., Rouxel, O.J., Rumble, D., 2007. S-33 constraints on the seawater sulfate contribution in modern seafloor hydrothermal vent sulfides. Geochim. Cosmochim. Acta 71, 1170-1182.
Ono, S., Wing, B., Johnston, D., Farquhar, J., Rumble, D., 2006. Mass-dependent fractionation of quadruple stable sulfur isotope system as a new tracer of sulfur biogeochemical cycles. Geochim. Cosmochim. Acta 70, 2238-2252.
Pavlov, A.A., Kasting, J.F., 2002. Mass-independent fractionation of sulfur isotopes in Archean sediments: strong evidence for an anoxic Archean atmosphere. Astrobiology 2, 27-41.
Penniston-Dorland, S.C., Wing, B.A., Nex, P.A.M., Kinnaird, J.A., Farquhar, J., Brown, M., Sharman, E.R., 2008. Multiple sulfur isotopes reveal a

magmatic origin for the Platreef platinum group element deposit, Bushveld Complex, South Africa. Geology 36, 979-982.

Philippot, P., Van Zuilen, M., Lepot, K., Thomazo, C., Farquhar, J., Van Kranendonk, M.J., 2007. Early Archaean Microorganisms Preferred Elemental Sulfur, Not Sulfate. Science 317, 1534-1537.

Philippot, P., van Zuilen, M., Rollion-Bard, C., 2012. Variations in atmospheric sulphur chemistry on early Earth linked to volcanic activity. Nat. Geosci. 5, 668-674.

Reimer, T.O., 1980. Archean sedimentary baryte deposits of the Swaziland Supergroup (Barberton Mountain Land, South Africa). Precambrian Res. 12, 393-410.

Rickard, D., Luther, G.W., III, 2007. Chemistry of Iron Sulfides. ChemInform 38, no-no.

Shen, Y., Buick, R., Canfield, D.E., 2001. Isotopic evidence for microbial sulphate reduction in the early Archaean era. Nature 410, 77-81.

Shen, Y., Farquhar, J., Masterson, A., Kaufman, A.J., Buick, R., 2009. Evaluating the role of microbial sulfate reduction in the early Archean using quadruple isotope systematics. Earth Planet. Sci. Lett. 279, 383-391.

Surkov, A.V., Böttcher, M.E., Kuever, J., 2012. Sulphur isotope fractionation during the reduction of elemental sulphur and thiosulphate by Dethiosulfovibrio spp. Isot. Environ. Health Stud. 48, 65-75.

Tada, A., Ueno, Y., Taka, K., Yoshida, N., 2008. Quadruple Sulphur Isotope Fractionation of Microbial Sulphur Reduction in Pure Culture. Proceedings Japanese Geoscience Union Meeting, Abstract C203-P006.

Thamdrup, B., Finster, K., Hansen, J.W., Bak, F., 1993. Bacterial Disproportionation of Elemental Sulfur Coupled to Chemical Reduction of Iron or Manganese. Appl. Environ. Microbiol. 59, 101-108.

Tice, M.M., Bostick, B.C., Lowe, D.R., 2004. Thermal history of the 3.5-3.2 Ga Onverwacht and Fig Tree Groups, Barberton greenstone belt, South Africa, inferred by Raman microspectroscopy of carbonaceous material. Geology 32, 37-40.

Ueno, Y., Ono, S., Rumble, D., Maruyama, S., 2008. Quadruple sulfur isotope analysis of ca. 3.5 Ga Dresser Formation: New evidence for microbial sulfate reduction in the early Archean. Geochim. Cosmochim. Acta 72, 5675-5691.

Ulrich, T., Long, D.G.F., Kamber, B.S., Whitehouse, M.J., 2011. In Situ Trace Element and Sulfur Isotope Analysis of Pyrite in a Paleoproterozoic Gold Placer Deposit, Pardo and Clement Townships, Ontario, Canada. Econ. Geol. 106, 667-686.

Wacey, D., Kilburn, M.R., Saunders, M., Cliff, J., Brasier, M.D., 2011. Microfossils of sulphur-metabolizing cells in 3.4-billion-year-old rocks of Western Australia. Nat. Geosci. 4, 698-702.

Wacey, D., McLoughlin, N., Whitehouse, M.J., Kilburn, M.R., 2010. Two coexisting sulfur metabolisms in a ca. 3400 Ma sandstone. Geology 38, 1115-1118.

Watanabe, Y., Farquhar, J., Ohmoto, H., 2009. Anomalous Fractionations of Sulfur Isotopes During Thermochemical Sulfate Reduction. Science 324, 370-373.

Watson, E.B., Cherniak, D.J., Frank, E.A., 2009. Retention of biosignatures and mass-independent fractionations in pyrite: Self-diffusion of sulfur. Geochim. Cosmochim. Acta 73, 4792-4802.

Whitehill, A.R., Ono, S., 2012. Excitation band dependence of sulfur isotope

mass-independent fractionation during photochemistry of sulfur dioxide using broadband light sources. Geochim. Cosmochim. Acta 94, 238-253.

Whitehouse, M.J., 2012. Multiple sulfur isotope determination by SIMS: Evaluation of reference sulfides for $\Delta^{33}S$ with observations and a case study on the determination of $\Delta^{36}S$. Geostand. Geoanal. Res. Accepted article, doi: 10.1111/j.1751-908X.2012.00188.x.

Whitehouse, M.J., Kamber, B.S., Fedo, C.M., Lepland, A., 2005. Integrated Pb- and S-isotope investigation of sulphide minerals from the early Archaean of southwest Greenland. Chem. Geol. 222, 112-131.

Londozi river valley near Ngwenya, Hhohho, Swaziland

Chapter 4

Geological and metamorphic history of Earth's oldest sulfate: the Londozi barite deposit in the Steynsdorp area of the Barberton Greenstone Belt, Swaziland

This chapter will be submitted to Precambrian Research with co-authors Paul R.D. Mason, Fraukje M. Brouwer, Noah Nhleko and Thomas Reimer.

ABSTRACT

Barite deposits in Archean greenstone belts provide unique insights into the early sulfur cycle and emergence of early life. Here, we report on the oldest stratiform barite on Earth that occurs in the Theespruit Formation of the Steynsdorp area, located in the southeasternmost part of the Barberton Greenstone Belt in the Londozi valley of Swaziland. We present petrological, geochemical, geochronological and thermobarometric data from its volcanic host rocks to establish the geological and metamorphic history of this sulfate deposit. Sediment-free successions of deformed pillow lavas and (ultra)mafic schists support initial submarine volcanism in an oceanic plateau setting, consistent with flat rare earth element (REE) patterns. Continuous eruptions and uplift by active plutonism resulted in shallowing water depths and the formation of local basins where barite and chert precipitated upon reaction of hydrothermal fluids with seawater. Zircon U-Pb ages demonstrate that felsic magmas erupted explosively at 3521 ± 9 Ma and covered the barite with a thick succession of pyroclastic deposits, but not necessarily in an active convergent margin. Similar REE patterns to nearby Steynsdorp gneisses suggests that the subaerial felsic volcanism represented the surface equivalent of deep-level magmatism around 3510 Ma. Inherited 3570-3610 Ma zircons and slight light REE-enrichments in mafic volcanics imply the presence of older crust-like material in the magma source region, whereas ~3450 Ma zircons reflect thermal resetting during the first accretionary event in the greenstone belt. Subsequent metamorphism of Theespruit Fm supracrustals around 3230 Ma produced peak metamorphic assemblages for which conventional thermobarometers and equilibrium assemblage modeling yielded temperatures of 650-700°C and pressures of 10-12 kbar, indicating preservation of barite despite burial to 30-40 km crustal depth. This work demonstrates that the Londozi barite represents the oldest-known stratiform sulfate preserved on Earth and provides an important geological framework for future studies on the earliest sulfur cycle.

4.1 INTRODUCTION

Barite deposits in Archean greenstone belts provide unique insights into the early sulfur cycle and the appearance of microbial life on Earth. Sulfide minerals found in association with the oxidized sulfur preserve evidence for ancient biological redox processes through the fractionation of stable sulfur isotopes (Shen et al., 2001; Philippot et al., 2007; Ueno et al., 2008; Shen et al., 2009), suggesting the presence of different microbial communities in the earliest marine environments. Previous work mainly focused on the well-characterized barite deposit in the 3490 Ma Dresser Formation from the Panorama Greenstone Belt in the Pilbara terrane of Western Australia, for which a hydrothermal origin was suggested on the basis of extensive field studies (Nijman et al., 1999; Van Kranendonk and Pirajno, 2004; Van Kranendonk, 2006). Furthermore, petrographic studies indicated only low degrees of deformation and prehnite-pumpellyite to lowermost greenschist facies metamorphism (Buick and Dunlop, 1990), so that secondary alteration of sulfide geochemistry was assumed negligible. Another well-preserved barite deposit occurs in the Barite Valley area of the Barberton Greenstone Belt of South Africa (Heinrichs and Reimer, 1977; Reimer, 1980), but its younger age (3260-3230 Ma) and partially detrital origin are significantly different from the Dresser barite.

A lesser known, but more metamorphosed and possibly older barite deposit occurs in the southeastern part of the Barberton greenstone belt, in the Londozi river valley of western Swaziland and east of the Steynsdorp tonalite-trondhjemite-granodiorite (TTG) dome (Reimer, 1980; Barton, 1982; Kisters and Anhaeusser, 1995). The volcanic succession in which the barite horizon occurs was interpreted by Reimer (1980) as part of the Theespruit Formation of the Lower Onverwacht Group. Felsic volcanics north of the Londozi area were dated at 3544-3548 Ma (Kröner et al., 1996) suggesting that this supracrustal sequence represents the oldest part of the greenstone belt, whereas mineral assemblages from the west side of the Steynsdorp dome indicated amphibolite facies metamorphism (Lana et al., 2010). However, more details on the geochronology, depositional environment and geodynamic setting of the Londozi barite deposit are required for comparison with other Paleoarchean barite occurrences. These data are essential for understanding the timing and formation of these sulfate-rich deposits in the earliest and very low-sulfate oceans (Habicht et al., 2002).

In this study, we therefore present geological, geochemical and petrographic data as well as zircon U-Pb ages from the host lithologies of the Londozi barite deposit, to establish the geological and metamorphic history of this sulfate deposit. Our results provide a firm temporal and geological background for the interpretation of pyrite sulfur isotope data from this deposit, and place further constraints on the age and nature of the Theespruit Formation in the Steynsdorp area. Based on field observations and rare earth element patterns, we propose an oceanic plateau environment of deposition similar to the Dresser Formation in Western Australia (Arndt et al., 2001; Van Kranendonk and Pirajno, 2004), with subaerial felsic volcanism at 3521 Ma. This confirms the ancient age of the Theespruit Formation (cf. 3453 Ma, Armstrong et al., 1990) and eliminates the requirement of subduction-related tectonic stacking of the younger and overlying Komati Formation (De Ronde and De Wit, 1994). Taking the metamorphic conditions determined in this paper and previous isotope work on the Londozi barite deposit into account (Roerdink et al., 2012), we conclude that the sulfate isotope record was unaffected by metamorphic temperatures as high as 700°C.

4.2 GEOLOGICAL BACKGROUND

The Barberton Greenstone Belt and surrounding granitoid terrane represents a well-preserved Archean succession of supracrustal volcanics and sediments of the Swaziland Supergroup and shallow intrusive rocks, ranging in age from circa 3550 to 3070 Ma (Viljoen and Viljoen, 1969; Armstrong et al., 1990; De Ronde and De Wit, 1994). The basal sequence of the belt consists of mafic to ultramafic volcanics, felsic tuffs and intrusives that make up the Onverwacht Group, which is overlain by volcaniclastic and terrigeneous clastic rocks of the Fig Tree Group and finally by coarse sandstone and conglomerate of the Moodies Group (Anhaeusser, 1973). The Londozi barite deposit is located in the southernmost part of the greenstone belt on the border of South Africa and Swaziland (see inset on Fig. 4.1), where a supracrustal sequence of Lower Onverwacht Group rocks curves around the Steynsdorp TTG dome (Kisters and Anhaeusser, 1995). On the eastern boundary of the TTG gneisses, the basal Sandspruit Formation is locally exposed and consists mainly of amphibolites and serpentinites. In contrast, the overlying Theespruit Formation is well-exposed and, in addition to dominant amphibolitic and talcose metabasalts contains minor units of felsic volcaniclastics altered to quartz-sericite schists and chert (Viljoen et al., 1969). These greenstone

lithologies have been folded into a large north-south trending synclinorium with Moodies Group clastics in the core to the east, and show strongly developed schistosity that is subparallel to the original bedding and similar to internal foliation in the TTG gneiss (Kisters and Anhaeusser, 1995). These structural data support solid-state doming of the Steynsdorp gneisses together with the overlying supracrustals during crustal shortening (Kisters and Anhaeusser, 1995; Lana et al., 2010). In contrast, strain intensities are significantly lower in the overlying Komati Formation consisting of massive and pillowed lavas of mafic to ultramafic composition (Viljoen et al., 1969; Kisters and Anhaeusser, 1995; Kröner et al., 1996). A tectonic contact (the Komati Shear Zone) marks the base of this formation elsewhere in the Barberton Greenstone Belt (De Ronde and De Wit, 1994; Dann, 2000).

4.3 FIELD OBSERVATIONS

4.3.1 General observations

Barite was mined until 1976 on a small scale in the Londozi area of western Swaziland (26°11'20"S, 31°0'28"E) (Barton, 1982). The deposit occurs in a succession of actinolite- and hornblende-rich schists and locally felsic schists (Fig. 4.1), which form the eastern flank of the Steynsdorp anticline with a dominant eastward-dip (175/30-E). The regional structure is relatively simple as the same lithologies can be followed along this strike for several kilometers. Strong foliation defined by biotite, feldspar and hornblende minerals was observed parallel or subparallel to the bedding and was particularly noticeable in weathered outcrops (Fig. 4.2a). Whereas primary fine-scale sedimentary layering was largely overprinted by this tectonic foliation, some volcano-sedimentary features were observed including deformed pillows (Fig. 4.2b) and fiamme textures in felsic schists (Fig. 4.2c). In addition, dark-colored textures resembling restites (40-80 cm wide) with associated felsic veins were observed in the felsic schists (Fig. 4.2d). Some mafic schist horizons contained coarse crystalline actinolite zones that were elongated approximately parallel to the bedding and foliation.

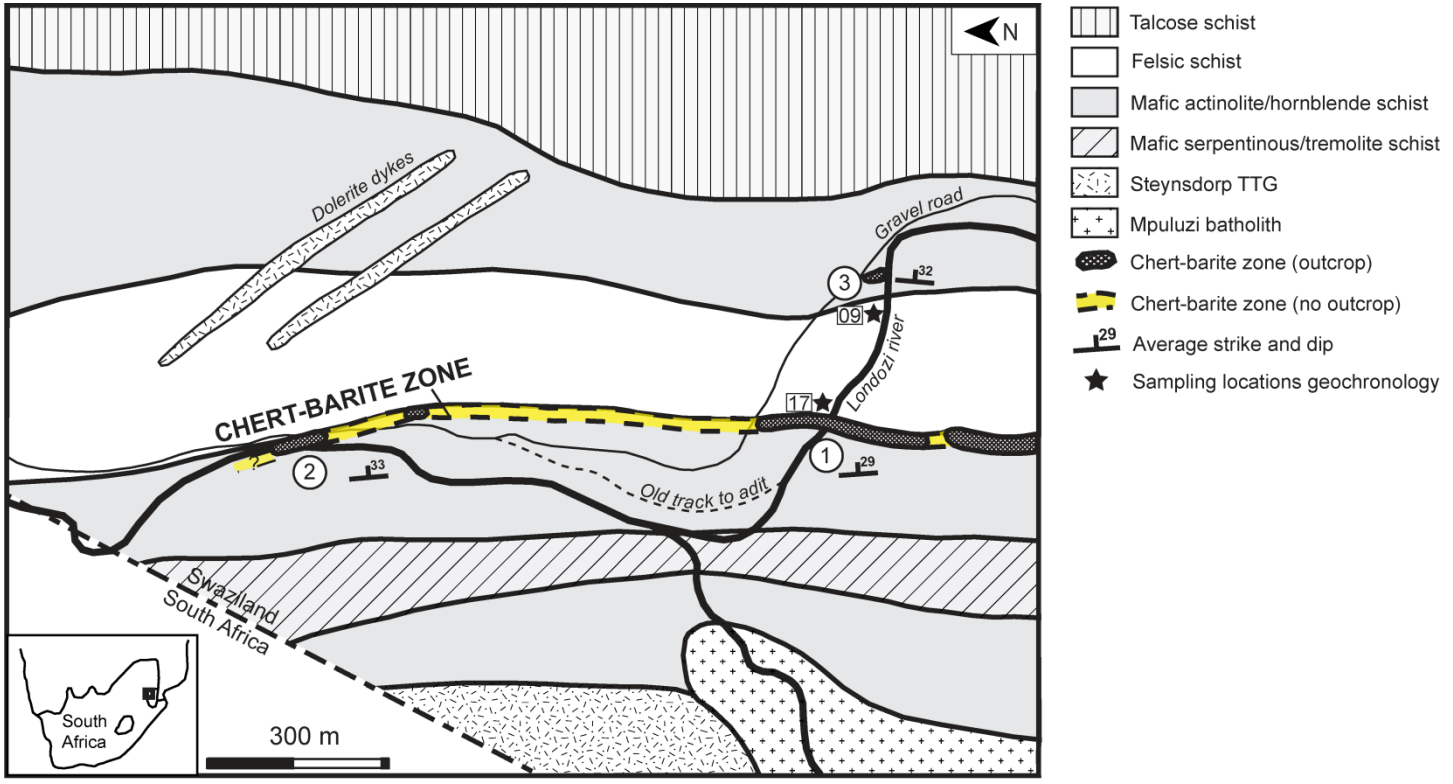

Figure 4.1 *Geological map of the Londozi barite deposit, after Viljoen et al (1969), Hunter et al (1979), Barton (1982) and Kröner et al. (1996). The area is located just east of the Steynsdorp TTG dome in the southeastern part of the Barberton Greenstone Belt, western Swaziland (see inset). Numbers indicate outcrops of barite: (1) waterfall section, (2) river section, (3) upper waterfall barite.*

Core drilling in the mine area and its vicinity indicated the presence of a silicified and barite-bearing zone that is up to twelve meters thick and contains up to nine barite bands that range in thickness from 0.3 to 1.8 m (Reimer, 1980; Barton, 1982). However, whether these bands are separate entities cannot be determined, as small isoclinal folds were observed in hand specimens and in the walls of the old mine adit. Fine-grained pyrite was found in association with barite and was concentrated in layers parallel to foliation and bedding. In addition, traces of sphalerite, chalcopyrite and galena were noted by Barton (1982). The entire chert-barite zone can be traced continuously over ~1.6 km along strike in a N-S direction in the mine area, but extensions found in South Africa and Swaziland suggest that the total lateral extent of the ore body is approximately 6.5 km (Barton, 1982).

In this study, we describe two outcrops of barite from well-exposed sections of the stream bed and river banks. The main occurrence (Fig. 4.1, #1) was found just above the lower waterfall in the NW-SE course of the Londozi river, and consists of a ~1 m thick barite horizon in between mafic and felsic schists (Fig. 4.2e). This particular baritic zone could be traced for approximately 400 m along strike into old quarries and mine adits north and south of the river, varying in thickness from ~50 cm to several meters. The second outcrop (Fig. 4.1, #2) was found further downstream in the valley and appeared to be an extension of outcrop #1, as bedding orientations were very similar for both locations (175/30-E) and the two deposits could be approximately connected along strike. The thickness of this chert-barite horizon (Fig. 4.2f) was smaller than at outcrop #1, but similar lithological associations with mafic and felsic schists were observed. A third and narrow seam of barite was observed ~130 meter above outcrop #1 (Fig. 4.1, #3), but the thickness of this horizon is small (~10 cm) and the lateral extent of the deposit appeared to be very limited. Therefore, we focused in this study on the two main barite outcrops, i.e. the one in near the lower waterfall (#1) and the one in the river (#2). The lithological context of both localities is described below.

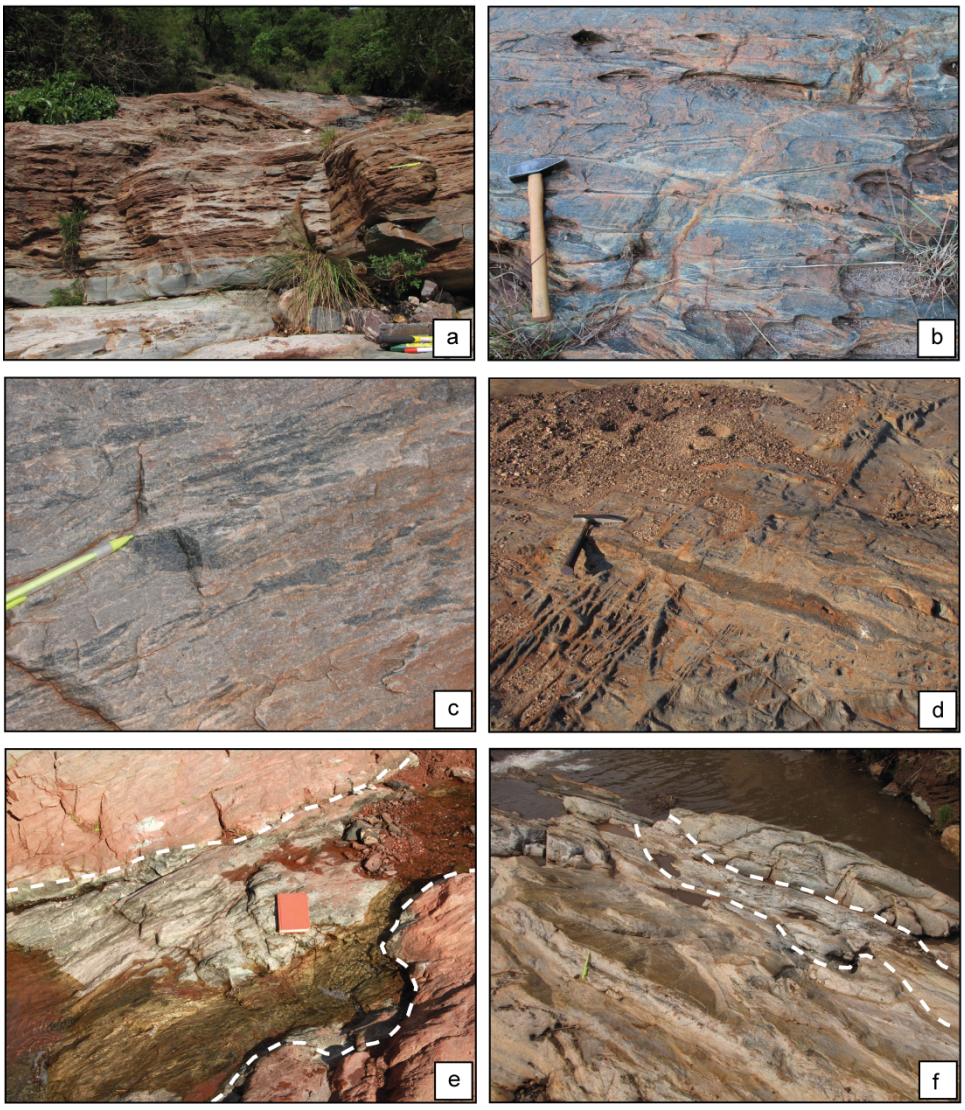

Figure 4.2 *Field photographs: (a) overview of bedding and bedding-parallel foliation as observed in the waterfall section, (b) deformed pillows in the river section, (c) fiamme textures in felsic schists from the waterfall section, (d) felsic veins radiating from restitic texture in felsic schists from the waterfall section, (e) barite horizon in the waterfall section and (f) barite in the river section (dashed lines indicate approximate boundaries).*

4.3.2 Waterfall section

The waterfall section was recorded between the lower and upper waterfall in the Londozi river over a vertical distance of 24.5 m, as shown in Fig. 4.3. Black and brown banded chert at the base of the section is overlain by 5 meters of strongly weathered finely foliated mafic schists with actinolite-hornblende, epidote, chlorite and muscovite. A ca. 20 cm thick layer of non-foliated massive amphibolite (LON-11-04) marked the transition towards mafic schists with green-colored zones of hornblende-actinolite aggregates, found as elongated and coarse-crystalline sheets. Mafic schists just below the barite horizon are strongly altered and contained small-scale witherite ($BaCO_3$) veins, as well as actinolite, diopside and Ba-rich feldspar. The contact with the barite (Fig. 4.2e) was relatively gradual and infills of barite into the underlying altered host rock were observed, whereas the barite itself contained chaotically orientated fragments of the mafic host rock - some of which exhibit tight small-scale isoclinal folds. However, in the quarry south of the waterfall section, centimeter-scale flat layers of barite interbedded with chert were observed. The upper contact of the barite is irregular and sharp, and represents a transition towards felsic schists with dominant quartz, K-feldspar, plagioclase and biotite. These schists are strongly foliated and contain abundant fiamme (Fig. 4.2c), of which several are elongated along the direction of foliation and subparallel to the bedding producing eutaxitic fabrics. Weathered fiamme reveal the presence of fibrous hornblende-actinolite within these textures. The uppermost felsic schists in the waterfall section showed strong compositional banding and clearly visible felsic veins oriented at roughly right angles to the foliation, which radiate from restitic textures with dark-colored interiors and light-colored rims (Fig. 4.2d).

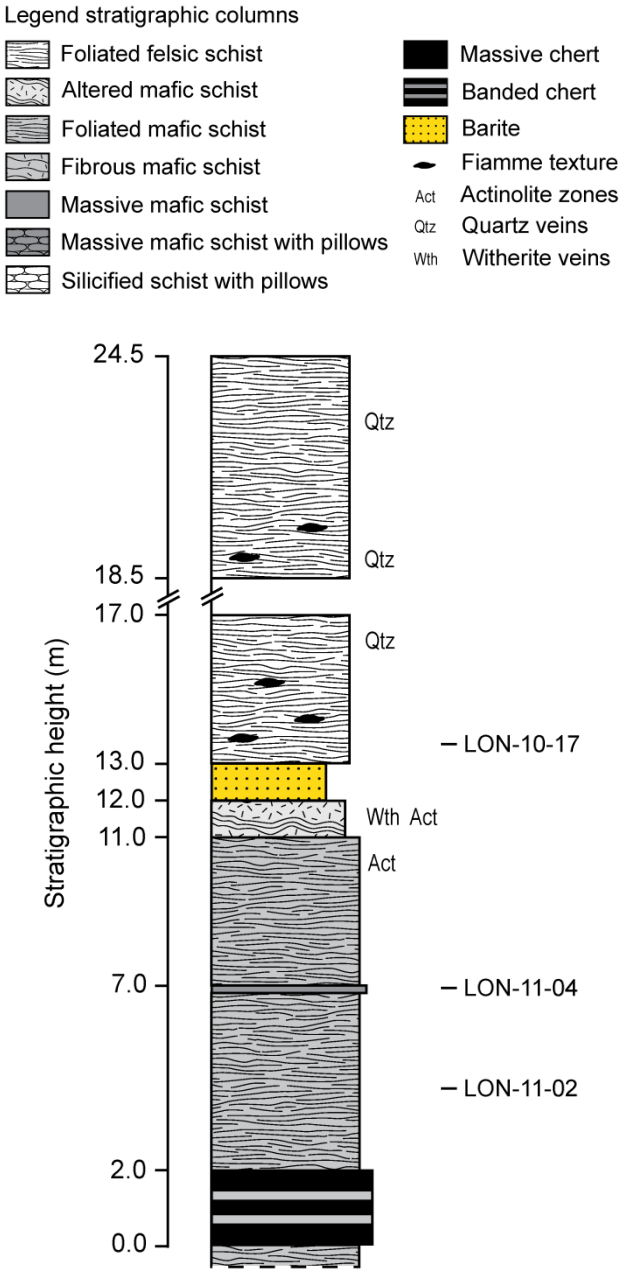

Figure 4.3 *Stratigraphic column of the waterfall section, showing the transition from foliated and massive mafic schists, towards altered mafic schists with barite and foliated felsic schists with fiamme textures. Samples used for thermobarometry or zircon geochronology are indicated to the right. Sample LON-10-09 was located higher up in the stratigraphy and therefore not shown on this figure.*

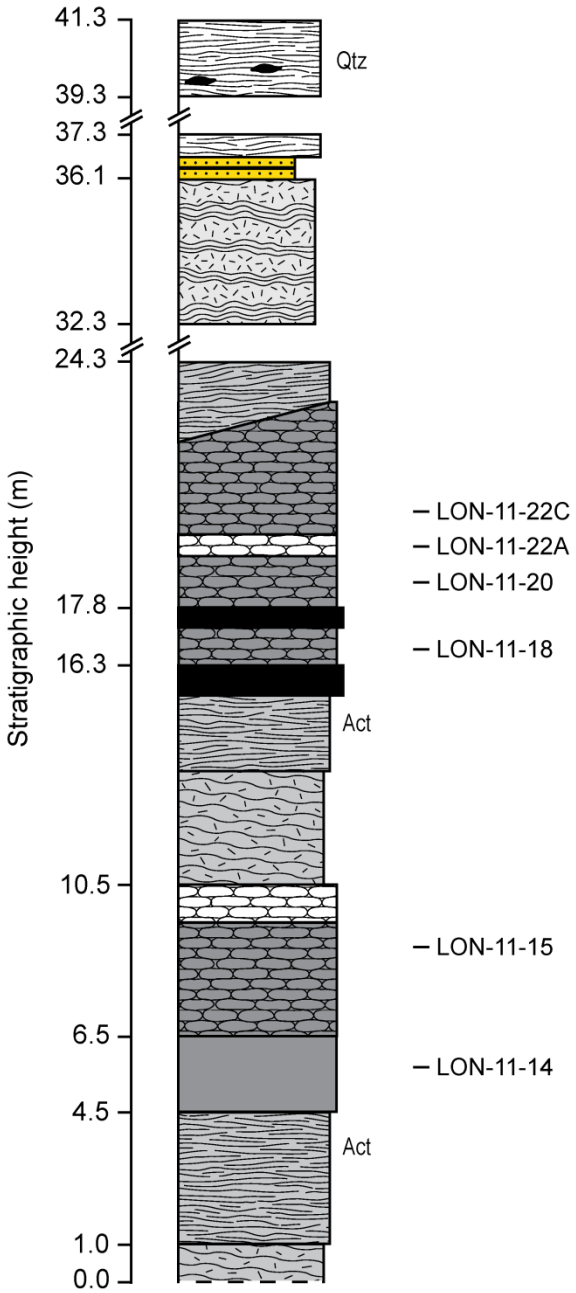

Figure 4.4 *Stratigraphic column of the river section, showing a similar transition from mafic to felsic schists as for the waterfall section. Barite occurs above strongly altered mafic schists. Samples used for thermobarometry are indicated to the right. See Fig. 4.3 for legend.*

4.3.3 River section

At the base of the river section (Fig. 4.4), fibrous actinolite and anthophyllite-rich amphibolites are overlain by foliated mafic schists with compositional banding. Coarse crystalline actinolite-rich zones appear towards the top of these schists and are oriented parallel to bedding. The foliated schists change abruptly into massive mafic schists with dominant hornblende, plagioclase and quartz, followed by a gradual transition into deformed mafic pillows. The uppermost meter of this bed shows intense silicification of pillow structures and strong alteration of the pillow lava rims. Mafic pillows are also observed higher in the stratigraphy, separated from the lower ones by a sequence of fibrous amphibole-rich schists changing into foliated mafic schists with bands of actinolite-rich material, and thin layers of massive green chert with clear slickensides on bedding surfaces. Pillow lavas at LON-11-22A (Fig. 4.4) are highly silicified in contrast to the overlying rocks (LON-11-22C). Strongly foliated mafic schists with abundant biotite were found above the pillow basalts grading into heavily silicified and light-colored schists with actinolite, epidote, armenite ($BaCa_2Al_6Si_9O_{30}.2H_2O$) and Ba-feldspar just below the barite horizon. A gradual transition into the barite was observed, with a baritic vein intersecting the underlying lithologies and terminating at the base of the chert-barite unit. Similar to the waterfall section, the deposit contains deformed fragments of silicified amphibolite, but the thickness of the barite horizon was smaller and more variable (Fig. 4.2f). Lithologies above the barite deposit exhibit a similar irregular but sharp contact and are of similar felsic composition as in the waterfall section, with compositional banding, fiamme textures as well as cross-cutting felsic veins.

4.4 SAMPLES AND ANALYTICAL METHODS

4.4.1 Whole-rock REE geochemistry

Rare earth element analyses were performed on 10 relatively unaltered mafic and 5 felsic schists from different stratigraphic levels in the waterfall and river sections. Rock samples were cut with a diamond blade saw to remove weathered rims, crushed with a jaw crusher and further pulverized in an automated crusher. Approximately 125 mg of rock powder was dissolved in 2.5 ml HF (48%) and 2.5 ml mix acid consisting of $HClO_4$ (72%) and ultrapure HNO_3 (65%) in the ratio

$HClO_4$:HNO_3 = 3:2. The mixture was heated in closed vessels at 90°C for at least eight hours and subsequently dried in open vessels at 160°C. The residual was dissolved again in a mixture of 2.5 ml concentrated HCl and 2.5 ml concentrated H_2O_2 to ensure near-total digestion. Five samples were analyzed in duplicate and two international soil standards ISE-912 (van Dijk and Houba, 2000) were included to test for reproducibility and element recovery in the digestion procedure. Solutions were analyzed for La, Ce, Pr, Nd, Sm, Eu, Gd, Tb, Dy, Ho, Er, Tm, Yb and Lu by quadrupole inductively-coupled plasma mass spectrometry (ThermoFinnigan X-Series ICP-MS) at Utrecht University. In addition, Ba concentrations were determined by inductively-coupled plasma optical emission spectrometry (ICP-OES), so that interferences of BaO on Eu could be corrected for using a calibration curve derived from ICP-MS measurements of ^{153}Eu in solutions spiked with 10 to 10000 ppb Ba. Duplicate analyses demonstrated reproducibility better than 91% for all REE except Tm and Lu, whereas measured La, Ce and Nd concentrations for the ISE-921 standard deviated less than 2% from reported values indicating good recovery of REE during total digestion. Relative errors were 3-5% for the light REE (La-Gd) and 9-12% for heavy REE. Analyses of Tm and Lu suffered from low precision due to concentrations near the detection limit, and were therefore excluded from the data set. Major elements were not considered for petrogenetic interpretations in this study due to extensive field evidence for silicification and secondary alteration processes, whereas other elements (e.g. Y, Zr) could not be fully recovered in the acid-digestion method.

4.4.2 Zircon geochronology and REE geochemistry

Felsic schists were sampled for zircon U-Pb dating at two different locations (see Fig. 4.1): just above the main barite occurrence in the waterfall section (LON-10-17), and just below barite #3 approximately 60 m higher in the stratigraphy (LON-10-09). Optical microscopy did not reveal zircons in the mafic lithologies below the main barite horizon. Zircons were separated from 10-15 kg of rock samples at the Mineral Separation Laboratory of the VU University, Amsterdam. Samples were cut with a diamond blade saw and subsequently crushed to 250 µm grain size with a jaw crusher and disk mill. Grains smaller than 30-60 µm were removed using a desliming machine. Zircon separation was performed in an overflow centrifuge using heavy liquids (lithium heteropolytungstate, methylene iodide), with an additional magnetic separation step to remove magnetite. The

remaining zircon-bearing fraction was sieved and further separated using a Frantz isodynamic separator, with an increasing electromagnetic current and decreasing front slope. Zircons were handpicked from the residual non-magnetizable fraction, mounted in epoxy resin and polished. Cathodoluminescence (CL) imaging by scanning electron microscope (SEM) was used to determine internal textures of the zircons and select spot locations for in situ U-Pb analysis at the Utrecht University laser ablation lab, using a ThermoFinnigan Element 2 ICP-MS and a Geolas 193 nm ArF excimer laser ablation system with 40 μm spot diameter.

Measured isotope ratios were referenced to the 91500 zircon standard with a reported ^{206}Pb-^{238}U age of 1062.4 ± 0.4 Ma (Wiedenbeck et al., 1995) and data was processed using the GLITTER data reduction software. Integration intervals were preferentially selected from the first part of each analytical run to avoid fractionation related to the geometry of the crater with progressive ablation (Mank and Mason, 1999). However, heterogeneous zircons that required integration intervals shorter than 10 seconds were rejected based on poor counting statistics. Analyses with ^{204}Pb count rates above the detection limit (100 cps) were discarded for their high common lead contents and runs with relative errors (2σ) larger than 5% were removed from the dataset. U-Pb ages were calculated, statistically assessed and plotted using the ISOPLOT software package by Ludwig (2008). Repeated analyses of zircon standard 91500 during analytical runs (Supplementary Table S4-1)* yielded a weighted average $^{207}Pb/^{206}Pb$ age of 1064 ± 9 Ma (MSWD = 1.1, probability = 0.3, n = 50), which is in good agreement with the reported value by Wiedenbeck et al. (1995). All uncertainties are quoted as 2σ errors.

Rare earth element compositions of a selection of zircons were measured by laser ablation ICP-MS in 40 μm spots adjacent to the craters used for U-Pb dating, using the NIST612 glass as calibration standard (Pearce et al., 1997) and Si as internal standard. Element concentrations were calculated assuming 32.7 wt% SiO_2 for all zircons, based on the reported composition of zircon standard 91500 (Wiedenbeck et al., 1995). Repeated measurements of zircon 91500 were used to confirm the accuracy of trace element results. Analyses with more than 1000 ppm P were discarded due to suspected analytical artifacts from apatite inclusions (cf.

* Supplementary tables for this chapter are available at http://hdl.handle.net/10411/10144

Whitehouse and Kamber, 2002), but no anomalously high Th contents from possible monazite inclusions were observed.

4.4.3 Thermobarometry

Seven relatively unaltered mafic schists were selected from the waterfall and river sections for the reconstruction of metamorphic conditions and examined using optical microscopy. Three of these samples contained garnet, but only LON-11-18 yielded a useful mineral assemblage with garnet, plagioclase, biotite and hornblende. In addition, coexisting hornblende and plagioclase were observed in samples LON-11-02, LON-11-04, LON-11-14 and LON-11-22C that allowed for the application of hornblende-plagioclase thermometry (Holland and Blundy, 1994). Selected samples were analyzed for their major element composition using the JEOL-JXA 8600 Superprobe electron microprobe at Utrecht University, using a 15 kV accelerating voltage with a 20 nA beam current. Elements were calibrated against the following synthetic and natural standards: diopside for Ca and Si, corundum for Al, TiO for Ti, jadeite for Na, forsterite for Mg, hematite for Fe, tephroite for Mn, $KTiPO_5$ for K, barite for Ba, celestine for S and Sr, metallic chromium for Cr and metallic nickel for Ni. Data were processed using the PROZA correction function. Amphibole compositions and Fe^{3+}/Fe^{2+} ratios were calculated following the procedure described by Holland and Blundy (1994). Ferric iron in garnet was recalculated using the method of Droop (1987) whereas all iron was assumed to be ferrous in biotite.

Mineral compositions of sample LON-11-18 were recalculated to element molar abundances for equilibrium assemblage modeling with Theriak-Domino (De Capitani and Petrakakis, 2010), using molar volumes from Holland and Powell (2011) and volumetric abundances of 60% hornblende, 10% chlorite, 10% biotite, 8% muscovite, 5% plagioclase, 5% garnet and 2% quartz estimated from optical microscopy. Calculations were performed using the Berman database (Berman, 1988) and assuming a water-saturated system, consistent with the significant amount of hydrous minerals in LON-11-18.

4.5 RESULTS

4.5.1 Whole-rock REE geochemistry

Rare earth element concentrations of selected mafic and felsic rocks are listed in Table 4.1 and shown as chondrite-normalized patterns in Fig. 4.5 (normalization values from McDonough and Sun, 1995). Two different REE patterns can be distinguished for mafic schists: flat patterns with $(La/Gd)_N \sim 1$, and slightly light REE enriched patterns with $(La/Gd)_N \sim 2\text{-}3$ and 20-70 times chondritic concentrations of La. Both groups show similar flat heavy REE patterns and enrichment factors, with negligible Eu-anomalies (Table 4.1). In contrast, felsic schists are significantly more LREE enriched with La concentrations of more than 100 times chondritic values and $(La/Gd)_N \sim 4\text{-}6$. Furthermore, small Eu-anomalies with $Eu/Eu^* \sim 0.75$ and flat heavy REE patterns were observed for the felsic lithologies. Rare earth element patterns are similar for rocks from the waterfall and river section and no correlation between stratigraphic height and REE concentrations was observed.

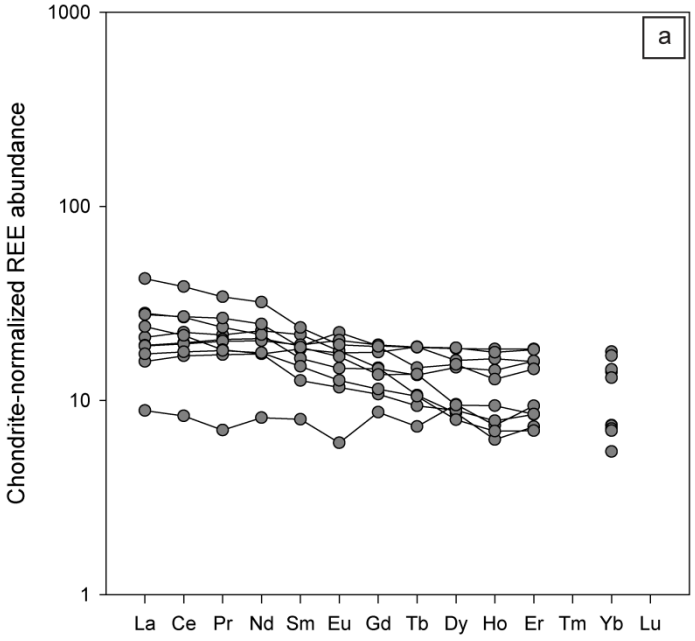

Figure 4.5a *Whole-rock REE abundances normalized to chondritic values (McDonough and Sun, 1995) for mafic schists at Londozi.*

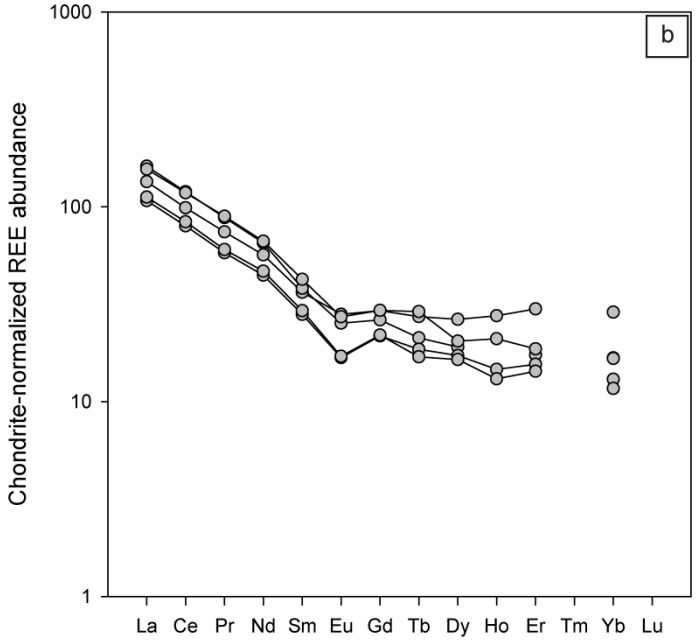

Figure 4.5b *Whole-rock REE abundances normalized to chondritic values (McDonough and Sun, 1995) for felsic schists at Londozi.*

4.5.2 Zircon geochronology and REE geochemistry

Zircons from samples LON-10-09 and LON-10-17 were colorless to slightly pink euhedral prismatic crystals with mostly undisturbed and concentric or lengthwise igneous growth zoning patterns (Fig. 4.6). Some of the grains display thin bright rims that possibly reflect uranium-poor overgrowths, but these were too small for U-Pb analysis by laser ablation. Grain sizes range from 100 to 250 µm, whereas zircons 17-43 and 17-44 appear to be fragments from larger grains. Xenocrystic cores were observed and analyzed in zircons 09-07, 09-15, 09-29 and 09-34. Results from 36 spot analyses in 29 zircons from LON-10-09, and 27 spots in 25 zircons from LON-10-17 are shown in Table 4.2. Calculated Th/U ratios range from 0.3 to 0.9.

Sample	11-01	11-02	11-03	11-04	11-08	11-09	11-10
Composition	Mafic	Mafic	Mafic	Mafic	Felsic	Felsic	Felsic
La	5.69	6.66	10.05	2.10	36.94	25.46	26.57
Ce	13.25	16.43	23.64	5.10	72.32	48.88	51.33
Pr	1.69	2.21	3.17	0.65	8.29	5.38	5.60
Nd	7.94	9.96	14.66	3.72	30.41	20.36	21.35
Sm	1.87	2.44	3.51	1.18	6.28	4.15	4.33
Eu	0.66	0.82	1.09	0.34	1.53	0.95	0.96
Gd	2.14	2.89	3.77	1.73	5.84	4.32	4.37
Tb	0.34	0.49	0.53	0.26	1.05	0.67	0.61
Dy	2.19	3.64	3.77	2.35	5.03	4.24	4.04
Ho	0.43	0.78	0.70	0.41	1.15	0.80	0.71
Er	1.35	2.55	2.32	1.50	2.98	2.49	2.29
Tm	0.09	0.29	0.19	0.07	0.56	0.24	0.12
Yb	1.15	2.32	2.11	1.20	2.68	2.10	1.88
Lu	0.14	0.32	0.21	0.14	0.54	0.22	0.14
Eu/Eu*	1.00	0.94	0.91	0.73	0.76	0.68	0.67

Table 4.1 *Whole-rock rare earth element concentrations in ppm, analyzed in acid-digested rock samples by ICP-MS. Samples 11-01 to 11-10 were collected from the waterfall section, and samples 11-12 to 11-28 from the river sections. Eu-anomalies are calculated as* $Eu/Eu^* = Eu_N/(0.5Sm_N + 0.5Gd_N)$*, where the subscript N indicates chondrite-normalized values.*

Sample	11-12	11-13	11-14	11-15	11-20	11-22C	11-27	11-28
Composition	Mafic	Mafic	Mafic	Mafic	Mafic	Mafic	Felsic	Felsic
La	4.11	6.56	3.76	5.01	4.55	4.52	31.89	38.26
Ce	10.89	16.54	10.40	13.73	12.14	11.99	60.57	73.18
Pr	1.68	2.46	1.60	2.02	1.91	1.87	6.89	8.16
Nd	8.04	11.30	7.93	10.44	9.52	9.27	25.89	29.81
Sm	2.21	2.78	2.73	3.23	2.82	2.86	5.39	5.65
Eu	0.71	0.95	0.99	1.01	1.26	1.15	1.58	1.42
Gd	2.27	2.70	3.53	2.93	3.80	3.85	5.83	5.23
Tb	0.38	0.49	0.68	0.38	0.68	0.68	0.98	0.77
Dy	1.96	2.33	3.96	2.12	4.55	4.59	6.51	4.69
Ho	0.38	0.51	0.90	0.34	1.00	0.97	1.51	0.01
Er	1.12	1.36	2.53	1.17	2.94	2.92	4.79	2.78
Tm	0.10	0.20	0.37	0.06	0.49	0.45	0.73	0.40
Yb	0.88	1.12	2.26	1.19	2.87	2.74	4.63	2.70
Lu	0.10	0.20	0.37	0.10	0.49	0.41	0.73	0.40
Eu/Eu*	0.96	1.04	0.97	0.98	1.17	1.06	0.86	0.78

Table 4.1 (continued)

4.5.2.1 Zircon U-Pb ages

Zircons from sample LON-10-09 show variable degrees of concordance (Table 4.2) and define a discordia line in the Tera-Wasserburg plot with an upper intercept age of 3513 ± 18 Ma (MSWD = 4.8), and an imprecise near-zero lower intercept age of -19 ± 300 Ma (Fig. 4.7a) suggesting recent lead loss. Therefore, the $^{207}Pb/^{206}Pb$ ages from both concordant (n = 13) and discordant zircons (n = 23) could be used to obtain reliable age estimates. Fig. 4.7b shows the histogram and probability plot for all analyses and demonstrates the presence of one dominant age peak with a weighted average of 3521 ± 6 Ma (MSWD = 1.2, n = 30), which is statistically similar to the upper intercept age derived from the Tera-Wasserburg plot. Four zircons with ages between 3429 ± 32 Ma and 3447 ± 33 Ma were significantly younger, whereas two zircons dated at 3572 ± 34 Ma and 3588 ± 33 Ma were considerably older. No systematic correlation was observed between $^{207}Pb/^{206}Pb$ age and Th/U ratio. However, xenocrystic cores 09-07, 09-15, 09-29 and 09-34 yielded relatively old ages between 3501 ± 33 and 3531 ± 32 Ma (Fig. 4.6c-d), which were statistically older or similar in age to their rims (09-14, 09-28, 09-33).

Zircons from LON-10-17 show generally higher levels of concordance (Table 4.1), but define a similar discordia line in the Tera-Wasserburg plot (Fig. 4.8a) with an upper intercept age of 3526 ± 18 Ma (MSWD = 3.8). However, the relatively small spread in the isotope data which are clustered around the upper intercept results in a poorly-defined and negative lower intercept age of 394 ± 890 Ma. Recent lead loss was assumed because the lower intercept is statistically indistinguishable from zero, so that both concordant (n = 22) and discordant (n = 5) zircons were included in age calculations. The probability plot (Fig. 4.8b) shows a single age peak with a weighted average of 3521 ± 9 Ma (MSWD = 1.7, n = 24), with one statistically younger zircon (3451 ± 36 Ma). The calculated average $^{207}Pb/^{206}Pb$ age is similar to the upper intercept age and the age of the main zircon population found in sample LON-10-09. Concordant zircons 17-15 and 17-44 represent the oldest grains in both datasets with ages of 3597 ± 38 Ma and 3610 ± 33 Ma. Similar to sample LON-10-09, the calculated ages from sample LON-10-17 do not show a correlation with Th/U ratio.

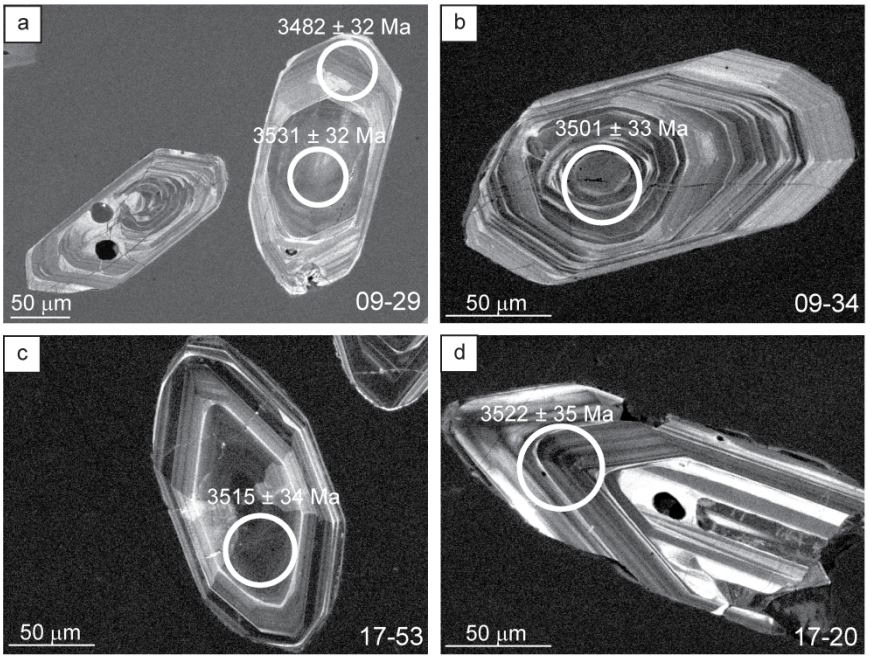

Figure 4.6 *Zircon cathodoluminescence images with ages determined by laser ablation ICP-MS (approximate location and size of 40 μm spot shown). Images show euhedral crystals with oscillatory zoning and older xenocrystic cores, consistent with a magmatic origin for the zircons.*

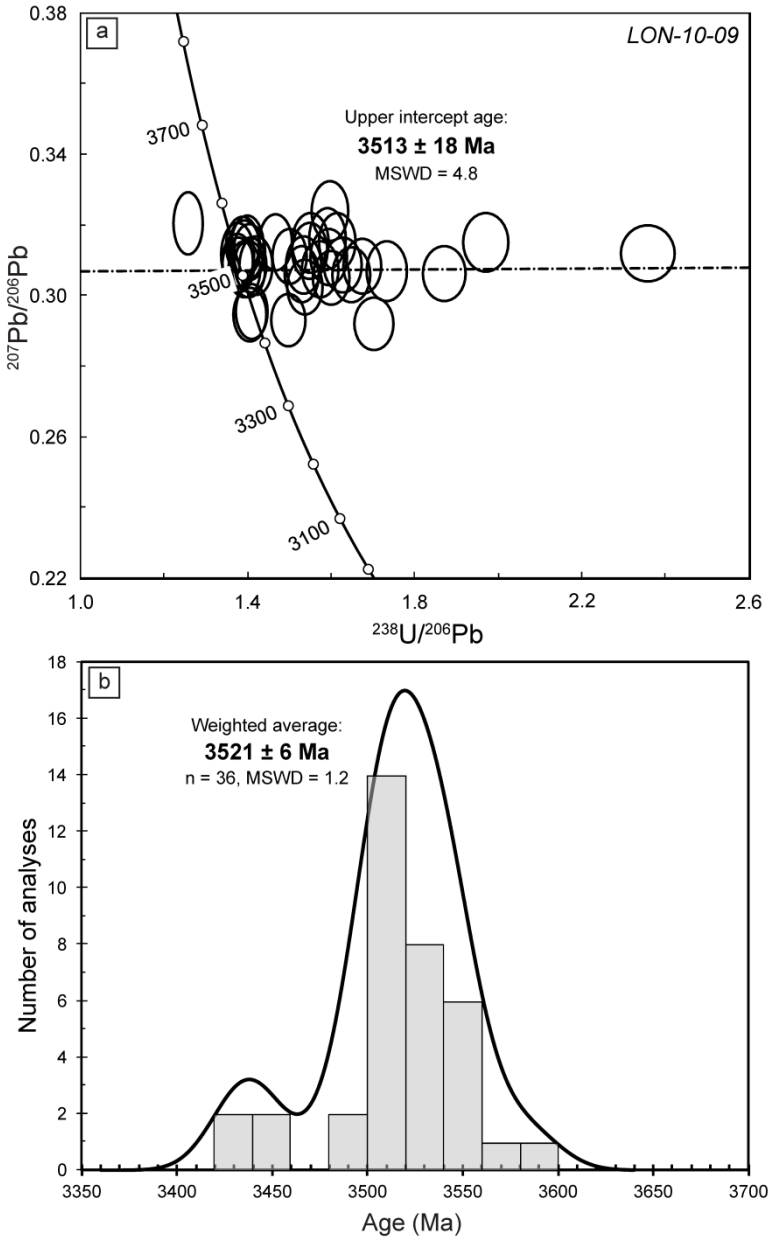

Figure 4.7 *Geochronological data from sample LON-10-09, with the Tera-Wasserburg plot (a) and histogram/probability diagram of $^{207}Pb/^{206}Pb$ ages (b) calculated using Isoplot (Ludwig, 2008). Both plots support a similar crystallization age of circa 3521 Ma.*

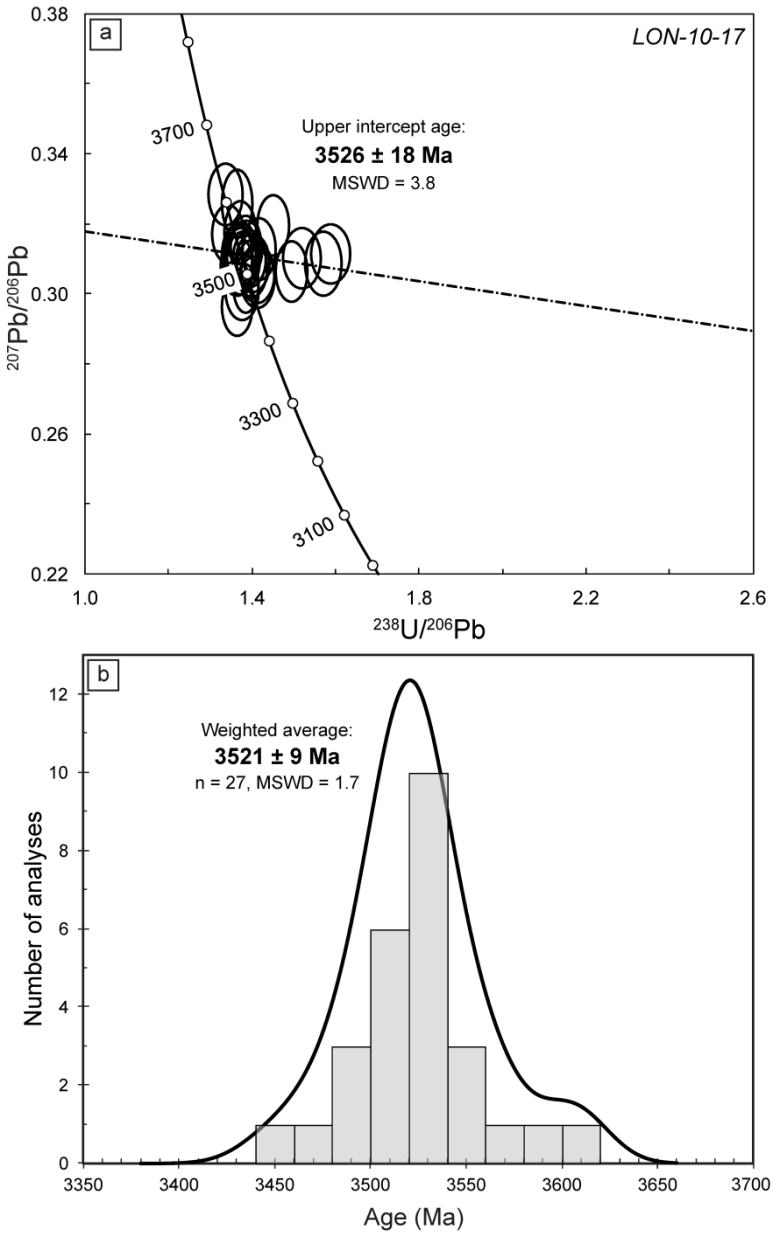

Figure 4.8 *Geochronological data from sample LON-10-17, with the Tera-Wasserburg plot (a) and histogram/probability diagram of $^{207}Pb/^{206}Pb$ ages (b) calculated using Isoplot (Ludwig, 2008). Both plots support a similar crystallization age of circa 3521 Ma.*

Zircon	Th/U	$^{207}Pb/^{206}Pb$	2σ	$^{207}Pb/^{235}U$	2σ	$^{206}Pb/^{238}U$	2σ	$^{206/238}$Age (Ma)	2σ	$^{207/206}$Age (Ma)	2σ	% Conc
09-03	0.56	0.3160	0.0071	27.06	1.30	0.628	0.014	3143	57	3550	35	89
09-05	0.63	0.3135	0.0075	30.85	1.95	0.714	0.017	3475	63	3538	37	98
09-06	0.67	0.3150	0.0069	28.80	1.30	0.645	0.015	3209	58	3545	34	91
09-07	0.94	0.3115	0.0073	32.79	1.99	0.726	0.017	3519	64	3529	36	100
09-08	0.60	0.3060	0.0063	25.77	0.77	0.607	0.014	3058	55	3501	32	87
09-09	0.63	0.3063	0.0064	23.07	0.73	0.535	0.012	2762	51	3502	32	79
09-10	0.60	0.3126	0.0064	27.37	0.77	0.646	0.014	3213	57	3534	32	91
09-11	0.58	0.3151	0.0069	21.39	0.87	0.508	0.012	2647	50	3546	34	75
09-12	0.72	0.2929	0.0061	27.27	0.85	0.668	0.015	3297	58	3433	32	96
09-13	0.76	0.2921	0.0061	24.77	0.78	0.588	0.013	2980	54	3429	32	87
09-14	0.53	0.3096	0.0064	31.39	0.92	0.727	0.016	3522	61	3519	32	100
09-15	0.65	0.3086	0.0064	31.99	1.01	0.726	0.016	3520	61	3514	32	100
09-16	0.56	0.3088	0.0064	26.90	0.81	0.614	0.014	3087	55	3515	32	88
09-17	0.46	0.3110	0.0063	28.96	0.71	0.666	0.015	3291	57	3526	31	93
09-19	0.82	0.3069	0.0069	22.70	1.07	0.577	0.013	2938	54	3505	35	84
09-20	0.55	0.3087	0.0063	32.32	0.85	0.711	0.016	3461	60	3514	32	98
09-21	0.68	0.3075	0.0064	29.41	0.10	0.636	0.014	3172	56	3508	32	90
09-22	0.55	0.3238	0.0069	28.57	1.06	0.626	0.014	3135	56	3588	33	87
09-23	0.62	0.3204	0.0071	33.81	1.70	0.796	0.018	3774	66	3572	34	106
09-25	0.60	0.3082	0.0064	27.17	0.84	0.598	0.013	3020	54	3512	32	86
09-26	0.60	0.3085	0.0068	30.96	1.48	0.704	0.016	3435	61	3513	34	98

Table 4.2 *U-Pb data of zircons from samples LON-10-09 and LON-10-17 as analyzed by laser ablation ICP-MS. Ages are calculated using Isoplot (Ludwig, 2008). The percentage of concordance is calculated as: ($^{206/238}$Age)/($^{207/206}$Age) x 100%.*

Zircon	Th/U	$^{207}Pb/^{206}Pb$	2σ	$^{207}Pb/^{235}U$	2σ	$^{206}Pb/^{238}U$	2σ	$^{206/238}$Age (Ma)	2σ	$^{207/206}$Age (Ma)	2σ	% Conc
09-28	0.52	0.3024	0.0062	27.47	0.78	0.650	0.014	3230	57	3482	32	93
09-29	0.91	0.3121	0.0065	19.11	0.56	0.424	0.009	2280	54	3531	32	65
09-31	0.57	0.3087	0.0066	28.24	1.11	0.652	0.015	3235	54	3515	33	92
09-33	0.61	0.3153	0.0068	27.40	1.07	0.619	0.014	3107	56	3547	33	88
09-34	0.74	0.3060	0.0067	27.47	0.97	0.654	0.015	3243	58	3501	33	93
09-35	0.61	0.3134	0.0065	31.38	0.92	0.718	0.016	3487	60	3538	32	99
09-36	0.54	0.3141	0.0067	30.32	1.13	0.721	0.016	3498	61	3541	33	99
09-37	0.69	0.2955	0.0062	29.42	1.05	0.709	0.016	3455	60	3447	33	100
09-38	0.63	0.3074	0.0065	29.26	1.09	0.713	0.016	3470	61	3508	33	99
09-42	0.92	0.2946	0.0062	28.93	0.98	0.712	0.016	3464	60	3442	33	101
09-46	0.41	0.3109	0.0066	28.50	1.05	0.627	0.014	3137	56	3525	33	89
09-49	0.59	0.3123	0.0065	29.95	0.99	0.712	0.016	3467	60	3532	32	98
09-50	0.60	0.3075	0.0066	30.19	1.19	0.718	0.016	3489	61	3508	33	99
09-52	0.71	0.3050	0.0063	26.26	0.75	0.625	0.014	3130	56	3496	32	90
09-53	0.61	0.3151	0.0065	29.22	0.86	0.682	0.015	3352	59	3546	32	95
17-04	0.56	0.3063	0.0070	29.19	1.10	0.669	0.014	3302	54	3503	35	94
17-06	0.42	0.3071	0.0067	30.38	1.10	0.715	0.015	3478	58	3506	34	99
17-07	0.46	0.3113	0.0069	27.81	1.13	0.630	0.015	3149	60	3527	34	89
17-08	0.43	0.3026	0.0067	31.55	0.85	0.722	0.013	3502	50	3484	34	101
17-09	0.46	0.3129	0.0071	29.77	1.37	0.705	0.016	3441	60	3535	35	97
17-10	0.56	0.3086	0.0074	27.04	1.31	0.637	0.014	3177	59	3514	37	90

Table 4.2 (continued)

Zircon	Th/U	$^{207}Pb/^{206}Pb$	2σ	$^{207}Pb/^{235}U$	2σ	$^{206}Pb/^{238}U$	2σ	$^{206/238}$Age (Ma)	2σ	$^{207/206}$Age (Ma)	2σ	% Conc
17-13	0.65	0.3100	0.0067	31.10	1.11	0.717	0.017	3487	63	3521	33	99
17-14	0.65	0.3111	0.0071	30.47	1.12	0.733	0.016	3545	59	3526	35	101
17-15	0.61	0.3258	0.0080	30.47	1.53	0.733	0.016	3545	59	3597	38	99
17-20	0.49	0.3102	0.0070	31.85	1.30	0.728	0.016	3525	58	3522	35	100
17-21	0.44	0.3108	0.0070	31.04	1.16	0.728	0.016	3527	59	3525	35	100
17-22	0.66	0.3112	0.0071	31.12	1.49	0.726	0.016	3519	60	3527	35	100
17-24	0.42	0.3102	0.0084	30.94	1.60	0.728	0.018	3527	69	3522	42	100
17-26	0.59	0.3094	0.0068	30.96	1.09	0.725	0.017	3515	63	3518	34	100
17-28	0.43	0.3176	0.0072	31.19	1.36	0.729	0.017	3530	63	3558	35	99
17-31	0.60	0.3079	0.0070	30.88	1.09	0.733	0.017	3543	64	3511	35	101
17-35	0.61	0.3045	0.0069	29.23	1.24	0.708	0.017	3451	65	3493	35	99
17-37	0.52	0.3143	0.0067	31.49	1.00	0.722	0.015	3505	57	3542	33	99
17-41	0.45	0.2963	0.0069	30.80	1.09	0.733	0.016	3543	59	3451	36	103
17-43	0.72	0.3007	0.0067	31.10	1.42	0.727	0.018	3521	59	3474	35	101
17-44	0.61	0.3284	0.0072	33.13	1.69	0.748	0.019	3599	66	3610	33	100
17-45	0.47	0.3195	0.0071	30.54	1.20	0.689	0.015	3381	69	3567	34	95
17-46	0.69	0.3102	0.0070	30.31	1.42	0.658	0.016	3261	58	3522	35	93
17-48	0.60	0.3128	0.0067	30.17	1.13	0.722	0.016	3502	63	3535	33	99
17-51	0.66	0.3171	0.0068	33.29	1.14	0.745	0.017	3590	61	3556	33	101
17-52	0.67	0.3057	0.0067	30.75	1.17	0.708	0.017	3450	64	3500	34	99
17-53	0.50	0.3087	0.0068	30.23	1.14	0.714	0.017	3472	63	3515	34	99

Table 4.2 (continued)

4.5.2.2 Zircon REE geochemistry

Trace element compositions of 22 zircons are shown in Supplementary Table S4-2 and Fig. 4.9. Concentrations normalized to CI chondrite (McDonough and Sun, 1995) show an increase from light to heavy REE with all elements being enriched relative to chondritic values (Fig. 4.9a). All zircons display positive Ce-anomalies and negative Eu-anomalies and show a relatively restricted range in Hf concentrations between 6250 and 9230 ppm. No correlation was observed between zircon Th + U concentrations and enrichment in LREE as indicated by $(La/Gd)_N$ (Fig. 4.9b), but Ce concentrations showed a positive correlation with Hf contents (Fig. 4.9c). Comparison of trace element compositions for zircons from LON-10-09 and LON-10-17 shows that zircons from the former are more enriched in light REE and Hf.

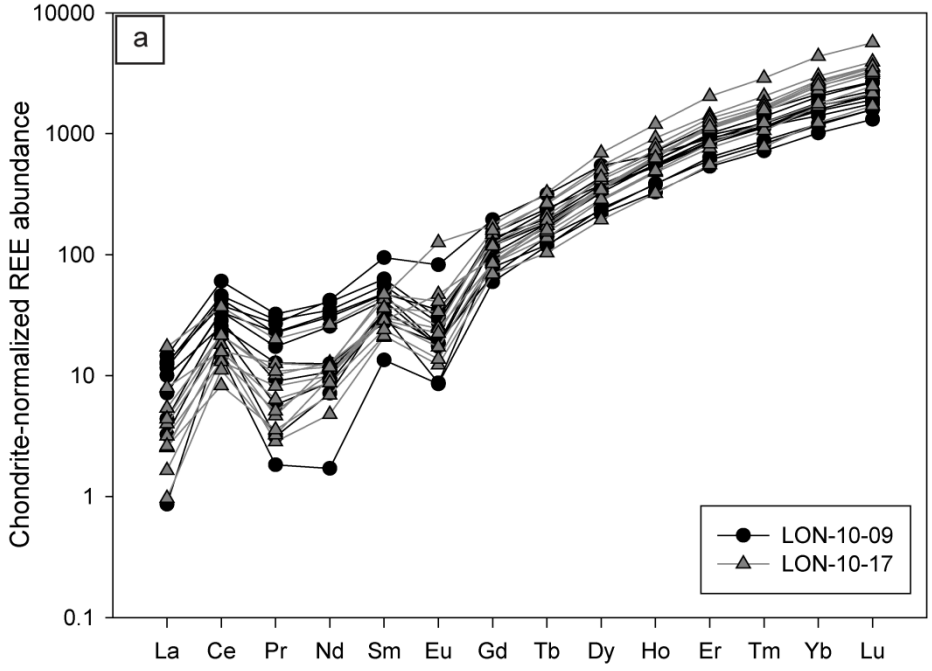

Figure 4.9 *Rare earth and trace elements measured in zircon by LA-ICP-MS. Panel (a) shows REE abundances normalized to chondritic values (McDonough and Sun, 1995), with slightly more LREE enriched patterns for sample LON-10-09.*

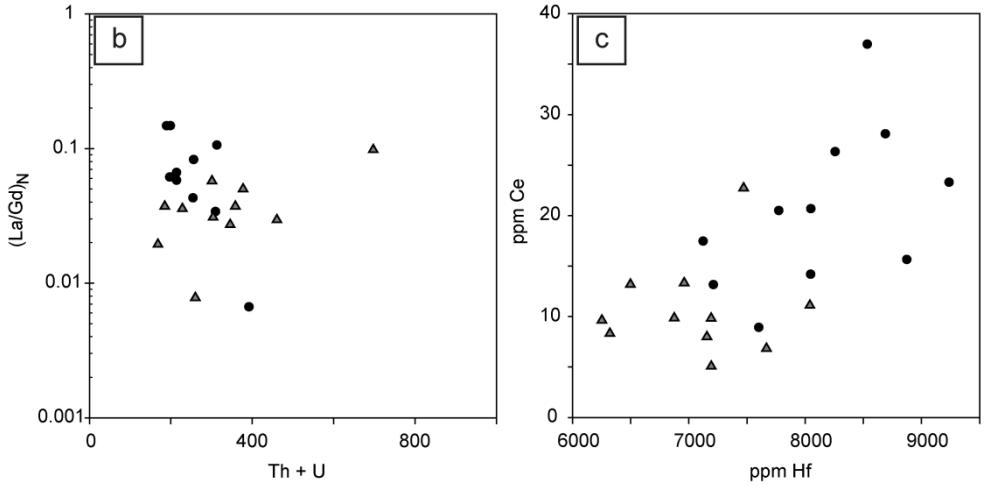

Figure 4.9 (continued from previous page) *Panel (b) demonstrates no clear correlation between LREE enrichment and total Th + U concentrations, suggesting no LREE incorporation due to damaged lattice sites (Whitehouse and Kamber, 2002). Panel (c): weak positive correlation between Ce and Hf concentrations suggesting that LREE enrichment was related to magma evolution. See legend in panel (a) for explanation of symbols.*

4.5.3 Thermobarometry

4.5.3.1 Mineral textures and compositions

Selected mafic schists show textures dominated by coexisting hornblende and plagioclase with minor quartz, biotite and ilmenite (Fig. 4.10a). Some hornblende minerals coexist with euhedral or subhedral actinolite. Sample LON-11-18 contains fractured porphyroblasts of garnet with small inclusions of hornblende and biotite in a matrix of hornblende, plagioclase, muscovite, biotite (partially altered to chlorite) and quartz (Fig. 4.10b). Fracture fills consist predominantly of chlorite and quartz.

Major element concentrations and calculated atoms per formula unit for mineral analyses in sample LON-11-18 are shown in Table 4.3. Garnet is relatively Mn-rich almandine (X_{Alm} = 0.58, X_{Sps} = 0.17) with no compositional differences between core and rim. In contrast, plagioclase occurs as both bytownite (X_{Ab} = 0.22) and andesine (X_{Ab} = 0.58), of which the latter is similar to the composition of twelve analyses of plagioclase in samples LON-11-02, LON-11-04, LON-11-14 and LON-11-22C with an average albite-content of X_{Ab} = 0.60. Amphibole is found as

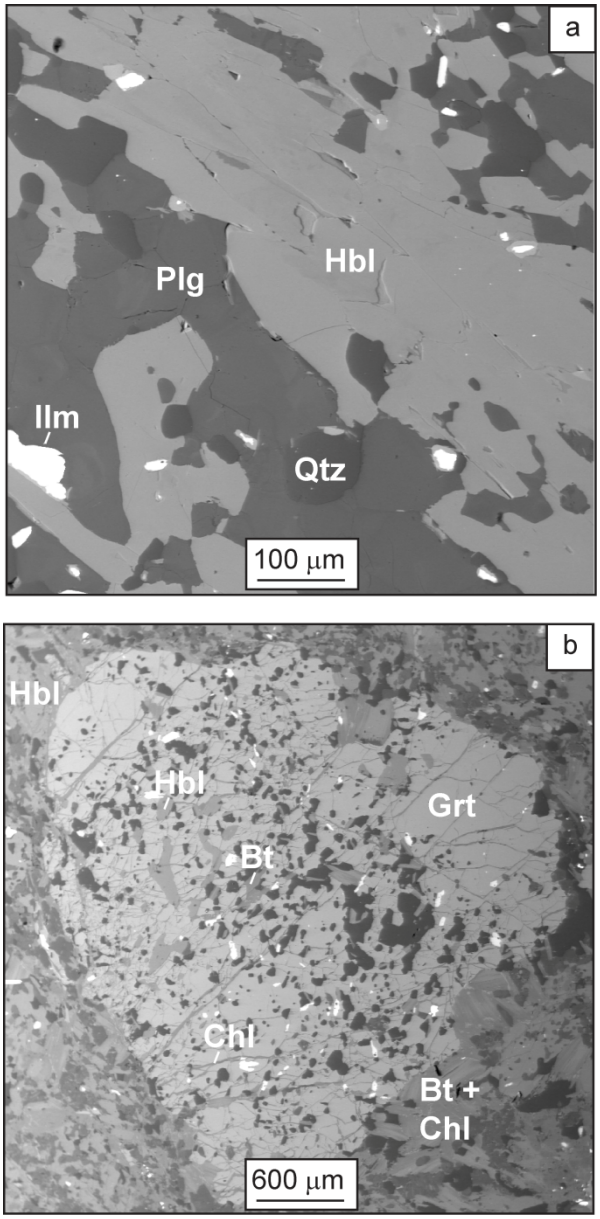

Figure 4.10 *Back-scattered electron images of schists and amphibolites used for thermobarometry, with (a) hornblende-plagioclase in LON-11-22C and (b) fractured garnet with biotite and hornblende occurring as inclusions and matrix minerals in LON-11-18.*

	Garnet	Garnet	Plagioclase	Plagioclase	Hornblende	Hornblende	Hornblende	Biotite	Muscovite	Chlorite
Oxide wt%	*core*	*rim*	*matrix*	*near grt*						
SiO_2	36.796	37.293	47.460	56.441	42.267	42.669	41.828	35.706	46.225	25.327
Al_2O_3	20.557	20.828	32.292	26.655	13.092	13.995	15.342	17.840	33.755	20.309
FeO	26.926	26.519	0.055	0.089	18.366	18.431	18.904	21.235	3.827	27.093
MnO	7.487	7.788	0.035	0.000	0.598	0.567	0.641	0.409	0.055	0.705
MgO	2.445	2.433	0.009	0.000	7.981	7.981	7.262	9.199	1.405	13.751
CaO	5.257	5.456	15.343	8.680	11.378	11.811	11.834	0.012	0.026	0.010
K_2O	0.000	0.000	0.030	0.081	0.533	0.457	0.663	9.075	10.887	0.000
Na_2O	0.006	0.000	2.455	6.640	1.051	1.105	1.147	0.041	0.155	0.000
TiO_2	0.110	0.040	0.000	0.000	0.493	0.488	0.487	2.013	0.096	0.027
Total	**99.584**	**100.357**	**97.679**	**98.586**	**95.759**	**97.504**	**98.108**	**95.53**	**96.431**	**87.223**
Element										
Si	2.97	2.98	2.22	2.57	6.41	6.35	6.22	2.73	3.08	2.72
Al	1.95	1.96	1.78	1.43	2.34	2.46	2.69	1.60	2.65	2.57
Fe^{2+}	1.71	1.70	0.00	0.00	1.75	1.74	1.81	1.36	0.21	2.43
Fe^{3+}	0.10	0.07	0.00	0.00	0.58	0.55	0.54	0.00	0.00	0.00
Mn	0.51	0.53	0.00	0.00	0.08	0.07	0.08	0.03	0.00	0.06
Mg	0.29	0.29	0.00	0.00	1.80	1.77	1.61	1.05	0.14	2.20
Ca	0.45	0.47	0.77	0.42	1.85	1.88	1.89	0.00	0.00	0.00
K	0.00	0.00	0.00	0.00	0.10	0.09	0.13	0.88	0.93	0.00
Na	0.00	0.00	0.22	0.59	0.30	0.32	0.33	0.01	0.02	0.00
Ti	0.01	0.00	0.00	0.00	0.06	0.06	0.05	0.12	0.00	0.00
Total	**7.99**	**8.00**	**4.99**	**5.01**	**15.27**	**15.29**	**15.35**	**7.78**	**7.03**	**9.98**

Table 4.3 *Major element concentrations of representative minerals in sample LON-11-18 as analyzed by electron microprobe. Amphibole compositions and Fe3+/Fe2+ ratios were calculated following the procedure described by Holland and Blundy (1994). Ferric iron in garnet was recalculated using the method of Droop (1987) whereas all iron was assumed to be ferrous in biotite, muscovite and chlorite.*

Mg-rich tschermakite-hornblende in all samples used for pressure-temperature calculations (see Table 4.2 and Supplementary Table S4-3). Biotite in sample LON-11-18 belongs to the annite-phlogopite series with Mg/(Mg + Fe) = 0.43, although rims of biotite crystals are frequently altered to Mg,Fe-rich chlorite.

4.5.3.2 Geothermometers

Peak metamorphic temperatures were estimated using the hornblende-plagioclase thermometer of Holland and Blundy (1994) and the garnet-biotite thermometer of Hodges and Spear (1982). Twelve pairs of tschermakite-hornblende and andesine from samples LON-11-02, LON-11-04, LON-11-14 and LON-11-22C yielded an average temperature of 700°C (±50°C estimated error) for thermometer B assuming a pressure of 11 kbar, with values ranging from 666 to 737°C (Supplementary Table S4-3). Results are shown as light grey lines in Fig. 4.11a. Thermometer A of Holland and Blundy (1994) yielded a similar average temperature of 693°C, but with a larger spread in results from 573 to 744°C. For sample LON-11-18 (black lines in Fig. 4.11a), temperatures were calculated using three different amphibole analyses with the composition of the sodic plagioclase adjacent to the garnet (Table 4.3). The calculated average of 705°C at 11 kbar pressure is similar to the results obtained from other samples. Slightly higher temperature estimates were obtained from the garnet-biotite thermometer of Hodges and Spear (1982) (dark grey line in Fig. 4.11a), which yielded a temperature of 723°C at 11 kbar with no significant difference between the core and the rim of the garnet. Application of the garnet-muscovite thermometer (Green and Hellman, 1982) to sample LON-11-18 was problematic as the high Mn-content of garnet was outside the calibrated range. Temperatures obtained from this geothermometer (736°C at 11 kbar) are likely to represent an overestimation of peak metamorphic conditions and are therefore discarded for further interpretations. Temperatures based on the Al-in-chlorite thermometer of Cathelineau and Nieva (1985) were significantly lower than estimates from garnet-biotite and hornblende-plagioclase thermometers, ranging from 219 to 310°C (19 analyses, see Supplementary Table S4-4).

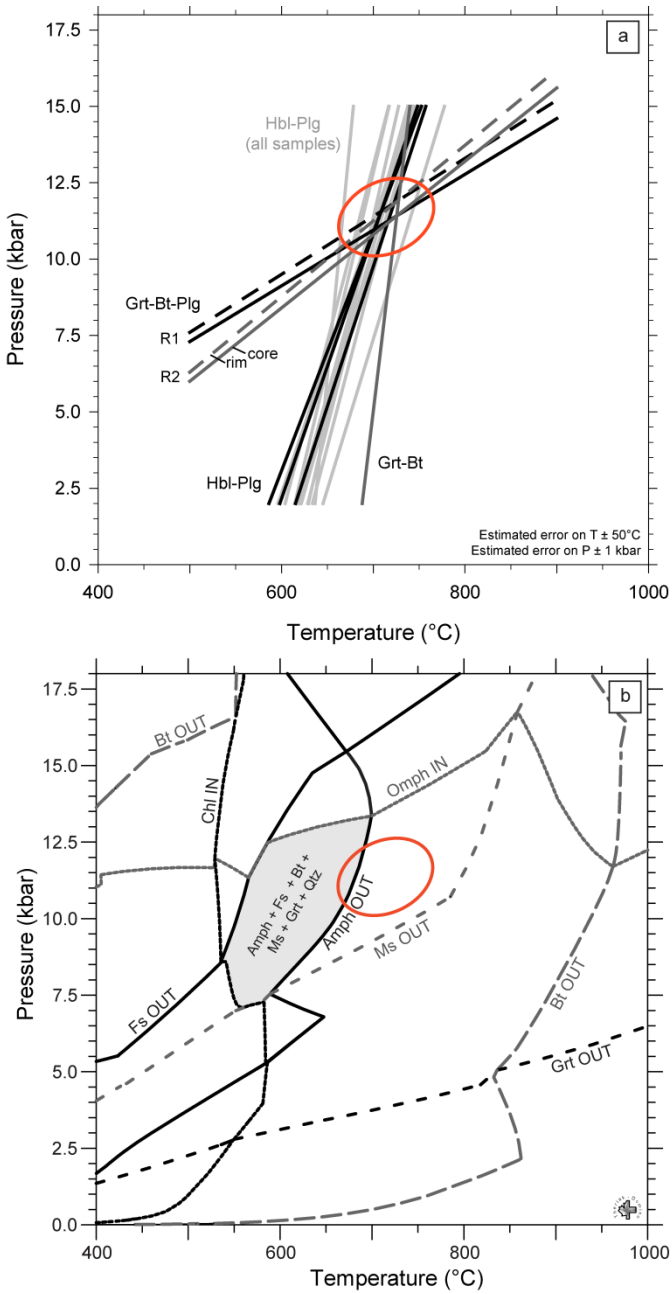

Figure 4.11 *Metamorphic conditions for mafic schists in the Londozi area based on sample LON-11-18. Fig. (a): P,T-conditions determined from conventional thermobarometers including hornblende-plagioclase (Holland and Blundy, 1994), garnet-biotite (Hodges and Spear, 1982) and garnet-biotite-plagioclase (reaction R1 and R2 from Hoisch, 1990). Grey*

Hbl-Plg lines indicate results calculated from all hornblende-plagioclase bearing samples, black Hbl-Plg lines are from sample LON-11-18 only. Ellipse indicates estimated pressure-temperature conditions taking errors on calculations into account. Fig. (b) from equilibrium assemblage modeling using Theriak-Domino (De Capitani and Petrakakis, 2010). Shaded area indicates pressure-temperature conditions at which the inferred peak metamorphic assemblage is stable, ellipse indicates conditions determined from conventional thermobarometers in Fig. (a).

4.5.3.3 Geobarometers

Pressure estimates were obtained from the garnet-biotite-plagioclase mineral assemblage in LON-11-18 by applying geobarometers R1 and R2 calibrated by Hoisch (1990). At 700°C, both reactions yielded a pressure of 10.9 kbar using the garnet composition of the core, whereas a slightly higher but statistically similar pressure of 11.4 kbar was calculated for the rim of the garnet (±1 kbar estimated error). Results are shown as near-horizontal lines in Fig. 4.11a. From the intersection of the hornblende-plagioclase and garnet-biotite thermometers with the garnet-biotite-plagioclase barometer in Fig. 4.11a, peak metamorphic conditions were estimated at 660 to 760°C and 10 to 12.5 kbar. Application of other geobarometers, including the garnet-hornblende-plagioclase barometer of Kohn and Spear (1990) and the garnet-muscovite-plagioclase barometers of Hoisch (1990) was compromised by the high Mn-content of the garnet and the relatively high Mg-content of the muscovite that were outside calibration limits. Calculating pressures based on these reactions for the mineral assemblage in LON-11-18 resulted in anomalously high values of 12.2 to 14.7 kbar at 700°C.

4.5.3.4 Equilibrium assemblage modeling

Equilibrium assemblages were modeled for temperatures between 400 and 1000°C and pressures of 0 to 18 kbar based on the recalculated composition of LON-11-18 and using the Theriak-Domino software package (De Capitani and Petrakakis, 2010). The resulting diagram is shown in Fig. 4.11b, with the shaded area representing the modeled stability field for the assemblage of hornblende, plagioclase, garnet, biotite, muscovite and quartz as observed in LON-11-18. These results suggest a maximum metamorphic temperature of 690°C based on the amphibole-out phase boundary, at pressures of 7.5 to 12.5 kbar.

4.6 DISCUSSION

4.6.1 Depositional environment

Barite can form by diagenetic replacement reactions, syngenetic hydrothermal processes or biological precipitation, of which only the first two are considered as important in the low sulfate Archean surface environment (Jewell, 2000; Huston and Logan, 2004). For the Londozi deposit, several lines of evidence argue for a synvolcanic origin of the barite. First, the two outcrops in the studied area appear to be part of the same circa one kilometer long deposit, with strong similarities in the stratigraphic position of the barite horizon, i.e. at the transition from strongly altered mafic schists to overlying felsic schists. This conformable nature of the barite with respect to volcanic bedding, the layered nature of the deposit and the considerable lateral extent that is significantly larger than the thickness are consistent with a stratiform orebody and suggestive of a synvolcanic or synsedimentary origin. Furthermore, contacts of the barite with underlying mafic schists are different (more gradual) from those with the overlying felsic schists, and alteration minerals and textures were mainly observed below the barite horizons. This asymmetry is inconsistent with secondary barite precipitation during later diagenetic or metasomatic events, but is compatible with synvolcanic barite deposition. Finally, we consider secondary replacement of evaporative gypsum by barium-rich fluids unlikely, because calcium and sulfate concentrations in the Paleoarchean oceans were probably too low for primary gypsum precipitation (Grotzinger and Kasting, 1993). Observed variations in orebody thickness could reflect primary paleorelief or might be related to relative rheological weakness of barite during deformation, as isoclinal folds within the barite suggest intense deformation in this zone. Below, we focus on the host rocks of the stratiform barite deposit to discuss the environment and tectonic setting of deposition.

4.6.1.1 Mafic volcanics

Lithologies in the studied area consist of mafic and felsic schists with no clastic metasedimentary rocks, suggesting a volcanically-dominated depositional environment for the Londozi barite deposit. Abundant pillow basalts in the river section (Fig.s 4.2b and 4.4) support subaqueous and non-explosive mafic volcanism in the Steynsdorp terrane, consistent with the submarine nature of the

Theespruit Formation inferred from occurrences elsewhere in the Barberton Greenstone Belt (Dziggel et al., 2006). Massive amphibolite layers in the two stratigraphic successions most likely represent sheet flows of basaltic lava, as these are also intimately associated with pillow lavas in modern ocean floor settings (Cas and Wright, 1988). Intense metamorphic recrystallization complicates the petrogenetic interpretation of strongly foliated mafic schists, but the absence of any primary volcano-sedimentary features suggests a similar effusive origin to the massive and pillowed amphibolites. Small initial compositional differences with non-foliated units might have controlled the development of foliation upon heating and deformation. Actinolite-rich zones within the mafic schists possibly represent areas of localized fluid flow during uplift and decompression, leading to the formation of retrograde hydrous mineral assemblages.

Chondrite-normalized REE patterns for these mafic lithologies (Fig. 4.5a) do not show light rare earth element depletions usually characteristic for modern mid-ocean ridge basalts, and this is consistent with the lack of sheeted dykes in the stratigraphic succession. Instead, these flat REE patterns are suggestive of intra-plate submarine mafic volcanism and very similar to the trace element compositions reported for Phanerozoic and Archean oceanic plateaux (Kerr et al., 2000; Arndt et al., 2001), with the lack of negative Eu-anomalies supporting relatively unevolved magmas without plagioclase crystallization. Moreover, the thick sequence of subaqueously-erupted mafic lavas, the lack of clastic sediments in the study area and the presence of komatiites reported lower in the stratigraphy by Barton (1982) are all characteristic for oceanic plateau settings (Kröner et al., 1996; Kerr et al., 2000). Slightly light REE-enriched patterns were observed for some of the mafic schists, suggesting contamination from LREE-enriched crustal components (Arndt et al., 2001). The basement of the plateau therefore possibly included accreted TTGs and co-magmatic felsic schists from older tectono-magmatic cycles (Lowe and Byerly, 2007).

4.6.1.2 Chert and silicified pillows

Massive cherts and silicified pillow lavas provide evidence for silicification processes during deposition of the volcanic sequence, most likely related to hydrothermal activity. Contacts between silicified and non-silicified lavas are sharp and suggestive of episodic silicification events, supporting periodic discharge of hydrothermal fluids into the seawater. Diffusive hydrothermal

venting of siliceous fluids on the ocean floor also explains the presence of two massive green chert beds above and below non-silicified pillow lavas in the river section (Fig. 4.4). Barite precipitation was probably closely linked to this hydrothermal activity. Siliceous alteration zones in basalts from the Theespruit Formation in the Tjakastad area several kilometers to the northwest showed strong enrichments in Ba, suggesting venting of barium- and silica-rich fluids in low-temperature hydrothermal systems during early mafic submarine volcanism (Hofmann and Harris, 2008). Furthermore, the low solubility product of barite requires separate sources for sulfate and barium (Huston and Logan, 2004). Supply of barium by hydrothermal fluids is, therefore, consistent with the inferred seawater-origin for sulfate in the Londozi barite deposit (see Chapter 2). In addition, a semi-closed system was inferred for barite precipitation based on the reservoir-effect observed in barite sulfur isotopic compositions (Chapter 2), which requires the development of local topographic relief. We hypothesize that continuous eruption of mafic lavas as well as uplift by active plutonism resulted in an emerging oceanic plateau, and that the development of local relief from volcanic eruptions and shallowing water depths facilitated the formation of local and isolated shallow marine basins. Hydrothermal circulation was probably driven by the heat from cooling of extrusive lava sequences (Hofmann and Harris, 2008) and delivered barium- and silica-rich fluids to the ocean floor via diffusive venting, possibly aided by local fissures in the crust (e.g. the baritic vein observed in the river section). Subsequently, chert and barite precipitated upon reaction with the silica- and sulfate-bearing seawater. The presence of Ba-feldspar and armenite in silicified zones below the barite horizons might also be related to extensive fluid interaction with barium-rich hydrothermal fluids, but further work on the geochemistry of these alteration zones is required to investigate the possibility of later metasomatic remobilization of barium (see Chapter 5).

4.6.1.3 Felsic volcanics

Felsic schists were observed in both stratigraphic sections above the barite horizon. Dense, black and bedding-parallel fiamme textures were observed in these lithologies (Fig. 4.2c) and resemble welding textures seen in modern pyroclastic flow and fall deposits (Cas and Wright, 1988). Associated pinch-and-swell structures suggest high-temperature plastic deformation of glassy fragments instead of low-temperature diagenetic compaction or autobrecciation (Bull and McPhie, 2007), supporting the interpretation by Barton (1982) that

these felsic schists represent welded rhyolitic ash-fall and ash-flow tuffs. Deposition of felsic pyroclastic material suggests the emergence of shallow submarine or even subaerial volcanism, because the explosive eruptions require water depths of less than 500-1000 m for the vapor pressure of exsolving volatiles to exceed the hydrostatic pressure (Cas, 1992). This is consistent with the shallower environment inferred for barite deposition in Section 4.6.3. In addition, the upward change towards felsic volcanism requires the formation of more evolved magmas in an oceanic plateau setting. Explosive eruptions of felsic magmas at the Cretaceous Kerguelen Plateau were linked to the final stages of voluminous basaltic magmatism, with fractional crystallization and wall-rock assimilation leading to the formation of highly evolved silicic magmas (Frey et al., 2000). Similar processes might have operated during early volcanism in the Steynsdorp area, as strongly light REE-enriched patterns with significant negative Eu-anomalies (Fig. 4.5b) are consistent with fractional crystallization of plagioclase. Rare earth element compositions of zircons from the felsic volcanics provide similar evidence for highly evolved magmas, showing negative Eu-anomalies and LREE enriched patterns (Fig. 4.9a). The lack of correlation between light REE enrichment and total Th + U concentrations (Fig. 4.9b) suggests that post-magmatic incorporation of LREE in radiation-damaged crystal lattices was not significant, and elimination of zircon analyses with anomalously high P or Th excludes LREE enrichment from ablated apatite or monazite inclusions (Whitehouse and Kamber, 2002). Instead, the positive co-variation between Ce and Hf contents, where the latter reflects progressive magma evolution (Claiborne et al., 2006), suggests that zircon LREE enrichment was coupled to an evolved melt after crystallization of hornblende (Whitehouse and Kamber, 2002). Higher Ce and Hf concentrations in zircons from the uppermost felsic volcanics (LON-10-09) suggest that the felsic succession reflects progressive magmatic evolution with increasing stratigraphic height.

Chondrite-normalized REE-patterns of felsic schists in the Londozi area are strikingly similar to REE profiles of the Steynsdorp TTGs, with Eu-anomalies (Eu/Eu*) between 0.72 and 0.83, strong LREE enrichments with $(La/Gd)_N$ = 4-8, and flat HREE patterns indicating relatively shallow melting depths with little residual garnet (Anhaeusser and Robb, 1983; Diener, 2004; Clemens et al., 2006). This provides evidence that the felsic volcanism in the Londozi area was part of the same magmatic event that generated the Steynsdorp TTGs, which was explained by shallow melting of mafic amphibolites at the base of an oceanic

plateau or tectonic stack of oceanic crust, and not by subduction-related processes (Moyen et al., 2007).

4.6.2 Geochronology

4.6.2.1 Age of the deposit

Geochronological data from zircons in the felsic schists overlying the main barite horizon revealed well-defined $^{207}Pb/^{206}Pb$ age populations with identical weighted averages of 3521 Ma (Fig.s 4.7 and 4.8), which we interpret at the age of crystallization of the felsic volcanics. An igneous age is consistent with Th/U ratios higher than 0.5 for most of the zircons (Williams et al., 1996; Rubatto, 2002; Hoskin and Schaltegger, 2003), and fits with the oscillatory and lengthwise zoning observed in euhedral crystals that is typical for zircons of magmatic origin (Corfu et al., 2003). Furthermore, the observed consistency between weighted average $^{207}Pb/^{206}Pb$ ages and upper intercept ages in the Tera-Wasserburg plots (Fig.s 4.7a and 4.8a) supports our assumption of recent lead loss and implies that the 3521 Ma age represents a robust age estimate for the felsic volcaniclastics.

Previous constraints on the age of the Theespruit Formation in the Steynsdorp area were based on single zircon dating of felsic tuffs located 5 km north of the Londozi barite deposit, which yielded slightly older ages between 3544 and 3548 Ma (Kröner et al., 1996). However, the origin of these felsic units has been a matter of debate. De Ronde and De Wit (1994) interpreted the dated rocks as tectonically-emplaced wedges of older tonalitic crust, whereas Kröner et al. (1996) suggested that the felsic schists were syn-volcanic and related to the magmatic event that generated 3538 Ma tonalitic gneisses in the Tjakastad area several kilometers northwest of the Steynsdorp dome (Armstrong et al., 1990; Kamo and Davis, 1994). More recently, Van Kranendonk et al. (2009) demonstrated that the Tjakastad gneisses also represent felsic volcaniclastic rocks and timed the eruption of these units between 3522 and 3539 Ma. Similar ages of 3508 to 3531 Ma were reported by Armstrong et al. (1990) in sedimentary diamictites from the same area, which were re-interpreted by Van Kranendonk et al. (2009) as felsic agglomerates supporting the existence of felsic volcanism in the Theespruit Formation between approximately 3520 and 3540 Ma. Our zircon U-Pb crystallization age of 3521 Ma for felsic tuffs in the Londozi area strongly agrees with this interpretation. Moreover, this age obtained for the felsic

Theespruit lithologies implies a coherent stratigraphic succession towards the overlying Komati Formation with a minimum age of 3450 Ma (Kröner et al., 1996) and obliterates the requirement of tectonic stacking of the latter, which was used by Armstrong et al. (1990), De Ronde and De Wit (1994)and Dziggel et al. (2006) to argue for a subduction-related tectonic setting of the Theespruit Formation.

Based on our zircon U-Pb ages, we conclude that the Londozi barite deposit was deposited before 3521 Ma. No maximum age could be determined in this study due to the absence of zircons in the mafic volcanics below the barite, but the minimum age for the barite is more than 30 million years older than the 3490 Ma model lead age published for barite in the Dresser Formation in the Pilbara craton, Australia (Thorpe et al., 1992), and implies that the Londozi deposit represents the oldest occurrence of large-scale stratiform sulfate on Earth known to date.

4.6.2.2 Inherited zircon

The presence of 3570 to 3610 Ma zircons in the Londozi volcaniclastics suggests that old crustal material was present in the magma source region, consistent with the crustal contamination inferred from the light REE-enriched compositions of underlying mafic schists (Section 4.6.1.1). Based on Nd isotope systematics, inclusion of a minor crustal component was also inferred for the Theespruit volcaniclastics, the Steynsdorp TTGs and the younger Vlakplaats granodiorite by Kröner et al. (1996). The latter granodiorite also contained two ~3.7 Ga inherited zircons, confirming the presence of older crustal material in the source region of the Steynsdorp felsics (Kröner et al., 1996). As outlined above, we hypothesize that this material represented felsic rocks from older tectono-magmatic cycles (Lowe and Byerly, 2007), possibly similar to the 3.55 to 3.64 Ga tonalitic and trondhjemitic gneisses in the Ancient Gneiss Complex of Swaziland (Barton et al., 1983; Compston and Kröner, 1988).

4.6.2.3 Metamorphic zircon

Significantly younger ages were obtained from three concordant and two discordant zircons dated at 3429 ± 32 Ma to 3451 ± 36 Ma (Table 4.1), which is similar to the 3453 ± 6 Ma population of zircons within the felsic agglomerate from Theespruit Formation in the Tjakastad area reported by Armstrong et al.

(1990). Whereas these authors used this result to argue for a younger age of the Theespruit Formation, Van Kranendonk et al. (2009) suggested that these younger ages reflect metamorphic zircon growth related to contact metamorphism during emplacement of the 3445 Ma Stolzburg and Theespruit plutons. Although our Th/U ratios are not indicative of zircon growth during metamorphism, the relatively low abundance of the younger zircons (8%) and the well-defined older age in morphologically typically igneous zircons leads us to speculate that these grains reflect similar thermal resetting in the Londozi area around 3430-3450 Ma. However, the absence of TTG plutons younger than 3500 Ma in this region suggests that heating was associated with the early accretionary tectonic event in the Barberton Greenstone Belt between 3445 and 3416 Ma (De Ronde and De Wit, 1994).

4.6.3 Metamorphism

4.6.3.1 Peak metamorphic conditions

Results from conventional thermobarometry suggest that mafic amphibolites in the Londozi area experienced temperatures of 660 to 760°C and pressures between 10 and 12.5 kbar, based on the mineral assemblage of garnet, hornblende, plagioclase, biotite, muscovite and quartz observed in mafic pillows of LON-11-18. We interpret these conditions to reflect the peak of metamorphism for the following reasons. First, almandine garnet compositions are relatively Mg-rich but Mn and Ca-poor (Table 1.3), which is very similar to the rims of prograde zoned garnet in sample LON-11-15 (not used for thermobarometric calculations) and suggests that garnet of LON-11-18 reflects peak metamorphic conditions. In addition, the presence of small inclusions of hornblende and biotite in the garnet (Fig. 4.10b) as well as in the sample matrix indicates the coexistence of these minerals at the peak of metamorphism. Peak metamorphic hornblende concurring with plagioclase or garnet in mafic amphibolites is predominantly tschermakite (Supplementary Table S4-3), whereas the presence of euhedral actinolite provides evidence for secondary amphibole growth during later retrograde metamorphism (Spear, 1993a). Furthermore, in all samples evaluated for thermobarometry, tschermakite-hornblende is texturally equilibrated with andesine (Supplementary Table S4-3). Compositionally similar sodic plagioclase was also found directly adjacent to garnet in LON-11-18 and, therefore, most probably reflects the

composition of plagioclase that was equilibrated with garnet during peak metamorphism. In contrast, the more calcic bytownite found in the matrix of LON-11-18 may represent a primary igneous phase. Most important, equilibrium assemblage modeling in Theriak-Domino demonstrates that the mineral assemblage outlined above is stable at temperatures of 550-690°C and pressures of 7.5-12.5 kbar (Fig. 4.11b), which overlaps with the peak metamorphic conditions derived from conventional thermobarometers (Fig. 4.11a). Slightly lower maximum temperatures obtained from Theriak-Domino based on the hornblende stability field may be related to uncertainties in compositional models for amphiboles, or small errors related to the absence of spessartine garnet in the applied database (Berman, 1988).

Based on what is outlined above, we conclude that temperatures of 650-700°C and pressures of 10-12 kbar represent the best estimate for the peak metamorphic conditions experienced by the mafic Theespruit amphibolites in the Londozi area. These conditions are consistent with the observation of anthophyllite in the lowermost parts of the river section, because this mineral has a restricted stability field in metamorphosed ultramafic rocks between approximately 600 and 800°C at pressures below 12 kbar (Spear, 1993b). In addition, we interpreted hornblende- rich textures in the felsic volcaniclastics to reflect restites related to local partial melting, which agrees with relatively high temperatures of ~700°C.

4.6.3.2 Retrograde metamorphic conditions

Evidence for retrograde metamorphism was derived from the presence of chlorite-rims on peak metamorphic biotite, fractured garnet porphyroblasts with fracture fills of chlorite and quartz, as well as magnesium-rich actinolite coexisting with tschermakite-hornblende. These observations suggest chlorite and actinolite growth post-dating the peak of metamorphism, related to hydration of the high-grade assemblages. Temperatures calculated from the Al-in-chlorite thermometer of Cathelineau and Nieva (1985) provide an estimate of the retrograde conditions, suggesting chlorite growth between 219 and 310°C (Supplementary Table S4-4).

4.6.3.3 Comparison with previous work and tectonic context

Our results are very similar to the metamorphic conditions determined for Theespruit supracrustals elsewhere in the Barberton Greenstone Belt. For the Tjakastad area, Dziggel et al. (2002) reported peak temperatures and pressures of

650-700°C and 8-11 kbar for mafic amphibolites and clastic metasediments in greenstone remnants within the Stolzburg pluton, whereas slightly lower pressure-temperature estimates (7.4 ± 1.0 kbar, 560 ± 20°C) were derived for the Tjakastad schist belt east of the Stolzburg pluton (Diener et al., 2005) and the Stolzburg schist belt north of the pluton (5.5 ± 0.9 to 6.3 ± 1.5 kbar, 491 ± 40°) (Kisters et al., 2003). Based on U-Pb data from metamorphic titanite and zircon, these peak metamorphic conditions were correlated to the main compressional event in the Barberton Greenstone Belt (D_2) between 3230 and 3225 Ma and subsequent orogenic collapse (De Ronde and De Wit, 1994; Dziggel et al., 2002; Kisters et al., 2003; Diener et al., 2005). More recently, mafic amphibolites west of the Steynsdorp dome were studied by Lana et al. (2010) who reported peak metamorphic conditions of 10-13 kbar and 640-660°C, which is identical to our results for equivalent lithological units in the Londozi area. Similar to the Theespruit amphibolites in the Tjakastad area, metamorphism was linked to burial of the supracrustals to depths of 35-40 km during the 3230 Ma tectonic collision. Although our geochronological data do not provide evidence for thermal resetting at 3230 Ma in the eastern Steynsdorp area (similar to results from Kröner et al., 1996), the strong similarities in metamorphic textures and pressure-temperature estimates with previously studied Theespruit volcanics suggests that our peak metamorphic assemblages reflect the same compressional event. However, the strong foliation defined by peak metamorphic hornblende, biotite and plagioclase in the mafic schists indicates that the fabric-forming deformation event occurred simultaneously with or after the peak of metamorphism.

4.6.4 Implications for the origin and preservation of Paleoarchean barite deposits

This work demonstrates that the Londozi barite is at least 30 million years older than the chert-barite unit in the Dresser Formation, and thus represents the oldest occurrence of stratiform sulfate on Earth. However, geological, geochemical and geochronological data suggest a remarkably similar environment of deposition for the early Paleoarchean barites in Western Australia and Swaziland. An intra-plate oceanic plateau with older crustal material present in the magma source region (cf. Section 4.6.1) was also suggested for the Dresser barite, based on the thick succession of subaqueous basalts and komatiites with nearly flat REE-patterns (Van Kranendonk et al., 2002; Van Kranendonk and Pirajno, 2004), as

well as LREE enrichments and inherited zircons older than 3700 Ma in overlying felsic volcanic horizons that support crustal contamination (Green et al., 2000; Bolhar et al., 2002).

Recently, the association of barite with felsic volcaniclastic units was used by Philippot et al. (2012) to argue for a genetic relationship between the release of sulfur dioxide during large subaerial felsic eruptions and precipitation of barite from this sulfur source. Our field observations demonstrate that barite is overlain by felsic pyroclastic flow deposits, but the lack of these lithologies below the sulfate deposit suggests that felsic volcanism was insignificant before barite deposition. The presence of barite at the base of the felsic volcanics is also inconsistent with the simultaneous eruption of sulfur dioxide and felsic material as source for the two lithologies, because we consider it highly unlikely that the production of sulfate from volcanic SO_2 in atmospheric photolysis (Farquhar et al., 2000) and subsequent rainout into the oceans was faster than the deposition of material from fast-moving pyroclastic flows. Second, no barite was reported from similar felsic Theespruit volcanics elsewhere in the Barberton Greenstone Belt (e.g. Van Kranendonk et al., 2009), suggesting that favorable conditions for barite precipitation existed only very locally. This is more consistent with local environmental controls on sulfate deposition rather than large-scale controls from volcanic eruptions (Philippot et al., 2012). Third, Chapter 2 showed that the barite reflects a residual marine reservoir after microbial reduction of sulfate, and not directly the photochemically-produced sulfate. We conclude that the transition from mafic to felsic volcanism is more likely to reflect shifting tectonic conditions that resulted in an environment temporally and locally favorable for barite precipitation.

Finally, our thermobarometric calculations support high-pressure and moderate-temperature metamorphism for the Londozi area, which is considerably higher than the sub-greenschist conditions inferred for the Dresser Formation (Buick and Dunlop, 1990). As such, these results provide evidence for the preservation of syngenetic barite deposits at metamorphic temperatures up to 700°C and burial to 30-40 km crustal depth. The preservation of a similar temporal trend in sulfate isotopic compositions from both the low metamorphic grade Dresser barite and significantly higher grade Londozi barite supports previous assumptions that the sulfur isotope record from Paleoarchean barite deposits is robust against metamorphism (Chapter 2). This result is of particular interest for the future exploration of barite and other sulfate-deposits on Mars

(Squyres et al., 2004), where conditions associated with shock metamorphism may be difficult to constrain.

4.7 CONCLUSIONS

This work represents the first integrated study of the petrology, geochemistry, geochronology and thermobarometry of Theespruit supracrustals in the oldest part of the Barberton Greenstone Belt, and provides new insights into the geological setting where the oldest-known sulfate deposit on Earth was formed. The lowermost amphibolites in the eastern Steynsdorp area record submarine volcanism on an oceanic plateau before 3521 Ma, resulting in the deposition of a sediment-free succession of mafic pillowed and massive lavas with flat REE patterns. Magmas were derived from a source that was slightly contaminated with older felsic crust. The basement of the plateau therefore probably included accreted TTGs and co-magmatic felsics from even older tectono-magmatic cycles. Continuous eruption of mafic lavas as well as uplift by active plutonism resulted in an emerging oceanic plateau, supported by the transition towards shallow subaqueous or subaerial felsic volcanism. Development of local topographic relief as a result of volcanic eruptions as well as shallowing water depths facilitated the formation of local and isolated shallow marine basins. Hydrothermal circulation driven by the heat from the cooling of extrusive volcanics or older TTG intrusion delivered silica- and barium-rich fluids to the ocean floor, from which chert and barite precipitated locally upon reaction with silica- and sulfate-bearing seawater. Felsic magmas erupted explosively at 3521 Ma, covering the barite horizon with a thick succession of rhyolitic ash-fall and ash-flow deposits. Similar REE patterns for the felsic schists and Steynsdorp TTGs indicate that the former represent the surface-equivalent of the deep-level TTG magmatism. Negative Eu-anomalies demonstrate fractional crystallization of plagioclase and relatively evolved magmas. The presence of 3570 to 3610 Ma inherited zircons in these felsic schists confirms the presence of older crust-like material in the source region, whereas the 3521 Ma age obtained for the felsic Theespruit lithologies implies a coherent stratigraphic succession towards the overlying 3476 Ma Komati Formation (Kamo and Davis, 1994) and obliterates the requirement of tectonic stacking of the latter, which was used to argue for a subduction-related tectonic setting for the Theespruit volcanics (Armstrong et al., 1990; De Ronde and De Wit, 1994; Dziggel et al., 2006).

The Steynsdorp oceanic plateau with the Theespruit supracrustals probably represented the proto-continent along which the younger Stolzburg domain was formed (Moyen et al., 2007). The formation of the 3445 Ma Stolzburg and Theespruit TTG plutons coincided with the first accretionary event in the Barberton Greenstone Belt from 3445 to 3416 Ma (De Ronde and De Wit, 1994), which was recorded by a small number of ~3430-3450 Ma zircons in the Londozi area. However, metamorphic minerals associated with this thermal event were fully overprinted by the metamorphism that accompanied the burial of the mafic and felsic volcanics to 30-40 km depth at 3230-3225 Ma (De Ronde and De Wit, 1994; Dziggel et al., 2002), with peak metamorphic assemblages in mafic pillow lavas recording pressures of 10-12 kbar and temperatures between 650 and 700°C. After the 3230 Ma tectonic collision, extensional orogenic collapse and folding resulted in exhumation of the Theespruit Formation and Steynsdorp TTG (Kisters et al., 2003; Lana et al., 2010), with extensive chlorite and actinolite formation during retrograde metamorphism.

Our work demonstrates that the Londozi barite represents the oldest known occurrence of stratiform sulfate preserved on Earth and supports deposition in an environment very similar to the setting inferred for the younger Dresser barite, but with significantly higher metamorphic temperatures of 700°C and burial to 30-40 km crustal depth during crustal shortening.

Acknowledgements

Simon Maphanga and the Geological Survey and Mines Department of Swaziland are gratefully acknowledged for their help with sample logistics and providing access to geological maps and mining reports. We thank Willem van der Bilt for extensive fieldwork assistance. Mario Hendriks, Roel van Elzas and Wynanda Koot are thanked for zircon separation and sample preparation, and we thank Otto Stiekema for the preparation of thin sections. We acknowledge Tilly Bouten for assistance with electron microprobe analyses and Helen de Waard for sample digestion and support during laser-ablation ICP-MS work. The manuscript benefitted from several informal discussions with Kalijn Peters. This research was funded by a grant from the User Support Programme Space Research and the Netherlands Organization for Scientific Research (NWO).

References

Anhaeusser, C.R., 1973. The Evolution of the Early Precambrian Crust of Southern Africa. Philosophical Transactions of the Royal Society of London. Series A, Mathematical and Physical Sciences 273, 359-388.

Anhaeusser, C.R., Robb, L.J., 1983. Chemical analyses of granitoid rocks from the Barberton Mountain Land. Geological Society of South Africa Special Publications 9, 189-223.

Armstrong, R.A., Compston, W., de Wit, M.J., Williams, I.S., 1990. The stratigraphy of the 3.5-3.2 Ga Barberton Greenstone Belt revisited: A single zircon ion microprobe study. Earth Planet. Sci. Lett. 101, 90-106.

Arndt, N., Bruzak, G., Reischmann, T., 2001. The oldest continental and oceanic plateaus: Geochemistry of basalts and komatiites of the Pilbara Craton, Australia. Geological Society of America Special Papers 352, 359-387.

Barton, C.M., 1982. Geology and mineral resources of Northwest Swaziland (Barberton Greenstone Belt). Bulletin of the Swaziland Geological Survey and Mines Department 10.

Barton, J.M., Robb, L.J., Anhaeusser, C.R., Van Nierop, D.A., 1983. Geochronologic and Sr-isotope studies of certain units of the Barberton granite-greenstone terrane, South Africa. Spec. Publ. Geol. Soc. S. Afr. 9, 73-79.

Berman, R.G., 1988. Internally-Consistent Thermodynamic Data for Minerals in the System Na2O-K2O-CaO-MgO-FeO-Fe2O3-Al2O3-SiO2-TiO2-H2O-CO2. J. Petrol. 29, 445-522.

Bolhar, R., Woodhead, J.D., Hergt, J.M., 2002. Comment on: "Growth and recycling of early Archaean continental crust: geochemical evidence from the Coonterunah and Warrawoona groups, Pilbara Craton, Australia" by Green, M.G. et al. (Tectonophysics 322, 69-88). Tectonophysics 344, 289-292.

Buick, R., Dunlop, J.S.R., 1990. Evaporitic sediments of Early Archaean age from the Warrawoona Group, North Pole, Western Australia. Sedimentology 37, 247-277.

Bull, K.F., McPhie, J., 2007. Fiamme textures in volcanic successions: Flaming issues of definition and interpretation. J. Volcanol. Geotherm. Res. 164, 205-216.

Cas, R.A.F., 1992. Submarine volcanism; eruption styles, products, and relevance to understanding the host-rock successions to volcanic-hosted massive sulfide deposits. Econ. Geol. 87, 511-541.

Cas, R.A.F., Wright, J.V., 1988. Volcanic successions, modern and ancient. Unwin Hyman Ltd, London.

Cathelineau, M., Nieva, D., 1985. A chlorite solid solution geothermometer - The Los Azufres (Mexico) geothermal system. Contrib. Mineral. Petrol. 91, 235-244.

Claiborne, L.L., Miller, C.F., Walker, B.A., Wooden, J.L., Mazdab, F.K., Bea, F., 2006. Tracking magmatic processes through Zr/Hf ratios in rocks and Hf and Ti zoning in zircons: An example from the Spirit Mountain batholith, Nevada. Mineral. Mag. 70, 517-543.

Clemens, J.D., Yearron, L.M., Stevens, G., 2006. Barberton (South Africa) TTG magmas: Geochemical and experimental constraints on source-rock petrology, pressure of formation and tectonic setting. Precambrian Res. 151, 53-78.

Compston, W., Kröner, A., 1988. Multiple zircon growth within early Archaean tonalitic gneiss from the Ancient Gneiss Complex, Swaziland. Earth Planet. Sci. Lett. 87, 13-28.

Corfu, F., Hanchar, J.M., Hoskin, P.W.O., Kinny, P., 2003. Atlas of zircon textures, in: Hanchar, J.M., Hoskin, P.W.O. (Eds.), Zircon. Reviews in Mineralogy and Geochemistry 53. Mineralogical Society of America.

Dann, J.C., 2000. The 3.5 Ga Komati Formation, Barberton Greenstone Belt, South Africa, Part I: New maps and magmatic architecture. S. Afr. J. Geol. 103, 47-68.

De Capitani, C., Petrakakis, K., 2010. The computation of equilibrium assemblage diagrams with Theriak-Domino software. Am. Mineral. 95, 1006-1016.

De Ronde, C.E.J., De Wit, M.J., 1994. Tectonic history of the Barberton greenstone belt, South Africa: 490 million years of Archean crustal evolution. Tectonics 13, 983-1005.

Diener, J.F.A., 2004. The tectono-metamorphic evolution of the Theespruit Formation in the Tjakastad schist belt and surrounding areas of the Barberton greenstone belt, South Africa, MSc thesis (unpublished). Stellenbosch University.

Diener, J.F.A., Stevens, G., Kisters, A.F.M., Poujol, M., 2005. Metamorphism and exhumation of the basal parts of the Barberton greenstone belt, South Africa: Constraining the rates of Mesoarchaean tectonism. Precambrian Res. 143, 87-112.

Droop, G.T.R., 1987. A general equation for estimating Fe^{3+} concentrations in ferromagnesian sillicates and oxides from microprobe analyses, using stoichiometric criteria. Mineral. Mag. 51, 431-435.

Dziggel, A., Stevens, G., Poujol, M., Anhaeusser, C.R., Armstrong, R.A., 2002. Metamorphism of the granite-greenstone terrane south of the Barberton greenstone belt, South Africa: an insight into the tectono-thermal evolution of the 'lower' portions of the Onverwacht Group. Precambrian Res. 114, 221-247.

Dziggel, A., Stevens, G., Poujol, M., Armstrong, R.A., 2006. Contrasting source components of clastic metasedimentary rocks in the lowermost formations of the

Barberton greenstone belt. Geol. Soc. Am. Spec. Pap. 405, 157-172.
Farquhar, J., Bao, H., Thiemens, M., 2000. Atmospheric Influence of Earth's Earliest Sulfur Cycle. Science 289, 756-758.
Frey, F.A., Coffin, M.F., Wallace, P.J., Weis, D., Zhao, X., Wise Jr, S.W., WÃ¤hnert, V., Teagle, D.A.H., Saccocia, P.J., Reusch, D.N., Pringle, M.S., Nicolaysen, K.E., Neal, C.R., Möller, R.D., Moore, C.L., Mahoney, J.J., Keszthelyi, L., Inokuchi, H., Duncan, R.A., Delius, H., Damuth, J.E., Damasceno, D., Coxall, H.K., Borre, M.K., Boehm, F., Barling, J., Arndt, N.T., Antretter, M., 2000. Origin and evolution of a submarine large igneous province: the Kerguelen Plateau and Broken Ridge, southern Indian Ocean. Earth Planet. Sci. Lett. 176, 73-89.
Green, M.G., Sylvester, P.J., Buick, R., 2000. Growth and recycling of early Archaean continental crust: geochemical evidence from the Coonterunah and Warrawoona Groups, Pilbara Craton, Australia. Tectonophysics 322, 69-88.
Green, T.H., Hellman, P.L., 1982. Fe-Mg partitioning between coexisting garnet and phengite at high pressure, and comments on a garnet-phengite geothermometer. Lithos 15, 253-266.
Grotzinger, J.P., Kasting, J.F., 1993. New Constraints on Precambrian Ocean Composition. The Journal of Geology 101, 235-243.
Habicht, K.S., Gade, M., Thamdrup, B., Berg, P., Canfield, D.E., 2002. Calibration of sulfate levels in the Archean ocean. Science 298, 2372-2374.
Heinrichs, T.K., Reimer, T., 1977. A sedimentary barite deposit from the Archean Fig Tree Group of the Barberton Mountain Land (South Africa). Econ. Geol. 72, 1426-1441.
Hodges, K.V., Spear, F.S., 1982. Geothermometry, geobarometry and the Al_2SiO_5 triple point at Mt. Moosilauke, New Hampshire. Am. Mineral. 67, 1118-1134.
Hofmann, A., Harris, C., 2008. Silica alteration zones in the Barberton greenstone belt: A window into subseafloor processes 3.5-3.3 Ga ago. Chem. Geol. 257, 221-239.
Hoisch, T.D., 1990. Empirical calibration of six geobarometers for the mineral assemblage quartz + muscovite + biotite + plagioclase + garnet. Contrib. Mineral. Petrol. 104, 225-234.
Holland, T., Blundy, J., 1994. Non-ideal interactions in calcic amphiboles and their bearing on amphibole-plagioclase thermometry. Contrib. Mineral. Petrol. 116, 433-447.
Holland, T.J.B., Powell, R., 2011. An improved and extended internally consistent thermodynamic dataset for phases of petrological interest, involving a new equation of state for solids. J. Metamorph. Geol. 29, 333-383.
Hoskin, P.W.O., Schaltegger, U., 2003. The Composition of Zircon and Igneous and Metamorphic Petrogenesis, in: Hanchar, J.M., Hoskin, P.W.O. (Eds.), Zircon. Reviews in Mineralogy and Geochemistry 53. Mineralogical Society of America.
Hunter, D.R., Jones, D.H., Urie, J.G., 1979. Swaziland 1:50.000 series sheet 2631AA, in: Wilson, A.C. (Ed.). Directorate of Overseas Surveys and the Geological Survey and Mines Department of Swaziland, Mbabane.
Huston, D.L., Logan, G.A., 2004. Barite, BIFs and bugs: evidence for the evolution of the Earth's early hydrosphere. Earth Planet. Sci. Lett. 220, 41-55.
Jewell, P.W., 2000. Bedded barite in the geologic record, Marine Authigenesis:

From Global to Microbial. SEPM (Society for Sedimentary Geology), pp. 147-161.

Kamo, S.L., Davis, D.W., 1994. Reassessment of Archean crustal development in the Barberton Mountain Land, South Africa, based on U-Pb dating. Tectonics 13, 167-192.

Kerr, A.C., White, R.V., Saunders, A.D., 2000. LIP Reading: Recognizing Oceanic Plateaux in the Geological Record. J. Petrol. 41, 1041-1056.

Kisters, A.F.M., Anhaeusser, C.R., 1995. The structural significance of the Steynsdorp pluton and anticline within the tectono-magmatic framework of the Barberton Mountain Land. S. Afr. J. Geol. 98, 43-51.

Kisters, A.F.M., Stevens, G., Dziggel, A., Armstrong, R.A., 2003. Extensional detachment faulting and core-complex formation in the southern Barberton granite-greenstone terrain, South Africa: evidence for a 3.2 Ga orogenic collapse. Precambrian Res. 127, 355-378.

Kohn, M.J., Spear, F.S., 1990. Two new geobarometers for garnet amphibolites, with applications to southeastern Vermont. Am. Mineral. 75, 89-96.

Kröner, A., Hegner, E., Wendt, J.I., Byerly, G.R., 1996. The oldest part of the Barberton granitoid-greenstone terrain, South Africa: evidence for crust formation between 3.5 and 3.7 Ga. Precambrian Res. 78, 105-124.

Lana, C., Kisters, A.F.M., Stevens, G., 2010. Exhumation of Mesoarchean TTG gneisses from the middle crust: Insights from the Steynsdorp core complex, Barberton granitoid-greenstone terrain, South Africa. Geol. Soc. Am. Bull. 122, 183-197.

Lowe, D.R., Byerly, G.R., 2007. Chapter 5.3 An Overview of the Geology of the Barberton Greenstone Belt and Vicinity: Implications for Early Crustal Development, in: Kranendonk, M.J.v., Smithies, R.H., Vickie, C.B. (Eds.), Earth's Oldest Rocks. Developments in Precambrian Geology. Elsevier, pp. 481-526.

Ludwig, K.R., 2008. User's Manual for Isoplot 3.70. Berkeley Geochronology Center Special Publication 4.

Mank, A.J.G., Mason, P.R.D., 1999. A critical assessment of laser ablation ICP-MS as an analytical tool for depth analysis in silica-based glass samples. J. Anal. At. Spectrom. 14, 1143-1153.

McDonough, W.F., Sun, S.S., 1995. The composition of the Earth. Chem. Geol. 120, 223-253.

Moyen, J.-F.o., Stevens, G., Kisters, A.F.M., Belcher, R.W., 2007. Chapter 5.6 TTG Plutons of the Barberton Granitoid-Greenstone Terrain, South Africa, in: Kranendonk, M.J.v., Smithies, R.H., Vickie, C.B. (Eds.), Earth's Oldest Rocks. Developments in Precambrian Geology. Elsevier, pp. 607-667.

Nijman, W., de Bruijne, K.H., Valkering, M.E., 1999. Growth fault control of Early Archaean cherts, barite mounds and chert-barite veins, North Pole Dome, Eastern Pilbara, Western Australia. Precambrian Res. 95, 247-274.

Pearce, N.J.G., Perkins, W.T., Westgate, J.A., Gorton, M.P., Jackson, S.E., Neal, C.R., Chenery, S.P., 1997. A Compilation of New and Published Major and Trace Element Data for NIST SRM 610 and NIST SRM 612 Glass Reference Materials. Geostand. Newslett. 21, 115-144.

Philippot, P., Van Zuilen, M., Lepot, K., Thomazo, C., Farquhar, J., Van Kranendonk, M.J., 2007. Early Archaean Microorganisms Preferred Elemental Sulfur, Not Sulfate. Science 317, 1534-1537.

Philippot, P., van Zuilen, M., Rollion-Bard, C., 2012. Variations in atmospheric sulphur chemistry on early Earth linked to volcanic activity. Nat. Geosci. 5, 668-674.

Reimer, T.O., 1980. Archean sedimentary baryte deposits of the Swaziland Supergroup (Barberton Mountain Land, South Africa). Precambrian Res. 12, 393-410.

Roerdink, D.L., Mason, P.R.D., Farquhar, J., Reimer, T., 2012. Multiple sulfur isotopes in Paleoarchean barites identify an important role for microbial sulfate reduction in the early marine environment. Earth Planet. Sci. Lett. 331-332, 177-186.

Rubatto, D., 2002. Zircon trace element geochemistry: partitioning with garnet and the link between U-Pb ages and metamorphism. Chem. Geol. 184, 123-138.

Shen, Y., Buick, R., Canfield, D.E., 2001. Isotopic evidence for microbial sulphate reduction in the early Archaean era. Nature 410, 77-81.

Shen, Y., Farquhar, J., Masterson, A., Kaufman, A.J., Buick, R., 2009. Evaluating the role of microbial sulfate reduction in the early Archean using quadruple isotope systematics. Earth Planet. Sci. Lett. 279, 383-391.

Spear, F.S., 1993a. Chapter 11 The metamorphism of mafic rocks, in: Ribbe, P.H. (Ed.), Metamorphic phase equilibria and Pressure-Temperature-Time paths. Mineralogical Society of America, Washington D.C.

Spear, F.S., 1993b. Chapter 13 Metamorphism of ultramafic and cordierite-anthophyllite rocks, in: Ribbe, P.H. (Ed.), Metamorphic phase equilibria and Pressure-Temperature-Time paths. Mineralogical Society of America, Washington D.C.

Squyres, S.W., Grotzinger, J.P., Arvidson, R.E., Bell, J.F., Calvin, W., Christensen, P.R., Clark, B.C., Crisp, J.A., Farrand, W.H., Herkenhoff, K.E., Johnson, J.R., Klingelhöfer, G., Knoll, A.H., McLennan, S.M., McSween, H.Y., Morris, R.V., Rice, J.W., Rieder, R., Soderblom, L.A., 2004. In Situ Evidence for an Ancient Aqueous Environment at Meridiani Planum, Mars. Science 306, 1709-1714.

Thorpe, R.I., Hickman, A.H., Davis, D.W., Mortensen, J.K., Trendall, A.F., 1992. U-Pb zircon geochronology of Archaean felsic units in the Marble Bar region, Pilbara Craton, Western Australia. Precambrian Res. 56, 169-189.

Ueno, Y., Ono, S., Rumble, D., Maruyama, S., 2008. Quadruple sulfur isotope analysis of ca. 3.5 Ga Dresser Formation: New evidence for microbial sulfate reduction in the early Archean. Geochim. Cosmochim. Acta 72, 5675-5691.

van Dijk, D., Houba, V.J.G., 2000. Homogeneity and stability of materials distributed within the wageningen evaluating programmes for analytical laboratories. Commun. Soil Sci. Plant Anal. 31, 1745-1756.

Van Kranendonk, M.J., 2006. Volcanic degassing, hydrothermal circulation and the flourishing of early life on Earth: A review of the evidence from c. 3490-3240 Ma rocks of the Pilbara Supergroup, Pilbara Craton, Western Australia. Earth-Science Reviews 74, 197-240.

Van Kranendonk, M.J., Hickman, A.H., Smithies, R.H., Nelson, D.R., Pike, G., 2002. Geology and Tectonic Evolution of the Archean North Pilbara Terrain, Pilbara Craton, Western Australia. Econ. Geol. 97, 695-732.

Van Kranendonk, M.J., Kröner, A., Hegner, E., Connelly, J., 2009. Age, lithology and structural evolution of

the c. 3.53 Ga Theespruit Formation in the Tjakastad area, southwestern Barberton Greenstone Belt, South Africa, with implications for Archean tectonics. Chem. Geol. 261, 115-139.

Van Kranendonk, M.J., Pirajno, F., 2004. Geochemistry of metabasalts and hydrothermal alteration zones associated with c. 3.45 Ga chert and barite deposits: implications for the geological setting of the Warrawoona Group, Pilbara Craton, Australia. Geochem. Explor. Environ. Anal. 4, 253-278.

Viljoen, M.J., Viljoen, R.P., 1969. An introduction to the geology of the Barberton granite-greenstone terrain. Geological Society of South Africa Special Publications 3, 419-432.

Viljoen, R.P., Saager, R., Viljoen, M.J., 1969. Metallogenesis and ore control in the Steynsdorp goldfield, Barberton mountain land, South Africa. Econ. Geol. 64, 778-797.

Whitehouse, M.J., Kamber, B.S., 2002. On the overabundance of light rare earth elements in terrestrial zircons and its implication for Earth's earliest magmatic differentiation. Earth Planet. Sci. Lett. 204, 333-346.

Wiedenbeck, M., Allé, P., Corfu, F., Griffin, W.L., Meier, M., Oberli, F., Quadt, A.V., Roddick, J.C., Spiegel, W., 1995. Three natural zircon standards for U-Th-Pb, Lu-Hf, trace element and REE analyses. Geostand. Newslett. 19, 1-23.

Williams, I.S., Buick, I.S., Cartwright, I., 1996. An extended episode of early Mesoproterozoic metamorphic fluid flow in the Reynolds Range, central Australia. J. Metamorph. Geol. 14, 29-47.

Malolotja Nature Reserve, Hhohho, Swaziland

Chapter 5

Geochemistry and mineralogy of alteration zones associated with the >3.52 Ga Londozi barite deposit in the Barberton Greenstone Belt, Swaziland: implications for the stability of barite during metasomatism

This chapter will be submitted to Chemical Geology with co-authors Paul R.D. Mason, Fraukje M. Brouwer, Noah Nhleko and Thomas Reimer.

ABSTRACT

Paleoarchean bedded barites represent the only occurrences of sulfate in the rock record prior to 2.4 Ga and are valuable prospects for early life studies. However, the stability and preservation of barite during high-grade metamorphism and metasomatism remains unknown. This study evaluates the geochemistry and mineralogy of the >3.52 Ga amphibolite facies Londozi barite deposit in the Theespruit Formation of the Lower Onverwacht Group, Barberton Greenstone Belt, Swaziland, to assess the impact of metasomatic alteration during and after barite deposition. Silica alteration of mafic to komatiitic volcanic precursors was observed as silicified pillow lavas and chert, whereas barite alteration was identified from green-colored schists with witherite-filled fractures immediately underlying the sulfate deposit. Silicification is associated with enrichment in Si, K, Ba versus depletion in major elements and transition metals, supporting low-temperature (100-150 °C) seafloor alteration in an oceanic plateau setting. On the other hand, the barite alteration zone showed distinct enrichment in Mg, S, Sr and transition metals Cr, Ni, Cu and Zn, which suggests formation by high-temperature (>300 °C) processes. Strong association of barium-rich silicates and retrograde actinolite in these alteration zones provides evidence for post-depositional barium mobility, whereas the high celsian-content of feldspar adjacent to barite supports barium mobilization from barite. The association of ferric iron (epidote, andradite) and carbonate minerals (witherite, calcite) with pyrite, barite and Ba-feldspar with 11% albite is consistent with reductive dissolution of barite during greenschist facies metamorphism. Reduced sulfur produced during metamorphic sulfate reduction may have formed a secondary sulfide population in addition to any primary pyrite, which could complicate the interpretation of pyrite sulfur isotope data.

5.1 INTRODUCTION

Paleoarchean bedded barites are unique mineral deposits that formed in the earliest marine environments and represent the only occurrences of sulfate in the rock record prior to 2.4 Ga (Huston and Logan, 2004). Stratiform beds have been reported from volcano-sedimentary successions in three different cratons, including the Pilbara craton of Western Australia, the Kaapvaal craton in South Africa and Swaziland, and the Dharwar craton in southern India (Jewell, 2000). The best documented occurrences of ancient barite are the 3.49 Ga Dresser barite in the Panorama Greenstone Belt of Western Australia (Barley et al., 1979; Buick and Dunlop, 1990), and the 3.26-3.23 Ga Barite Valley deposit in the Fig Tree Group of the Barberton Greenstone Belt in South Africa (Heinrichs and Reimer, 1977; Reimer, 1980). Low degrees of metamorphism qualified these deposits and associated pyrite as useful prospects for sulfur isotope studies on the early biosphere (Chapter 2 and Shen et al., 2001; Philippot et al., 2007; Ueno et al., 2008; Shen et al., 2009), because secondary alteration of pyrite geochemistry could be assumed minimal.

In contrast, amphibolite facies metamorphism and intense metasomatism (see Chapter 4) may complicate the interpretation of sulfide isotope data from the oldest sulfate deposit on Earth, the >3.52 Ga Londozi barite in the Theespruit Formation of the Lower Onverwacht Group, Barberton Greenstone Belt, Swaziland. In Chapter 4 we reported on the presence of silicified pillow lavas, massive green chert and altered mafic schists below the chert-barite horizons at Londozi, which suggests that extensive fluid-rock interactions occurred during and possibly after formation of the mafic volcanics and stratiform barite. Understanding the nature of these alteration zones is essential to obtain insights into high-temperature redox reactions during seafloor hydrothermal exhalation and to evaluate the possibility of fluid-assisted sulfur remobilization during metamorphism, which may be a widespread process to obscure primary sulfur isotope signatures in pyrite.

In this chapter, we report on the petrography, geochemistry and mineralogy of silica and barite alteration zones found in association with the Londozi barite deposit, in order to evaluate hydrothermal conditions during barite formation and post-depositional metasomatism. The preservation of an intact volcano-sedimentary succession with limited chemical variability in the mafic precursor rocks enables comparison of altered rock compositions with those from unaltered pillow basalts and lavas, and provides insights into geochemical variations with

stratigraphic depth. Results are used to assess the environment of barite deposition and determine whether sulfide may have been remobilized during metasomatic alteration at Londozi.

5.2 GEOLOGICAL BACKGROUND

The Londozi barite deposit is located in the southeastern part of the Barberton Greenstone Belt in western Swaziland, where foliated supracrustal rocks of the Sandspruit and Theespruit Formation surround the Steynsdorp tonalite-trondhjemite-granodiorite (TTG) dome (Kisters and Anhaeusser, 1995; Kröner et al., 1996; Lana et al., 2010). A detailed description of the deposit and its host lithologies is given in Chapter 4, of which a summary is given below.

Barite occurs within a bimodal volcanic succession with deformed pillow lavas and mafic schists in the footwall, and felsic volcanics in the hanging wall. Flat rare earth element patterns from unaltered mafic amphibolites were interpreted to reflect submarine volcanism in an oceanic plateau setting, with hydrothermal circulation driven by cooling lavas. Barite and chert were most likely deposited on topographic highs in local marine basins, where siliceous and barium-rich hydrothermal fluids mixed with silica and sulfate derived from seawater (consistent with sulfur isotope data in Chapter 2). U-Pb dating of zircon minerals from felsic volcanics overlying the barite yielded a crystallization age of 3521 Ma, reflecting the explosive eruption of felsic magmas that covered the deposit with a thick succession of pyroclastic rocks. This subaerial felsic volcanism probably represented the surface equivalent of deep-level magmatism around 3510 Ma, which resulted in the formation of the 3511-3502 Ma Steynsdorp TTGs (Kröner et al., 1996) that intruded into the Theespruit supracrustals. However, mineral assemblages associated with this contact metamorphism were overprinted by amphibolite facies metamorphism, that occurred in association with the main compressional event in the Barberton Greenstone Belt at 3230-3225 Ma (De Ronde and De Wit, 1994; Dziggel et al., 2002; Kisters et al., 2003; Diener et al., 2005). Deformation during or after the peak of metamorphism resulted in the formation of strongly foliated rocks with foliation defined by hornblende, plagioclase and biotite. Peak metamorphic mineral assemblages were replaced by chlorite and actinolite during subsequent retrograde metamorphism that accompanied exhumation of the volcanics from 30-40 km crustal depths.

5.3 FIELD OBSERVATIONS AND PETROGRAPHY

Previous work focused on two barite outcrops and associated stratigraphic successions in the Londozi area, referred to as the waterfall section (Chapter 4.3.2) and the river section (Chapter 4.3.3) of which detailed lithological descriptions are given in these chapters. Complementary field observations support at least two types of metasomatic alteration in these volcanic rocks. First, silicified pillow lavas and massive green chert interbedded with relatively unaltered mafic extrusives are found in the river section and suggestive of silicification processes. These rocks are referred to as the silica alteration zone in this paper. Second, altered mafic schists with witherite veins and barium-feldspar occurring below the barite horizon in the waterfall section hint at possible barium metasomatism, and are discussed as the barite alteration zone. A comprehensive description of the field relations and petrography of these altered rocks is given below.

5.3.1 Silica alteration zone

Silicified pillow lavas were observed at two stratigraphic levels in the river section (Fig. 5.1a), with gradual lower contacts and sharp contacts with overlying mafic volcanics (Fig. 5.1b). In addition, a massive green chert horizon was found between mafic amphibolites with sharp lithological contacts (Fig. 5.1c). The mineralogy of the silicified volcanics was dominated by recrystallized quartz, with minor amounts of garnet, hornblende, muscovite and chlorite in the pillow lavas and microscopic fragments of hyalophane and Ba-muscovite in the green chert (see Table 5.1 for mineral compositions). Similar to petrographic relations in unaltered mafic schists (Chapter 4), chlorite occurred as fracture infills in garnet and was found to replace biotite in the silicified pillow lavas. Foliation was not strongly developed in these lithologies due to the high abundance of quartz, but Ba-muscovite in the green chert showed a weak preferred orientation.

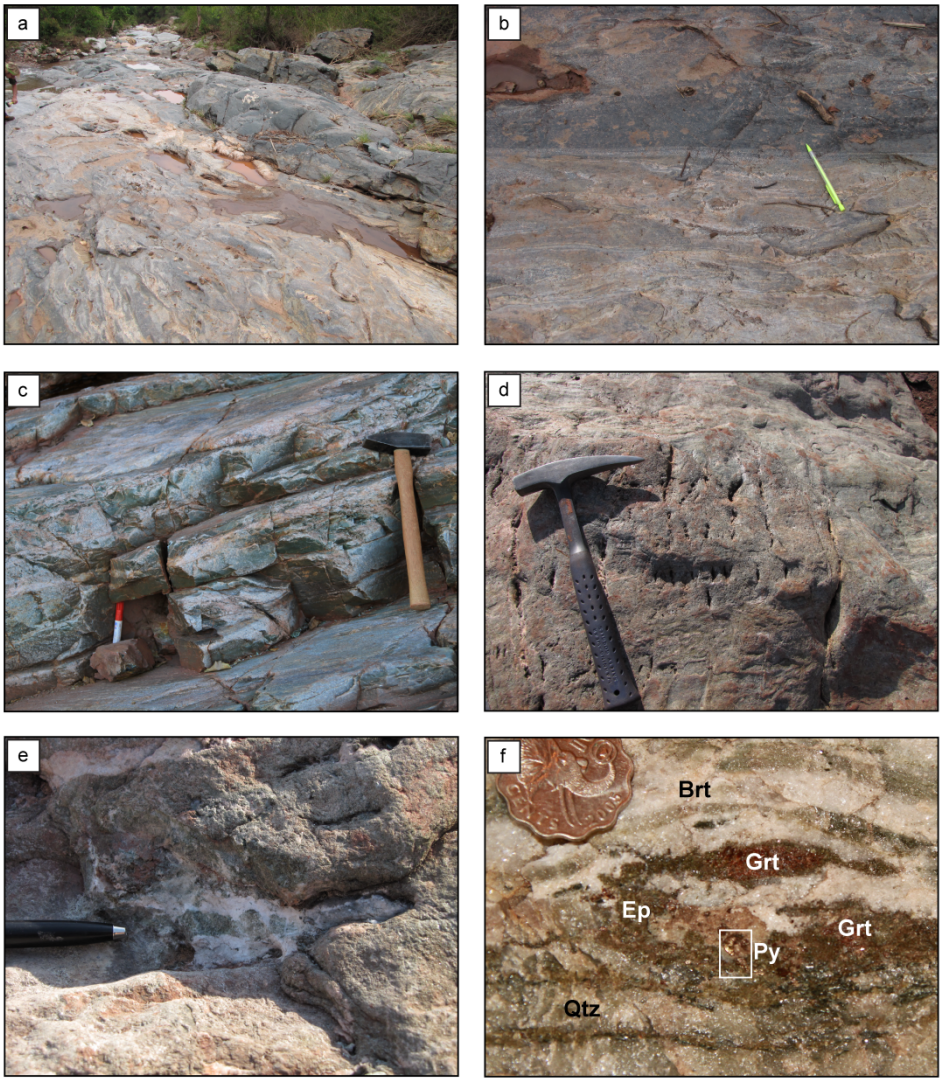

Figure 5.1 *Field photos of alteration zones in the Londozi river valley: (a) overview of white-colored silicified pillow lavas and overlying unaltered mafic pillows in the river section; (b) detail of the contact between the silicified and non-silicified pillow lavas; (c) massive green chert in the river section; (d) alteration textures in the barite alteration zone of the waterfall section; (e) witherite veins in the barite alteration zone; (f) hand specimen showing the mineralogical association between barite, quartz, pyrite, monomineralic epidote and garnet.*

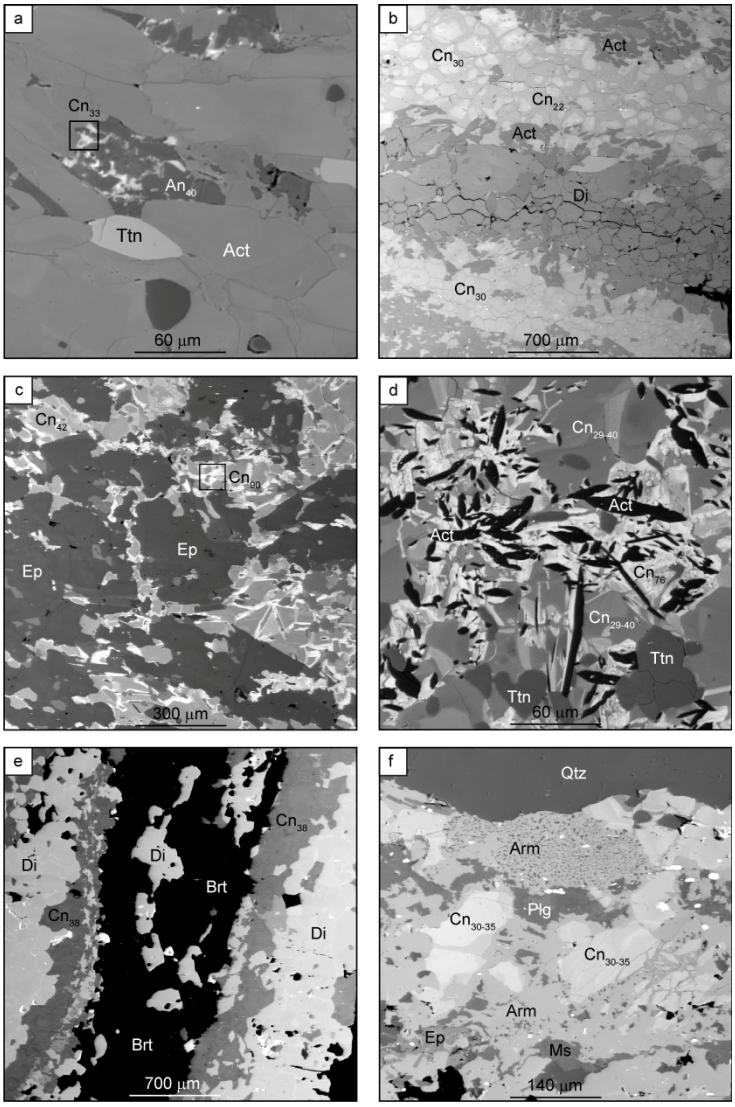

Figure 5.2 *Backscattered electron images (BSE) of Ba-rich feldspar: (a) patchy hyalophane associated with plagioclase in hornblende matrix of unaltered mafic volcanics, LON-11-04; (b) massive hyalophane with Ba-rich cores associated with actinolite in diopside matrix of altered volcanics, LON-11-05; (c) massive hyalophane with Ba-rich rims associated with epidote in altered volcanics, LON-11-07; (d) celsian associated with randomly oriented and texturally late actinolite in matrix of hyalophane and titanite in altered volcanics, LON-11-07; (e) inversed BSE image of small-scale barite vein with rims of hyalophane in diopside matrix, LON-11-07; (f) poikiloblastic armenite associated with hyalophane, plagioclase, epidote, muscovite and quartz in altered volcanics, LON-11-25.*

Mineral	Chemical formula
Celsian	$BaAl_2Si_2O_8$
Hyalophane	$(K,Ba)Al(Si,Al)Si_2O_8$
Witherite	$BaCO_3$
Armenite	$BaCa_2Al_6Si_9O_{30}.2H_2O$
Ba-muscovite	$(K,Ba)(Al,Mg)_2AlSi_3O_{10}(OH)_2$

Table 5.1 *Overview of barium-rich mineral compositions used in this study.*

5.3.2 Barite alteration zone

The barite alteration zone was identified in the field as light-green colored and highly silicified mafic rocks immediately below the main barite horizon in the waterfall section (see Chapter 4). The zone contains actinolite-rich lenses and fractures with one dominant orientation (Fig. 5.1d) that were filled with witherite (Fig. 5.1e). Macroscopic garnet, epidote and pyrite were found at the contact between the barite and altered volcanics (Fig. 5.1f). In contrast to the relatively unaltered schists below the alteration zone that contain patchy hyalophane associated with plagioclase and muscovite (Fig. 5.2a), barium-feldspar becomes a major rock-forming mineral within the altered lithologies. Hyalophane and celsian were found in association with recrystallized quartz and inequigranular-polygonal diopside (Fig. 5.2b), inequigranular-interlobate epidote (Fig. 5.2c) and aggregates of acicular actinolite (Fig. 5.2d). In addition, hyalophane was observed directly adjacent to a small-scale barite vein in a matrix of diopside (Fig. 5.2e), suggesting a genetic relationship between barite and the barium-feldspar. Barium-rich rims were observed in feldspar minerals that were texturally associated with epidote and actinolite, as indicated by the bright rims in back-scattered electron images of Fig. 5.2c and Fig. 5.2d. Modal abundances of hyalophane and celsian decreased significantly in the felsic volcanics overlying the barite, and were absent in the uppermost part of the stratigraphy. Similar field relations and mineral assemblages were observed below the barite horizon in the river section, where additional armenite (see Table 5.1 for mineral composition) was found in association with plagioclase and muscovite in the silicified rocks.

5.4 SAMPLES AND ANALYTICAL METHODS

5.4.1 Major and trace element geochemistry

To investigate the enrichment and depletion of elements in association with metasomatic alteration at the Londozi barite deposit, geochemical analyses were performed on rocks collected from, below and above the silica and barite alteration zones. Samples were obtained from surface outcrops, but show low degrees of weathering due to their high silica contents. In addition, weathered rims were removed with a diamond blade saw before crushing with a jaw crusher and further pulverization in an automated crusher. Preliminary X-ray fluorescence (XRF) measurements on fused disks revealed strong interferences of spectral peaks in samples with high barium contents, which made this analytical method unsuitable for the most altered rocks. Therefore, major and trace elements were analyzed in solution by inductively-coupled plasma optical emission spectroscopy (ICP-OES) and mass spectrometry (ICP-MS) following acid digestion of the rock powders. Circa 125 mg of each sample was dissolved in 2.5 ml HF (48%) and 2.5 ml mix acid consisting of $HClO_4$ (72%) and ultrapure HNO_3 (65%) in the ratio $HClO_4$:HNO_3 = 3:2. The mixture was heated overnight in closed vessels at 90°C and subsequently dried in open vessels at 160°C. An additional digestion step was performed by reacting the residual with a mixture of 2.5 ml concentrated HCl and 2.5 ml concentrated H_2O_2, which ensured complete dissolution of all phases except the highly acid-resistant minerals of zircon, barite and chromite. Five samples were digested and analyzed in duplicate, and two international soil standards ISE-921 (van Dijk and Houba, 2000) were included to test reproducibility and element recovery in the digestion procedure. Solutions were analyzed for Al, Ti, Fe, Mg, Mn, Ca, K, Na, Sc, V, Cr, Zn, Ba and S by ICP-OES, and Ni, Cu, Sr and REE by quadrupole ICP-MS (ThermoFinnigan X-Series) at Utrecht University. Corrections for interferences of BaO on Eu during ICP-MS measurements were made using a calibration curve obtained from analyses of ^{153}Eu in solutions spiked with 10 to 10000 ppb Ba. Recovery during total digestion was better than 91% for all of the analyzed elements in the ISE-921 standard, and precision is better than 2% for elements analyzed by ICP-OES, better than 5% for trace elements and light REE (La-Gd) analyzed by ICP-MS, and 9-12% for heavy REE (except Tm and Lu). Major element concentrations in ppm were converted into weight percentages of oxides assuming all Fe is present as FeO, and SiO_2

contents were determined by subtracting the sum of all oxides (including BaO) from 100%.

5.4.2 Mineral geochemistry

Compositions of feldspar, epidote and garnet in the altered and unaltered schists were determined using the JEOL-JXA 8600 Superprobe electron microprobe at Utrecht University, using a 15 kV accelerating voltage with a 20 nA beam current. Elements were calibrated against the following synthetic and natural standards: diopside for Ca and Si, corundum for Al, TiO for Ti, jadeite for Na, forsterite for Mg, hematite for Fe, tephroite for Mn, $KTiPO_5$ for K, barite for Ba, celestine for S and Sr, metallic chromium for Cr and metallic nickel for Ni. Data were processed using the PROZA correction function and ferric iron contents in epidote and garnet were calculated using the method of Droop (1987).

5.5 RESULTS

5.5.1 Geochemical depth profiles

Major and trace element compositions of altered and unaltered schists from the river and waterfall sections are shown in Table 5.2 and 5.3, respectively (note that rare earth element data from the least altered mafic schists were reported earlier in Chapter 4). A selection of geochemical data is plotted versus stratigraphic depth for the silica alteration zone in the river section in Fig. 5.3 (samples LON-11-14 to LON-11-22C), and the barite alteration zone in the waterfall section in Fig. 5.4 (samples LON-11-01 to LON-11-10).

5.5.1.1 Silica alteration zone

Fig. 5.3 shows that ratios of Al_2O_3/TiO_2 varied between 10 and 15 for samples associated with the silica alteration zone, except for samples LON-11-16 and LON-11-17 with Al_2O_3/TiO_2 = 4.8. Chondrite-normalized rare earth element ratios of La/Yb showed similar limited variability with an average of 1.7 corresponding to relatively flat REE-patterns. Variations in concentration were large for SiO_2, increasing from 52-55 wt% in the unaltered rocks to 97 wt% in the green chert (LON-11-19) and 83 wt% in the silicified pillow lavas (LON-11-22A). Major

element oxides FeO and MgO showed an opposite depth profile, being highest in unaltered mafics (11-15 wt% FeO and 5-6 wt% MgO) and decreasing towards the silicified volcanics, with 1.5 wt% FeO and 0.6 wt% MgO in sample LON-11-22A. Abundances of K_2O, MnO and CaO were roughly similar throughout the studied section or did not show clear systematic variations with depth or distance to the altered units. Ba levels were highest in the green chert and surrounding mafic pillow lavas (1890-2340 ppm Ba) and elevated in the silicified pillows (1165 ppm), versus 90-600 ppm Ba in the unaltered lithologies. However, the highest levels of Ba were measured in the river section in the altered schists underlying the barite horizon (not shown in Fig. 5.3), with 5700-15000 ppm Ba.

5.5.1.2 Barite alteration zone

Fig. 5.4 displays the variation in element ratios and concentrations with stratigraphic depth for the barite alteration zone in the waterfall section, and shows a similar range in Al_2O_3/TiO_2 ratios (10-15) as for the silica alteration zone. The transition from mafic to felsic volcanics above the barite horizon is represented by higher Al_2O_3/TiO_2 ratios of 25-30, as well as significantly higher $(La/Yb)_N$ ratios. SiO_2 concentrations are highly variable, decreasing from 74 wt% in mafic schists just above the banded chert at the base of the stratigraphy, to 48-53 wt% in unaltered mafic schists, and subsequently increasing to 67 wt% in the lower part of the barite alteration zone (LON-11-06). However, SiO_2 decreases again to 60 wt% immediately below the barite horizon (LON-11-07). The variation of FeO with depth is opposite to the depth profile for SiO_2 but very similar to MgO, being highest in the mafic amphibolite of LON-11-04 and lowest in the lower part of the barite alteration with FeO = 1.8 wt% and MgO = 0.1 wt%. Levels of FeO and MgO increase again directly below the barite, similar to concentrations of MnO and CaO. In contrast, the distribution of K_2O is roughly similar to SiO_2, being relatively depleted immediately below the barite. Finally, Ba is significantly elevated in the altered lithologies with 30000-65000 ppm Ba, versus an average of 1770 ppm Ba below the alteration zone. Above the barite horizon, concentrations decline rapidly from 8500 ppm Ba at 1.5 m relative height (LON-11-08) to 612 ppm at 5.0 m (LON-11-10). Sr shows a similar depth profile with the highest levels in the altered lithologies (330-380 ppm Sr).

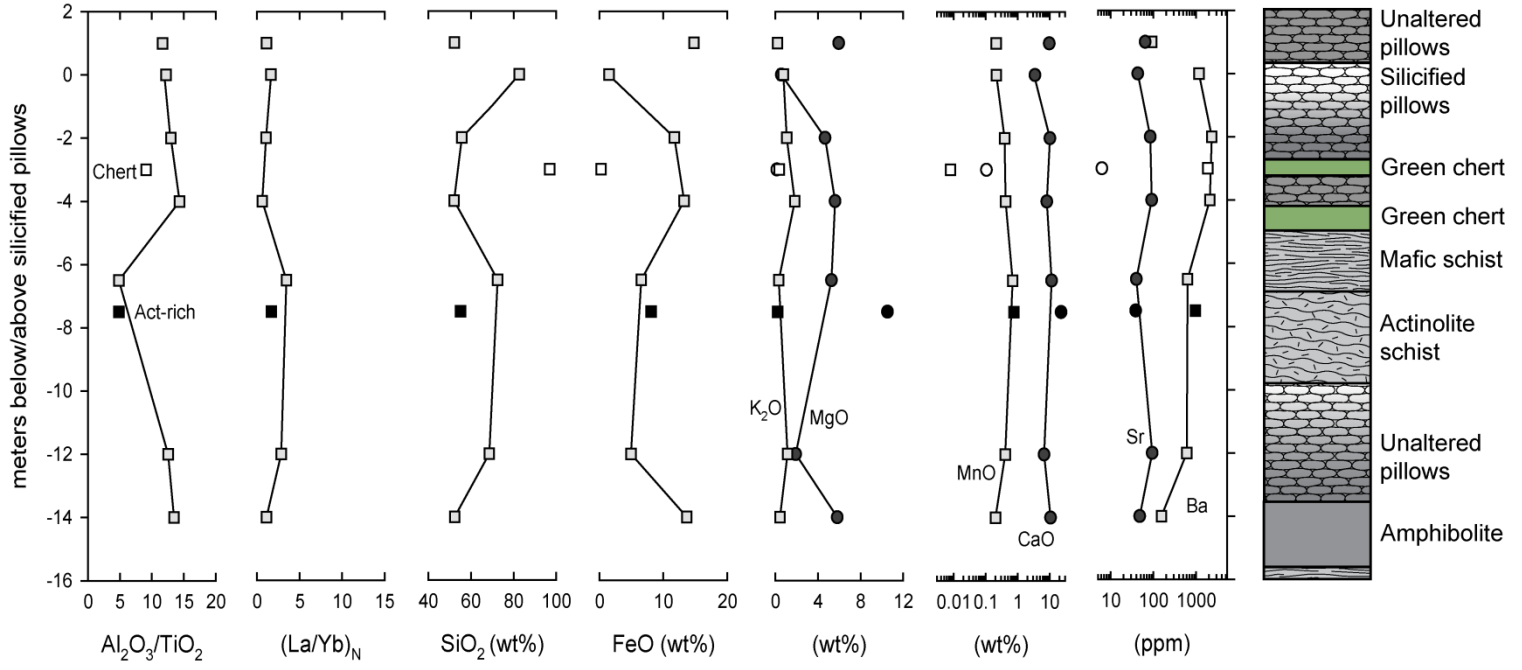

Figure 5.3 *Depth profiles of selected geochemical data for rocks in, above and below the silica alteration zone (silicified pillow lavas) in the river section (LON-11-14 until LON-11-22C).*

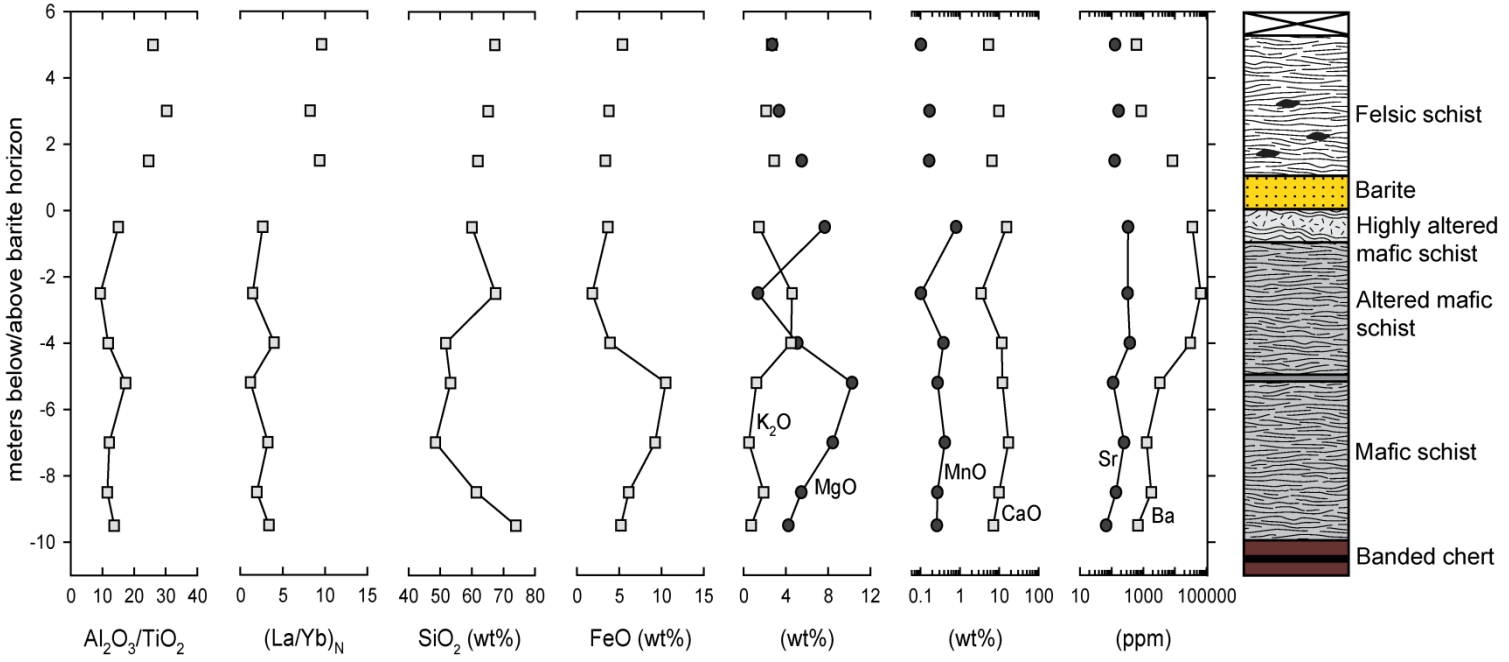

Figure 5.4 *Depth profiles of selected geochemical data for rocks in, above and below the barite alteration zone in the waterfall section (LON-11-01 until LON-11-10).*

Sample	11-14	11-15	11-16	11-17	11-18	11-19	11-20	11-22A	11-22C	11-23	11-24	11-25	11-27	11-28
m to sil. pillows	-14.0	-12.0	-7.5	-6.5	-4.0	-3.0	-2.0	0.0	1.0	13.0	15.0	15.5	19.0	20.5
SiO_2	52.42	68.62	55.16	72.51	52.08	96.92	55.73	82.73	52.28	87.42	94.42	94.52	62.49	65.24
Al_2O_3	13.64	14.43	1.73	2.36	16.46	1.52	13.82	8.15	13.38	5.58	2.55	1.96	17.17	17.17
TiO_2	1.01	1.15	0.36	0.49	1.15	0.17	1.06	0.67	1.15	0.41	0.08	0.16	0.69	0.70
FeO	13.66	4.95	8.10	6.56	13.26	0.27	11.74	1.51	14.81	0.76	0.34	0.74	4.71	3.36
MgO	5.83	1.92	10.53	5.28	5.61	0.15	4.68	0.58	5.95	0.80	0.50	0.56	3.15	1.58
MnO	0.20	0.40	0.76	0.69	0.42	0.01	0.39	0.22	0.21	0.05	0.03	0.04	0.22	0.10
CaO	10.66	6.70	22.74	11.47	8.16	0.11	10.16	3.45	9.67	1.88	0.76	1.05	6.68	3.78
K_2O	0.45	1.16	0.23	0.33	1.84	0.37	1.08	0.76	0.22	1.20	0.51	0.07	3.16	6.90
Na_2O	2.12	0.60	0.27	0.24	0.78	0.27	1.08	1.80	2.32	0.21	0.14	0.27	0.72	0.98
Sc	34.5	36.5	16.4	14.8	40.0	*6.2*	36.3	24.7	35.3	12.8	*1.8*	*5.5*	13.2	*7.8*
V	291.7	290.4	85.5	86.2	362.9	51.3	295.5	187.5	312.8	71.4	*6.9*	46.6	71.1	51.1
Cr	143.4	158.4	722.7	1050.8	163.0	343.2	129.3	67.4	121.6	672.5	*7.3*	37.0	39.9	*6.5*
Ni	121.7	94.6	626.4	567.0	246.6	118.6	156.8	71.3	113.6	446.6	43.7	28.2	104.9	13.9
Cu	112.6	72.9	37.4	126.8	239.2	32.7	290.3	47.6	76.7	54.2	34.1	47.3	78.8	25.0
Zn	129.7	71.8	110.0	96.7	152.9	207.8	156.2	29.5	123.9	221.3	170.5	551.4	143.4	80.0
Ba	153.9	605.9	963.7	630.5	2108.5	1887.7	2333.9	1165.5	90.9	15132.2	5939.6	5680.3	9072.4	1723.3
Sr	47.8	94.0	38.5	39.9	91.0	6.2	84.2	42.9	63.9	71.8	26.8	38.1	203.8	174.7
S	*74.5*	*110.8*	*51.3*	750.9	1890.0	734.5	3450.9	205.1	227.6	1010.7	216.4	562.1	2265.0	*44.2*

Table 5.2 *Major and trace element geochemistry of the river section analyzed by ICP-OES and ICP-MS. Major element oxides are given in wt% and trace elements in ppm. SiO2 was calculated as 100% minus the sum of all oxides including BaO. Results given in italics were measured outside the calibration range and represent indicative values.*

Sample	11-14	11-15	11-16	11-17	11-18	11-19	11-20	11-22A	11-22C	11-23	11-24	11-25	11-27	11-28
m to sil. pillows	-14.0	-12.0	-7.5	-6.5	-4.0	-3.0	-2.0	0.0	1.0	13.0	15.0	15.5	19.0	20.5
La	3.8	5.0	0.4	3.8	4.9	0.1	4.6	3.6	4.5	5.8	8.4	1.1	31.9	38.3
Ce	10.4	13.7	2.2	10.5	13.4	0.5	12.1	10.0	12.0	13.3	18.5	2.6	60.6	73.2
Pr	1.6	2.0	0.2	1.4	1.9	nd	1.9	1.6	1.9	1.8	2.4	0.4	6.9	8.2
Nd	7.9	10.4	2.1	7.5	10.3	0.3	9.5	8.1	9.3	8.0	9.5	1.7	25.9	29.8
Sm	2.7	3.2	0.8	1.9	4.0	0.1	2.8	2.6	2.9	1.9	1.9	0.6	5.4	5.6
Eu	1.0	1.0	0.2	0.6	1.4	nd	1.3	1.1	1.1	0.8	0.6	0.4	1.6	1.4
Gd	3.5	2.9	0.9	2.1	7.4	0.0	3.8	3.3	3.8	2.1	1.9	0.7	5.8	5.2
Tb	0.7	0.4	0.1	0.2	1.4	nd	0.7	0.5	0.7	0.4	0.3	0.2	1.0	0.8
Dy	4.0	2.1	0.8	1.9	10.2	nd	4.6	3.5	4.6	2.2	1.9	0.6	6.5	4.7
Ho	0.9	0.3	0.0	0.3	2.1	nd	1.0	0.7	1.0	0.5	0.5	0.2	1.5	0.0
Er	2.5	1.2	0.4	1.1	6.3	nd	2.9	1.9	2.9	1.3	1.3	0.4	4.8	2.8
Tm	0.4	0.1	nd	nd	0.7	nd	0.5	0.3	0.5	0.2	0.3	0.2	0.7	0.4
Yb	2.3	1.2	0.1	0.7	5.3	nd	2.9	1.5	2.7	1.2	1.5	0.4	4.6	2.7
Lu	0.4	0.1	nd	nd	0.6	nd	0.5	0.2	0.4	0.2	0.3	0.2	0.7	0.4
Al_2O_3/TiO_2	13.5	12.5	4.8	4.8	14.3	9.1	13.0	12.2	11.7	13.6	30.2	12.2	24.8	24.5
$(La/Yb)_N$	1.1	2.9	1.7	3.5	0.6	-	1.1	1.6	1.1	3.2	3.9	1.9	4.7	9.6
Mg#	43	41	70	59	43	50	42	41	42	65	72	58	54	46

Table 5.2 (continued)

Sample	11-01	11-02	11-03	11-04	11-05	11-06	11-07	11-08	11-09	11-10
m to barite	-9.5	-8.5	-7.0	-5.2	-4.0	-2.5	-0.5	1.5	3.0	5.0
SiO_2	73.98	61.47	48.51	53.31	51.77	67.53	60.09	61.94	65.21	67.32
Al_2O_3	7.44	12.98	13.91	10.34	17.36	12.10	6.33	17.54	14.48	14.98
TiO_2	0.54	1.12	1.14	0.60	1.47	1.29	0.42	0.71	0.48	0.58
FeO	5.20	6.12	9.25	10.50	3.90	1.80	3.67	3.36	3.78	5.39
MgO	4.25	5.47	8.44	10.28	5.10	1.37	7.69	2.89	2.14	2.66
MnO	0.26	0.27	0.41	0.27	0.38	0.10	0.81	0.17	0.17	0.10
CaO	7.07	9.90	17.24	12.06	11.59	3.45	15.31	6.54	9.78	5.35
K_2O	0.72	1.90	0.51	1.22	4.50	4.60	1.46	5.50	3.36	2.71
Na_2O	0.46	0.56	0.44	1.05	0.49	0.45	0.25	0.41	0.51	0.85
Sc	18.5	36.5	36.6	41.4	46.3	27.8	15.1	*8.7*	*5.9*	*7.4*
V	115.7	217.4	227.5	276.4	273.6	100.2	99.8	61.1	45.0	50.8
Cr	1805.4	2112.4	2341.0	882.0	3052.2	1075.1	726.9	*18.8*	*4.1*	*14.4*
Ni	647.0	452.7	796.4	196.0	770.8	134.4	230.1	31.7	8.3	17.0
Cu	142.5	102.7	89.3	98.5	64.4	89.8	80.2	44.9	36.0	55.8
Zn	192.4	93.3	165.2	136.0	132.3	57.7	128.7	43.9	35.7	91.0
Ba	677.0	1787.4	1276.9	3351.7	30881.5	65406.2	35619.3	8417.9	864.4	612.8
Sr	67.6	137.7	248.6	112.5	379.0	324.7	333.2	125.3	168.5	129.8
S	1014.2	*126.0*	589.3	*112.3*	*61.2*	198.8	2036.6	*50.8*	*32.6*	*74.6*

Table 5.3 *Major and trace element geochemistry of the waterfall section analyzed by ICP-OES and ICP-MS. Major element oxides are given in wt% and trace elements in ppm. SiO2 was calculated as 100% minus the sum of all oxides including BaO. Results given in italics were measured outside the calibration range and represent indicative values.*

Sample	11-01	11-02	11-03	11-04	11-05	11-06	11-07	11-08	11-09	11-10
m to barite	-9.5	-8.5	-7.0	-5.2	-4.0	-2.5	-0.5	1.5	3.0	5.0
La	5.7	6.7	10.0	2.1	16.1	3.7	7.6	36.9	25.5	26.6
Ce	13.2	16.4	23.6	5.1	37.1	9.9	15.7	72.3	48.9	51.3
Pr	1.7	2.2	3.2	0.7	4.9	1.2	2.0	8.3	5.4	5.6
Nd	7.9	10.0	14.7	3.7	21.4	5.7	9.0	30.4	20.4	21.3
Sm	1.9	2.4	3.5	1.2	4.8	1.8	2.3	6.3	4.1	4.3
Eu	0.7	0.8	1.1	0.3	1.5	0.7	0.9	1.5	0.9	1.0
Gd	2.1	2.9	3.8	1.7	5.0	2.2	3.0	5.8	4.3	4.4
Tb	0.3	0.5	0.5	0.3	0.8	0.3	0.5	1.0	0.7	0.6
Dy	2.2	3.6	3.8	2.3	4.7	2.4	3.6	5.0	4.2	4.0
Ho	0.4	0.8	0.7	0.4	1.0	0.5	0.8	1.1	0.8	0.7
Er	1.4	2.6	2.3	1.5	3.0	1.7	2.3	3.0	2.5	2.3
Tm	0.1	0.3	0.2	0.1	0.4	0.2	0.2	0.6	0.2	0.1
Yb	1.2	2.3	2.1	1.2	2.7	1.7	2.0	2.7	2.1	1.9
Lu	0.1	0.3	0.2	0.1	0.4	0.2	0.3	0.5	0.2	0.1
Al_2O_3/TiO_2	13.7	11.6	12.2	17.3	11.8	9.4	15.0	24.7	30.3	26.0
$(La/Yb)_N$	3.4	1.9	3.2	1.2	4.0	1.4	2.6	9.4	8.2	9.6
Mg#	59	61	62	64	70	58	79	61	50	47

Table 5.3 (continued)

5.5.1.3 Isocon analysis

Isocon analysis (Grant, 1986) provides insights into the relative changes in element abundances between the least altered and the most altered samples, calculated relative to the change in immobile element concentrations. Degrees of enrichment or depletion can be quantified using equation 5.1 from Grant (1986):

$$(\Delta C/C^0) = (C^0/C^A)_i \times (C^A/C^0)_j - 1 \qquad [5.1]$$

where C^0 represents the concentration of immobile element i or element of interest j in the least altered sample, and C^A the concentration in the most altered sample. Following this method, elements that are enriched relative to the assumed immobile element yield positive values, whereas depleted elements are characterized by negative values of $\Delta C/C^0$. In addition, an isocon line can be constructed from immobile element concentrations in a plot of C^A versus C^0 for which the slope yields the volume change during alteration, with values >1 indicating volume loss and values <1 indicating volume increase.

Results of isocon analyses for the silica and barite alteration zones are shown in Table 5.4 and Fig. 5.5 and Fig. 5.6, respectively. For the river section, LON-11-22C was selected as the least altered sample based on its field appearance as massive dark pillows, its mineralogy consisting of hornblende, plagioclase, quartz and ilmenite, and the relatively low SiO_2 content (52 wt%). Similar criteria were used to select the amphibolite of LON-11-03 as least altered rock for the waterfall section, showing the lowest abundances of SiO_2 (48.5 wt%) and K_2O (0.51 wt%). Immobility of the rare earth elements was assumed for all alteration zones, because of similar chondrite-normalized abundances in altered and unaltered rocks versus strong variability in concentrations of Al_2O_3 and TiO_2 which are normally considered immobile. For the silica alteration zone, an isocon slope of 0.83 (R^2 = 0.99) was calculated corresponding to a 17% volume increase. Significantly enriched elements include SiO_2, K_2O, Ba and MnO versus significant depletions in FeO, MgO and CaO. Transition metals Sc, V, Cr, Ni, Cu and Zn are all depleted relative to the immobile elements. The isocon for the barite alteration zone in the waterfall section yielded a slope of 0.67 (R^2 = 0.98) corresponding to 33% volume increase. Elements that are enriched are SiO_2, MgO, MnO, CaO, K_2O, Ba, Sr and S as well as transition metals Cu and Zn, whereas FeO, Na_2O, Al_2O_3 and TiO_2 are depleted. Table 5.4 also shows the results from comparison of the

	Silica alteration zone		Barite alteration zone		Barite vs. silica alteration	
	$(\Delta C/C^0)_{dV=0}$	$(\Delta C/C^0)_{isocon}$	$(\Delta C/C^0)_{dV=0}$	$(\Delta C/C^0)_{isocon}$	$(\Delta C/C^0)_{dV=0}$	$(\Delta C/C^0)_{isocon}$
SiO_2	0.6	0.9	0.2	0.8	-0.3	-0.2
Al_2O_3	-0.4	-0.3	-0.5	-0.3	-0.3	-0.2
TiO_2	-0.4	-0.3	-0.6	-0.4	-0.4	-0.4
FeO	-0.9	-0.9	-0.6	-0.4	1.3	1.4
MgO	-0.9	-0.9	-0.1	0.4	11.3	12.3
MnO	0.0	0.2	1.0	1.9	2.5	2.7
CaO	-0.6	-0.6	-0.1	0.3	3.1	3.4
K_2O	2.5	3.2	1.9	3.3	0.8	0.9
Na_2O	-0.2	-0.1	-0.4	-0.2	-0.9	-0.9
Sc	-0.3	-0.2	-0.6	-0.4	-0.4	-0.4
V	-0.4	-0.3	-0.6	-0.3	-0.5	-0.5
Cr	-0.4	-0.3	-0.7	-0.5	9.0	9.8
Ni	-0.4	-0.2	-0.7	-0.6	2.9	2.2
Cu	-0.4	-0.3	-0.1	0.3	0.6	0.7
Zn	-0.8	-0.7	-0.2	0.2	3.0	3.4
Ba	11.8	14.4	26.9	40.6	27.3	29.6
Sr	-0.3	-0.2	0.3	1.0	6.2	6.8
S	-0.1	0.1	2.5	4.2	8.2	8.9
La	-0.2	0.0	-0.2	0.1	0.9	1.1
Ce	-0.2	0.0	-0.3	0.0	0.5	0.6
Pr	-0.2	0.0	-0.4	-0.1	0.2	0.3
Nd	-0.1	0.0	-0.4	-0.1	0.0	0.1
Sm	-0.1	0.1	-0.3	0.0	-0.2	-0.1
Eu	0.0	0.2	-0.2	0.2	-0.3	-0.2
Gd	-0.1	0.0	-0.2	0.2	-0.2	-0.1
Tb	-0.2	0.0	0.0	0.5	-0.1	-0.1
Dy	-0.2	-0.1	0.0	0.4	0.0	0.0
Ho	-0.3	-0.1	0.1	0.6	0.0	0.1
Er	-0.3	-0.2	0.0	0.5	0.1	0.2
Tm	-0.4	-0.2	0.3	0.9	-0.2	-0.1
Yb	-0.4	-0.3	-0.1	0.4	0.2	0.3
Lu	-0.4	-0.3	0.2	0.8	0.0	0.1

Table 5.4 *Isocon analysis for the silica alteration zone (C^0 = LON-11-22C, C^A = LON-11-22A), barite alteration zone (C^0 = LON-11-03, C^A = LON-11-07) and a comparison of altered rocks from both zones (C^0 = LON-11-22A, C^A = LON-11-07). Columns with $(\Delta C/C^0)_{dV=0}$ assume zero-volume change, $(\Delta C/C^0)_{Isocon}$ assume volume change defined by the slope of the isocon.*

compositions of most altered rocks in the silica alteration zone (C^0) and the barite zone (C^A), and demonstrates that major elements Mg, Fe, Mn and Ca as well as trace elements are relatively enriched in the latter.

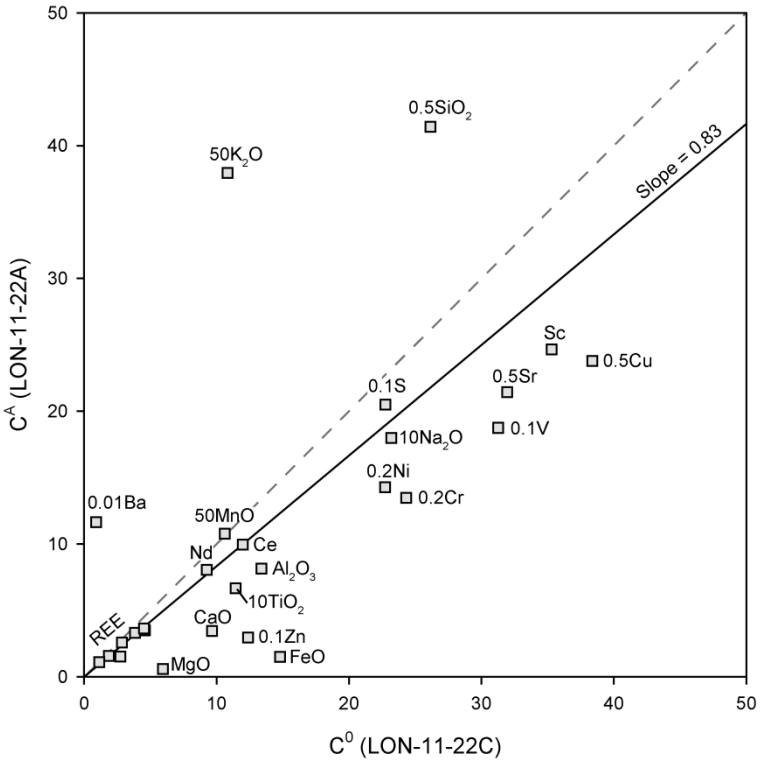

Figure 5.5 *Isocon diagram for the silica alteration zone with LON-11-22A (silicified pillows) as most altered (C^A) and LON-11-22C (unaltered pillows) as least altered (C^0) rocks. Scaling factors are indicated for each element. Black line indicates the isocon defined by immobile elements (REE), dashed line represent an alteration scenario with zero-volume change. Elements plotting above the isocon are enriched relative to immobile elements, whereas elements plotting below the line are depleted.*

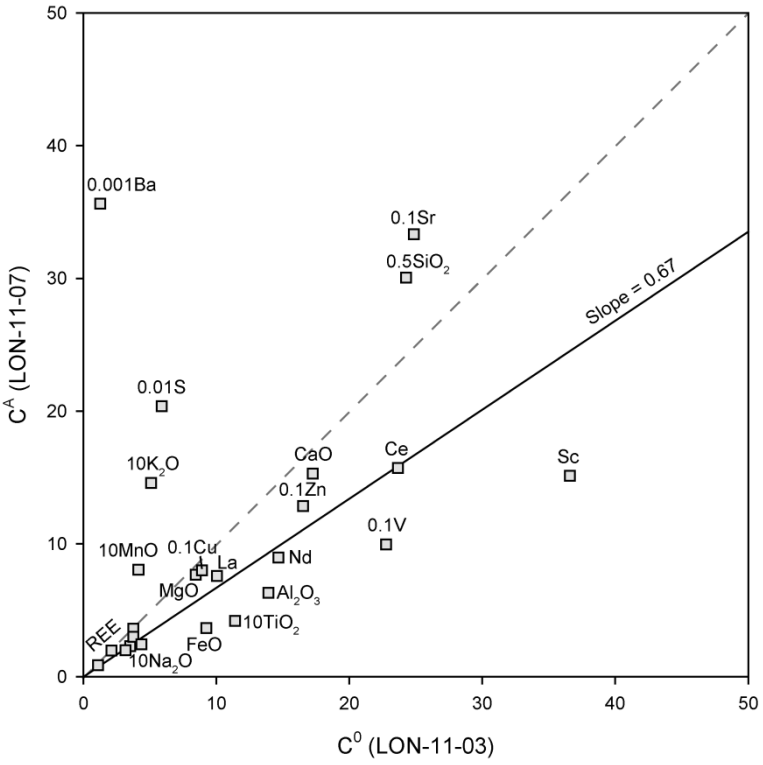

Figure 5.6 *Isocon diagram for the barite alteration zone in the waterfall section with LON-11-07 as most altered (C^A) and LON-11-03 as least altered (C^0) rocks. Scaling factors are indicated for each element. Black lines indicate the isocons defined by immobile REE, dashed lines represent zero-volume change.*

5.5.2 Mineral geochemistry

5.5.2.1 Silica alteration zone

Mineral assemblages of silicified pillow lavas consisted of more than 90% quartz, with minor occurrences of almandine garnet, chlorite and muscovite. Similarly, green chert was dominated by quartz with minor muscovite and hyalophane. Barium contents of the muscovite ranged from 0.1 to 5.6 wt% BaO, whereas hyalophane in chert sample LON-11-19 contained 12 wt% BaO corresponding to a mole fraction of celsian (X_{Cn}) of 0.23 (see Supplementary Table S5-1a)*. Epidote compositions from the river section and the silicified pillow lavas shown in Supplementary Table S5-2a.

5.5.2.2 Barite alteration zone

The mineralogy of the barite alteration zone in the waterfall section was found to be dominated by feldspar from the celsian-hyalophane series, epidote and garnet, for which major element compositions are reported in Supplementary Tables S5-1b, S5-2b and S5-3. Barium contents of feldspar, expressed as the mole fraction of celsian (X_{Cn}), increase with decreasing distance to the barite horizon as shown in Fig. 5.7. Feldspar minerals in the most altered volcanics directly below the barite contain up to 40 wt% BaO, corresponding to nearly pure celsian with X_{Cn} = 0.93 (Table S5-1b). Average fractions of Cn decrease in the waterfall section from X_{Cn} = 0.56 in volcanics directly underlying the barite, to X_{Cn} = 0.34 in rocks 2-5 m below and X_{Cn} = 0.27 in rocks more than 5 m below the barite horizon. Similar patterns were observed in the river section, from X_{Cn} = 0.51 immediately below the barite to X_{Cn} = 0.32 and 0.16 in lithologies 2-5 m and more than 5 m below the barite, respectively. Hyalophane in the felsic volcanics overlying the barite horizon was characterized by an average X_{Cn} of 0.08 in the waterfall section and 0.10 in the river section. The amount of sodium (expressed as the mole fraction of albite, X_{Ab}) in hyalophane minerals is relatively low, with an average X_{Ab} = 0.05 for the waterfall section and X_{Ab} = 0.06 for the river section. The highest albite contents were found in altered mafics just below the barite horizons (X_{Ab} = 0.09 and 0.10 for the waterfall and river section, respectively), except for one anomalous feldspar in sample LON-11-01 with X_{Ab} = 0.18. Epidote is relatively rich in ferric iron and is characterized by pistacite (Ps) contents up to 26% (Ps = [(Fe^{3+}/Al) + 1]

* Supplementary tables for this chapter are available at http://hdl.handle.net/10411/10145.

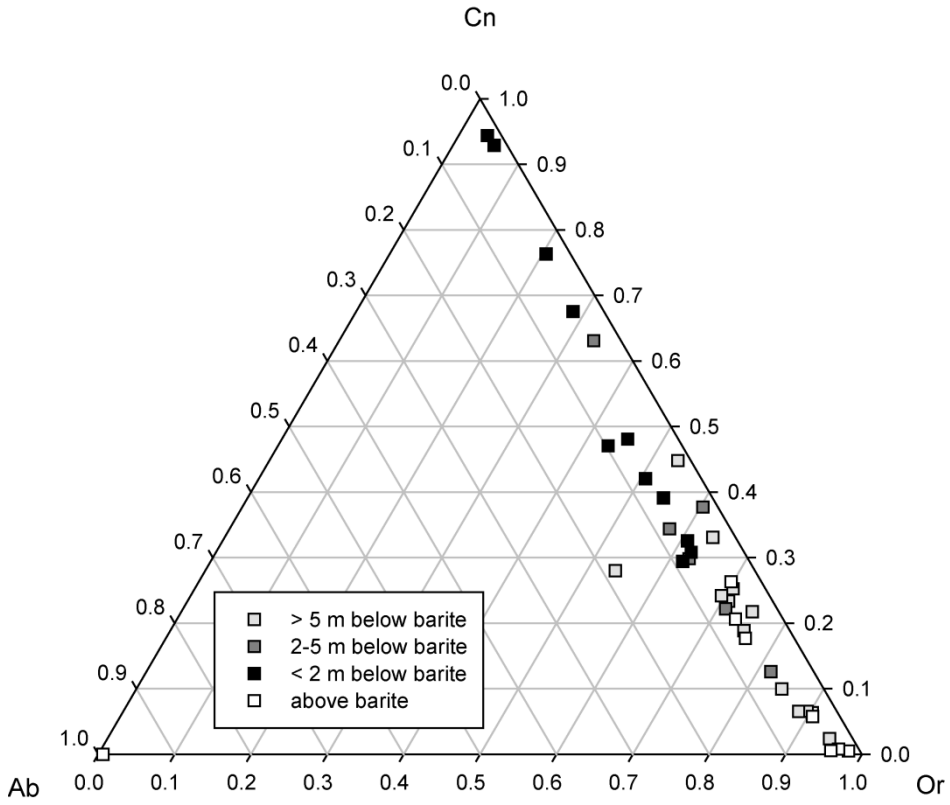

Figure 5.7 *Ternary plot showing compositions of barium-rich alkali feldspar found at different distances to the barite horizons. Or = orthoclase ($KAlSi_3O_8$), Cn = celsian ($BaAl_2Si_2O_8$), Ab = albite ($NaAlSi_3O_8$).*

x 100%), with an average Ps of 15.9% for the barite alteration zones versus Ps = 7.9% and 10.1% for rocks outside alteration zones in the waterfall and river section, respectively (Supplementary Table S5-2). Epidote is petrographically related to barite and garnet (cf. Fig. 5.1f), which was identified as grossular-andradite (Supplementary Table S5-3).

5.6 DISCUSSION

5.6.1 Precursor rocks

Amphibolites in the Londozi area were previously interpreted to reflect submarine mafic to ultramafic volcanism in an oceanic plateau setting, based on their nearly flat chondrite-normalized rare earth element patterns and the lack of clastic sediments in the stratigraphy (Chapter 4 and Reimer, 1980). Major and trace element compositions of the mafic volcanics analyzed in this study are consistent with this interpretation. Ratios of Al_2O_3/TiO_2 show limited variability and are relatively low (average 12.8 ± 2.0) in the unaltered mafics, except for two very Al-poor samples with Al_2O_3/TiO_2 = 4.8 (see Fig. 5.3 and Fig. 5.4). These values are similar to ratios reported for Barberton-type komatiites typical for ~3.4 Ga greenstone belts, which were linked to deep melting processes below oceanic plateaus (Sun, 1987; Arndt and Condie, 1994; Arndt et al., 2001; Arndt, 2003). Mg-numbers also support the presence of mafic to ultramafic precursor rocks in the Londozi area, although lower values for the pillowed schists in the river section (40 to 43) compared to mafic schists from the waterfall section (59 to 64) suggest the existence of small primary compositional differences between erupted magmas. Furthermore, although primary trace element abundances may have been obscured by amphibolite facies metamorphism, generally high concentrations of Cr and Ni in mafic schists from the waterfall section (Table 5.3) agree with an ultramafic precursor. Finally, higher Al_2O_3/TiO_2 and La/Yb ratios in unaltered felsic schists overlying the barite compared to the (ultra)mafic rocks in the footwall (Fig. 5.4) indicate that the felsic compositions are related to a different precursor rock, and not to silicification processes.

5.6.2 Origin of silica alteration zones

5.6.2.1 Element mobility and conditions of metasomatic alteration

Depth profiles (Fig. 5.3) and isocon analyses (Fig. 5.5) indicate that enrichment of SiO_2 in the silicified pillows and underlying lithologies was associated with depletion of major elements including Fe, Mg, Ca and to a lesser extent Na. This is not surprising considering the mineralogical evidence for replacement of initial mafic minerals, now metamorphosed to hornblende, garnet and plagioclase, by quartz and minor amounts of chlorite and muscovite. However, the leaching of

these specific elements provides important insights into alteration processes and hydrothermal fluid chemistry. First, the depletion in Mg, Ca and Na is inconsistent with high-temperature hydrothermal processes, because scavenging of magnesium, calcium and sodium from fluids in hot (>350°C) hydrothermal systems typically results in the fixation of these elements in secondary solid phases (Mottl and Holland, 1978; Seyfried, 1987; Seewald and Seyfried Jr, 1990; Elderfield and Schultz, 1996). Second, the strong depletion in iron supports reducing conditions during hydrothermal alteration, because Fe can only be significantly remobilized as soluble Fe^{2+} (cf. Hofmann and Wilson, 2007). Major element data thus support relatively low-temperature and reducing fluids during formation of the silica alteration zone.

Trace elements compositions provide similar constraints on chemical conditions during silica alteration. K, Ba, Cs and Rb are sensitive indicators of water-rock interactions, since these elements are taken up by basalts during low-temperature alteration and leached from these rocks at high temperatures (Staudigel, 2003). As such, the observed enrichment in K and Ba in the silicified volcanics supports low-temperature processes. Similarly, enrichment in transition metals (e.g. Cu, Zn, Ni) is typically associated with high-temperature deposits, because the solubility of metal-ligand complexes increases significantly with increasing temperature (Seewald and Seyfried Jr, 1990; Candela, 2003; Staudigel, 2003). Variably depleted transition metals in the silica alteration zone thus suggest that the formation of these complexes was insignificant at Londozi, providing further evidence for alteration at temperatures below ~200°C. Below, we discuss the setting in which this metasomatism most likely occurred.

5.6.2.2 Timing and setting of metasomatic alteration

Low-temperature metasomatism can occur in near-surface environments by hydrothermal processes in volcanically active regions, or by chemical weathering processes that are not associated with volcanism. For example, Lowe and Byerly (1986) suggested that silica alteration in the Barberton Greenstone Belt was related to subaerial weathering of komatiitic flow tops during periods of volcanic quiescence, resulting in silicification of the ultramafics by brine-like fluids. However, several lines of evidence argue against such processes at Londozi. First, the formation of pillow lavas requires subaqueous conditions and argues against syndepositional subaerial exposure. Second, the occurrence of barite higher in the stratigraphy also argues against subaerial exposure of the mafic extrusives

because water must have been present to precipitate barite from seawater-derived sulfate (cf. Chapter 2). Finally, chemical changes are inconsistent with weathering processes since SiO_2, K and Ba would have been removed during subaerial weathering of komatiite (Duchac and Hanor, 1987). Therefore, we conclude that the formation of silica alteration zones in the Londozi (ultra)mafics was related to hydrothermal processes in a subaqueous volcanic environment. The confined nature of the silica-rich horizons suggests that silicification occurred during or very soon after extrusion of the lava, as overlying mafic pillows do not show petrological or geochemical evidence for post-depositional silicifying fluids. It is possible that such synvolcanic alteration was related to palagonite formation during subaqueous alteration of basaltic glass, consistent with the depletion in Mg, Ca and Na versus the enrichment in K and Ba (Staudigel and Hart, 1983). Although Staudigel and Hart (1983) reported SiO_2depletion in modern oceanic settings during palagonite formation, the strong SiO_2 enrichment in the Londozi silica alteration zone may be related to the geochemistry of Paleoarchean seawater that was probably silica-saturated (Siever, 1991). Likewise, the discrepancy between immobility of Fe in modern systems versus the strong depletion in the silicified pillows could be attributed to the reduced nature of the Paleoarchean seawater (Huston and Logan, 2004).

The geochemistry and inferred setting of silica alteration at Londozi is very similar to the low-temperature seafloor metasomatism suggested for other Paleoarchean silicified volcanics and chert deposits in the Barberton Greenstone Belt (Hofmann and Harris, 2008; Hofmann, 2011). Hofmann and Harris (2008) estimated that chert precipitation occurred at temperatures of ~125°C, and suggested that most of the silica was derived from seawater with minor hydrothermal inputs. In addition, these authors concluded that this low-temperature hydrothermal activity was related to diffuse venting of fluids instead of black-smoker type systems, and suggested that fluid circulation was driven by the heat of cooling mafic extrusives in an oceanic plateau-like setting. A similar tectonic setting was inferred for the Londozi barite deposit (Chapter 4) and observation of exclusively low-temperature alteration (100-120°C) on modern oceanic plateaus (Kurnosov et al., 2003; Banerjee et al., 2004; Zhao et al., 2004) indicates that such low-grade metasomatism presents a plausible explanation for the silica alteration zones at Londozi.

5.6.3 Origin of barite alteration zones

5.6.3.1 Element mobility and conditions of metasomatic alteration

Depth profiles for the waterfall section display similar element enrichment-depletion patterns compared to the silica alteration zone outlined above (i.e. enrichment in SiO_2, K, Ba and depletion in Fe, Mg, Ca), except for the most altered schists (LON-11-07) immediately below the barite horizon in the barite alteration zone (Fig. 5.4). The geochemistry of these lithologies is significantly different, showing depletion in SiO_2 and K_2O and enrichment in Fe, Mg, Mn and Ca relative to the underlying rocks (LON-11-06). Al_2O_3/TiO_2 and La/Yb ratios are similar for all mafic volcanics in the waterfall section, indicating that the major element variations are related to alteration processes and do not reflect different precursor compositions. Together with field evidence for different mineral assemblages in these rocks (Section 5.3.2), geochemical data thus suggests that the barite alteration zone represents distinct metasomatism that predominantly affected the lithologies immediately below the barite.

Isocon results confirm the dissimilar geochemistry of the barite alteration zone and demonstrate enrichment in transition metals Cu and Zn, as well as Ba, S and Sr compared to the least altered mafics in the succession (Fig. 5.6). In addition to these elements, the barite alteration zone is also enriched in Fe, Mg, Mg, Ca, Cr and Ni compared to the composition of the silica alteration zone (Table 5.4). Although enrichment in barium, sulfur and strontium could be related to partial digestion of barite during sample preparation, no barite was found during optical microscopy and back-scattered electron imaging of these samples, and the molar Ba/S ratio of 4.1 is inconsistent with the stoichiometry of barite dissolution (Ba/S = 1). Instead, the presence of barium-rich silicates and sulfides in this sample could explain the elevated levels of Ba and S. Furthermore, and in contrast to the silica alteration zone, the observed enrichment of transition metals in the barite alteration zone is suggestive of high-temperature alteration processes, because quantitative mobilization of these elements requires temperatures above ~300°C (Seewald and Seyfried Jr, 1990; Candela, 2003; Staudigel, 2003). Additional evidence for relatively high-temperature alteration comes from the relative enrichment in Mg, Ca and Mn (cf. Section 5.6.2 and Seyfried, 1987; Seewald and Seyfried Jr, 1990).

5.6.3.2 Timing and setting of metasomatic alteration

The inferred localized and high-temperature metasomatism associated with the barite deposit could be explained by two different scenarios, including (1) a change in temperature and fluid composition during syn-depositional hydrothermal alteration, or (2) post-depositional metasomatism by fluids released during amphibolite facies metamorphism. The presence of strongly altered lithologies below the barite versus limited chemical alteration in the hangingwall is suggestive of syn-depositional metasomatism (cf. Van Kranendonk and Pirajno, 2004), and the observed Ba-enrichment is consistent with fluids providing a barium source for barite precipitation. However, episodic high-temperature alteration appears inconsistent with the oceanic plateau setting inferred for the Londozi volcanics (Chapter 4), as no high-temperature hydrothermal activity has been observed in similar tectonic settings on the modern Earth (Kurnosov et al., 2003; Banerjee et al., 2004; Zhao et al., 2004). Most important, the mineralogy of the barite alteration zone provides evidence for a late stage of barium remobilization. Celsian and barium-rich hyalophane were found to be strongly associated with randomly oriented aggregates of acicular actinolite (Fig. 5.2d), which grew during retrograde metamorphism replacing peak-metamorphic hornblende (see Chapter 4). In addition , the random orientation of the elongate actinolite minerals supports growth after the development of the tectonic foliation, which was linked to deformation post-dating the peak of metamorphism in the Steynsdorp region (Chapter 4 and Lana et al., 2010). Thus, the textural association between actinolite and barium-rich feldspar suggests that growth of the latter also occurred during retrograde metamorphism. In addition, hyalophane formation under greenschist facies conditions is consistent with Na-contents of 11% Ab in hyalophane coexisting with albite (Supplementary Table S5-4), according to the empirical geothermometer defined by Essene et al. (2005). Significantly higher Ab-contents of 14-30% would be expected if the hyalophane had equilibrated with albite at the middle to upper amphibolite facies conditions during regional metamorphism of the Londozi volcanics (Chapter 4 and Essene et al., 2005).

Barium for retrograde hyalophane and celsian could have been derived from primary feldspar, but the strong textural relationship between these minerals and barite (Fig. 5.2e) as well as the correlation between the Ba-content of barium-feldspar and the distance to the barite (Fig. 5.7) supports barite a the major source for barium. The highest molar fractions of Cn were observed directly

adjacent to barite crystals at Londozi, which is similar to compositional relationships between feldspar and barite associated with the Hemlo gold deposit in Canada, where the occurrence of celsian-rich feldspar was restricted to barite-rich units and relatively Ba-poor feldspar was observed in green mica schists away from the barite (Pan and Fleet, 1991). Consequently, Pan and Fleet (1991) concluded that Ba was introduced from barite during breakdown reactions at amphibolite facies metamorphism, and analogous models for the formation of barium-rich silicates in association with metamorphic breakdown of barite were reported by Tracy (1991) for Ba-rich feldspar in the Sterling Hill skarn deposit, by Chabu and Boulègue (1992) for the Kipushi Zn-Pb-Cu deposit in the Democratic Republic of the Congo (previously Zaire), and by Grapes (1993) for Ba-muscovite in metacherts and siliceous schists in the Southern Alps of New Zealand. All of these petrogenetic models require reducing conditions to remobilize barium from barite by reduction of the sulfate, for example by CH_4, H_2, CO, NH_4, H_2S or carbonaceous material (Kritsotakis and Von Platen, 1980). It is likely that such fluids were present during metasomatism of the Londozi deposit, since ubiquitous sulfide in the altered schists support a reducing environment whereas late witherite veins reflect conditions under which barite was (at least temporally) instable (Blount, 1977). Methane and H_2 may have been derived from high-temperature abiotic serpentinization of ultramafic volcanics by CO_2-bearing fluids derived from prograde metamorphism at depth (Powell et al., 1991; Lazar and Manning, 2005; McCollom and Bach, 2009), or alternatively ferrous iron in olivine and pyroxene minerals may have acted as a reducing agent for the sulfate released from barite (Mottl et al., 1979; Shanks et al., 1981), facilitating reductive dissolution of barite. The strong association between reversely zoned Ba-feldspar and ferric iron minerals epidote and grossular-andradite in barite-amphibolite contact zones (Fig. 5.1f and Fig. 5.2c) possibly reflects this coupled iron oxidation-sulfate reduction reaction.

Finally, the stronger degree of alteration below the barite could be explained by the relatively impermeable nature of the chert-barite unit and the release of fluids from underlying seafloor basalts during burial and heating of the succession. Fluids generated by the dehydration of hydrous mafic minerals during prograde metamorphism could have been retained at depth and released during uplift of the metamorphic pile when the decreasing lithostatic pressure facilitated transport through hydraulic fracturing (Morris and Henley, 1976). Following the model by Etheridge et al. (1983), localized and active circulation of these fluids

would be expected below the less permeable chert-barite unit with significant (more than 5 km) lateral extent (Barton, 1982). The subsequent increase in fluid pressure below this impermeable layer would result in localized hydraulic fracturing (Etheridge et al., 1983; Pirajno, 2009), consistent with the presence of extensional fractures with witherite and the large volume increase inferred from isocon analyses. Chemical exchange between rocks underlying and overlying the barite horizon was probably limited due to this impermeable barrier (Etheridge et al., 1983), which explains the minimal barium enrichment and lack of Ba-feldspars in the felsic schists.

5.6.4 Implications

5.6.4.1 Environment of barite deposition

Geochemical data from the silica alteration zone provide evidence for venting of barium-rich hydrothermal fluids into the Paleoarchean marine environment, since barium concentrations in the silicified pillows were significantly elevated above the 91 ppm Ba in the unaltered pillows (Table 5.2), or 155 ppm Ba in the Onverwacht Group komatiites located 40 m below the main barite zone (Barton, 1982). This confirms earlier suggestions that the barium in barite was derived from a hydrothermal source and that sulfate came from seawater (as outlined in Chapter 2). In addition, the low-temperature alteration inferred for the Londozi succession was similar to hydrothermal settings proposed for the formation of chert deposits and silicified volcanics elsewhere in the Barberton Greenstone Belt (Hofmann and Wilson, 2007; Hofmann and Harris, 2008; Hofmann, 2011), which host textural and chemical evidence for rich microbial ecosystems (Walsh, 1992; Westall et al., 2001; Furnes et al., 2004; Tice and Lowe, 2006). As such, the presence of sulfate-reducing micro-organisms in basins where barite was deposited and their important role in the early marine sulfur cycle (Chapter 2) is consistent with the low-temperature conditions inferred for the environment of barite deposition.

5.6.4.2 Sulfide mobility during metasomatic alteration

Reductive barite dissolution during metamorphism could result in significant remobilization of barium and sulfur (Kritsotakis and Von Platen, 1980). Although dissolution processes probably occurred on a relatively small scale since evidence

for complete remobilization of the barite deposit at Londozi is lacking, the amount of sulfide produced from sulfate reduction can be significant compared to the volume of the microscopic pyrite grains. For example, precipitation of an arbitrary spherical pyrite grain with a diameter of 100 µm requires circa 8.7 x 10^{-4} moles of sulfur, which corresponds to the dissolution of less than 0.05 cm^3 of barite (see Appendix 5A for calculation). Thus, the remobilization of small quantities of barite can result in the formation of secondary microscopic sulfides in addition to the primary pyrite that survived high-grade metamorphism, as was previously suggested for sphalerite in the Sterling Hill skarn deposit of New Jersey (Tracy, 1991) and sulfides in schists from the Southern Alps of New Zealand (Grapes, 1993). Both authors linked sulfide formation to the breakdown of barite and metamorphic sulfate reduction. Microscopic pyrite associated with the Londozi barite deposit may be of similar abiotic origin. Thus, whereas dissolution of primary pyrite was unlikely under the reducing conditions of barium metasomatism (e.g. Rickard and Luther, 2007), the possible formation of mixed populations of sulfides by these abiotic pathways must be taken into account when interpreting pyrite sulfur isotope data.

5.7 CONCLUSIONS

Geochemical and mineralogical data presented in this study provide insights into seafloor hydrothermal processes during and metasomatic alteration after deposition of the 3.52 Ga Londozi barite deposit and related volcanics in the Barberton Greenstone Belt, Swaziland. Field observations revealed the presence of silica alteration zones in association with silicified pillow lavas, derived from mafic and komatiitic volcanic precursors. Strong enrichment in SiO_2, K_2O and Ba versus depletion in major elements and transition metals was interpreted to reflect widespread low-temperature (100-150°C) seafloor alteration processes, consistent with submarine volcanism in an oceanic plateau setting (Chapter 4) and equivalent geochemical patterns from other Paleoarchean silicified successions (Hofmann and Wilson, 2007; Hofmann and Harris, 2008; Hofmann, 2011). The associated barium-enrichment supports hydrothermal input of barium during barite precipitation and therefore agrees with the sulfur isotopic composition of the Londozi barite reported in Chapter 2. A second type of alteration zone was observed immediately below the barite horizon in the waterfall section and was characterized by highly altered, silicified and green-

colored schists with witherite-bearing fractures. Element depth profiles provide evidence for metasomatic events different from low-temperature silica alteration, and comparison with the least altered schists demonstrates enrichment in Si, K, Mg, Ba, Sr, S and transition metals Cu, Zn, Cr and Ni suggesting high-temperature processes (above 300°C). Barium-rich silicates celsian, hyalophane and armenite were abundant in this alteration zone and were closely associated with retrograde actinolite, suggesting post-depositional mobility of barium. The strong link between barite and high-celsian feldspar supports remobilization of barium from barite by reductive dissolution during metamorphism, probably accompanied by the oxidation of methane forming carbonate minerals witherite and calcite, or ferrous iron in pyroxene and amphibole resulting in the formation of monomineralic epidote and grossular-andradite. Reduced sulfur produced during metamorphic sulfate reduction may have precipitated as pyrite, resulting in a secondary sulfide population in addition to any primary sedimentary or igneous pyrite.

Acknowledgements

We gratefully acknowledge Simon Maphanga and the Geological Survey and Mines Department of Swaziland for their help with sample logistics and providing access to geological maps and mining reports. Willem van der Bilt is thanked for his field assistance and help with sample collection. We thank Otto Stiekema for the preparation of thin sections, Tilly Bouten for technical support during electron microprobe analyses and Helen de Waard for sample digestion, ICP-OES and ICP-MS analyses. This research was funded by a grant from the User Support Programme Space Research and the Netherlands Organization for Scientific Research (NWO).

References

Arndt, N., 2003. Komatiites, kimberlites, and boninites. J. Geophys. Res. 108, 2293.

Arndt, N., Bruzak, G., Reischmann, T., 2001. The oldest continental and oceanic plateaus: Geochemistry of basalts and komatiites of the Pilbara Craton, Australia. Geological Society of America Special Papers 352, 359-387.

Arndt, N.T., Condie, K.C., 1994. Chapter 1 Archean Komatiites, Dev. Precambrian Geol. Elsevier, pp. 11-44.

Banerjee, N.R., Honnorez, J., Muehlenbachs, K., 2004. Low-temperature alteration of submarine basalts from the Ontong Java Plateau. Geological Society, London, Special Publications 229, 259-273.

Barley, M.E., Dunlop, J.S.R., Glover, J.E., Groves, D.I., 1979. Sedimentary evidence for an archaean shallow-water volcanic-sedimentary facies, Eastern Pilbara Block, Western Australia. Earth Planet. Sci. Lett. 43, 74-84.

Barton, C.M., 1982. Geology and mineral resources of Northwest Swaziland (Barberton Greenstone Belt). Bulletin of the Swaziland Geological Survey and Mines Department 10.

Blount, C.W., 1977. Barite solubilities and thermodynamic quantities up to 300 degrees C and 1400 bars. Am. Mineral. 62, 942-957.

Buick, R., Dunlop, J.S.R., 1990. Evaporitic sediments of Early Archaean age from the Warrawoona Group, North Pole, Western Australia. Sedimentology 37, 247-277.

Candela, P.A., 2003. 3.12 - Ores in the Earth's Crust, in: Holland, H.D., Turekian, K.K. (Eds.), Treatise on Geochemistry. Pergamon, Oxford, pp. 411-430.

Chabu, M., Boulègue, J., 1992. Barian feldspar and muscovite from the Kipushi Zn-Pb-Cu deposit, Shaba, Zaire. Can. Mineral. 30, 1143-1152.

De Ronde, C.E.J., De Wit, M.J., 1994. Tectonic history of the Barberton greenstone belt, South Africa: 490 million years of Archean crustal evolution. Tectonics 13, 983-1005.

Diener, J.F.A., Stevens, G., Kisters, A.F.M., Poujol, M., 2005. Metamorphism and exhumation of the basal parts of the Barberton greenstone belt, South Africa: Constraining the rates of

Mesoarchaean tectonism. Precambrian Res. 143, 87-112.

Droop, G.T.R., 1987. A general equation for estimating Fe^{3+} concentrations in ferromagnesian sillicates and oxides from microprobe analyses, using stoichiometric criteria. Mineral. Mag. 51, 431-435.

Duchac, K.C., Hanor, J.S., 1987. Origin and timing of the metasomatic silicification of an early archean komatiite sequence, barberton mountain land, South Africa. Precambrian Res. 37, 125-146.

Dziggel, A., Stevens, G., Poujol, M., Anhaeusser, C.R., Armstrong, R.A., 2002. Metamorphism of the granite-greenstone terrane south of the Barberton greenstone belt, South Africa: an insight into the tectono-thermal evolution of the 'lower' portions of the Onverwacht Group. Precambrian Res. 114, 221-247.

Elderfield, H., Schultz, A., 1996. Mid-ocean ridge hydrothermal fluxes and the chemical composition of the ocean. Annual Review of Earth and Planetary Sciences 24, 191-224.

Essene, E.J., Claflin, C.L., Giorgetti, G., Mata, P.M., Peacor, D.R., Arkai, P., Rathmell, M.A., 2005. Two-, three- and four-feldspar assemblages with hyalophane and celsian: implications for phase equilibria in $BaAl_2Si_2O_8$-$CaAl_2Si_2O_8$-$NaAlSi_3O_8$-$KAlSi_3O_8$. Eur. J. Mineral. 17, 515-535.

Etheridge, M.A., Wall, V.J., Vernon, R.H., 1983. The role of the fluid phase during regional metamorphism and deformation. J. Metamorph. Geol. 1, 205-226.

Furnes, H., Banerjee, N.R., Muehlenbachs, K., Staudigel, H., de Wit, M., 2004. Early Life Recorded in Archean Pillow Lavas. Science 304, 578-581.

Grant, J.A., 1986. The isocon diagram; a simple solution to Gresens' equation for metasomatic alteration. Econ. Geol. 81, 1976-1982.

Grapes, R., 1993. Barian mica and distribution of barium in metacherts and quartzofeldspathic schists, Southern Alps, New Zealand. Mineral. Mag. 57, 265-272.

Heinrichs, T.K., Reimer, T., 1977. A sedimentary barite deposit from the Archean Fig Tree Group of the Barberton Mountain Land (South Africa). Econ. Geol. 72, 1426-1441.

Hofmann, A., 2011. Archaean Hydrothermal Systems in the Barberton Greenstone Belt and Their Significance as a Habitat for Early Life, in: Golding, S.D., Glikson, M. (Eds.), Earliest Life on Earth: Habitats, Environments and Methods of Detection. Springer Netherlands, pp. 51-78.

Hofmann, A., Harris, C., 2008. Silica alteration zones in the Barberton greenstone belt: A window into subseafloor processes 3.5-3.3 Ga ago. Chem. Geol. 257, 221-239.

Hofmann, A., Wilson, A.H., 2007. Chapter 5.5 Silicified basalts, bedded cherts and other sea floor alteration phenomena of the 3.4 Ga Nondweni Greenstone Belt, South Africa, in: Kranendonk, M.J.v., Smithies, R.H., Vickie, C.B. (Eds.), Earth's Oldest Rocks. Developments in Precambrian Geology. Elsevier, pp. 571-605.

Huston, D.L., Logan, G.A., 2004. Barite, BIFs and bugs: evidence for the evolution of the Earth's early hydrosphere. Earth Planet. Sci. Lett. 220, 41-55.

Jewell, P.W., 2000. Bedded barite in the geologic record, Marine Authigenesis: From Global to Microbial. SEPM (Society for Sedimentary Geology), pp. 147-161.

Kisters, A.F.M., Anhaeusser, C.R., 1995. The structural significance of the Steynsdorp pluton and anticline

within the tectono-magmatic framework of the Barberton Mountain Land. S. Afr. J. Geol. 98, 43-51.

Kisters, A.F.M., Stevens, G., Dziggel, A., Armstrong, R.A., 2003. Extensional detachment faulting and core-complex formation in the southern Barberton granite-greenstone terrain, South Africa: evidence for a 3.2 Ga orogenic collapse. Precambrian Res. 127, 355-378.

Kritsotakis, K., Von Platen, H., 1980. Reduktive Barytmobilisation. Neues Jahrb. Mineral. Abh. 137, 282-306.

Kröner, A., Hegner, E., Wendt, J.I., Byerly, G.R., 1996. The oldest part of the Barberton granitoid-greenstone terrain, South Africa: evidence for crust formation between 3.5 and 3.7 Ga. Precambrian Res. 78, 105-124.

Kurnosov, V., Zolotarev, B., Artamonov, A., Garanina, S., Petrova, V., Eroshchev-Shak, V.S., A., 2003. Data report: Alteration of basalts from the Kerguelen Plateau, in: Frey, F.A., Coffin, M.F., Wallace, P.J., Quilty, P.G. (Eds.), Proceedings of the Ocean Drilling Program, Scientific Results: vol. 183.

Lana, C., Kisters, A.F.M., Stevens, G., 2010. Exhumation of Mesoarchean TTG gneisses from the middle crust: Insights from the Steynsdorp core complex, Barberton granitoid-greenstone terrain, South Africa. Geol. Soc. Am. Bull. 122, 183-197.

Lazar, C., Manning, C.E., 2005. Thermodynamic modeling of methane production in Early Archean crust by serpentinization: implications for atmospheric methane. Eos Trans. Am. Geophys. Union 86, Abstract V51B-1484.

Lowe, D.R., Byerly, G.R., 1986. Archaean flow-top alteration zones formed initially in a low-temperature sulphate-rich environment. Nature 324, 245-248.

McCollom, T.M., Bach, W., 2009. Thermodynamic constraints on hydrogen generation during serpentinization of ultramafic rocks. Geochim. Cosmochim. Acta 73, 856-875.

Morris, R.J., Henley, R.W., 1976. Dewatering of a metamorphic pile. Geology 4, 333-336.

Mottl, M.J., Holland, H.D., 1978. Chemical exchange during hydrothermal alteration of basalt by seawater--I. Experimental results for major and minor components of seawater. Geochim. Cosmochim. Acta 42, 1103-1115.

Mottl, M.J., Holland, H.D., Corr, R.F., 1979. Chemical exchange during hydrothermal alteration of basalt by seawater--II. Experimental results for Fe, Mn, and sulfur species. Geochim. Cosmochim. Acta 43, 869-884.

Pan, Y., Fleet, M.E., 1991. Barian feldspar and barian-chromian muscovite from the Hemlo area, Ontario. Can. Mineral. 29, 481-498.

Philippot, P., Van Zuilen, M., Lepot, K., Thomazo, C., Farquhar, J., Van Kranendonk, M.J., 2007. Early Archaean Microorganisms Preferred Elemental Sulfur, Not Sulfate. Science 317, 1534-1537.

Pirajno, F., 2009. Orogenic, Amagmatic and Hydrothermal Mineral Systems of Uncertain Origin, Hydrothermal Processes and Mineral Systems. Springer Netherlands, pp. 885-1023.

Powell, R., Will, T.M., Phillips, G.N., 1991. Metamorphism in Archean greenstone belts: calculated fluid compositions and implications for gold mineralization. J. Metamorph. Geol. 9, 141-150.

Reimer, T.O., 1980. Archean sedimentary baryte deposits of the Swaziland Supergroup (Barberton Mountain

Land, South Africa). Precambrian Res. 12, 393-410.
Rickard, D., Luther, G.W., III, 2007. Chemistry of Iron Sulfides. ChemInform 38, no-no.
Seewald, J.S., Seyfried Jr, W.E., 1990. The effect of temperature on metal mobility in subseafloor hydrothermal systems: constraints from basalt alteration experiments. Earth Planet. Sci. Lett. 101, 388-403.
Seyfried, W.E., 1987. Experimental and Theoretical Constraints on Hydrothermal Alteration Processes at Mid-Ocean Ridges. Annual Review of Earth and Planetary Sciences 15, 317-335.
Shanks, W.C., Bischoff, J.L., Rosenbauer, R.J., 1981. Seawater sulfate reduction and sulfur isotope fractionation in basaltic systems: Interaction of seawater with fayalite and magnetite at 200-350°C. Geochim. Cosmochim. Acta 45, 1977-1995.
Shen, Y., Buick, R., Canfield, D.E., 2001. Isotopic evidence for microbial sulphate reduction in the early Archaean era. Nature 410, 77-81.
Shen, Y., Farquhar, J., Masterson, A., Kaufman, A.J., Buick, R., 2009. Evaluating the role of microbial sulfate reduction in the early Archean using quadruple isotope systematics. Earth Planet. Sci. Lett. 279, 383-391.
Siever, R., 1991. The silica cycle in the Precambrian. Geochim. Cosmochim. Acta 56, 3265-3272.
Staudigel, H., 2003. 3.15 - Hydrothermal Alteration Processes in the Oceanic Crust, in: Holland, H.D., Turekian, K.K. (Eds.), Treatise on Geochemistry. Pergamon, Oxford, pp. 511-535.
Staudigel, H., Hart, S.R., 1983. Alteration of basaltic glass: Mechanisms and significance for the oceanic crust-seawater budget. Geochim. Cosmochim. Acta 47, 337-350.
Sun, S.S., 1987. Chemical composition of Archaean komatiites: implications for early history of the earth and mantle evolution. J. Volcanol. Geotherm. Res. 32, 67-82.
Tice, M.M., Lowe, D.R., 2006. The origin of carbonaceous matter in pre-3.0 Ga greenstone terrains: A review and new evidence from the 3.42 Ga Buck Reef Chert. Earth-Science Reviews 76, 259-300.
Tracy, R.J., 1991. Ba-rich micas from the Franklin Marble, Lime Crest and Sterling Hill, New Jersey. Am. Mineral. 76, 1683-1693.
Ueno, Y., Ono, S., Rumble, D., Maruyama, S., 2008. Quadruple sulfur isotope analysis of ca. 3.5 Ga Dresser Formation: New evidence for microbial sulfate reduction in the early Archean. Geochim. Cosmochim. Acta 72, 5675-5691.
van Dijk, D., Houba, V.J.G., 2000. Homogeneity and stability of materials distributed within the wageningen evaluating programmes for analytical laboratories. Commun. Soil Sci. Plant Anal. 31, 1745-1756.
Van Kranendonk, M.J., Pirajno, F., 2004. Geochemistry of metabasalts and hydrothermal alteration zones associated with c. 3.45 Ga chert and barite deposits: implications for the geological setting of the Warrawoona Group, Pilbara Craton, Australia. Geochem. Explor. Environ. Anal. 4, 253-278.
Walsh, M.W., 1992. Microfossils and possible microfossils from the early archean onverwacht group, Barberton mountain land, South Africa. Precambrian Res. 54, 271-293.
Westall, F., de Wit, M.J., Dann, J., van der Gaast, S., de Ronde, C.E.J., Gerneke, D., 2001. Early Archean fossil bacteria and biofilms in hydrothermally-influenced sediments from the

Barberton greenstone belt, South Africa. Precambrian Res. 106, 93-116.
Zhao, X., Antretter, M., Kroenke, L., Rilsager, P., Hall, S., 2004. Relationships between physical properties and alteration in basement rocks from the Ontong Java Plateau, in: Fitton, J.G., Mahoney, J.J., Wallace, P.J., Saunders, A.D. (Eds.), Proceedings of the Ocean Drilling Program, Scientific Results: vol. 192.

APPENDIX 5A

Amount of barite dissolution required for one pyrite grain

In this calculation, we assume a spherical pyrite grain with a diameter of 100 μm, similar to the dimensions of pyrite found in association with the Londozi barite deposit. The volume of this a spherical pyrite grain with a diameter of 100 μm is equal to:

$V = 4/3\pi r^2 = 4/3 \times \pi \times (50 \times 10^{-6}\ m)^2 = 1.05 \times 10^{-8}\ m^3$.

Assuming a density of 5000 kg m^{-3} for pyrite (www.mindat.org), the mass of this grain is:

$5000\ kg\ m^{-3} \times 1.05 \times 10^{-8}\ m^3 = 5.24 \times 10^{-5}$ kg.

Using a molar weight for FeS_2 of 0.120 kg mol^{-1}, this equals the following number of moles:

5.24×10^{-5} kg/0.120 kg $mol^{-1} = 4.36 \times 10^{-4}$ moles of FeS_2,

which is equal to half the number of moles of S in the pyrite grain:

$2 \times 4.36 \times 10^{-4} = 8.73 \times 10^{-4}$ moles of S

Based on the stoichiometry of the reaction for barite dissolution, e.g. by reduced carbon: $BaSO_4 + C_{org} = Ba^{2+} + S^{2-} + 2CO_2$, the required number of moles of barite is equal to the number of moles S in pyrite.

Using a molar weight for $BaSO_4$ of 0.234 kg mol^{-1}, this equals this amount of barite:

8.73×10^{-4} mol x 0.234 kg $mol^{-1} = 2.04 \times 10^{-4}$ kg,

which is equal to the following volume (assuming a density of 4500 kg m^{-3} for barite):

2.04×10^{-4} kg/4500 kg $m^{-3} = 4.54 \times 10^{-8}\ m^3$ or 0.045 cm^3 of barite.

Thus: the formation of a pyrite grain with a diameter of 100 μm requires the dissolution of only 0.045 cm^3 or 0.2 g of barite, if all sulfide that is formed is trapped in the pyrite.

White rhinoceros in Hlane Royal National Park, Lumbobo, Swaziland

Chapter 6

Assessing the origin of ^{34}S-depleted pyrite from the >3.52 Ga Londozi barite deposit, Swaziland using high-resolution quadruple sulfur isotope data

This chapter will be submitted to Geology with co-authors Paul R.D. Mason, Martin J. Whitehouse and Thomas Reimer.

ABSTRACT

Sulfur isotopes in Paleoarchean pyrite provide important insights into the earliest metabolic processes on Earth. Here, we present quadruple sulfur isotopic compositions (^{32}S, ^{33}S, ^{34}S, ^{36}S) of pyrite from the >3.52 Ga Londozi barite deposit and associated mafic amphibolites in the Theespruit Formation of the Lower Onverwacht Group, Barberton Greenstone Belt, Swaziland, and assess the biogenicity of these signatures. Results obtained by secondary ion mass spectrometry demonstrate the presence of two distinct pyrite populations in the barite and the metavolcanics. Amphibolite-hosted pyrite displays near-zero $\delta^{34}S$ and less negative $\Delta^{33}S$ than observed in the barite, suggesting mixing of mantle-derived sulfur with hydrothermally or microbially-reduced seawater sulfate. In contrast, barite-hosted pyrite is strongly ^{34}S-depleted relative to the barite (5-18‰), with similar $\Delta^{33}S$ to the barite but significantly more positive $\Delta^{36}S$. Although $\delta^{34}S$-values agree with microbial sulfate reduction, minor isotope signatures are inconsistent with results from laboratory culture studies. Alternatively, pyrite $\delta^{34}S$-values and ^{36}S-enrichment could be explained by high-temperature equilibrium fractionation and small-scale mixing processes related to complex reaction pathways, consistent with the reductive dissolution of barite during metamorphism. This study demonstrates that measurement of ^{36}S is essential for the correct interpretation of sulfur isotope data from deposits with a complex geological history.

6.1 INTRODUCTION

Multiple sulfur isotopic compositions of pyrite from Paleoarchean barite deposits preserve a comprehensive record of atmospheric and biological processes involved in the early sulfur cycle. Significant mass-dependent isotope fractionation ($\delta^{34}S$) observed in pyrite from well-preserved barite in the low-metamorphic grade 3.49 Ga Dresser Formation of Western Australia provide evidence for early microbial sulfate reduction (Shen et al., 2001; Ueno et al., 2008; Shen et al., 2009) and elemental sulfur metabolisms (Philippot et al., 2007), whereas anomalous fractionation of the minor isotopes ($\Delta^{33}S$, $\Delta^{36}S$) was interpreted to reflect photochemical reactions of volcanic sulfur dioxide in an anoxic atmosphere (Farquhar et al., 2000; Farquhar et al., 2001; Pavlov and Kasting, 2002). Similar conclusions were obtained from quadruple sulfur isotope signatures of pyrite from the 3.26-3.23 Ga Barite Valley deposit of South Africa (Chapter 3 and Philippot et al., 2012), demonstrating the preservation of distinct isotopic arrays in relation to variable sulfate concentrations.

Disseminated pyrite was also found in association with the >3.52 Ga Londozi barite deposit from the Theespruit Formation in the Lower Onverwacht Group of the Barberton Greenstone Belt, Swaziland, which represents the oldest-known occurrence of sulfate on Earth and therefore enables expansion of the sulfide isotope record back in time by at least 30 million years. Geological and geochemical evidence indicates that the barite deposit formed in an oceanic plateau setting with submarine mafic volcanism and widespread low-temperature hydrothermal activity (Reimer, 1980; Chapter 4 and Chapter 5), providing a plausible habitat for early sulfate-reducing micro-organisms as previously suggested from sulfur isotopic compositions of the barite in Chapter 2. Further insights into the microbial metabolisms present during barite deposition could be obtained from isotopic analyses of the pyrite grains, but the amphibolite facies metamorphism (Chapter 4) and extensive metasomatism (Chapter 5) that affected the Londozi deposit requires analyses of all four stable sulfur isotopes (^{32}S, ^{33}S, ^{34}S, ^{36}S) to evaluate evidence for high-temperature abiotic fractionation pathways in addition to biological processes.

This study reports on the quadruple sulfur isotopic compositions of pyrite from the Londozi barite deposit, analyzed in situ by secondary ion mass spectrometry (SIMS). Our high-resolution analytical technique enables us to compare isotope signatures in barite-hosted and amphibolite-hosted pyrite grains, whereas the supplementary measurement of $\Delta^{36}S$ provides important

insights into the biogenicity of observed isotopic variability. We assess the origin of strongly ^{34}S-depleted pyrite in the oldest sulfate deposit on Earth and postulate an abiotic, not biological origin for these isotope effects.

6.2 MATERIAL AND METHODS

6.2.1 Pyrite samples

Samples were collected from surface outcrops and within disused mine and quarry workings of the Londozi barite deposit in the Barberton Greenstone Belt, Swaziland (Fig. 6.1). Three pyrite-bearing rock fragments were selected for isotopic analyses, of which two samples contained subhedral to euhedral pyrite of 100-600 μm within amphibolite host rock consisting of feldspar, quartz and hornblende minerals. The other sample consisted of a barite matrix with disseminated anhedral to subhedral pyrite grains of ca. 100-400 μm. Rock fragments were mounted in epoxy blocks, polished and gold coated using preparation procedures for SIMS sulfur isotope analyses described in Chapter 3.

6.2.2 Quadruple sulfur isotope analyses

Measurement of all four stable sulfur isotopes (^{32}S, ^{33}S, ^{34}S, ^{36}S) in pyrite was done using a CAMECA IMS-1280 instrument at the Swedish Museum of Natural History (Nordsim facility) during three sessions in 2009, 2010 and 2012. Instrument parameters and methods followed those described by Whitehouse et al. (2005), Kamber and Whitehouse (2007) and Ulrich et al. (2011) for the collection of triple isotope data (^{32}S, ^{33}S, ^{34}S), and by Whitehouse (2012) for quadruple isotope data. The Ruttan pyrite standard was used as the primary reference to correct raw sulfur isotope ratios for instrumental mass bias, while both Ruttan and Balmat reference pyrites were used to constrain the mass dependent fractionation line (Crowe and Vaughan, 1996). Measured isotopic compositions of these standards are reported in Supplementary Tables S6-1 and S6-2[*]. External precision on $\delta^{34}S$, $\Delta^{33}S$ and $\Delta^{36}S$ was propagated together with

[*] Supplementary tables from this chapter are available at http://hdl.handle.net/10411/10146.

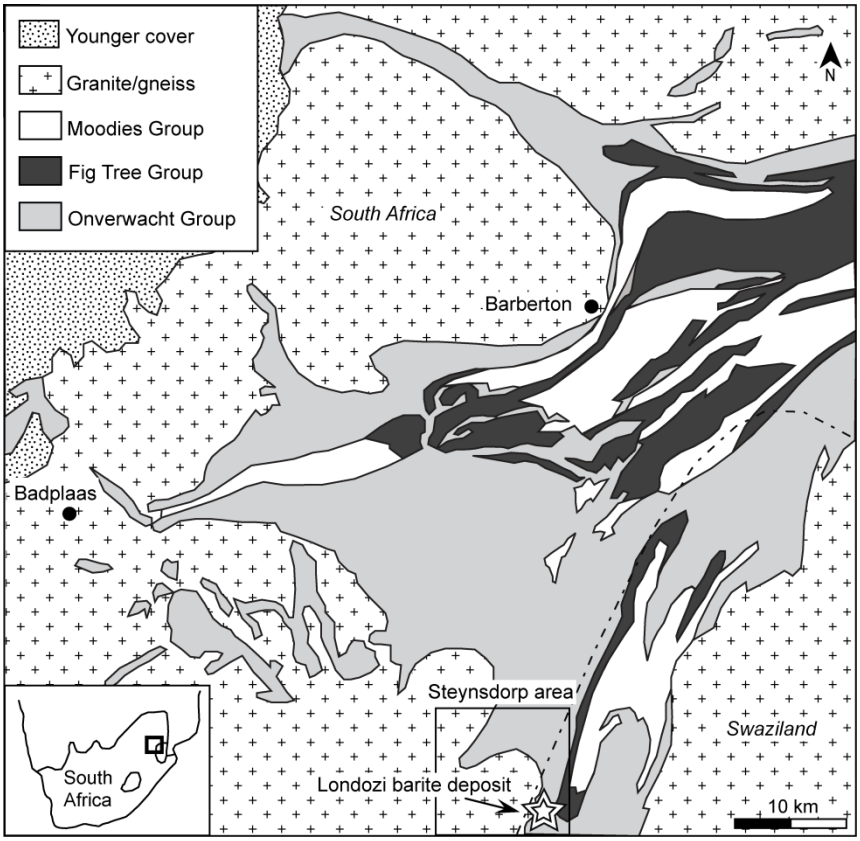

Figure 6.1 *Map of the Barberton Greenstone Belt in South Africa and Swaziland, showing the location of the Londozi barite deposit within the Steynsdorp area. Modified after Hofmann (2005).*

internal errors to yield typical overall 1σ uncertainties of 0.2‰ on $\delta^{34}S$ and $\Delta^{33}S$, and 0.5‰ on $\Delta^{36}S$ for analyses where the secondary ion signal on ^{32}S was ~10^9 cps. Analyses of the Isua sulfide monitor (Supplementary Table S6-3) yielded weighted averages of $\delta^{34}S$ = 2.54 ± 0.06‰ (n = 31, MSWD = 1.2), $\Delta^{33}S$ = 3.18 ± 0.05‰ (n = 31, MSWD = 0.7) and $\Delta^{36}S$ = -2.14 ± 0.20‰ (n = 19, MSWD = 1.2), which is in good agreement with previously published results from conventional and SIMS sulfur isotope analyses (Baublys et al., 2004; Whitehouse, 2012). In addition, mass-dependent fractionation lines defined by the Ruttan and Balmat standards yielded slopes of $\delta^{33}S/\delta^{34}S$ = 0.5123 ± 0.0047 and $\delta^{36}S/\delta^{34}S$ = 1.923 ± 0.02, which are consistent with fractionation relationships for equilibrium processes (Hulston and

Thode, 1965). Finally, highly anomalous isotope effects ($\Delta^{33}S$ = +10‰ and $\Delta^{36}S$ = -80‰) were observed when DTFA-settings exceeded 5000 for the y-position, reflecting excessive de-centering of the secondary ion beam to the field aperture for these spot locations. Results were therefore filtered to include only analyses with DTFA y-values between -5000 and +5000.

6.3 RESULTS

Sulfur isotopic compositions of analyzed pyrite grains are shown in Fig. 6.2 and Fig. 6.3 and listed in Supplementary Table S6-4. Measured $\delta^{34}S$-values of amphibolite-hosted pyrite (n = 93) include both negative and positive values, with $\delta^{34}S$ between -3.0 and +2.1‰ (average $\delta^{34}S$ = -0.1‰, Fig. 6.2a). Covariation between $\delta^{33}S$ and $\delta^{34}S$ is defined by $\delta^{33}S/\delta^{34}S$ = 0.525 ± 0.035 and intercept $\delta^{33}S$ = -0.55 ± 0.036‰, consistent $\Delta^{33}S$-values between -1.0 and 0.0‰ (average $\Delta^{33}S$ = -0.5‰). These values are less negative in $\Delta^{33}S$ than those reported for the barite-sulfate in Chapter 2. Measurement of $\Delta^{36}S$ demonstrates variability from -0.7 to +1.9‰ (n = 27; Fig. 6.2b), with data points plotting both above and below the Archean reference line of $\Delta^{36}S/\Delta^{33}S$ = -1 (Farquhar et al., 2000; Kaufman et al., 2007; Ueno et al., 2008). The average slope of $\Delta^{36}S$ versus $\Delta^{33}S$ was calculated as -3.1 ± 1.5.

Distinct isotopic values were measured in barite-hosted pyrite (n = 30), with $\delta^{34}S$-values ranging from -9.1 to -1.0‰ with an average of -6.1‰ (Fig. 6.3a) and showing depletion in ^{34}S of 5-18‰ relative to the isotopic composition of the Londozi barite (Chapter 2). Values of $\delta^{34}S$ co-vary with $\delta^{33}S$ following $\delta^{33}S/\delta^{34}S$ = 0.532 ± 0.032 (MSWD = 1.5) and a non-zero intercept for $\delta^{33}S$ of -0.82 ± 0.21‰, corresponding to mass-independent isotope signatures for $\Delta^{33}S$ between -0.7 and -1.2‰ (average $\Delta^{33}S$ = -0.9‰). In addition, $\Delta^{36}S$-values (n = 14) were measured between 1.1 and 3.1‰ (Fig. 6.3b). The relatively small range in $\Delta^{33}S$ hampers calculation of accurate values for $\Delta^{36}S/\Delta^{33}S$, but Fig. 6.4b demonstrates that mass-independent signatures plot above the Archean reference array with $\Delta^{36}S/\Delta^{33}S$ = -1 (Farquhar et al., 2000; Kaufman et al., 2007; Ueno et al., 2008) and are shifted towards more positive $\Delta^{36}S$-values relative to the barite.

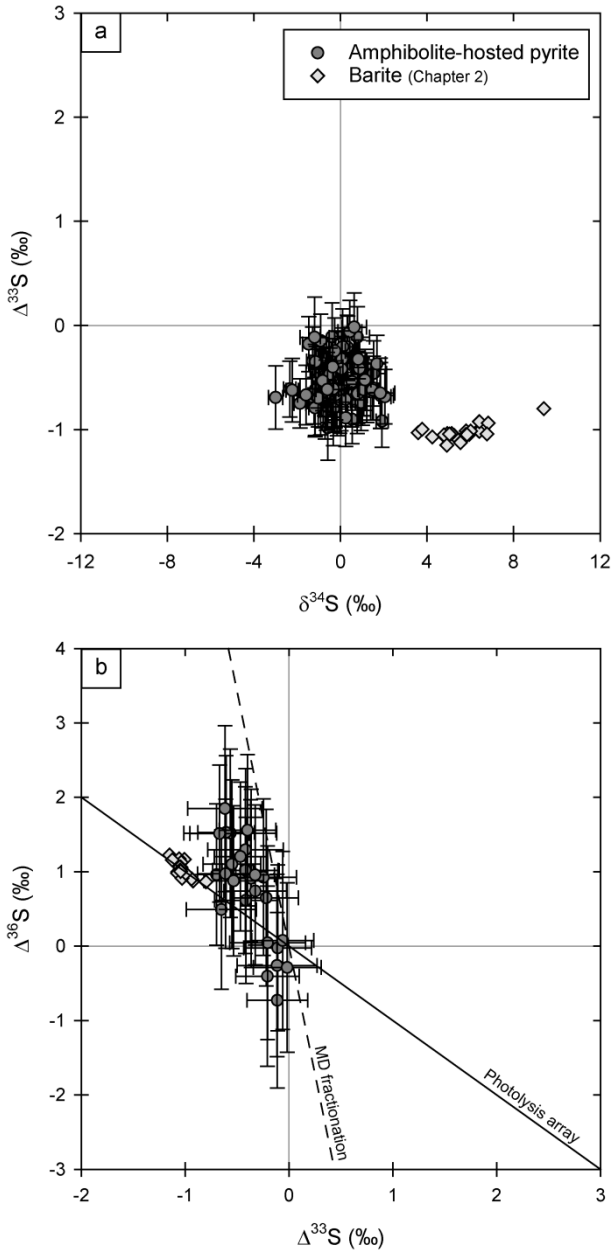

Figure 6.2 *Sulfur isotopic compositions of amphibolite-hosted pyrite, with (a) $\Delta^{33}S$ versus $\delta^{34}S$ and (b) $\Delta^{36}S$ versus $\Delta^{33}S$. The isotopic composition of the Londozi barite (bulk analyses) is shown for comparison (see Chapter 2). Lines indicate trends expected for mass-dependent (MD) fractionation (Ono et al, 2006) and the Archean reference array with $\Delta^{36}S/\Delta^{33}S = -1$ (Farquhar et al., 2000; Kaufman et al., 2007; Ueno et al., 2008). Error bars indicate 2σ errors.*

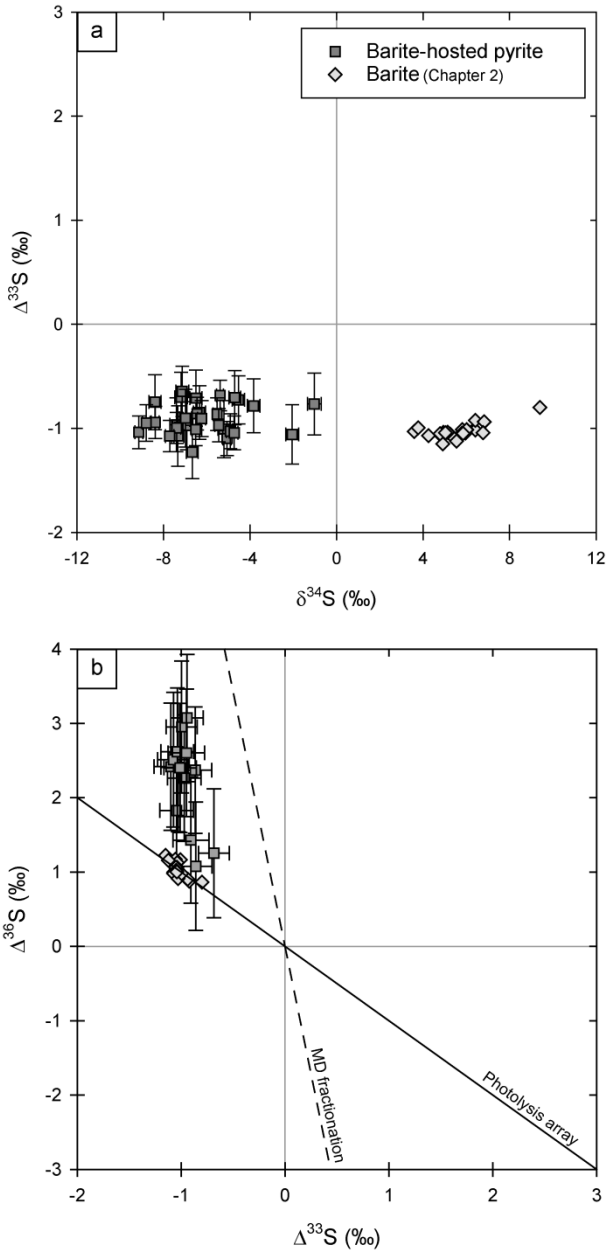

Figure 6.3 *Quadruple sulfur isotopic compositions of amphibolite-hosted pyrite, with (a) plot of $\Delta^{33}S$ versus $\delta^{34}S$ and (b) plot of $\Delta^{36}S$ versus $\Delta^{33}S$. See caption of Fig. 6.2 for explanation of lines. Error bars indicate 2σ errors.*

6.4 DISCUSSION

Our in situ quadruple sulfur isotope data demonstrate the presence of two compositionally distinct sulfide populations in association with two different lithological units in the >3.52 Ga Londozi barite deposit, suggesting that different pathways of pyrite formation operated during the formation and metamorphism of these Paleoarchean supracrustal rocks. In the following discussion, we focus on the processes that produced this variability in amphibolite-hosted and barite-hosted pyrite, and evaluate the presence of potential microbial signatures using the minor sulfur isotopes ^{33}S and ^{36}S.

6.4.1 Mixing of mantle- and seawater-derived sulfide

Mafic amphibolites underlying the Londozi barite deposit were previously interpreted to reflect precursor rocks produced by submarine volcanism in an oceanic plateau setting (Chapter 4), overprinted by low-temperature (100-150°C) diffuse venting of hydrothermal fluids (Chapter5). Therefore, the pyrite found in these lithologies could be associated with sulfur from magmatic sources related to the eruption of mafic and ultramafic volcanics, hydrothermal reduction of seawater sulfate at temperatures above 100°C (Shanks et al., 1981; Machel, 2001), or microbial sulfate reduction in relatively low-temperature niches. The near-zero average $\delta^{34}S$ of the amphibolite-hosted pyrite and the small variation in $\delta^{34}S$-values from -3.0 to +2.1‰ (Fig. 6.2a) is consistent with mantle-derived juvenile sulfur and significant inputs of magmatic sulfide (Marini et al., 2011). However, non-zero mass independent signatures indicate that atmospherically-derived sulfur was also present (Farquhar et al., 2000), with negative $\Delta^{33}S$-values indicating a sulfide component derived from the reduction of seawater sulfate. Isotopic compositions range from $\Delta^{33}S$-values similar to the average value of $\Delta^{33}S$ = -1.03‰ reported for the Londozi barite (Chapter 2) to near-zero values reflecting juvenile sulfur, suggesting that the pyrite-sulfur represents a mixture of sulfide from both sources. Mixing pathways are also consistent with the variation observed in minor isotope signatures (Fig. 6.2b). Calculations by Ono et al. (2006) demonstrated that mixing of two sulfur pools produces compositions with higher $\Delta^{36}S$, so that mixing of juvenile sulfide with mass-independently fractionated sulfide derived from sulfate produces sulfur compositions that plot slightly above the Archean reference array. Although error bars are relatively large, similar weak

^{36}S-enrichment appears to be present in the amphibolite-hosted pyrite (Fig. 6.2b). As such, these data seem consistent with mixing of sulfur from a hydrothermal or magmatic source ($\Delta^{33}S = \Delta^{36}S = 0‰$) and sulfide derived from seawater-sulfate through microbial or hydrothermal reduction. Unfortunately, it is difficult to distinguish between these biological and abiotic pathways on the basis of mass-independent signatures (as done by Ueno et al., 2008; Shen et al., 2009), because primary changes in $\Delta^{33}S$ and $\Delta^{36}S$ are overprinted by secondary mixing processes. The presence of a sulfide pool derived from local microbial sulfate reduction was suggested from the co-variation of sulfur isotopic signatures in the Londozi barite in Chapter 2, but this cannot be confirmed from the amphibolite-hosted pyrite sulfur isotope signatures.

Isotopic compositions of the amphibolite-hosted pyrite at Londozi are very similar to the sign and magnitude of $\delta^{34}S$ and $\Delta^{33}S$ observed in Neoarchean VMS deposits and komatiite-hosted nickel sulfides, which record $\delta^{34}S$-values of 0 ± 5‰ and negative $\Delta^{33}S$-values of -0.5 ± 0.5‰ (Bekker et al., 2009; Fiorentini et al., 2012a; Fiorentini et al., 2012b). Bekker et al. (2009) proposed that this variation was related to magmatic assimilation of crustal sulfur that was ultimately derived from thermochemical reduction of seawater sulfate and leaching of juvenile sulfur from underlying volcanic rocks, resulting in the dilution of mass-independent signatures and re-equilibration of isotope ratios with the silicate melt. Similar mixing processes may have occurred before the eruption of the komatiitic and mafic lavas at Londozi, because isotopic data (Fig. 6.2b) provide evidence for dilution of $\Delta^{33}S$ and $\Delta^{36}S$ with juvenile sulfur, and $\delta^{34}S$-values overlap with the range observed in mantle-derived sulfides (Marini et al., 2011) Although geological evidence for assimilation of hydrothermal massive sulfides is lacking for the Londozi amphibolites (cf. Fiorentini et al., 2012a), observation of sulfides in the hydrothermally-altered mafic schists underlying the barite (Chapter 5) suggests that these rocks may have acted as a source of surface-derived sulfur.

6.4.2 Abiotic sulfate reduction during metamorphism

Isotopic compositions of barite-hosted pyrite at Londozi show strong depletion in ^{34}S relative to the barite (Fig. 6.3a), similar to mass-dependent isotope effects observed in pyrite from the low-metamorphic grade 3.49 Ga Dresser barite of Western Australia (Shen et al., 2001; Ueno et al., 2008; Shen et al., 2009) and the

3.26-3.23 Ga Barite Valley deposit in the Barberton Greenstone Belt of South Africa (Chapter 3). These fractionations were interpreted to reflect microbial reduction of seawater sulfate because $\Delta^{33}S$-values were similar to those in the barite (Chapter 2 and Farquhar et al., 2000; Bao et al., 2007; Shen et al., 2009; Ueno et al., 2009), and geological evidence for high-temperature thermochemical or magmatic reduction pathways was lacking (Shen et al., 2001). In addition, mass-independent signatures of the sulfides showed slightly less negative $\Delta^{33}S$ and slightly more negative $\Delta^{36}S$ compared to the sulfate, which agreed with minor isotope fractionation observed in laboratory culture experiments with sulfate reducers (Farquhar et al., 2003; Johnston et al., 2005) and predicted from metabolic models (Johnston et al., 2007).

In contrast, isotopic compositions of all barite-hosted pyrite at Londozi are shifted towards significantly more ^{36}S-enriched values in comparison with the sulfate (Fig. 6.3b), and are therefore inconsistent with simple microbial reduction of sulfate. Although Rayleigh fractionation during closed-system biological sulfate reduction, as modeled by Ono et al. (2006), can shift the $\Delta^{36}S$ of the residual sulfate towards more positive values if the fractionation factor $^{34}\alpha$ is close to unity (e.g. $^{34}\alpha = 0.99$), the calculated compositions of the sulfide generated from this pool are considerably less positive in $\Delta^{36}S$ than measured values (see Fig. 6.4 and caption for equations used). Most importantly, the relatively ^{36}S-enriched sulfide is only produced when more than 90% of all sulfate is reduced (Fig. 6.4), but $\delta^{34}S$-values corresponding to these large degrees of closed-system sulfate reduction are much more ^{34}S-enriched than observed in the barite-hosted pyrite grains (Fig. 6.4, dashed line). Therefore, we conclude that closed-system microbial sulfate reduction is also inconsistent with the isotopic compositions of ^{34}S-depleted pyrite at Londozi. Alternatively, sulfur disproportionation pathways can produce minor shifts in $\Delta^{36}S$ towards more positive values (Johnston et al., 2005; Johnston et al., 2007), but negative $\Delta^{33}S$-values observed in the pyrite imply redox processing of atmospheric sulfate, not elemental sulfur (Farquhar et al., 2000).

In addition to biological pathways, abiotic redox processes at high temperatures (above 100°C) can produce fractionation in $\delta^{34}S$ between sulfate and sulfide, for example during the reduction of seawater sulfate by organic matter or ferrous iron minerals in hydrothermal systems (Shanks et al., 1981; Shanks and Seyfried, 1987; Machel et al., 1995; Machel, 2001). Magnitudes of isotope effects are similar to or smaller than those observed during microbial reduction (Shanks et al., 1981; Machel et al., 1995; Ohmoto and Goldhaber, 1997),

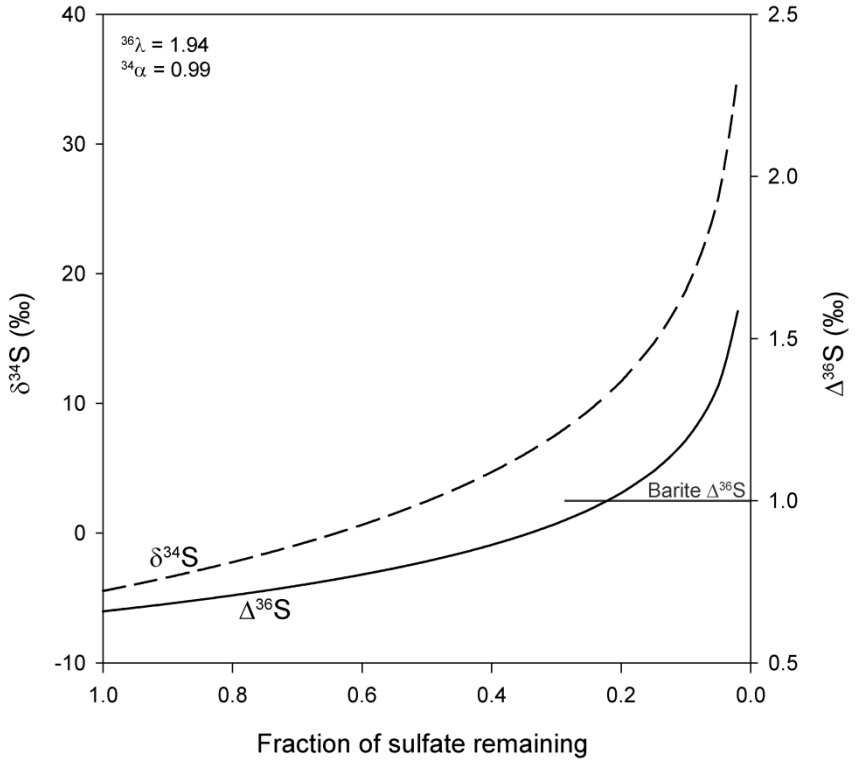

Figure 6.4 *Modeled evolution of $\delta^{34}S$ (dashed line) and $\Delta^{36}S$ (black line) of instantaneously formed sulfide during closed-system microbial sulfate reduction. Values of $\delta^{34}S$ and $\delta^{36}S$ were calculated using Rayleigh equations similar to those used by Ono et al. (2006), with isotope ratios for the residual sulfate defined by $^{34}R_{SO4} = R_i\ f^{(\alpha-1)}$ and for the instantaneously precipitating sulfide by $^{34}R_{H2S} = \alpha\ ^{34}R_{SO4}$ (note that in situ analyses of individual pyrite grains are assumed to reflect the instantaneously precipitated pyrite and not the cumulative sulfide composition). A fractionation factor (α) of 0.99 was used for $\delta^{34}S$, and the fractionation factor for $\delta^{36}S$ was recalculated using an exponent $^{36}\lambda$ = 1.94 after Johnston et al. (2007). The average composition of the sulfate $\Delta^{36}S$ is shown for comparison ($\Delta^{36}S$ = 1.03‰).*

but consistent with the difference in $\delta^{34}S$ between the barite-hosted pyrite and Londozi barite (Fig. 6.3a). However, the lack of sulfide with a juvenile isotopic composition in this pyrite population (Fig. 6.3a) suggests that sulfate reduction in a hydrothermal setting represents an unlikely source reaction for the formation of the ^{34}S-depleted pyrite, because Ono et al. (2007) demonstrated significant (73-89%) contributions of sulfide leached from volcanic rocks in modern hydrothermal vent systems. In addition, if large-scale hydrothermal sulfate

reduction occurred during deposition of the barite, then isotopic mass balance requires that the $\Delta^{36}S$ of the barite should be shifted from the Archean reference array towards more negative values in order to compensate for the strongly positive $\Delta^{36}S$ in pyrite. However, this effect was not observed in Chapter 2.

An alternative explanation for the isotopic variations in barite-hosted pyrite is that reduction of sulfate occurred at a smaller scale after deposition of the barite, related to amphibolite facies metamorphism (Chapter 4) or retrograde metasomatism (Chapter 5). Temperatures calculated from differences in $\delta^{34}S$ between individual pyrite grains and average barite (Fig. 6.5) are consistent with the conditions of peak and retrograde metamorphism at Londozi (i.e. 650-700°C at the peak of metamorphism, see Chapter 4), but the associated metamorphic equilibrium fractionation alone does not explain the observed shifts towards more positive $\Delta^{36}S$-values in pyrite compared to the barite, because isotopic equilibration reactions should leave $\Delta^{36}S$ either unaffected or produce only very small shifts since $^{36}\theta \approx {}^{36}\theta_{ref} = 1.91$ (Ono et al., 2006)†. On the other hand, anomalous isotope effects were reported for ^{36}S during thermochemical sulfate reduction (TSR) experiments by Watanabe et al. (2009), and in subsequent experimental work Oduro et al. (2011) attributed this increase in $\Delta^{36}S$ to mixing and mass-conservation effects related to the complex reaction pathways of abiotic sulfate reduction. Similar small-scale mixing effects could explain the relative ^{36}S-enrichment observed in barite-hosted pyrite at Londozi, although calculations by Ono et al. (2006) predict slightly smaller changes in $\Delta^{36}S$ than measured in our pyrite sulfur isotope data. Nevertheless, we consider that the generation of ^{36}S-enriched sulfide is more likely to occur during such abiotic reaction pathways, than during biological processes with their intrinsic negative shifts in $\Delta^{36}S$ (Johnston et al., 2007). Finally, we consider the occurrence of mass-independent fractionation of ^{36}S during thermochemical sulfate reduction unlikely since Oduro et al. (2011) found only deviations in $^{33}S/^{32}S$ associated with magnetic isotope effects during TSR, and the lack of hydrocarbons in the barite-rich sediments suggests that the anomalous fractionation mechanism proposed by Lasaga et al. (2008) did not occur. In addition, mass-independent fractionation is inconsistent with the observed slope in $\Delta^{36}S/\Delta^{33}S$ that is similar to the array expected for mass-dependent processes (Fig. 6.3b).

† The variable $^{36}\theta$ represents the mass-dependent exponent and is approximately equal to 1.91 for equilibrium exchange reactions (Ono et al., 2006). Because 1.91 is also used as the reference value to calculate $\Delta^{36}S$, processes with $^{36}\theta \neq 1.91$ (e.g. microbial sulfate reduction) result in small shifts in $\Delta^{36}S$.

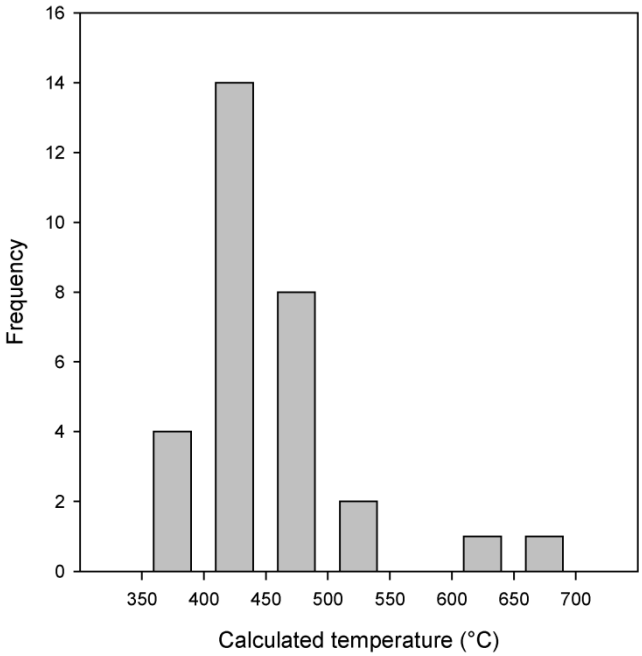

Figure 6.5 *Equilibration temperatures calculated from the differences in $\delta^{34}S$ between the barite-hosted pyrite and the average for the Londozi barite ($\delta^{34}S$ = 5.6‰) after Chapter 2, following equilibrium fractionation factors between barite and pyrite defined by Seal (2000). Temperatures are similar to or lower than the peak metamorphic conditions at Londozi, with T = 650-700°C (Chapter 4). A similar approach was used by Whelan et al. (1984) to assess the possibility of metamorphic re-equilibration.*

An abiotic origin for the ^{34}S-depleted pyrite is also consistent with mineralogical and geochemical evidence for metamorphic remobilization of barite through reductive dissolution processes at Londozi (discussed in Chapter 5), described by the reaction:

$BaSO_4$ + reductant (e.g. CH_4, C_{org}) = Ba^{2+} (in feldspar) + S^{2-} (in pyrite) + CO_2

Furthermore, it agrees with small-scale and post-depositional sulfate reduction as outlined above, and explains why bulk barite $\Delta^{36}S$-values were unaffected by these fractionation processes. Therefore, we conclude that the ^{34}S-depleted barite-hosted pyrite was not derived from microbial sulfate reduction or syn-depositional abiotic reduction in hydrothermal systems, but propose that the

observed isotope effects may be linked to equilibrium fractionation and associated small-scale mixing processes during localized metamorphic reduction of the barite-sulfate. Further experimental work will be required to verify the mechanisms and magnitude of sulfur isotope fractionation during reductive barite dissolution.

6.5 CONCLUSIONS

This study reports on the quadruple sulfur isotopic compositions of pyrite from the >3.52 Ga Londozi barite deposit and associated amphibolites in the Barberton Greenstone Belt of Swaziland, determined in situ by secondary ion mass spectrometry. Results demonstrate the presence of two distinct pyrite populations in the barite and the metavolcanics. Amphibolite-hosted pyrite displays near-zero $\delta^{34}S$-values, with negative $\Delta^{33}S$ that is distinct from mass-independent signatures observed in the barite. These isotopic compositions are very similar to those observed in Neoarchean VMS deposits and komatiite-hosted nickelsulfides (Bekker et al., 2009; Fiorentini et al., 2012a; Fiorentini et al., 2012b), suggesting a similar origin with mixing of hydrothermally or microbially-reduced seawater sulfate with juvenile sulfur during magmatic assimilation of altered volcanic rocks. In contrast, barite-hosted pyrite shows strong depletion in $\delta^{34}S$ (5-18‰) compared to the barite, with similar $\Delta^{33}S$-values but significantly more positive $\Delta^{36}S$ than observed in the sulfate. Magnitudes of $^{34}S/^{32}S$ fractionation are consistent with microbial sulfate reduction, but minor isotopic variations oppose previous experimental and modeling results for this metabolic pathway (Farquhar et al., 2003; Johnston et al., 2005; Johnston et al., 2007). Alternatively, equilibrium isotope fractionation and small-scale mixing associated with complex reaction pathways during high-temperature abiotic sulfate reduction, possibly associated with metamorphic remobilization of barite, are more consistent with pyrite $\delta^{34}S$-values and the observed ^{36}S-enrichment. These data demonstrate that measurement of $\Delta^{36}S$ is essential for the correct interpretation of pyrite sulfur isotope data from deposits with complex geological and metamorphic histories.

Acknowledgements

Otto Stiekema and Kerstin Lindén are thanked for their help with sample preparation. This project (SE-TAF-629) received support from SYNTHESYS (www.synthesys.info) which is financed by the European Community – Research Infrastructure Action under the FP7 "Capacities" Specific Program (awarded to DR), and a grant from the User Support Programme Space Research and the Netherlands Organization for Scientific Research (NWO). The Nordsim facility is operated under a contract between the research funding agencies of Denmark, Iceland, Norway and Sweden, the Geological Survey of Finland and the Swedish Museum of Natural History.

References

Bao, H., Rumble Iii, D., Lowe, D.R., 2007. The five stable isotope compositions of Fig Tree barites: Implications on sulfur cycle in ca. 3.2 Ga oceans. Geochim. Cosmochim. Acta 71, 4868-4879.

Baublys, K.A., Golding, S.D., Young, E., Kamber, B.S., 2004. Simultaneous determination of 33S V-CDT and 34S V-CDT using masses 48, 49 and 50 on a continuous flow isotope ratio mass spectrometer. Rapid Commun. Mass Spectrom. 18, 2765-2769.

Bekker, A., Barley, M.E., Fiorentini, M.L., Rouxel, O.J., Rumble, D., Beresford, S.W., 2009. Atmospheric Sulfur in Archean Komatiite-Hosted Nickel Deposits. Science 326, 1086-1089.

Crowe, D.E., Vaughan, R.G., 1996. Characterization and use of isotopically homogeneous standards for in situ laser microprobe analysis of 34S/32S ratios. Am. Mineral. 81, 187-193.

Farquhar, J., Bao, H., Thiemens, M., 2000. Atmospheric Influence of Earth's Earliest Sulfur Cycle. Science 289, 756-758.

Farquhar, J., Johnston, D.T., Wing, B.A., Habicht, K.S., Canfield, D.E., Airieau, S., Thiemens, M.H., 2003. Multiple sulphur isotopic interpretations of biosynthetic pathways: implications for biological signatures in the sulphur isotope record. Geobiology 1, 27-36.

Farquhar, J., Savarino, J., Airieau, S., Thiemens, M.H., 2001. Observation of wavelength-sensitive mass-independent sulfur isotope effects during SO_2 photolysis: Implications for the early atmosphere. J. Geophys. Res. 106, 32829-32839.

Fiorentini, M., Beresford, S., Barley, M., Duuring, P., Bekker, A., Rosengren, N., Cas, R., Hronsky, J., 2012a. District to Camp Controls on the Genesis of Komatiite-Hosted Nickel Sulfide Deposits, Agnew-Wiluna Greenstone Belt, Western Australia: Insights from the Multiple Sulfur Isotopes. Econ. Geol. 107, 781-796.

Fiorentini, M.L., Bekker, A., Rouxel, O., Wing, B.A., Maier, W., Rumble, D., 2012b. Multiple Sulfur and Iron Isotope Composition of Magmatic Ni-Cu-(PGE) Sulfide Mineralization from Eastern Botswana. Econ. Geol. 107, 105-116.

Hulston, J.R., Thode, H.G., 1965. Variations in the S33, S34, and S36 Contents of Meteorites and Their Relation to Chemical and Nuclear Effects. J. Geophys. Res. 70, 3475-3484.

Johnston, D.T., Farquhar, J., Canfield, D.E., 2007. Sulfur isotope insights into microbial sulfate reduction: When microbes meet models. Geochim. Cosmochim. Acta 71, 3929-3947.

Johnston, D.T., Farquhar, J., Wing, B.A., Kaufman, A.J., Canfield, D.E., Habicht, K.S., 2005. Multiple sulfur isotope fractionations in biological systems: A case study with sulfate reducers and sulfur disproportionators. Am. J. Sci. 305, 645-660.

Kamber, B.S., Whitehouse, M.J., 2007. Micro-scale sulphur isotope evidence for sulphur cycling in the late Archean shallow ocean. Geobiology 5, 5-17.

Kaufman, A.J., Johnston, D.T., Farquhar, J., Masterson, A.L., Lyons, T.W., Bates, S., Anbar, A.D., Arnold, G.L., Garvin, J., Buick, R., 2007. Late Archean Biospheric Oxygenation and Atmospheric Evolution. Science 317, 1900-1903.

Lasaga, A.C., Otake, T., Watanabe, Y., Ohmoto, H., 2008. Anomalous fractionation of sulfur isotopes during heterogeneous reactions. Earth Planet. Sci. Lett. 268, 225-238.

Machel, H.G., 2001. Bacterial and thermochemical sulfate reduction in diagenetic settings -- old and new insights. Sediment. Geol. 140, 143-175.

Machel, H.G., Krouse, H.R., Sassen, R., 1995. Products and distinguishing criteria of bacterial and thermochemical sulfate reduction. Appl. Geochem. 10, 373-389.

Marini, L., Moretti, R., Accornero, M., 2011. Sulfur Isotopes in Magmatic-Hydrothermal Systems, Melts, and Magmas. Rev. Mineral. Geochem. 73, 423-492.

Oduro, H., Harms, B., Sintim, H.O., Kaufman, A.J., Cody, G., Farquhar, J., 2011. Evidence of magnetic isotope effects during thermochemical sulfate reduction. Proceedings of the National Academy of Sciences 108, 17635-17638.

Ohmoto, H., Goldhaber, M.B., 1997. Sulfur and carbon isotopes, in: Barnes, H.L. (Ed.), Geochemistry of hydrothermal ore deposits. John Wiley & Sons, New York.

Ono, S., Shanks Iii, W.C., Rouxel, O.J., Rumble, D., 2007. S-33 constraints on the seawater sulfate contribution in modern seafloor hydrothermal vent sulfides. Geochim. Cosmochim. Acta 71, 1170-1182.

Ono, S., Wing, B., Johnston, D., Farquhar, J., Rumble, D., 2006. Mass-dependent fractionation of quadruple stable sulfur isotope system as a new tracer of sulfur biogeochemical cycles. Geochim. Cosmochim. Acta 70, 2238-2252.

Pavlov, A.A., Kasting, J.F., 2002. Mass-independent fractionation of sulfur isotopes in Archean sediments: strong evidence for an anoxic Archean atmosphere. Astrobiology 2, 27-41.

Philippot, P., Van Zuilen, M., Lepot, K., Thomazo, C., Farquhar, J., Van Kranendonk, M.J., 2007. Early Archaean Microorganisms Preferred Elemental Sulfur, Not Sulfate. Science 317, 1534-1537.

Philippot, P., van Zuilen, M., Rollion-Bard, C., 2012. Variations in atmospheric sulphur chemistry on early Earth linked to volcanic activity. Nat. Geosci. 5, 668-674.

Reimer, T.O., 1980. Archean sedimentary baryte deposits of the Swaziland Supergroup (Barberton Mountain

Land, South Africa). Precambrian Res. 12, 393-410.

Seal, R.R., Alpers, C.N., Rye, R.O., 2000. Stable Isotope Systematics of Sulfate Minerals, in: Alpers, C.N., Jambor, J.L., Nordstrom, D.K. (Eds.), Reviews in Mineralogy and Geochemistry. Sulfate Minerals. Crystallography, Geochemistry and Environmental Significance. Mineralogical Society of America, Washington D.C.

Shanks, W.C., Bischoff, J.L., Rosenbauer, R.J., 1981. Seawater sulfate reduction and sulfur isotope fractionation in basaltic systems: Interaction of seawater with fayalite and magnetite at 200-350°C. Geochim. Cosmochim. Acta 45, 1977-1995.

Shanks, W.C., Seyfried, W.E., 1987. Stable isotope studies of vent fluids and chimney minerals, Southern Juan de Fuca Ridge: Sodium metasomatism and seawater sulfate reduction. J. Geophys. Res. 92, 11387-11399.

Shen, Y., Buick, R., Canfield, D.E., 2001. Isotopic evidence for microbial sulphate reduction in the early Archaean era. Nature 410, 77-81.

Shen, Y., Farquhar, J., Masterson, A., Kaufman, A.J., Buick, R., 2009. Evaluating the role of microbial sulfate reduction in the early Archean using quadruple isotope systematics. Earth Planet. Sci. Lett. 279, 383-391.

Ueno, Y., Johnson, M.S., Danielache, S.O., Eskebjerg, C., Pandey, A., Yoshida, N., 2009. Geological sulfur isotopes indicate elevated OCS in the Archean atmosphere, solving faint young sun paradox. Proc. Nat. Acad. Sci. U.S.A. 106, 14784-14789.

Ueno, Y., Ono, S., Rumble, D., Maruyama, S., 2008. Quadruple sulfur isotope analysis of ca. 3.5 Ga Dresser Formation: New evidence for microbial sulfate reduction in the early Archean. Geochim. Cosmochim. Acta 72, 5675-5691.

Ulrich, T., Long, D.G.F., Kamber, B.S., Whitehouse, M.J., 2011. In Situ Trace Element and Sulfur Isotope Analysis of Pyrite in a Paleoproterozoic Gold Placer Deposit, Pardo and Clement Townships, Ontario, Canada. Econ. Geol. 106, 667-686.

Watanabe, Y., Farquhar, J., Ohmoto, H., 2009. Anomalous Fractionations of Sulfur Isotopes During Thermochemical Sulfate Reduction. Science 324, 370-373.

Whelan, J.F., Rye, R.O., deLorraine, W.F., 1984. The Balmat-Edwards zinc-lead deposits; synsedimentary ore from mississippi valley-type fluids. Econ. Geol. 79, 239-265.

Whitehouse, M.J., 2012. Multiple sulfur isotope determination by SIMS: Evaluation of reference sulfides for $\Delta^{33}S$ with observations and a case study on the determination of $\Delta^{36}S$. Geostand. Geoanal. Res. Accepted article, doi: 10.1111/j.1751-908X.2012.00188.x.

Whitehouse, M.J., Kamber, B.S., Fedo, C.M., Lepland, A., 2005. Integrated Pb- and S-isotope investigation of sulphide minerals from the early Archaean of southwest Greenland. Chem. Geol. 222, 112-131.

Zebras in Mlilwane Wildlife Sanctuary, Hhohho, Swaziland

Chapter 7

Conclusions and future directions

7.1 GENERAL CONCLUSIONS

Sulfur isotopes in ancient sulfate and sulfide minerals provide unique insights into the Earth's earliest sulfur cycle, but the correct interpretation of these isotopic signatures requires information on the geological context of the samples. This thesis reports on a combined study of the geology and multiple sulfur isotope geochemistry of Paleoarchean pyrite and barite from the Barberton Greenstone Belt in South Africa and Swaziland, and assesses the geobiology of these deposits. An overview of the main conclusions from this work and future directions is given below. Specific conclusions about the Londozi barite deposit are given in Chapters 4 and 5.

7.1.1 Role of microbial activity in the formation of Paleoarchean barite and pyrite

In contrast to recent studies suggesting that the early sulfur cycle was largely abiotic (Halevy et al., 2010; Philippot et al., 2012), the isotopic compositions of oxidized and reduced sulfur described in this thesis provide evidence for an important role for microbial sulfate reduction in the Paleoarchean marine environment. Positive $\delta^{34}S$-values measured in different barite deposits from the Barberton Greenstone Belt imply ^{34}S-enrichment relative to the composition of photochemical sulfate, which was interpreted to reflect drawdown of ^{32}S by biological sulfate reduction. Strong overlap with isotopic compositions of other Paleoarchean barites from India and Western Australia indicates that this process occurred on a large, and possibly global scale. Most importantly, the observed co-variation between $\delta^{34}S$ and $\Delta^{33}S$ in individual deposits cannot be explained by abiotic mixing in magmatic-hydrothermal systems (cf. Bao et al., 2007), but requires fractionation by sulfate reducers in the basins were barite precipitated.

This barite-based evidence for local biological redox pathways is consistent with pyrite sulfur isotope data from the low-metamorphic grade Barite Valley deposit (South Africa), which demonstrate that both microbial sulfate reduction and elemental sulfur metabolisms were involved in the formation of distinct small-scale sulfide pools. The weakly positive array in $\Delta^{33}S/\delta^{34}S$ observed in barite-hosted pyrite from this deposit argues against an abiotic photochemical origin for the isotopic fractionations as suggested by Philippot et al. (2012), because sulfate with positive $\Delta^{33}S$-values (required for the atmospheric model)

was not found. Together with geochemical evidence for low-temperature (100-150°C) hydrothermal venting, it is thus concluded that the basins in the Barberton Greenstone Belt where barites formed in the Paleoarchean era represented habitats for early sulfur metabolizing hyperthermophiles.

7.1.2 Abiotic controls on sulfur isotope signatures: the environment

Strong depositional and geographical controls on sulfur isotope signatures were previously reported by Ono et al. (2009) for sulfide from Neoarchean sedimentary successions. This thesis demonstrates that similar environmental factors are important for the interpretation of Paleoarchean isotope data, and that sulfur isotope fractionation recorded in the rock record does not inevitably represent a single (atmospheric) process (cf. Philippot et al., 2012). Although strong correlations between $\Delta^{36}S$ and $\Delta^{33}S$ measured in barite are consistent with SO_2 photolysis in the early atmosphere, secondary oceanic mixing processes resulted in decreasing magnitudes of these mass-independent signatures from 3.5 to 3.2 Ga as well as large-scale homogeneity in $\delta^{34}S$. On a smaller scale, pyrite isotopic arrays in sedimentary rocks from Barite Valley (South Africa) were strongly correlated with the presence of barite in the stratigraphy and therefore explained by variations in sulfate availability in the depositional environment, instead of primary atmospheric processes.

From these results it is thus concluded that, in addition to atmospheric pathways, both oceanic and environmental processes significantly affected the isotopic compositions of ancient sulfur deposits, and that local conditions exerted a stronger control on the final isotope signatures preserved in the rock record than primary photochemical processes. This is particularly important to take into account when comparing isotope data from different basins and depositional environments.

7.1.3 Abiotic controls on sulfur isotope signatures: metamorphism

In contrast to carbon isotope signatures in reduced sulfur compounds, which were shown by Van Zuilen et al. (2002) to be highly susceptible to metamorphic resetting, effects of metamorphism on the isotopic composition of stratiform barites were concluded to be minimal in this thesis, since temporal trends in $\Delta^{33}S$

and $\Delta^{36}S$ have been preserved and values of $\delta^{34}S$ strongly overlap in deposits from different cratons, ages and metamorphic grades. These results thus imply that the barite sulfur isotope record provides a robust tracer for ancient processes in the sulfur cycle. On the other hand, the integration of sulfur isotope and geological data on conditions of metamorphism and metasomatism at the Londozi barite deposit – identified as the oldest stratiform sulfate on Earth in this study – indicates that microscale processes may have affected pyrite sulfur isotope signatures during high-grade metamorphism (650-700°C and 10-12 kbar). Petrological evidence from barium-rich silicates for small-scale reductive barite dissolution supports an abiotic origin for sulfide, consistent with the observation of abiogenic $\Delta^{36}S$-values in strongly ^{34}S-depleted barite-hosted pyrite. Thus, although primary pyrite minerals appear to have survived metamorphism in the Barberton Greenstone Belt, the generation of such secondary sulfides requires caution when interpreting the ancient pyrite sulfur isotope record from high-metamorphic grade deposits.

7.2 FUTURE DIRECTIONS

7.2.1 Linking photolysis experiments and models to the Archean rock record

The interpretation of sulfur isotope data from Archean barite and pyrite relies heavily on the assumed composition of atmospherically-produced sulfur, as was demonstrated in this thesis. For example, sulfur isotopic compositions of Barberton barites in *Chapter 2* were interpreted to be ^{34}S-enriched relative to photochemical sulfate, based on a photolytic array with $\Delta^{33}S/\delta^{34}S$ that was observed in sulfide minerals from Neoarchean and Paleoarchean rocks (Ono et al., 2003; Kamber and Whitehouse, 2007; Kaufman et al., 2007; Ueno et al., 2008; Ono et al., 2009), photolysis models (Lyons, 2009) and experiments (Masterson et al., 2011; Whitehill and Ono, 2012). However, others have argued for the existence of a negative array in $\Delta^{33}S/\delta^{34}S$ (Philippot et al., 2007; Philippot et al., 2012) corresponding to results from 193 nm photolysis experiments (Farquhar et al., 2001), which would imply that there is minimal fractionation in $\delta^{34}S$ between barite and atmospheric sulfate. Similarly, uncertainty about the composition of photochemical reduced sulfur hampers the interpretation of isotopic arrays in pyrite sulfur isotope data, because the lack of constraints on $\delta^{34}S$ and $\Delta^{33}S$-values

of elemental sulfur limits the evaluation of whether Archean pyrite with positive $\Delta^{33}S$ directly reflects photolysis products, or was affected by biological fractionation. Improved knowledge of photolysis arrays relevant for the Archean sulfur cycle would thus help to confirm the extent at which sulfate and sulfide reservoirs were affected by early microbial and oceanic processes. In particular, the current discrepancies between isotopic compositions derived from experimental and modeling work and those observed in the ancient rock record need to be resolved. Recent experimental work by Masterson et al. (2011) and Whitehill and Ono (2012) provide valuable starting points for this.

7.2.2 Investigating metamorphic sulfate reduction

Minor sulfur isotope signatures of barite-hosted pyrite from the Londozi barite deposit suggested that this sulfide was not of biological origin, but related to the abiotic reduction of barite under metamorphic conditions (*Chapter 6*). Although similar reductive dissolution pathways have been suggested for other metamorphosed barite deposits (Pan and Fleet, 1991; Tracy, 1991; Chabu and Boulègue, 1992; Grapes, 1993) and the thermodynamics of the process were investigated by Kritsotakis and Von Platen (1980), the sign and magnitude of sulfur isotope fractionation associated with this process remains unknown. Previous experiments on the high-temperature (250-350°C) reduction of seawater sulfate by ferrous iron minerals in hydrothermal systems suggested that equilibrium isotope fractionation occurred and that isotopic evolution of the produced sulfide could be modeled as a Rayleigh distillation processes (Shanks et al., 1981). Similar fractionation mechanisms may apply to metamorphic sulfate reduction and generate isotope effects as long as residual sulfate is present, but this remains to be quantified in high-temperature experiments.

7.2.3 Expanding the *in situ* Archean quadruple sulfur isotope record

Significant advances in secondary ion mass spectrometry (Whitehouse, 2012) enabled us to report the first *in situ* quadruple sulfur isotope data for Paleoarchean pyrite in *Chapter 2* and *Chapter 6.* At outlined in these chapters, the addition of $\Delta^{36}S$ data provided critical constraints on processes involved in the formation of pyrite, and allowed us to distinguish between biological and abiotic

redox pathways. Although the current level of precision is sufficient to yield geologically meaningful data, future work would substantially benefit from an improved precision on $\Delta^{36}S$ following suggestions made by Whitehouse (2012).

Most of all, the results obtained by SIMS are intriguing because they contrast strongly with sulfur isotope data for Paleoarchean pyrite from bulk sulfur extractions and conventional gas source mass spectrometry. Similar differences between bulk and *in situ* techniques were observed in laser ablation work by Ohmoto et al. (1993), and SIMS analyses by Philippot et al. (2007) that were considerably different to bulk pyrite data from the same locality reported by Shen et al. (2009) and Ueno et al. (2008). A possible explanation for these discrepancies is that bulk techniques result in average isotopic compositions that obscure small-scale trends, as the average of our *in situ* $\Delta^{36}S/\Delta^{33}S$ data from amphibolite-hosted pyrite in the Londozi barite deposit (*Chapter 6*) results in an apparent bulk composition that is consistent with the Archean reference array. Expanding the *in situ* quadruple sulfur isotope record of Paleoarchean to Neoarchean sulfide is thus required to determine whether similar differences are found in other occurrences of sedimentary pyrite, and to obtain insights into the origin and global significance of these trends.

7.2.4 Measuring all four sulfur isotopes in modern hydrothermal systems

Geochemical and sulfur isotope data indicate that the barite deposits and associated pyrite investigated in this thesis formed in hydrothermal, or at least hydrothermally-influenced depositional environments. As such, the interpretation of the observed isotopic variability in the ancient rock record can benefit significantly from our knowledge of biogeochemical processes and sulfur isotope fractionation in modern hydrothermal systems. Despite the lack of significant mass-independently fractionated sulfur in the Proterozoic and Phanerozoic, Ono et al. (2007) demonstrated that additional measurement of $\Delta^{33}S$ in modern hydrothermal systems provides valuable constraints on mixing processes and inputs of biogenic versus hydrothermal sulfide. Complementary analyses of $\Delta^{36}S$, when measured at sufficiently high precision to identify any small biological shifts, would provide further insights into the roles of abiotic and microbial sulfate reduction in modern high-sulfate systems. In addition, such work is required to determine whether abiotic shifts in $\Delta^{36}S$, as observed in this thesis and

by Watanabe et al. (2009), are significant in nature. Such studies present an important framework for the interpretation of major and minor sulfur isotope fractionations in Archean hydrothermal systems.

7.2.5 Integrating the sulfur isotope record with non-traditional stable isotopes

Additional information on early microbial processes can be obtained when the sulfur isotope record is integrated with other stable isotope systems. Fe isotopes are of particular interest because geochemical cycles of iron and sulfur are strongly linked. In addition, Fe isotopes can be measured *in situ* in pyrite and can therefore confirm the small-scale pathways of pyrite formation inferred from sulfur isotopes in this thesis (cf. Hofmann et al., 2009), as well as identify coupled microbial iron and sulfate reduction in the early environment (Archer and Vance, 2006). Other metabolisms coupled with sulfate reduction include anaerobic methane oxidation or reverse methanogenesis (Hoehler et al., 1994), which might be traceable from the rock record using Ni isotopes as nickel represents an essential element for methanogens (M. Balk, pers. comm., 2012 and Konhauser et al., 2009). If correct, then combined nickel and sulfur isotopes could identify the role of this biological process.

7.3 SULFUR ISOTOPES AND PLANETARY EXPORATION

Results in this thesis demonstrate that multiple sulfur isotopes, when carefully applied, represent a viable tool for identifying ancient biological sulfur cycling in the terrestrial rock record. Thus, a similar approach could help to elucidate whether microbial life was once present on other planetary bodies. Mars is particularly suitable for sulfur isotope analyses because of the presence of both oxidized sulfur in gypsum and jarosite deposits (Squyres et al., 2004), as well as reduced sulfur in pyrite that was reported from the Martian meteorite ALH84001 (McKay et al., 1996).

However, results from this study raise two important issues that need to be addressed before successful application of this isotopic biomarker on Mars. First, *Chapter 3* and *Chapter 6* demonstrate that high-precision analysis of all four stable

isotopes of sulfur is required to assess whether ^{34}S-depleted pyrite is of biological or abiotic origin. This involves either complex wet chemistry sample preparation procedures (Canfield et al., 1986) and online fluorination gas source mass spectrometry (Farquhar et al., 2007) for bulk analyses, or large secondary ion mass spectrometers for the *in situ* determination of $\delta^{34}S$, $\Delta^{33}S$ and $\Delta^{36}S$. Such analytical procedures and instruments would require sample return missions, instead of chemical analyses performed on Mars. Second, this thesis demonstrates that that information about the geological context of analyzed samples is critical for the correct interpretation of sulfur isotope data. For example, *Chapter 3* shows that knowledge of the depositional environment is needed to understand the variability in isotope signatures, whereas interpretations in *Chapter 6* required results from previous chapters on the geological history, metamorphism and metasomatism. Although fieldwork and subsequent laboratory analyses can provide us with such information on Earth, the collection of geological data on Mars must be done by exploration rover with more limited equipment (e.g. the current NASA Curiosity rover carries a laser-induced breakdown spectrometer and x-ray diffractometer, but no electron microprobe for detailed microanalysis of mineral compositions). This imposes limitations to the application of the stable sulfur isotope biomarker on Mars, in particular because the more soluble sulfate phases of gypsum and jarosite may be more easily affected by fluid-rock interactions than terrestrial barite deposits, so that insights into the effects of metasomatism are essential.

Despite these practical issues, the preservation of an abiological sulfur reservoir on Mars that can be used as a reference for isotope data as well as the significant fractionation associated with biological processes (cf. C, N and Fe isotopes reviewed by van Zuilen, 2008) makes the stable sulfur isotope biomarker still one of the best methods for tracing signs of early microbial activity on Mars.

References

Archer, C., Vance, D., 2006. Coupled Fe and S isotope evidence for Archean microbial Fe(III) and sulfate reduction. Geology 34, 153-156.

Bao, H., Rumble Iii, D., Lowe, D.R., 2007. The five stable isotope compositions of Fig Tree barites: Implications on sulfur cycle in ca. 3.2 Ga oceans. Geochim. Cosmochim. Acta 71, 4868-4879.

Canfield, D.E., Raiswell, R., Westrich, J.T., Reaves, C.M., Berner, R.A., 1986. The use of chromium reduction in the analysis of reduced inorganic sulfur in sediments and shales. Chem. Geol. 54, 149-155.

Chabu, M., Boulègue, J., 1992. Barian feldspar and muscovite from the Kipushi Zn-Pb-Cu deposit, Shaba, Zaire. Can. Mineral. 30, 1143-1152.

Farquhar, J., Kim, S.-T., Masterson, A., 2007. Implications from sulfur isotopes of the Nakhla meteorite for the origin of sulfate on Mars. Earth Planet. Sci. Lett. 264, 1-8.

Farquhar, J., Savarino, J., Airieau, S., Thiemens, M.H., 2001. Observation of wavelength-sensitive mass-independent sulfur isotope effects during SO2 photolysis: Implications for the early atmosphere. J. Geophys. Res. 106, 32829-32839.

Grapes, R., 1993. Barian mica and distribution of barium in metacherts and quartzofeldspathic schists, Southern Alps, New Zealand. Mineral. Mag. 57, 265-272.

Halevy, I., Johnston, D.T., Schrag, D.P., 2010. Explaining the Structure of the Archean Mass-Independent Sulfur Isotope Record. Science 329, 204-207.

Hoehler, T.M., Alperin, M.J., Albert, D.B., Martens, C.S., 1994. Field and laboratory studies of methane oxidation in an anoxic marine sediment: Evidence for a methanogen-sulfate reducer consortium. Global Biogeochem. Cycles 8, 451-463.

Hofmann, A., Bekker, A., Rouxel, O., Rumble, D., Master, S., 2009. Multiple sulphur and iron isotope composition of detrital pyrite in Archaean sedimentary rocks: A new tool for provenance analysis. Earth Planet. Sci. Lett. 286, 436-445.

Kamber, B.S., Whitehouse, M.J., 2007. Micro-scale sulphur isotope evidence for sulphur cycling in the late Archean shallow ocean. Geobiology 5, 5-17.

Kaufman, A.J., Johnston, D.T., Farquhar, J., Masterson, A.L., Lyons, T.W., Bates, S., Anbar, A.D., Arnold, G.L., Garvin, J., Buick, R., 2007. Late Archean Biospheric Oxygenation and Atmospheric Evolution. Science 317, 1900-1903.

Konhauser, K.O., Pecoits, E., Lalonde, S.V., Papineau, D., Nisbet, E.G., Barley, M.E., Arndt, N.T., Zahnle, K., Kamber, B.S., 2009. Oceanic nickel depletion and a methanogen famine before the Great Oxidation Event. Nature 458, 750-753.

Kritsotakis, K., Von Platen, H., 1980. Reduktive Barytmobilisation. Neues Jahrb. Mineral. Abh. 137, 282-306.

Lyons, J.R., 2009. Atmospherically-derived mass-independent sulfur isotope signatures, and incorporation into sediments. Chem. Geol. 267, 164-174.

Masterson, A.L., Farquhar, J., Wing, B.A., 2011. Sulfur mass-independent fractionation patterns in the broadband UV photolysis of sulfur dioxide: Pressure and third body effects. Earth Planet. Sci. Lett. 306, 253-260.

McKay, D.S., Gibson Jr, E.K., Thomas-Keprta, K.L., Vali, H., Romanek, C.S., Clemett, S.J., Chillier, X.D.F., Maechling, C.R., Zare, R.N., 1996. Search for past life on Mars: Possible relic biogenic activity in martian meteorite ALH84001. Science 273, 924-930.

Ohmoto, H., Kakegawa, T., Lowe, D.R., 1993. 3.4-Billion-Year-Old Biogenic Pyrites from Barberton, South Africa: Sulfur Isotope Evidence. Science 262, 555-557.

Ono, S., Eigenbrode, J.L., Pavlov, A.A., Kharecha, P., Rumble Iii, D., Kasting, J.F., Freeman, K.H., 2003. New insights into Archean sulfur cycle from mass-independent sulfur isotope records from the Hamersley Basin, Australia. Earth Planet. Sci. Lett. 213, 15-30.

Ono, S., Kaufman, A.J., Farquhar, J., Sumner, D.Y., Beukes, N.J., 2009. Lithofacies control on multiple-sulfur isotope records and Neoarchean sulfur cycles. Precambrian Res. 169, 58-67.

Ono, S., Shanks Iii, W.C., Rouxel, O.J., Rumble, D., 2007. S-33 constraints on the seawater sulfate contribution in modern seafloor hydrothermal vent sulfides. Geochim. Cosmochim. Acta 71, 1170-1182.

Pan, Y., Fleet, M.E., 1991. Barian feldspar and barian-chromian muscovite from the Hemlo area, Ontario. Can. Mineral. 29, 481-498.

Philippot, P., Van Zuilen, M., Lepot, K., Thomazo, C., Farquhar, J., Van Kranendonk, M.J., 2007. Early Archaean Microorganisms Preferred Elemental Sulfur, Not Sulfate. Science 317, 1534-1537.

Philippot, P., van Zuilen, M., Rollion-Bard, C., 2012. Variations in atmospheric sulphur chemistry on early Earth linked to volcanic activity. Nat. Geosci. 5, 668-674.

Shanks, W.C., Bischoff, J.L., Rosenbauer, R.J., 1981. Seawater sulfate reduction and sulfur isotope fractionation in basaltic systems: Interaction of seawater with fayalite and magnetite at 200-350°C. Geochim. Cosmochim. Acta 45, 1977-1995.

Shen, Y., Farquhar, J., Masterson, A., Kaufman, A.J., Buick, R., 2009. Evaluating the role of microbial sulfate reduction in the early Archean using quadruple isotope systematics. Earth Planet. Sci. Lett. 279, 383-391.

Squyres, S.W., Grotzinger, J.P., Arvidson, R.E., Bell, J.F., Calvin, W., Christensen, P.R., Clark, B.C., Crisp, J.A., Farrand, W.H., Herkenhoff, K.E., Johnson, J.R., KlingelhÃ¶fer, G., Knoll, A.H., McLennan, S.M., McSween, H.Y., Morris, R.V., Rice, J.W., Rieder, R., Soderblom, L.A., 2004. In Situ Evidence for an Ancient Aqueous Environment at Meridiani Planum, Mars. Science 306, 1709-1714.

Tracy, R.J., 1991. Ba-rich micas from the Franklin Marble, Lime Crest and Sterling Hill, New Jersey. Am. Mineral. 76, 1683-1693.

Ueno, Y., Ono, S., Rumble, D., Maruyama, S., 2008. Quadruple sulfur isotope analysis of ca. 3.5 Ga Dresser Formation: New evidence for microbial sulfate reduction in the early Archean. Geochim. Cosmochim. Acta 72, 5675-5691.

van Zuilen, M., 2008. Stable Isotope Ratios as a Biomarker on Mars. Space Science Reviews 135, 221-232.

Van Zuilen, M.A., Lepland, A., Arrhenius, G., 2002. Reassessing the evidence for the earliest traces of life. Nature 418, 627-630.

Watanabe, Y., Farquhar, J., Ohmoto, H., 2009. Anomalous Fractionations of Sulfur Isotopes During Thermochemical Sulfate Reduction. Science 324, 370-373.

Whitehill, A.R., Ono, S., 2012. Excitation band dependence of sulfur isotope mass-independent fractionation during photochemistry of sulfur dioxide using broadband light sources. Geochim. Cosmochim. Acta 94, 238-253.

Whitehouse, M.J., 2012. Multiple sulfur isotope determination by SIMS: Evaluation of reference sulfides for $\Delta^{33}S$ with observations and a case study on the determination of $\Delta^{36}S$. Geostand. Geoanal. Res. Accepted article, doi: 10.1111/j.1751-908X.2012.00188.x.

Barberton Greenstone Belt from Malolotja Nature Reserve, Hhohho, Swaziland

ENGLISH SUMMARY

Sulfur isotopes in ancient sulfate and sulfide minerals provide a comprehensive record of microbial processes involved in the early sulfur cycle on Earth. However, the interpretation of these isotopic signatures requires information on the geological context of such samples, because abiotic chemical reactions can produce similar degrees of isotope fractionation to biological pathways. This thesis presents an integrated study of the geology and sulfur isotope geochemistry (^{32}S, ^{33}S, ^{34}S, ^{36}S) of Paleoarchean pyrite and barite deposits from the Barberton Greenstone Belt in South Africa and Swaziland, to explore to what extent sulfur isotope ratios in these rocks record ancient microbial activity and how they were affected or overprinted by abiotic processes.

High-precision sulfur isotope analyses of four different 3.5-3.2 Ga barite occurrences reveal constant mass-independent signatures ($\Delta^{36}S/\Delta^{33}S = -1.0 \pm 0.2$), supporting an important role for atmospheric photolysis reactions in the production of oxidized sulfur. Enrichment in ^{34}S relative to the inferred composition of this photochemical sulfur suggests that barites reflect a residual pool after microbial sulfate reduction, and the compositional overlap with deposits from cratons in Western Australia and India suggests that this occurred on a large, possibly global scale. In addition, co-variation between $\delta^{34}S$ and $\Delta^{33}S$ within individual deposits requires local fractionation by sulfate reducers in the basins where barite precipitated, instead of abiotic mixing in magmatic-hydrothermal systems.

This important role for local biological processing of sulfate is confirmed by high-resolution quadruple sulfur isotope data from 3.26-3.23 Ga low-metamorphic grade sedimentary rocks at Barite Valley, South Africa. Barite-hosted pyrite is strongly depleted in ^{34}S and shows similar negative $\Delta^{33}S$-values as the barite, consistent with microbial sulfate reduction at sulfate levels above 200 μM. In contrast, pyrite from barite-free sedimentary rocks defines an array in $\Delta^{33}S/\delta^{34}S$ that extends from the isotopic composition of the barite towards positive $\Delta^{33}S$-values. This was interpreted to reflect suppressed isotope fractionation at sulfate concentrations of less than 200 μM, consistent with the absence of sulfate minerals from these rocks, and mixing with sulfide derived from elemental sulfur metabolisms. These results demonstrate that local conditions exerted a strong control on the final isotopic signatures preserved in the rock record, and that

primary atmospheric compositions were overprinted by oceanic and environmental processes.

The presence of microbial isotope signatures in a high-metamorphic grade barite deposit at Londozi, Swaziland was evaluated by integrating geological, geochemical and sulfur isotope data. Field observations and geochemical analyses show that the barite occurs in a bimodal volcanic succession formed in an oceanic plateau setting, with low-temperature (100-150°C) hydrothermal activity. Zircon U-Pb ages indicate that felsic volcanics overlying the barite deposit were erupted at 3521 ± 6 Ma, which demonstrates that the Londozi deposit represents the oldest occurrence of stratiform sulfate on Earth. Thermobarometric calculations show that regional metamorphism at 3.2 Ga exposed the barite to temperatures of 650-700°C at a pressure of 10-12 kbar, corresponding to 30-40 km crustal depths. Mineralogical data indicate that barium-metasomatism accompanied subsequent retrograde metamorphism, with petrological evidence from barium-rich silicates for small-scale reductive barite dissolution processes and the associated generation of secondary sulfide. This abiotic process is consistent with positive $\Delta^{36}S$-values observed in strongly ^{34}S-depleted pyrite within the barite deposit, which cannot be explained by microbial sulfate reduction. On the other hand, pyrite hosted by the mafic amphibolites at Londozi shows different isotopic signatures that reflect mixing of mantle-derived sulfur with surface-derived sulfide, possibly from local biological processes.

Results in this thesis demonstrate that measurement of all four stable isotopes of sulfur, as well as detailed geological information on depositional environment and secondary alteration are required for the correct interpretation of sulfur isotope signatures. However, when carefully applied, multiple sulfur isotopes represent a useful tool for identifying ancient biological sulfur cycling on Earth, as well as tracing signs of early microbial activity on Mars.

SAMENVATTING IN HET NEDERLANDS

Stabiele isotopen van het element zwavel, gemeten in miljarden jaren oude sulfaten en sulfiden, geven potentieel waardevolle informatie over microbiologische processen in het begin van de Aardse geschiedenis. Het interpreteren van dit soort data vraagt echter om gegevens over de geologische context van de gesteentemonsters, omdat chemische (niet-biologische) reacties tot een gelijksoortige fractionatie van isotopen kunnen leiden. Dit proefschrift beschrijft daarom zowel de geologie als de zwavel isotopen geochemie (^{32}S, ^{33}S, ^{34}S, ^{36}S) van vroeg Archaeische pyriet en bariet uit de Barberton Greenstone Belt in Zuid-Afrika en Swaziland. Er wordt verkend in hoeverre de zwavel isotopen verhoudingen in deze gesteenten bewijs leveren voor vroege microbiologische activiteit, en hoezeer deze ratios zijn beïnvloed door abiotische processen.

De nauwkeurige bepaling van stabiele zwavel isotopen in vier verschillende bariet afzettingen uit Zuid-Afrika en Swaziland van 3.5 tot 3.2 miljard jaar oud, onthult gelijke massa-onafhankelijke isotopenverhoudingen ($\Delta^{36}S/\Delta^{33}S = -1.0 \pm 0.2$), en levert daarmee bewijs voor een belangrijke rol voor atmosferische reacties in the productie van geoxideerde zwavel op de vroege Aarde. Verrijking in ^{34}S ten opzichte van de samenstelling van dit atmosferische zwavel suggereert dat de bariet het sulfaat reflecteert dat achterbleef na biologische reductie, en de overlap met afzettingen uit West Australië en India betekent dat dit gebeurde op een grote, mogelijk globale schaal. Bovendien toont de correlatie tussen $\delta^{34}S$ en $\Delta^{33}S$ in individuele afzettingen aan dat er op kleine schaal isotopenfractionatie plaatsvond door sulfaat-reducerende micro-organismen in de bekkens waar bariet gevormd werd, in plaats van mengprocessen in magmatische of hydrothermale systemen.

De belangrijke rol voor biologische verwerking van sulfaat op de vroege Aarde wordt bevestigd door hoge-resolutie zwavel isotopen data van 3.26 tot 3.23 miljard jaar oude pyriet in sedimentaire gesteenten uit Barite Valley in Zuid-Africa, die slechts laaggradige metamorfose hebben ondergaan. Pyriet mineralen in bariet zijn sterk verarmd in ^{34}S en laten gelijke negatieve waarden voor $\Delta^{33}S$ zien als de bariet, in overeenstemming met biologische sulfaat reductie bij sulfaat concentraties van meer dan 200 μM. Daarentegen vertoont pyriet in bariet-vrije sedimentaire gesteenten (chert, conglomeraat) een negatieve correlatie tussen $\Delta^{33}S$ en $\delta^{34}S$, die reikt van de isotopensamenstelling van de bariet naar positieve

Δ^{33}S-waarden. Deze trend reflecteert hoogstwaarschijnlijk de beperkte microbiologische isotopen fractionatie onder zeer lage sulfaat concentraties (minder dan 200 µM), wat strookt met de afwezigheid van sulfaatmineralen in deze gesteenten, en het mengen met sulfide afkomsting van micro-organismen die elementair zwavel reduceerden. Deze resultaten laten zien dat lokale omstandigheden, zoals de hoeveelheid sulfaat in het water, een sterke invloed hebben gehad op de uiteindelijke isotopenratios die bewaard zijn gebleven in oude gesteenten, en dat primaire atmosferische signalen zijn overschreven door processen in het afzettingsmilieu.

De aanwezigheid van biologische isotopen signalen in een hooggradig metamorfe bariet afzetting in de Londozi vallei in Swaziland is onderzocht door gebruik te maken van zowel geologische, geochemische en zwavel isotopen data. Veldobservaties en geochemische analyses tonen aan dat de bariet zich bevindt in een bimodale vulkanische opeenvolging die gevormd is op een oceanisch plateau, met lage-temperatuur (100-150°C) hydrothermale activiteit. Zirkoondateringen laten zien dat de barietafzetting bedekt werd met felsische vulkanische gesteenten rond 3521 ± 6 Ma, wat bewijst dat de Londozi bariet de oudste stratiforme sulfaatafzetting op Aarde is. Door middel van een thermobarometrische studie van mineralen in de omliggende gesteenten is bovendien aangetoond dat tijdens regionale metamorfose rond 3.2 miljard jaar geleden de bariet is blootgesteld aan temperaturen van 650 tot 700°C bij een druk van 10 tot 12 kbar, overeenkomend met een diepte van 30 tot 40 km in de korst. Verder vormt de kenmerkende mineralogie van deze gesteenten bewijs voor barium-metasomatisme tijdens de opeenvolgende retrograde metamorfose, waarbij barium-rijke silicaten duiden op het zeer lokaal oplossen van bariet door de reductie van sulfaat. De vorming van secundaire sulfiden tijdens dit abiotische proces is in overeenstemming met de zwavel isotopen samenstelling van pyriet in de bariet, omdat sterk positieve Δ^{36}S-waarden in deze ^{34}S-verarmde mineralen niet verklaard kunnen worden door biologische processen. Aan de andere kant vertoont de pyriet in de mafische gesteenten rondom de Londozi bariet isotopen ratios die duiden op het mengen van zwavel afkomstig uit zowel de mantel als het zeewater, mogelijk van lokale biologische processen.

De resultaten in dit proefschrift laten zien dat het meten van alle vier de isotopen van zwavel (inclusief ^{36}S), evenals het verkrijgen van gedetailleerde geologische en geochemische informatie over het afzettingsmilieu en secundaire

alteratieprocessen, van belang zijn voor de correctie interpretatie van zwavel isotopen data uit vroeg Archaeische gesteenten. Echter, indien op weloverwogen wijze toegepast, vormen stabiele zwavel isotopen een geschikte methode voor het identificieren van biologische activiteit in de vroegste zwavel cyclus op Aarde, alsmede voor het opsporen van vroeg microbieel leven op Mars.

ACKNOWLEDGEMENTS

The last four years have been a challenging but rewarding journey towards finishing this thesis. But no road is long with good company, and I am grateful for the help and support of so many people both inside and outside of academia.

First of all, I would like to thank my advisor Paul Mason for his support and openness to endless brainstorm sessions about results that did not seem to make sense at first sight. Thank you for letting me chose my own path in the project (swapping lab hours for fieldwork in Swaziland and heading back to Stockholm in my final year for even more isotope analyses), and your trust in me as an independent researcher. I am grateful that you encouraged me to work with great research groups abroad and visit as many places as possible, including South Africa, Greenland and Australia in less than five months time - definitely a high score in the Archean craton bingo! Despite somewhat limited contact, I would also like to thank my other co-promotor Colin Peach and promotor Martyn Drury for their assistance and careful reading of my thesis in the final hours before submission.

Many results in this thesis would not have been there without the help of people from outside Utrecht University and I consider myself incredibly lucky to have worked with them. James Farquhar, thank you for providing me with the opportunity to lock myself up in your lab for three weeks to analyze all of my barite samples, and for your great help with improving the paper. Martin Whitehouse, even though my first visits to the Nordsim lab ended up enjoying the early Spring sunshine in Stockholm instead of collecting sulfur isotope data from sample BBBB-something, later visits have been incredibly fruitful and I am thankful for your help and effort in getting more than 500 SIMS analyses in this thesis. Thank you for finding time in the busy Nordsim schedule to play with ^{36}S and trace element measurements. Fraukje Brouwer, your help during my fieldwork in Swaziland has been invaluable and without our discussions on metamorphism and metasomatism, this isotope geochemist would never have been able to write a chapter that includes thermobarometric calculations. Thomas Reimer, even though we have never actually met in person, thank you for your inputs on the geological backgrounds in my manuscripts and for providing some of the samples analyzed in this work. Finally, David Lowry and Nathalie Grassineau, although the results did not make it into this thesis, I am thankful for

your help with selecting pyrite samples from your extensive collection of Dalradian shales.

Three of the chapters in this thesis are based on fieldwork performed in Swaziland in 2010 and 2011, and I am grateful to Noah Nhleko, the Geological Survey and Mines Department of Swaziland and its director Simon Maphanga for their logistical support and for providing me with the right documents to ship over 120 kg of rocks back to the Netherlands. I would also like to thank Mario Hendriks and Willem van der Bilt for their assistance in collecting these rock samples (sorry Willem, next time I will choose a field area without terribly hard chert and asbestos-rich rocks…), and the people of Swaziland for their genuine warm welcome. The photos printed in this thesis were all taken during or after fieldwork and represent a little tribute to this small but beautiful country.

Rocks would have just been rocks if I had not received so much help in the lab analyzing them. Thank you Aubrey Zerkle for getting me started with the sulfur isotope measurements and providing me with caffeine-support, and Kerstin Lindén for patiently cutting, polishing and gold coating my samples for the SIMS. Special words of appreciation also go out to the lab team at Utrecht University. Helen de Waard, thank you for patiently digesting and analyzing my rock samples, for your technical support during my laser ablation work, and for your help with setting-up the barite reduction procedure (no more boiling of concentrated strong acids, pfew!). Tilly Bouten, your help has been invaluable during those many weeks of electron microprobe analyses. Thank you for letting me call you at home on your day off whenever something had to be fixed, and for the Libelles during long analytical runs. I would also like to acknowledge Dineke van der Meent, Arnold van Dijk, Peter van Krieken, Gert Kastelein, Jan Drenth and Pieter Kleingeld for their help and support, from ordering chemicals to learning me how to weld and finding ingenious ways to get miniscule amounts of fluids out of a pressurized gold jacket. Furthermore, none of this work would have been possible without the rock polishing and thin section preparation skills of Otto Stiekema - rock polishing is clearly not one of my greatest talents, so thank you for helping me out.

Niet in het lab, maar wel onmisbaar: Pien van Minnen, bedankt voor alle adminstratieve support de afgelopen jaren en het regelen van de praktische zaken rondom dit proefschrift.

Most of all, there is no doctorate diploma without an assessment committee, so I am highly grateful to James Farquhar, Gary Stevens, Harald Strauss, Jan Wijbrans and Martin Whitehouse for their time and patience to read through nearly 250 pages of PhD thesis.

Thanks to great friends and colleagues at Utrecht University, I managed to stick around for almost ten years at the Department of Earth Sciences. Manfred (thanks for your support ever since my BSc thesis), Igor (Շնորհակալություն, I guess…), Marjolijn, Kristen, Melike, Kathrin, Inge, Alejandro (thanks for the chocolates on International Woman's Day!), Aleksandra, Nicole, Dewany and Sonja from the Petrology group, thanks for your support and the fun times we have shared in the last four years. Marjolijn, het is alweer jaren geleden dat wij samen promovendi waren, maar met jou kon ik als geen ander alle frustraties delen die horen bij het doen van promotie-onderzoek. Ik ben blij dat we ook na jouw promotie goed bevriend zijn gebleven en er heel wat roddels en slechte grappen met lekker fractionerende sulfaatjes over de kaasfondue heen en weer zijn gevlogen (sorry Michel). Super dat je mijn paranimf wil zijn! Inge, jij arriveerde pas in het laatste jaar van mijn promotie-onderzoek, maar bent sindsdien een grote inspiratiebron geweest. Jouw enthousiasme is enorm aanstekelijk en je oprechte betrokkenheid heb ik erg gewaardeerd. Niet alleen op wetenschappelijk vlak, maar ook als het ging om fødselsnummers en afscheid nemen. Thanks for looking after me en de spontane diners tijdens mijn laatste paar maanden in Utrecht, en ik hoop dat we samen een mooie publicatie kunnen schrijven waarin we onze expertises kunnen combineren. Sonja, we have shared a lot of frustrations, fun and science in our stuffed little office for more than three years… Thanks for everything and good luck finishing your own thesis! From other research groups in the department, thanks Maartje, Côme, Gill, Reinoud, Herman, Marie-Louise, Rick, Peter (the tube whisperer), Mathilde, Mariette, Douwe, Cedric, Appy, Martijn, Lennart, Maud, Frits and Wout for the fun times in Utrecht and abroad. Maartje, mijn PhD partner-in-crime met een proefschrift deadline slechts twee weken na die van mij: WE ZIJN KLAAR!! Jeuh! Dank voor alle koffieleutsessies bij het scheldende koffie-apparaat, en op naar café Mieke.

Er zijn gelukkig heel wat avonden geweest waarop ik de afgelopen vier jaar even stoom heb kunnen afblazen bij vrienden. Lieve Kalijn, sinds onze kennismaking op de Aarde.nu prijsuitreiking in 2003 hebben we samen heel wat avonturen mee

mogen maken, van valpartijen in rozenstruiken op veldwerk tot een wandeltocht met veel te zware rugzakken in Wales. Jouw opgewekte humeur en passie voor buitensport is aanstekelijk en ik ben jou en Sander dankbaar om de vele gezellige avondjes in Utrecht en Werkhoven die even de druk van de promotie-ketel haalden. Geweldig dat jullie zo snel al naar Noorwegen kwamen om die traditie voort te zetten, en dankjewel dat je mijn paranimf wil zijn.

Mijn dank gaat ook uit naar Agnes (bedankt voor alle borrels en ontspannende sauna bezoekjes!) en Anne, Sietske (bedankt voor de gezellige trips naar Portsmouth, Londen en Sicilië!), Sanne, Matthijs en Agnes, Felix, Rick, Jet (bijna klaar!), Peter en Tessa, Peter en Isis, Eric en Marieke, Mark, Mark en Bette, Mark en Jenny voor alle gezellige avonden in de afgelopen vier jaar. Dank voor alle biertjes en etentjes!

In het bijzonder wil ik mijn oud-huisgenootjes Mette, Larissa en Jenita bedanken voor een fantastische tijd aan de Frits Coerslaan en daarna. Ook al zullen jullie van mijn promotie-onderzoek zelf weinig mee hebben gekregen, de hilarische middagen en avonden met het ophalen van herinneringen uit wc-schriftjes, complexe sinterklaasspellen en lekkere lange spatels waren voor mij een fijne afleiding uit de wereld van de beta-nerds.

Het allergrootste dankjewel gaat echter uit naar mijn familie. Lieve pap en mam, bedankt voor alle jaren van steun en liefde die jullie aan mij hebben gegeven en het warme nest waarin ik altijd thuis kon komen. Dankzij jullie kon ik mijn dromen waarmaken en Aardwetenschappen gaan studeren, en zonder die support en betrokkenheid had het kleine meisje dat ooit gefascineerd naar het wiel van een Concorde stond te kijken en uitleg kreeg over het zonnestelsel met sinaasappels en een pak Brinta (arme Felix...) nooit dit boekje kunnen produceren. Lieve Mariska en Dennis, wat was het fijn dat jullie altijd letterlijk en figuurlijk in de buurt waren in de afgelopen jaren dat ik in Utrecht heb gewoond! Als zussen hebben we heel wat mooie tijden samen beleefd, adviezen aan elkaar uitgewisseld en met elkaar gelachen om gekke mede-wandelaars en piña colada oplospoeder. Dankjewel dat jullie tot het allerlaatste moment voor mij klaarstonden met schroevendraaiers en de broodnodige afleiding van de promotie- en verhuisstress! Ook mijn schoonfamilie Eric, Mirjam, Emma, Nora en Arne, bedankt voor jullie nuchtere blik op de wereld van het promoveren, de onuitputtelijke hoeveelheid biertjes en de rustgevende wandelingen in de Drentse natuur.

Tot slot, lieve Willem, jij moet je als kwartairgeoloog toch regelmatig hebben afgevraagd wat ik nou toch moest met die ouwe zooi. Toch was je gek genoeg om in een oud camperbusje meer dan 7000 kilometer door Australië te rijden omdat ik graag de banded iron formations van de Pilbara wilde zien, en wisselde je jouw laatste vakantiedagen van 2011 in om mij te helpen met mijn veldwerk in Swaziland. Bovenal heb je het geduld weten op te brengen om in Utrecht te blijven tot het einde van mijn promotie, ondanks dat er voor jou elders nieuwe carrièreperspectieven aan de horizon lonkten. Het is eigenlijk onmogelijk om hier te beschrijven hoeveel dat voor mij betekent. Ik ben je dankbaar voor je nuchterheid en je immer kritische blik op de wereld en de wetenschap, de spontane weekendjes en weekjes weg die je stiekem boekte om even er tussenuit te zijn en de diepe gesprekken die ik met je kon voeren over alles dat me bezig hield. Met jou in de buurt verveel ik me nooit. Bedankt dat je er bent!

CURRICULUM VITAE

Desirée Lisette Roerdink was born on February 26, 1985 in Apeldoorn, The Netherlands. She followed her secondary education (Atheneum) at De Heemgaard in Apeldoorn (1997-2003), and won both the Aarde.nu thesis competition and the National Geography Olympiad in her final year. After completing her BSc in Earth Sciences *cum laude* (2006), she also obtained her MSc in Geology *cum laude* from Utrecht University in 2008. For her MSc thesis, she investigated the fractionation of stable silicon isotopes during precipitation of silica in batch-reactor experiments, as analogue for the formation of Archean chert deposits. Her work was awarded with the KNGMG Escher Prize for the best Master thesis in Earth Sciences in the Netherlands in 2009. After three months of voluntary research in gas geochemistry at the USGS Hawaiian Volcano Observatory, she returned to Utrecht in early 2009 to start her PhD project with dr. Paul Mason. During her doctoral research, she visited stable isotope laboratories at the University of Maryland (United States) and the Swedish Museum for Natural History in Stockholm, attended field workshops in Greenland and South Africa and performed geological fieldwork in Swaziland in 2010 and 2011. Results from her work were presented by Desiree at workshops in South Africa, Finland and Germany, the Netherlands Earth Scientific Congress (2010, 2012), the International Archean Symposium in Perth, Australia (2010), and the Goldschmidt conferences in Prague, Czech Republic (2011) and Montreal, Canada (2012). Desiree now works as a researcher at the Center for Geobiology at the University of Bergen in Norway.